LBNL-48818

ERNEST ORLANDO LAWRENCE BERKELEY NATIONAL LABORATORY

Structure and Properties of Co-Based Thin Films and Multilayers with Perpendicular Magnetic Anisotropy

Grzegorz J. Kusinski

Materials Sciences Division

December 2001

Ph.D. Thesis

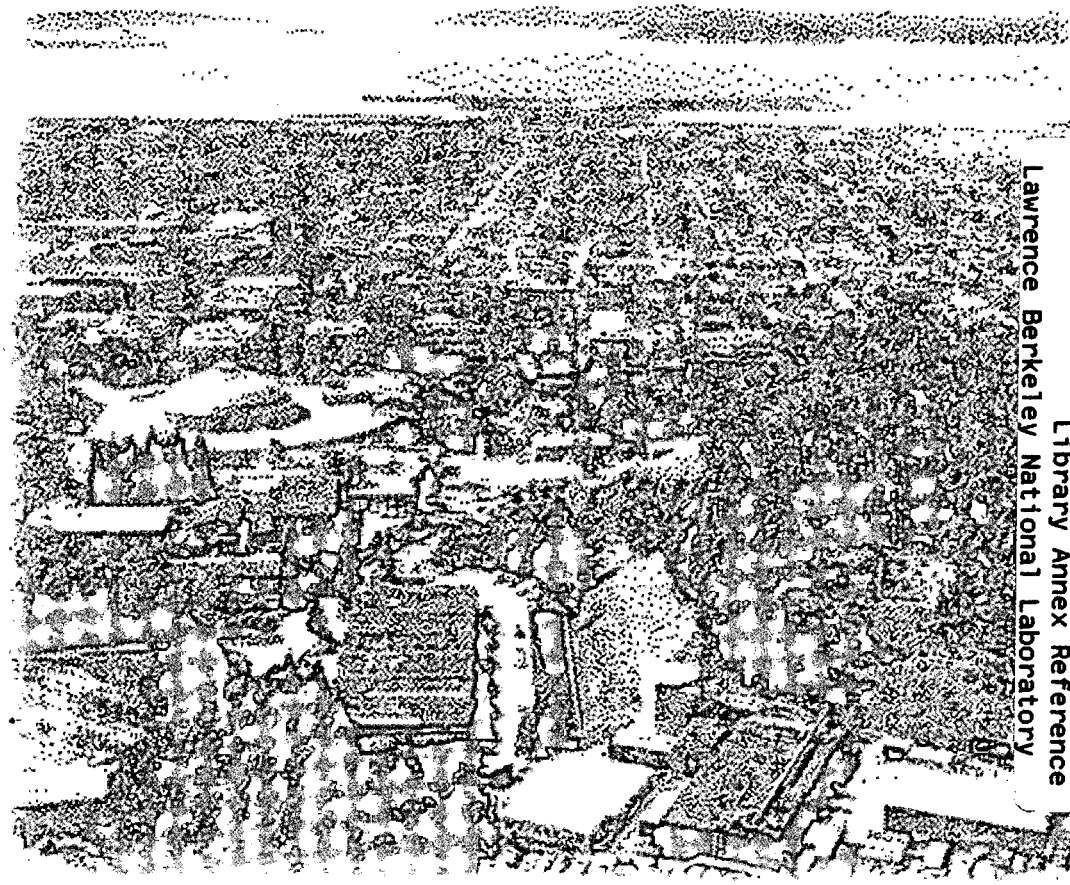

REFERENCE COPY
Does Not
Circulate
Library Annex Reference
Lawrence Berkeley National Laboratory
LBNL-48818
Copy 1

DISCLAIMER

This document was prepared as an account of work sponsored by the United States Government. While this document is believed to contain correct information, neither the United States Government nor any agency thereof, nor the Regents of the University of California, nor any of their employees, makes any warranty, express or implied, or assumes any legal responsibility for the accuracy, completeness, or usefulness of any information, apparatus, product, or process disclosed, or represents that its use would not infringe privately owned rights. Reference herein to any specific commercial product, process, or service by its trade name, trademark, manufacturer, or otherwise, does not necessarily constitute or imply its endorsement, recommendation, or favoring by the United States Government or any agency thereof, or the Regents of the University of California. The views and opinions of authors expressed herein do not necessarily state or reflect those of the United States Government or any agency thereof or the Regents of the University of California.

LBNL-48818

Structure and Properties of Co-Based Thin Films and Multilayers with Perpendicular Magnetic Anisotropy

Grzegorz Jan Kusinski
Ph.D. Thesis

Department of Materials Science and Engineering
University of California, Berkeley

and

Materials Sciences Division
Ernest Orlando Lawrence Berkeley National Laboratory
University of California
Berkeley, CA 94720

December 2001

This work was supported by the Director, Office of Science, Office of Basic Energy Sciences, Materials Sciences Division, of the U.S. Department of Energy under Contract No. DE-AC03-76SF00098.

STRUCTURE AND PROPERTIES OF CO-BASED THIN FILMS AND MULTILAYERS WITH PERPENDICULAR MAGNETIC ANISOTROPY

by

Grzegorz Jan Kusinski

B.S. (University of California, Berkeley) 1996
M.S. (University of California, Berkeley) 1998

A dissertation submitted in partial satisfaction of the

requirements for the degree of

Doctor of Philosophy
in

Engineering-Materials Science and Engineering

in the

GRADUATE DIVISION

of the

UNIVERSITY OF CALIFORNIA, BERKELEY

Committee in charge:

Professor Gareth Thomas, Chair
Professor Ronald Gronsky
Professor Alan Portis
Professor Kannan M. Krishnan

Fall 2001

Structure and Properties of Co-Based Thin Films and Multilayers with Perpendicular Magnetic Anisotropy

Copyright © 2001

by

Grzegorz Jan Kusinski

The U.S. Department of Energy has the right to use this document
for any purpose whatsoever including the right to reproduce
all or any part thereof.

Abstract

Structure and properties of Co-based thin films and multilayers with perpendicular magnetic anisotropy

by

Grzegorz Jan Kusinski

Doctor of Philosophy in Engineering-Materials Science and Engineering

University of California, Berkeley

Professor Gareth Thomas, Chair

The effects of growth temperature, T_G, and ion-irradiation on the magnetic properties and microstructure of Co/Pt multilayers with perpendicular anisotropy were investigated. The columnar-grain size and the <111> texture were found to increase with an increase in T_G. Up to a critical temperature, T_{crit}, a monotonic increase in coercivity, H_C, with T_G was measured, followed by a decrease in coercivity above T_{crit}. The magnetic domains of films grown below T_{crit} were irregular and paisley-like and their sub-micron size decreased with increasing T_G. Above T_{crit}, sub-100 nm domains were found. A decrease in H_C and domain size was measured when multilayers were exposed to ion-irradiation. The ion-induced changes in the magnetic properties are associated with a decrease in interfacial anisotropy, K_S. Transmission electron microscopy, the ion-irradiation simulations and the calculations of interface anisotropy found the ion-induced changes of magnetic properties not to be caused by the large microstructural changes but to be associated with localized ion-beam induced atomic disordering at the Co/Pt interfaces. At high enough doses, K_S becomes comparable to the shape anisotropy and a transition to in-plane magnetization results. The principles of ion-

modification were applied to pattern the magnetic properties of the Co/Pt multilayers down to below 100 nm periodic arrays by irradiation through a stencil mask or direct focused ion beam writing. The magnetic domain confinement and changes in the magnetic reversal processes due to the ion-irradiation patterning were studied for two types of magnetic arrays: (a) in-plane magnetized dots surrounded by out-of plane matrix and (b) of out-of-plane bits surrounded by in-plane lines. Two complementary magnetic imaging techniques were utilized: Lorentz transmission electron microscopy sensitive to in-plane magnetization and magnetic transmission x-ray microscopy sensitive to perpendicular magnetization. The boundaries of the patterns, defined by the transition from out-of-plane to in-plane magnetization, were determined by the irradiation pattern. Softening of the in-plane regions (H_C < 300 Oe) as compared to the out-of-plane coercivity was found. The perpendicular reversals were found to always originate at the pattern boundaries at substantially reduced nucleation fields and to be influenced by the microstructure. Bit patterns larger than ~100 nm islands were found to be multi-domain and below 100 nm, single-domain bits were recorded.

C-axis oriented CoCr films were grown and the magnetic domain structure was investigated as a function of sample thickness and temperature. A transition thickness from large in-plane domains to up-down stripe domains was found to increase with temperature.

Dla moich rodziców Jadwigi i Jana

(To my parents Jadwiga and Jan)

TABLE OF CONTENTS

Table of Contents iii

List of Figures ix

List of Tables xvii

Acronyms xix

Acknowledgements xxi

Chapter 1 1

Introduction 1

1.1. Outline 1

1.2. Introduction to magnetic recording 5

1.2.1. History of magnetic recording 5

1.2.2. Principles of longitudinal magnetic recording 8

1.2.2.1. Thermal stability, superparamagnetic limit 11

1.2.3. Approaches to overcome superparamagnetic limits 15

1.2.3.1. Perpendicular magnetic recording 15

1.2.3.2. Patterned media 17

1.3. Categories of magnetic materials 19

1.4. Ferromagnetism and magnetic domains 23

1.4.1. Exchange energy 25

1.4.2. External field energy 26

1.4.3. Magnetostatic energy 26

1.4.4. Magnetic anisotropy 26

1.4.5. Magnetic domains 27

1.4.6. Ferromagnetic thin film 28

1.4.7. Systems with perpendicular magnetic anisotropy 30

Chapter 2 35

Experimental methods background 35

2.1. Magnetic measurements 35

2.1.1. Magnetic curves and anisotropy 35

2.1.2. Vibrating sample magnetometer 36

2.1.3. Magneto-optical Kerr effect 37

2.2. Structural characterization techniques 39

2.2.1. Transmission electron microscopy 39

2.2.1.1. Dark-field hollow-cone imaging 40

2.2.1.2. Energy-filtered imaging 41

2.3. Magnetic imaging techniques 44

2.3.1. Lorentz transmission electron microscopy 45

2.3.1.1. Fresnel and Foucault imaging 46

2.3.1.2. Quantitative Foucault imaging 51

2.3.2. X-ray techniques 53

2.3.3. Magnetic contrast formation by XMCD 54

2.3.4. Full field magnetic transmission x-ray microscopy 56

2.3.4.1. Magnetic contrast at XM-1 58

2.3.4.2. Imaging variables and challenges 61

2.3.5. Magnetic force microscopy 61

Chapter 3. Experimental: 63

Cobalt-Platinum multilayers 63

3.1. Objective of the research 66

3.2. Experimental procedures 66

3.3. Microstructural characterization 70

3.3.1. Analysis of the multilayers as a function of growth temperature 83

3.3.2. Structure as a function of Co thickness 90

3.4. Magnetic properties 92

3.4.1. Magnetic hysteresis loops 92

3.4.2. Magnetic domain structures 96

3.5. Summary 100

Chapter 4 101

Ion modification of magnetic properties 101

4.1. Motivation 101

4.2. Modification of magnetic properties by ion irradiation 103

4.2.1. Experimental procedures 103

4.2.2. Results and discussion 104

4.3. Physical modification, mechanism 108

4.3.1. Results and discussion 108

4.3.2. Cross-sectional investigation 115

4.3.3. TRIM simulation of ion irradiation 121

4.3.4. Modeling 122

4.4. Magnetic domain-structure as a function of ion dose. 124

4.4.1. Experimental Procedures 124

4.4.2. Results and discussion 125

4.5. Summary 129

Chapter 5 131

Magnetizing experiments in patterned Co/Pt multilayers 131

5.1. Magnetic patterning by selective ion-irradiation 131

5.2. Experimental procedures 132

5.2.1. Choice of the multilayers system for patterning 132

5.2.2. Irradiation through a stencil mask 133

5.2.3. Patterning with a focused ion beam 135

5.3. Experimental results and discussion 136

5.3.1. Sample #I, mask irradiation $1 \cdot 10^{16}$ 700 keV N^+/cm^2 136

5.3.1.1. Magnetic imaging with Lorentz TEM (LTEM) 136

5.3.1.2. Magnetic transmission x-ray microscopy (MTXM) 149

5.3.2. Sample #II, mask $1 \cdot 10^{16}$ and plain $5 \cdot 10^{14}$ 700 keV N^+/cm^2 165

5.3.3. Sample #III, mask $5 \cdot 10^{14}$ and plain $5 \cdot 10^{14}$ 700 keV N^+/cm^2 167

5.3.4. Focused ion-beam patterning 170

5.3.4.1. Pattern FIB#1 173

5.3.4.2. Pattern FIB#2 175

5.4. Summary 177

Chapter 6 179

Spin reorientation studies in c-axis oriented Co-Cr films 179

6.1. Introduction 179

6.2. C-axis oriented Co-based thin films 180

6.3. Experimental procedures 184

6.4. Experimental results 186

6.4.1. Co-Cr microstructure and magnetic properties 186

6.4.2. Stripe domain patterns and spin reorientation. 194

6.5. Summary 200

Chapter 7 201

Conclusions 201

Appendix A. Values of Selected Physical Constants 205

Appendix B. Units CGS and SI. 206

Appendix C. Background of ion-matter interaction. 207

Nuclear stopping 208

Electronic stopping 209

Damage-physics of recoil cascades 210

References: 213

LIST OF FIGURES

Figure 1–1. The rate of growth of areal recording density. 7

Figure 1–2. (a) Schematic diagram illustrating the basic principles of a magnetic recording system. (b) Lorentz TEM image of overwrite experiment on 1 Gbit/in^2 media..... 9

Figure 1–3. Schematic of a typical thin film architecture used in longitudinal magnetic recording. 9

Figure 1–4. Schematic illustrating longitudinal and perpendicular bit arrangement showing destabilizing and stabilizing fields, respectively. 16

Figure 1–5. Magnetization versus applied magnetic field. (a) Diamagnetic material, χ is a negative constant. (b) Paramagnetic material, χ is a positive constant. (c) Ferromagnetic material, the path of magnetization exhibits hysteresis; magnetic susceptibility is not a simple constant..... 21

Figure 1–6. A graphical representation of (a) diamagnet (b) paramagnet, (c) ferromagnet and (d) antiferromagnetic powder. T_N is the Néel temperature. 23

Figure 1–7. A schematic plot of the hysteresis loop of a ferromagnetic material defining the relevant parameters. H_N is the nucleating field, H_S is the saturating field, and H_C is the coercive field. Similarly M_S is the saturation magnetization and M_R is remanent magnetization..... 24

Figure 1–8. Magnetization curves for magnetic thin films having (a) in-plane preferential magnetization, (b) perpendicular magnetization and small domains, (c) perpendicular magnetization with large magnetic domains..... 28

Figure 1–9. Plot of $K_{eff} \cdot t$ versus t for Co/Pd system after [den Boreder - 1991]... 32

Figure 2–1. Principles of beam tilting in the TEM. 40

Figure 2–2. Electron energy loss about Co L_3-edge. Rectangular areas show energy ranges used to obtain energy-filtered images with 20 eV slit. 42

Figure 2–3. The principle of the Fresnel technique of Lorentz TEM. The object plane is fixed (a) below the specimen and (b) above the specimen. Images show domains in a polycrystalline Permalloy (note domain-wall contrast reversal). 48

Figure 2–4. The principle of the Foucault imaging mode of Lorentz TEM. Images show the same areas as Figure 2–3. Note contrast-reversal when the objective aperture is moved. 49

Figure 2–5. Principles of quantitative Foucault imaging in TEM (see text). 52

Figure 2–6. Principles of X-ray magnetic circular dichroism, for the case of L edge absorption in a d band transition metal. 55

Figure 2–7. (a) The XM-1 Soft X-ray Microscope at the Advanced Light Source, Beam-line 6.1.2. (b) Scanning electron micrograph of the 25 nm zone plates (courtesy G. Denbeaux, E. Anderson [Anderson - 2000]). 57

Figure 2–8. Schematic diagrams illustrating the magnetic contrast mechanism in the MTXM. (a) L_3 and L_2 absorption edges with three levels of μ depending on the relative orientation of **M** and σ_{photon}. (b) Magnetic sample with up, down and in-plane domains and a recorded image displaying three intensity levels measured in the X-ray microscope at the L_3 edge. 59

Figure 2–9. Principles of Magnetic Force Microscopy (MFM). 62

Figure 3–1. Binary Co-Pt phase diagram [Massalski - 1990]. 65

Figure 3–2. (a) Plan-view TEM micrograph and (b) SAD pattern of a 10×(3 Å Co / 10 Å Pt) multilayer grown at T_G = 250°C, (c) SAD with 30° sample tilt showing arcing of the rings. 71

Figure 3–3. Simulated diffraction pattern for polycrystalline *fcc* Pt film overlayed on the recorded SADs from Figure 3–2. (a) 0° sample tilt (b) 30° sample tilt. 73

Figure 3–4. Enlarged section of the SAD pattern presented in Figure 3–2, showing closely spaced Pt(220) and Co(220) rings. 75

Figure 3–5. (a) SAD pattern for the discussed Co/Pt multilayer and simulated plan-view diffraction patterns for (b) Pt_{fcc} and $CoPt_3$, (c) Pt_{fcc} and Co_{hcp}, and (d) Pt_{fcc} and Co_{fcc}. Triangles label Pt rings (see text)..... 76

Figure 3–6. Simulated plan-view diffraction patterns of Pt_{fcc} and Co_{fcc} at various strains as indicated on images. Numbers label rings: 1) Pt(111), 2) Co(111), 3) Pt(002), 4) Co(002), 5) Pt(022), 6) Co(022), 7) Pt(113), 8) Pt(222), 9) Co(113), 10) Co(222). 77

Figure 3–7. Cross-sectional micrographs of a 10×(3 Å Co / 10 Å Pt) multilayer grown at T_G = 250°C. 80

Figure 3–8. Plan-view BF TEM images, SAD patterns and (111)DF images of the Co/Pt ML's grown at T_G = 190°C, T_G = 250°C and T_G = 390°C, displayed in rows. All SAD's were collected with a 5 μm aperture.. 84

Figure 3–9. BF image of samples grown at T_G = 250°C, and line profiles across some of the Moiré fringe contrast. 85

Figure 3–10. Enlarged SAD patterns from (a) T_G = 190°C, (b) T_G = 250°C, (c) T_G = 300°C, and (d) T_G = 390°C samples..... 86

Figure 3–11. HRTEM image of 15 Å, Co layer in the Co/Pt multilayer..... 91

Figure 3–12. Magnetic hysteresis vs. multilayer growth temperature. (a) T_G = 190°C, (b) T_G = 250°C, (c) T_G = 300°C and (d) T_G = 390°C. 93

Figure 3–13. Growth-temperature dependence of the room temperature perpendicular coercivity of a series of 10×(3 Å Co / 10 Å Pt) multilayers..... 94

Figure 3–14. MTXM images showing magnetic domains in the as-grown Co/Pt multilayers. Samples grown at different T_G: (a) 190°C, (b) 250°C, (c) 390°C..... 97

Figure 3–15. Sample T_G = 250°C imaged at (a) As-grown $H_\perp$ = 0 kOe, (b) $H_\perp$ = 1.8 kOe (c) $H_\perp$ = +3.5 kOe (d) $H_\perp$ = 0 kOe, (e) $H_\perp$ = -1.8 kOe and (f) $H_\perp$ = -3.5 kOe. 99

Figure 4–1. Polar Kerr hysteresis loops of a Co/Pt multilayer subjected to N^+ ion irradiation at various doses..... 105

Figure 4–2. Normalized perpendicular coercivity and perpendicular remanence as a function of N^+ ion dose for two samples with different initial coercivity (see text). 106

Figure 4–3 Dependence of coercivity on ion-beam exposure for Co/Pt multilayer sample. Coercivities are normalized to zero-dose values. The curves are a fit to exponential decay. Data courtesy of C. Rettner [Rettner - submitted]. 107

Figure 4–4. Bright field TEM images of Co/Pt multilayer $T_G = 250°C$ (a) as grown (b) irradiated with $5 \cdot 10^{16}$ N^+/cm^2. 109

Figure 4–5. SAD patterns of Co/Pt multilayer $T_G = 250°C$ (a) as grown (b) irradiated with $5 \cdot 10^{16}$ N^+/cm^2. 111

Figure 4–6. TEM bright field images in the vicinity of the boundary between irradiated and non-irradiated areas. Irradiation fluence was $2 \cdot 10^{16}$ of 30 keV Ga^+/cm^2 (b) larger magnification 114

Figure 4–7. Schematic of the Co/Pt multilayer structure used to study resolution limits of electron energy loss TEM imaging 116

Figure 4–8. Energy filtered imaging of the Co/Pt resolution test sample from Figure 4–7. Images show: (a) pre-edge 1, (b) pre-edge2, (c) post-edge, (d) pre-edge1/pre-edge2, (e) Co jump-ratio, (f) Co elemental map. (g) and (h) Line profiles across image (e) 119

Figure 4–9. Profiles of Co versus ion dose, calculated with TRIM (T-DYN 4.0), see text. 121

Figure 4–10. Magnetic domain structure in Co/Pt multilayers (a) as-grown (b) after ion irradiation with 700 keV $5 \cdot 10^{14}$ N^+/cm^2 126

Figure 4–11. Magnetic domain structure in Co/Pt multilayers (a) as-grown (b) after ion irradiation with 30 keV $3 \cdot 10^{12}$ Ga^+/cm^2, (c) 30 keV $3 \cdot 10^{14}$ Ga^+/cm^2. 126

Figure 4–12. Magnetic domain structure and H_C versus T_G and the ion dose..... 128

Figure 5–1. TRIM simulation of absorption of 700 keV N^+ ions in Si. 134

Figure 5–2. (a) Fresnel LTEM image of the Co/Pt multilayer patterned by ion-irradiation through a stencil mask with a dose of $1 \cdot 10^{16}$ N^+/cm^2, (b) magnified image, (c) schematic of the patterning geometry..... 139

Figure 5–3. Foucault images of the Co/Pt multilayer patterned by ion-irradiation through a stencil mask with a dose of $1 \cdot 10^{16}$ N^+/cm^2. Arrows show the direction of the beam tilt (a) +X, (b) –X. Two circles indicate same sample locations..... 140

Figure 5–4. Schematic diagram illustrating the tilting in TEM. Chart shows the perpendicular and in-plane components of the magnetic field as a function of the sample tilt angle. 142

Figure 5–5. Fresnel images of the patterned sample with in-plane field of: (a) $H_{||}$ = +264 Oe and (b) $H_{||}$ = -264 Oe. (c) and (d) Respective schematics explaining the contrast..... 144

Figure 5–6. A series of Fresnel images of patterned multilayers recorded at different sample tilts. a) tilt =10°; $H_{||}$ = 264 Oe, b) tilt = 0.3°; $H_{||}$ = 7 Oe, c) tilt = -2°; $H_{||}$ = -54 Oe, d) tilt = -3.1°; $H_{||}$ = -82 Oe, e) tilt = -5.1°; $H_{||}$ = -135 Oe, f) tilt = -10°; $H_{||}$ = -264 Oe..... 146

Figure 5–7. Foucault images of the Co/Pt multilayer patterned by ion-irradiation through a stencil mask with a dose of $1 \cdot 10^{16}$ N^+/cm^2. Arrows show the direction of the beam tilt. Two circles indicate same sample locations. (a) $H_{||}$ = 0, +X, (b) $H_{||}$ = 0, -X, (c) $H_{||}$ = -400 Oe, +X, (d) $H_{||}$ = -400 Oe, -X, (e) $H_{||}$ = +400 Oe, -X..... 148

Figure 5–8. MXTM images of the patterned Co/Pt multilayers recorded at the Co L_3 absorption edge. Both images recorded at remanence after saturation with (a) $H_\perp$ = +14 kOe, and (b) $H_\perp$ = –14 kOe. (c), (d) normalized line profiles obtained from the areas labeled with rectangles on images (a) and (b) respectively. 150

Figure 5–9. MTXM images showing a progress of an *ex-situ* magnetizing experiment. (a) $H_\perp$ = –14 kOe, (b) Onset of nucleation at the edges of irradiated patterns, $H_\perp$ = +1 kOe (c) $H_\perp$ = +2 kOe, (d) $H_\perp$ = +3 kOe, (e) $H_\perp$ = +4 kOe, (f) $H_\perp$ = +5 kOe, (g) $H_\perp$ = +6 kOe, (h) $H_\perp$ = +7 kOe,

(i) Normalized MOKE hysteresis loop of an as-grown Co/Pt multilayer. 153

Figure 5–10. Larger area MTXM images showing tree-like rough growth. Image recorded after saturation at $H_\perp$ = -14 kOe and subsequent application of $H_\perp$ = +5 kOe to nucleate black domains. A normalized line profile is obtained from the area labeled with the rectangle.... 156

Figure 5–11. Same location and opposite contrast. (a) $H_\perp$ = -14 kOe and $H_\perp$ = +4 kOe (b) $H_\perp$ = +14 kOe and $H_\perp$ = -4 kOe. 157

Figure 5–12. MTXM image, showing magnetic reversal, superimposed onto the TEM image, detailing the microstructure. Both images are shown at the same magnification. 158

Figure 5–13. MTXM image recorded at remanence after a following magnetizing sequence: (1) saturation with $H_\perp$ = +14 kOe, (2) application of $H_\perp$ = -5 kOe, (3) application of $H_\perp$ = +3 kOe. Schematic shows the domain evolution during these three magnetizing steps. 161

Figure 5–14. Progress of the in-situ magnetizing experiment. Images were acquired with the applied magnetic field. (a) $H_\perp$ = -3 kOe, (b) $H_\perp$ = 0, (c) $H_\perp$ = +3 kOe and (d) $H_\perp$ = 0. 163

Figure 5–15. Schematic of the reversal process in the ion-irradiation patterned Co/Pt multilayers. Sample colors indicate the orientation of magnetization: black – up, white – down, gray – in-plane. Large arrows show magnitude and direction of the applied field H_A. 164

Figure 5–16. Sample #II, progress of an *in-situ* MTXM experiment. (a) $H_\perp$ = 0, (b) $H_\perp$ = +0.47 kOe, (c) $H_\perp$ = +0.67 kOe, (d) $H_\perp$ = +1.00 kOe, (e) $H_\perp$ = +1.04 kOe, (f) $H_\perp$ = +1.20 kOe, (g) $H_\perp$ = +1.35 kOe, (h) $H_\perp$ = +2.85 kOe and (i) $H_\perp$ = -1.30 kOe. 166

Figure 5–17. Sample #III, progress of an *in-situ* MTXM experiment. 169

Figure 5–18. Comparison of the stencil mask patterns with the FIB patterns. All images are displayed at same magnification, except for insert in (e). See text for details. 172

Figure 5–19. MTXM images of pattern FIB#1 with a period of 450 nm for different doses of 1 pA 30 keV Ga^+ beam. The exposures were (a) 3 s, (b) 6 s, (c) 12 s and (d) 14 s. Images were recorded after 1)-14 kOe and then 2) +3 kOe. 174

Figure 5–20. Sample FIB#2, progress of an *in-situ* MTXM experiment. 176

Figure 6–1. (a) Schematic drawing of the lattice planes of Si(111), Ag(111) and Co (0001), and their lattice parameters. (b) Schematic of the cross-section of the designed structure. 182

Figure 6–2. CoCr phase diagram [Massalski - 1990] 183

Figure 6–3. (a) θ-2θ X-ray diffraction spectra of a $Co_{95}Cr_5$ 100nm/Ag 500nm/Si(111) film (b) rocking curves (θ-scans) for the Ag (111) and $Co_{95}Cr_5$ (0002) peaks 187

Figure 6–4. Rutherford back-scattering analysis data. 187

Figure 6–5. (a) Bright field TEM image of the $Co_{95}Cr_5$, (b) SAD pattern. 188

Figure 6–6. (a) Magnetic hysteresis loops for both in-plane and perpendicular field directions, measured with VSM. (b) Enlarged portion of the perpendicular loop. 189

Figure 6–7. Fresnel image showing change of the magnetic domain pattern with increasing sample thickness 191

Figure 6–8. Series of images taken at different defocus above t_c (a) Bright field TEM image, (b) Fresnel image of the same area, defocus f = -15 um (c) f = +15um. 191

Figure 6–9. Images obtained by summing series of images according to the quantitative Foucault technique: (a) Σ(+x), (b) Σ(-x), (c) Σ(+y), (d) Σ(-y). The differential signal images, which are proportional to in-plane magnetization (e) Σ(+x) -Σ(-x), (f) Σ(+y) - Σ(-y). 192

Figure 6–10. Vector plot of the U and V components from Figure 6–9 (e) and (f). The length of the arrows corresponds to the magnitude of the in-plane component of magnetization. 193

Figure 6–11. Anisotropy constant versus temperature [Cullity - 1972] 195

Figure 6–12. (a) EELS thickness map. (b) Fresnel image of the area where *in-situ* heating was done, see Figure 6–13. 197

Figure 6–13. Fresnel images summarizing the temperature-dependent domain patterns. (a) – (f) Heating, (g) – (l) cooling. 198

Figure 6–14. Plot of the critical transition thickness $t_c = 13.6\ M_S^2 \cdot (A)^{1/2}/(K_u)^{3/2}$, as a function of temperature measured during an *in-situ* TEM experiment. 199

LIST OF TABLES

Table 3–1. Selected data for Co-Pt system. 65

Table 3–2. List of Co/Pt multilayers with structure 68

Table 3–3. Calculated Moiré spacing for Pt and strained Co layers. 89

Table 4–1. Summary of data from TRIM calculations and data calculated from Eq. 4–2. 123

Table 5–1. List of samples patterned by irradiation through a Si stencil mask. 134

Table 5–2. List of FIB patterned samples 135

Table 6–1. Lattice parameters and lattice misfit for Si, Ag and Co films. 182

Table C–1. Minimum and average displacement energies for Co and Pt 211

ACRONYMS

ALS	Advanced Light Source
BF	Bright Field imaging in TEM
DF	Dark Field imaging in TEM
DPC	Differential Phase Contrast in electron microscopy
EELS	Electron Energy Loss Spectroscopy
EFI	Energy Filtered Imaging
EFTEM	Energy Filtered Transmission Electron Microscopy
FFT	Fast Fourier Transform
FIB	Focused Ion Beam
FWHM	Full-Width-Half-Maximum
GMR	Giant Magnetoresistance
HRTEM	High Resolution Transmission Electron Microscopy
LCP	Left Circularly Polarized
LTEM	Lorentz Transmission Electron Microscopy
MFM	Magnetic Force Microscopy
ML	Multilayer
MO	Magneto-Optical
MOKE	Magneto-Optical Kerr Effect
MR	Magnetoresistive
MTXM	Magnetic Transmission X-ray Microscopy
PMA	Perpendicular Magnetic Anisotropy
RCP	Right Circularly Polarized
SAD	Selected Area Diffraction
SRIM	The Stopping and Range of Ions in Matter
SRT	Spin Reorientation Transition
STEM	Scanning Transmission Electron Microscopy
TEM	Transmission Electron Microscopy
TRIM	TRansport of Ions in Matter
VSM	Vibrating Sample Magnetometer
XMCD	X-ray Magnetic Circular Dichroism

ACKNOWLEDGEMENTS

First of all, I would like to express my gratitude to my advisor Professor Gareth Thomas for his support and supervision. His guidance over the years has allowed me to develop as a scientist.

I would like to thank Professor Kannan M. Krishnan for his scientific advise, many discussions and review of my dissertation, and Professors Ron Gronsky and Alan Portis for their support, and time and effort reviewing my dissertation. I am also grateful to my qualifying exam committee: Professors Ron Gronsky, Alan Portis, Tim Sands, and Daryl Chrzan.

Thanks to the entire scientific staff of the National Center for Electron Microscopy at Lawrence Berkeley National Laboratory, where I spent most of my graduate work-time. Thanks to Chris Nelson, John Turner, Doreen Ah Tye, Jane Cavlina, Seth Taylor, Tamara Radetic, Velimir Radmilovic, Erich Stach, Roar Kilaas, Michael O'Keefe, ChengYu Song, Ning Cheng, Erol Girt, Victor Puntes and Uli Dahmen.

I am indebted to my collaborators at the Advanced Light Source, especially Dr. Gregory P. Denbeaux, who introduced me to joys of x-ray microscopy. Thanks to the staff of the CXRO and their many hours of hard work and support which made my work possible.

Bruce Terris, Charles Rettner, Dieter Weller John Baglin, Andrew Kellock, Mike Toney, Liesl Folks, and the staff at the IBM Almaden Research Center helped me greatly with sample preparation, magnetic measurements, and ion-beam patterning; their efforts and useful discussions are greatly appreciated.

My graduate work was founded in large part by generous support from IBM through the Research Fellowship. The experimental work carried at the Lawrence Berkeley National Laboratory was supported by the Director, Office of Science, Office of Basic Energy Sciences, of the U.S. Department of Energy under Contract No. DE-AC03-76SF00098.

I would also like to thank all the fellow graduate students for their friendship, assistance, and many stimulating and mostly not scientific discussions. Special thanks to the "Strada boys"; the I-house-connection friends, and all of my soccer, basketball and volleyball teammates. ALL of you made my stay in Berkeley very enjoyable.

Special thanks to Stephanie; Thank you for being there for me and tolerating my weird and long work hours. And of course, thanks for proof reading the manuscript and understanding what my work was about!

Finally, thanks to my parents and family who encouraged me to STUDY HARD and have been supportive throughout my LONG educational career. They worked very hard so I could purse an undergraduate and graduate studies at Berkeley; Dziękuję!

Chapter 1.

INTRODUCTION

"Writing is easy; all you do is sit staring at a blank sheet of paper until the drops of blood form on your forehead." - Gene Fowler

1.1. Outline

Magnetic recording, a multimillion-dollar industry, is the backbone of the information age by reliably storing bits, (i.e. "1's" and "0's"). The areal magnetic storage density of hard disks has been increasing at a rate of 60% per annum during the 1990s. Extrapolation of this growth rate leads to a 100 Gb/in^2 density by about 2003. However, it is believed that increases much beyond this density will be limited using current technology based on longitudinal bit architecture. Thermal instability above the superparamagnetic limit of the grains comprising the magnetic media is one of the limiting factors. Hence, it is desired to move to new systems and to new recording architectures; this creates challenges for materials science.

This dissertation investigates Co-based thin films and multilayers with perpendicular magnetic anisotropy since they are good candidates for future

magnetic recording systems. The aim of this work is to gain a better understanding of how the easy axis of magnetization can be changed with varying processing parameters. Two systems with perpendicular magnetic anisotropy were investigated. These were Co/Pt multilayers and c-axis-oriented highly textured CoCr films. In the former system, the perpendicular anisotropy is governed by the Co/Pt interface contribution. In the latter one, the magnetocrystalline anisotropy of the hcp Co alloy was used to achieve out-of-plane magnetization.

For the case of the Co/Pt system, which was the main focus of this dissertation, the effects of processing parameters (growth condition and ion irradiation) on the magnetic properties were investigated. In particular, the aim was to gain a better understanding of the modification of magnetic properties by ion-beam irradiation. This involved investigation of the structure of the as-grown and irradiated multilayers with transmission electron microscopy (TEM), utilizing selected area diffraction (SAD), high-resolution TEM (HRTEM) and energy-filtered TEM (EFTEM). Local patterning of magnetic properties by spatially varying the irradiation dose was of particular interest. For this reason, the goal was to investigate magnetic domain confinement in patterned samples as well as the changes in magnetic reversal processes due to the ion-irradiation patterning process.

For the case of CoCr films, the balance between the magnetocrystalline and magnetostatic anisotropy energies was studied by observing the magnetic domain configurations. In particular, the effects of sample thickness, sample temperature

and applied magnetic field on this dynamic magnetic equilibrium were determined from the *in-situ* magnetic imaging experiments.

In order to place this research in perspective, the principles of magnetic recording, including the challenges and limits of the current technology, are outlined first. In light of these limitations, possible future approaches are then discussed, leading to the choice of systems studied in this dissertation. The basic ideas of ferromagnetism, magnetic anisotropy and magnetic domain structure are then explored. Readers not familiar with magnetism should begin with this section, which summarizes the basics.

The characterization techniques used in this research are briefly summarized in Chapter 2. The principles of all techniques, along with certain experimental challenges, are outlined with the magnetic imaging techniques receiving a more complete discussion.

Chapter 3 introduces processing, deposition conditions, and initial structural characterization of the Co/Pt multilayers. In particular, the effects of growth temperature on magnetic properties and structure of the multilayers are discussed.

The main results of this dissertation present ion-irradiation as a processing parameter affecting the magnetic properties of Co/Pt multilayers. Chapter 4 first introduces the basics of ion–matter interactions. Subsequently, the analysis and correlation of ion-induced magnetic and structural changes is presented (coercivity, magnetic domain structure and microstructure). Chapter 5 describes patterning of magnetic properties of Co/Pt multilayers by spatially varying ion

irradiation dose. The results form two patterning methods: 1) ion irradiation through a mask and 2) focused ion beam writing are presented and discussed.

Chapter 6 concerns all the work carried out on thin films of CoCr with perpendicular anisotropy. Emphasis is placed on the evolution of the domain patterns with changes in anisotropy contributions. The research presented in this chapter is separate from the rest of the thesis, as it discusses a different material. However, the commonality is the perpendicular anisotropy and its influence on the magnetic domain structure.

Both Co/Pt and c-axis Co based alloys are possible candidates for magnetic devices. This research impacts not only the fundamental science but also the technological applications.

1.2. Introduction to magnetic recording

1.2.1. History of magnetic recording

Storage of information can be accomplished in many different ways, one of which is magnetic recording. This technique relies on storage of information by permanently changing the magnetization of a recording medium by application of a magnetic field. The information can be later retrieved and reproduced from these recorded changes in magnetization.

Perhaps the first magnetic storage system know is the earth's crust, where magnetic rocks carry information about changes in the direction of the earth's magnetic field. The geomagnetic field is recorded at the time of rock formation and then retained over geological time. During the process of plate tectonics, new rock is formed by solidification of the magma, which is pushed up from the earth's interior through the tectonic fault. When initially paramagnetic rock cools down through its Curie temperature, it is magnetized by earth's magnetic field and it stores the direction of earth's magnetization at the time of solidification. As this processes continues, the new rock pushes the earlier one outward and, hence, the magnetization of the rock at a distance from the fault carries information about the history of the earth's magnetic field [Gass - 1993].

The first practical demonstration of magnetic recording was carried out by Valdemar Poulsen at the end of the nineteenth century [Jorgensen - 1999], [Daniel - 1998]. During the 1900 World Fair in Paris, Poulsen demonstrated Telegraphon, which used a steel wire as a magnetic storage medium. In the 1930's, a new

concept of thin media coated with small magnetic particles was introduced and magnetic storage moved into two dimensions. This principle was further developed and improved by changing the shape and size of magnetic particles (current tapes use acicular γ-Fe_2O_3 particles). The next big step in the area of magnetic recording took place in 1950's when thin magnetic films were introduced. In 1956, IBM's first computer hard drive was introduced. The RAMAC 305 was the size of two large refrigerators and had a capacity of 5 megabytes. Then, in the 1970's, Co-based thin film systems were introduced and this, coupled with the evolution of personal computers, lead to a rapid increase of areal density. Current commercial magnetic data-storage media are based on polycrystalline Co-based magnetic alloys with longitudinal (in-plane) recording geometry.

Magnetic recording systems represent the most rapidly developing area of high technology in the world, surpassing even the semiconductor industry, where the growth is governed by Moore's law[i] [Watanbe - 1983], [Watanabe - 1984], [Studt - 1995], [Streetman - 2000]. For example, since 1998, the capacity of commercially available hard drives had more than doubled every 12 months. The driving force in magnetic recording is primarily economical and derives from the growth in demand for ever-cheaper information storage systems. In 1956, the first hard drive product was about $10,000 per megabyte (MB) of memory. In 1988 the

---

[i] Gordon Moore co-founder of Intel stated in 1965, that each new memory integrated circuit contained roughly twice as much capacity as its predecessor, and each chip was released within 18-24 months of the previous chip. If this trend continued, he reasoned, computing power would rise exponentially with time. It did and it still is, with the doubling occurring every 18 months.

price of magnetic storage had dropped to $11.54 per MB and in 1999 it averaged less than 2 cents per MB [Daniel - 1998]. This tremendous rate of evolution of rigid disk magnetic recording industry is presented in Figure 1–1 [Thompson - 2000]. Currently, the recording densities in commercial products exceed 30 Gbit/in^2 and, recently, areal bit densities as high as 65 Gbit/in^2 have been demonstrated for conventional longitudinal recording [Terris - 2001]. It should be mentioned that Poulsen's steel wire had an areal density of only 8 bit/mm^2 [Jorgensen - 1999].

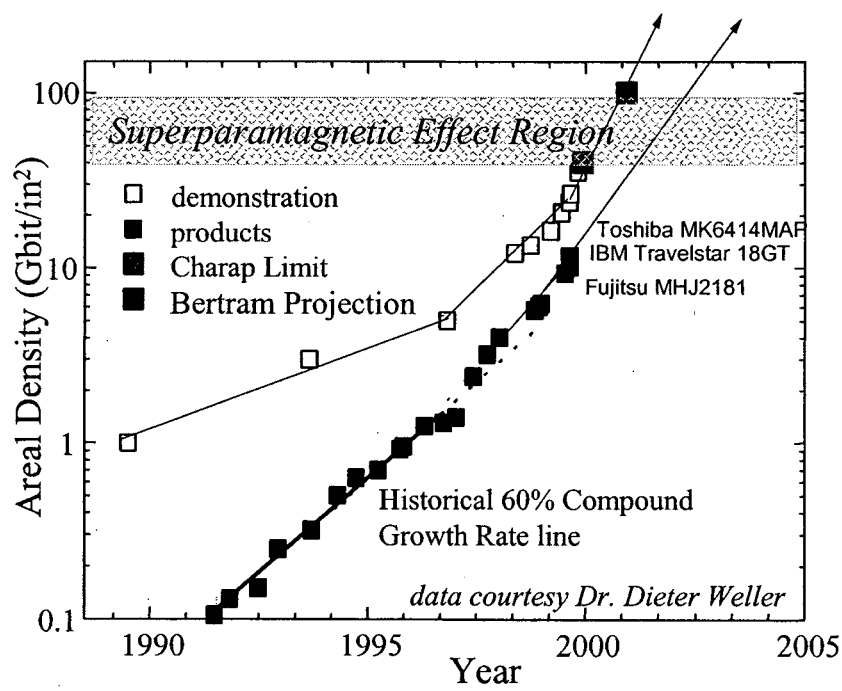

Figure 1–1. The rate of growth of areal recording density.

Areal density growth is dominated by reading head considerations. The shift from 40% per annum growth to 60% was due to introduction of magnetoresistive read-heads by IBM in 1992. Similarly, the recent change to

100% per annum growth was driven by the introduction of giant magnetoresistive (GMR) heads by IBM in 1998 [White - 1992], [White - 1994]. However, the development of magnetic media requires an ongoing improvement to support a dramatic reduction in the size of the information bit.

1.2.2. Principles of longitudinal magnetic recording

The principles of a current digital magnetic recording system are schematically outlined in Figure 1–2 [White - 1985], [Bertram - 1994], [Comstock - 1999]. As illustrated, the recording geometry is longitudinal; that is, the magnetization is stored in the plane of the film along the direction of the relative motion of the disk and the head. The bit of information is stored by applying a pulsed field in a direction opposing to that in a previously saturated material. The output signal, a voltage pulse, is produced at transitions between two adjacent bits magnetized in opposite direction due to the interaction of magnetostatic fields. During reading, the magnetization reversals are detected by an inductive coil or, in more modern systems, by a magnetoresistive sensor .

The media in current magnetic thin-film storage systems are comprised granular Co-based thin films. Typically, a $Co_{1-x}Cr_x$ (x = 12-20 %) film alloyed with Pt, Ta and B is used in order to tailor the magnetic properties and enhance grain decoupling. The layer-by-layer architecture of typical media is schematically illustrated in Figure 1–3.

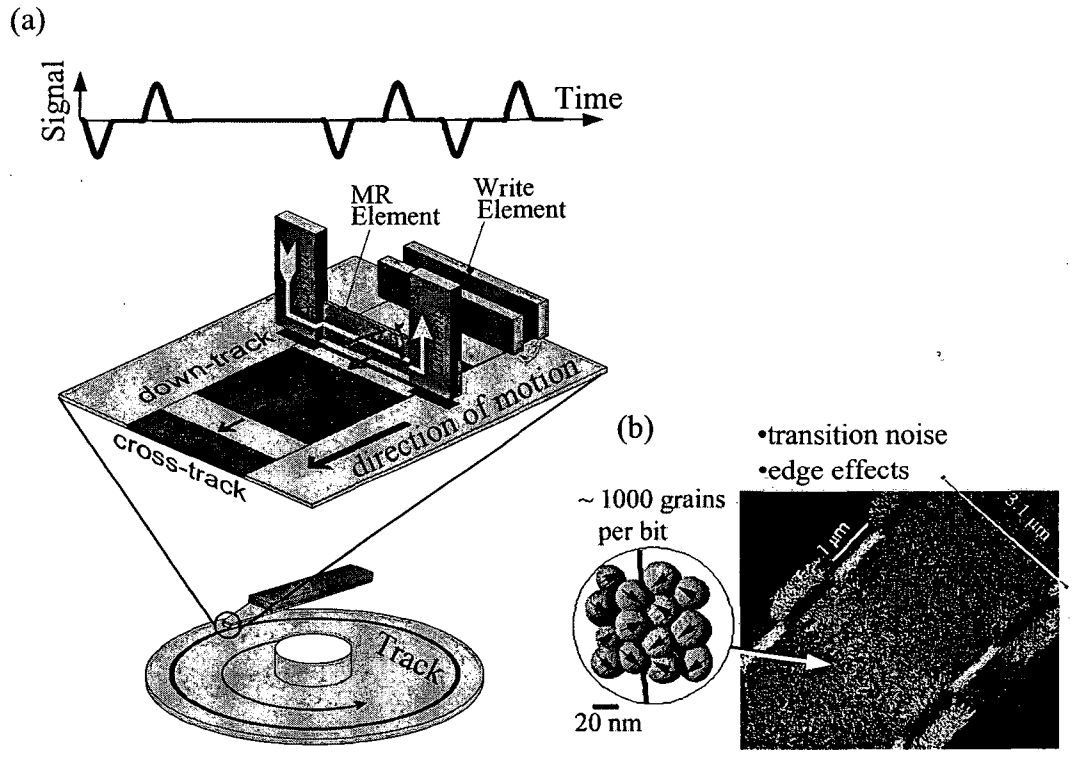

Figure 1–2. (a) Schematic diagram illustrating the basic principles of a magnetic recording system. (b) Lorentz TEM image of overwrite experiment on 1 Gbit/in^2 media.

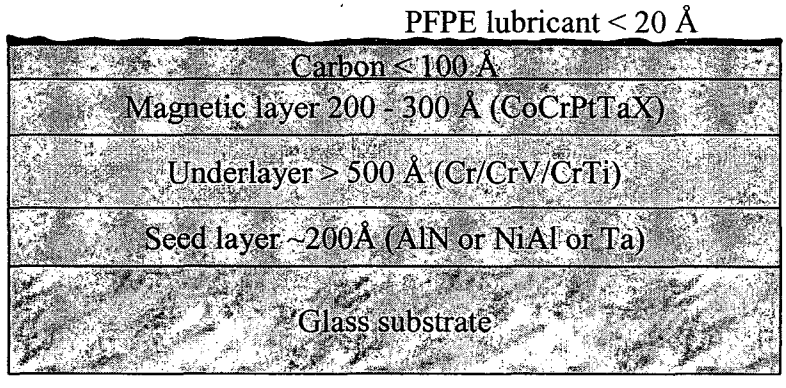

Figure 1–3. Schematic of a typical thin film architecture used in longitudinal magnetic recording.

A rigid disk substrate consists of Al disk that are polished to obtain uniform flatness. Glass substrates are now often preferred and are more widely used, particularly for hard drives in laptop computers [Mirzamaani - 1998], [Doerner - 2001]. In the case of the metal substrates, approximately 10 μm of $Ni_{88\%}P_{12\%}$ is first electro-deposited as a durability coating and to improve surface smoothness. Next, the chromium underlayer is deposited. Then, various texturing techniques, such as scratching of the Al disks, are implemented to promote circumferential texture for the CoCr. The c-axis of the CoCr grains align with the scratches and follow the circumference of the disk (i.e. the direction of relative motion of disc and the head) [Mirzamaani - 1994]. This procedure is not possible with glass substrates as the scratches would mechanically weaken the brittle surface. Hence, NiAl seed layers are deposited directly onto smooth glass substrates to achieve appropriate epitaxy [Lee - 1994], [Lee - 1996], followed by deposition of a Cr underlayer. The Cr layer is used to provide a crystallographic template for the Co-based magnetic layer, such that the latter grows with the anisotropy c-axis in-plane [Guruswamy - 1998], [Lu - 1999], and also follows the circumferential in-plane texturing. After the magnetic layer, a carbon overcoat is deposited for anti-oxidant purposes. Finally, the disk is dip-lubricated in a PFPE lubricant [Johnson - 1996].

Typical current magnetic thin-film storage media are based on CoCr alloyed with Pt, Ta and B to tailor the magnetic properties and enhance grain decoupling. The Cr content of the alloy is in the 12-20% range. For this composition range, the ferromagnetic hcp ε-Co_f phase is stable. However, when the Cr content is above about 23%, depending on the minor alloying elements, the

paramagnetic ε-Co_p is stable as depicted in Figure 6–2, which shows the CoCr phase diagram. The growth of the CoCr alloy is characterized by segregation of Cr into grain boundaries, which has a beneficial effect on the magnetic properties. The Co-rich grains are ferromagnetic ε-Co_f, while the Cr-rich boundary has just enough Cr to stabilize the magnetically dead paramagnetic ε-Co_p phase. This Cr-rich paramagnetic grain boundary layer provides magnetic isolation between grains and prevents switching by domain wall motion. In recent years, Cr segregation has received much scientific interest and methods promoting it are implemented in the industry to improve the media characteristics [Kemner - 1996], [Inaba - 1997], [Wittig - 1998], [Inaba - 2000], [Grogger - 2001].

1.2.2.1. Thermal stability, superparamagnetic limit

As mentioned earlier, the current magnetic recording medium is continuous and unpatterned with single-domain magnetically decoupled grains. Using such a system as a recording medium, the positions and the shapes of the recorded bits are determined entirely by the write head. Traditionally, the bits are rectangular. Bit length, the short direction, is parallel to the recorded track (i.e. direction of motion of disc). Bit width, the longer dimension, is perpendicular to the track direction, as shown in Figure 1–2. The previous approach to increase magnetic storage density relied on scaling down the dimensions of individual bits. However, the primary components of medium noise are the transition noise and the statistical noise. Since the transition between bits must follow the grain boundary, the granularity of the medium is an important parameter. When the bits become smaller, the magnetic roughness, governed by the transition between

bits, becomes comparable to the bit size, leading to increased media noise. In the past, when the areal densities were on the order of 1 MB per square inch, the number of grains per bit was on the order of 10^5 and granularity was not a problem. However, when the bit sizes were reduced to achieve densities in the range of 1 Gbit/in^2, the number of grains per bit was reduced to approximately 1000, and the raggedness in bit transition became the primary source of media noise.[i]

The solution to this problem appears to be trivial. In principle, a simple reduction of the media grain size should solve the transition noise problem, as it would reduce bit edge roughness. This approach did work very well in the past, with the decrease in bit size accompanied by a reduction of the media grain size to ensure low media noise [Futamoto - 1999]. This arbitrary reduction in grain size, however, cannot be sustained forever [Pu-Ling - 1994], [Pu-Ling - 1995]. The grain size cannot be shrunk significantly below its present state-of-the-art value of approximately 90 Ångstroms, without the magnetization of the individual grains becoming thermally unstable [Charap - 1997], [Moser - 1999a], [Moser - 1999b], [Weller - 1999].

The thermal stability of the magnetic orientation of a ferromagnetic particle (grain) with respect to ambient thermal fluctuations can be understood

---

[i] The other reason to shrink the grain size stems from the statistical noise problem. In magnetic recording, the signal from a bit is proportional to the number of grains in the bit, N, while the statistical noise scales with $\sqrt{N}$. The signal to noise ratio, *SNR* is thus proportional to $\sqrt{N}$. Moreover, signal processing dictates a minimum value of $SNR \cong 20$ dB. This implies a minimum of approximately 1000 grains per bit. Hence, as the bits shrink to increase the recording density, so must the grains shrink to keep the SNR at the same level.

based on the Arrhenius-Néel model. Assuming a magnetic anisotropy axis along a certain crystallographic direction (which is in the plane of the film), the magnetization of the grain will be either in the positive or negative direction along that axis. In order to reverse the magnetization of a grain, an energy barrier created by the magnetic anisotropy must be overcome. In the absence of an applied field, the magnitude of the barrier is given by the product of $K_u \cdot V$, where K_u is the anisotropy constant for the material and V is the effective magnetic volume of the grain. At a temperature, T, thermal excitation might be sufficient to overcome this energy barrier and may induce the particle to reverse its magnetization spontaneously. The frequency of magnetization reversal of the grain, due to thermal excitation over the anisotropy barrier is given by:

$$f = f_o \cdot \exp\left(-\frac{K_u \cdot V}{k \cdot T}\right) \qquad \text{Eq. 1–1}$$

where f_o is the attempt frequency, typically in the 10^9/s range, and k is the Boltzmann factor. The decay of magnetization of an ensemble of such grains (magnetic bit) is directly related to the frequency of the reversal of the individual grains. Hence, at time t, the magnetization of such an ensemble of particles is:

$$M(t) = M_o \cdot \exp\left(-\frac{t}{\tau}\right) \qquad \text{Eq. 1–2}$$

where τ is the lifetime of the state of one of the particles, and is given by $\tau = 1/f$.

For a magnetic material to be suitable for data storage, each written bit must retain about 95% of its initial magnetization over 10 years.[i] Assuming the anisotropy value of pure Co ($K_u = 4 \cdot 10^6 erg/cm^3$), a uniform grain size

[i] There are also corrosion and oxidation considerations, which introduce interesting materials problems. These are not discussed here.

distribution and ideal grain decoupling,[i] equations Eq. 1–1 and Eq. 1–2 require a minimum 8 nm grain size to ensure thermal stability. Smaller grains will be susceptible to thermally activated reversal and loss of information over time.

Another way to look at the problem is the following: Assuming a certain grain size such that the thermal reversal time is 10 years, a reduction in grain diameter by a factor of 2 will reduce the thermal reversal to only tens of nanoseconds! For the former case, the particles can be considered thermally stable. However, for the latter case, such ensemble of particles represents a permanent magnet only in a philosophic sense. Macroscopically, no magnetic remanence and only a small permeability can be measured, even though at any instant each particle is fully magnetized in some direction. This condition is called superparamagnetism because the macroscopic properties of such small grains (particles) are similar to those of paramagnetic moments. When the magnetization is measured slowly compared with the thermal decay time, a linear dependence of magnetization along the magnetic field is found, just as for paramagnetic materials.

Clearly, magnetic recording, which utilizes thin-film continuous magnetic media with longitudinal bit alignment, faces a fundamental limit due to the loss of magnetization of the superparamagnetic grains. The perceived limits are being

---

[i] In fact, real systems are more complicated. First, there is a distribution of actual grain sizes, and in thermally "stable" media, some of the smaller grains can already be at the border line of thermal stability. In addition, the magnetic isolation between grains is not perfect. The local energy barrier to thermal reversal can be substantially reduced as it depends on the stored bit pattern and on the magnetic interaction between adjacent grains.

pushed further and further by continued improvements in grain size distribution, grain segregation, and development of higher anisotropy alloys, as well as improvements in signal processing. In fact, current demonstrations of 65 Gbits/in^2 are exceeding the 40 Gbits/in^2 limits predicted earlier by Charap. However, the recent tremendous growth rate in the storage capacity (> 1 Gbit/in^2/month) cannot be sustained much beyond 100 Gbit/in^2 with the longitudinal bit format, due to thermal stability problems (i.e. the superparamagnetic limit) [White - 2000], [O'Grady - 1999], [Speliotis - 1999], [Lambeth - 2000]. Alternative approaches to magnetic recording are outlined in the next section.

1.2.3. Approaches to overcome superparamagnetic limits

1.2.3.1. Perpendicular magnetic recording

As an alternative, based on an analysis of the demagnetization mechanisms, Iwasaki and Takemura [Iwasaki - 1975], [Iwasaki - 1977] suggested the possibility of perpendicular magnetic recording (PMR). The initial work on perpendicular magnetic recording was carried out mainly in Japan using CoCr based systems [Ouchi - 1994], utilizing a perpendicular head design [Nakamura - 1990b], [Nakamura - 1990a], [Yamamoto - 1990], [Yamamoto - 1991]. A single-pole head was found more suitable for PMR, as it produced an ideally sharp field distribution because of a strong head-medium magnetic interaction. The advantage of perpendicular magnetic recording is that an isolated magnetization transition is much sharper than that in longitudinal recording. Moreover, the demagnetizing fields for the perpendicular bit alignment are stabilizing rather than destabilizing, as is the case for the longitudinal systems, as schematically

shown in Figure 1–4. Also, due to increased thickness, the effective magnetic volume of the bits can be larger, leading to an increased energy barrier to thermal reversal, (see Eq. 1–1).

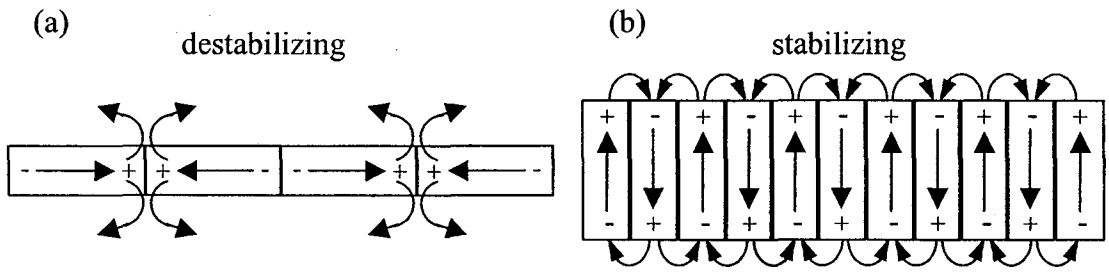

Figure 1–4. Schematic illustrating longitudinal and perpendicular bit arrangement showing destabilizing and stabilizing fields, respectively.

Extensive computer simulations were used to study the effects of the magnetic interaction between a single-pole head and a double-layer medium [Tagawa - 1990], [Nakamura - 1991], [Tagawa - 1991]. Such simulations predicted that areal densities of more than 300 Gbit/in^2 could be routinely obtained for this recording configuration [Tagawa - 1994]. A review of the progress of the research on PMR can be found in reference [Nakamura - 1999]. However, before perpendicular magnetic recording can be technologically realized, materials with easy axis of magnetization perpendicular to the film plane must be well analyzed. One such system is a c-axis oriented CoCr alloy where perpendicular magnetic anisotropy is achieved via magnetocrystalline anisotropy. A detailed analysis of the magnetic domain structure of such a material is presented in Chapter 6.

It is clear, however, that in perpendicular magnetic recording, the bits are still linked to the grain size, as the transition between bits is determined by grain

boundaries. Ultimately, perpendicular recording is limited by the superparamagnetism of the media, just as was described for longitudinal media.

1.2.3.2. Patterned media

The new approach to ultrahigh-density magnetic storage, which will perhaps move the industry beyond the presently perceived superparamagnetic limits, is based on patterning of perpendicular magnetic media into individual single domain elements. Recently, such patterning processes have generated much scientific attention and, in general, such media are referred to as patterned magnetic media [Lambert - 1991], [White - 1997].

Patterned media consists of a regular array of magnetic elements, each of which has uniaxial magnetic anisotropy. The easy axis can be oriented parallel or perpendicular to the substrate. Each element stores one bit, depending on its magnetization state. For example, magnetization up could represent 1, and down could represent 0. Unlike the thin film medium, the grains within each patterned element are coupled so that the entire element behaves as a single magnetic domain.

As discussed previously, bit locations for conventional unpatterned media are determined by the write-head and, more importantly, the transitions between bits are a strong function of write-head field-gradient, demagnetizing effects and the grain size. This is where patterned media are superior. In patterned media, each bit is defined by some kind of lithography process. The bit location and bit length are predetermined and, in principle, are not dependent on either the underlaying microstructure or the characteristics of the write-head. Theoretically,

such patterned bits can be reduced in size down to one thermally stable grain. Hence, for patterned media, magnetic storage densities can be increased n times as compared to conventional recording where bits consisting of n grains must be used to overcome the statistical noise problems. The major advantages of patterned media are, first, that transition noise is eliminated because the bits are now defined by the physical location of the elements and not by the boundary between two oppositely magnetized regions of a thin film. Second, very high data densities can be obtained because the stability criterion now refers to the volume and anisotropy of the entire magnetic element, not to the individual grains of which it is composed. In pattern media configurations, the 100 Gb/in^2 density would be achieved if ~80 nm magnetic regions could be successfully produced. However, for the industry to make a technological transition to new patterned media technology, a possible growth up to ~1 Tb/in^2 must be feasible and economical. These constraints require the ability to pattern 25 nm periodicity.

Previously, small isolated islands of magnetic material were produced by a number of techniques [Farhoud - 1998], [Ross - 1999], [Wong - 1999], [Ganesan - 2000], [Ross - 2001], all of which required a resist-step and subsequent deposition or etch step. The cleanliness of media surfaces is a key parameter, with the head-to-disk spacing in the range of 10 nm. For this reason, it is desirable to develop a non-contact magnetic patterning method that preserves surface smoothness and planarity. Ion-beam patterning of magnetic thin films through suitable stencil masks [Chappert - 1998] has been suggested as a good candidate for producing such planar patterned media. Co/Pt multilayers, in particular, are ideally suited for this application, since bombardment with a suitable dose of energetic ions has

been shown to change the magnetic easy axis of the multilayer from out-of-plane to in-plane [Ferre - 1999]. The irradiation may induce interface mixing [Carcia - 1990a], [Weller - 2000], thereby triggering a spin reorientation transition (SRT) from the out-of-plane to the in-plane easy axis. In addition, ion-irradiation through a resist layer [Devolder - 1999] and, in particular, through non-contact stencil masks [Terris - 1999] was shown to produce a patterned magnetic film. Understanding the switching mechanism of sub-micron magnetic elements is an essential step for the implementation of such patterned media for data storage.

Summarizing, longitudinal magnetic recording faces fundamental limits due to the superparamagnetic limit. It is desired to move to new systems with perpendicular recording architectures and toward patterning of such perpendicular magnetic media into individual single domain elements. This creates challenges for materials scientists as systems with perpendicular anisotropy must be developed and characterized. Before introducing the systems studied in this dissertation, the basics of magnetism and magnetic anisotropy are briefly summarized. The approaches to perpendicular magnetic anisotropy are then outlined.

1.3. Categories of magnetic materials

Materials that respond to a magnetic field are called magnetic materials. The English word magnetism derives from the name of the naturally occurring magnetic mineral, magnetite. The stone itself was named magnetite after the Magnesia region in Asia Minor, where it was found. It is believed that magnetite was found there as early as several centuries BC. As early as the 2nd century

A.D., the Chinese found that unmagnetized iron ore became magnetized when brought close to naturally magnetized magnetite. Several centuries later, it was discovered that suspended magnetized rods always pointed in the same north-south direction. This led to what was probably the earliest application of magnets—a navigational aid [Osborne - 2001].

The various kinds of magnetic materials are characterized by their magnetic structure and their characteristic response to an applied magnetic field, **H,** [Chikazumi - 1965], [Cullity - 1972], [Jiles - 1995], [Jakubovics - 1994]. The units of magnetic field in the SI system are the ampere per meter (A/m). For conversion between two commonly used unit systems, namely the SI and the CGS, please refer to the Appendix on page 206 of this dissertation. The reader is also referred to an excellent tutorial paper by Brown [Brown - 1984] for a more in-depth discussion.

The magnetic moment per unit volume of a magnetic substance is referred to as magnetization density and is denoted by **M**. The vector associated with magnetization points from the S pole to the N pole for any part of the material isolated from the rest of the specimen. In the SI system, 1 Wb/m^2 is the unit of **M**. The magnetic induction, **B**, also known as the magnetic flux density, is given by the following equation:

$$\mathbf{B} = \mu_o \cdot (\mathbf{M} + \mathbf{H}) \quad \text{(SI units)} \qquad \text{Eq. 1–3}$$

where μ_o is the permeability of vacuum measured in units of henry per meter and it is equal to $\mu_o = 4\pi \times 10^{-7}$[H/m].

The magnetic behavior of various materials can always be interpreted in the context of the relative magnetic susceptibility, χ, which describes the relation between the magnetization and magnetic field and is given by:

$$\chi = \frac{\mathbf{M}}{\mathbf{H}} \quad \text{(SI units)} \qquad \text{Eq. 1–4}$$

The values of susceptibility range from negative 10^{-5} to positive 10^{6} for weak and strong magnetism, respectively. Magnetic materials are classified by the value of their relative magnetic susceptibility. The kinds of magnetism commonly discussed are: Diamagnetism, Paramagnetism, Ferromagnetism, Antiferromagnetism and Ferrimagnetism. Figure 1–5 shows a typical response of diamagnetic, paramagnetic and ferromagnetic material to the applied magnetic field.

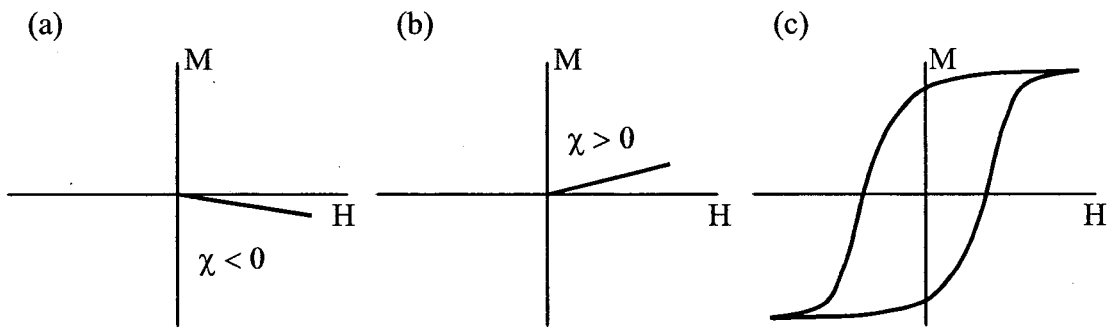

Figure 1–5. Magnetization versus applied magnetic field. (a) Diamagnetic material, χ is a negative constant. (b) Paramagnetic material, χ is a positive constant. (c) Ferromagnetic material, the path of magnetization exhibits hysteresis; magnetic susceptibility is not a simple constant.

Substances with a negative magnetic susceptibility are referred to as **diamagnetic**, and their χ is usually small with values of approximately -10^{-5}. Examples of diamagnetic materials are Beryllium, Bismuth, Copper, Gold and

Silver. These materials are called diamagnetic because their magnetic response acts against the applied magnetic field. The origin of diamagnetism is an orbital rotation of electrons about the nuclei induced by the application of an external field. The induced current according to Lenz's law opposes any change in the local field. Superconductors are considered ideal diamagnets as the induced magnetic moment fully opposes the applied magnetic field. Hence, for superconductors $\chi = -1$.

Paramagnetic materials are characterized by small and positive susceptibility where $\chi \approx 10^{-6}$ to 10^{-3}. The magnetization of a paramagnet is weak but aligned in the direction of the applied magnetic field. Most paramagnetic materials contain magnetic atoms or ions possessing a net spin. At finite temperature, the spins are randomly oriented due to thermal agitation. With the application of a magnetic field, the spins are predominantly in the direction of the magnetic field and a weak magnetization is induced. As larger fields are applied, more of the spins predominate and the magnetization is proportional to the applied field. In addition, χ is inversely proportional to the absolute temperature according to the Curie law ($\chi = C/T$). Examples of paramagnetic materials include Aluminum, Platinum and Manganese.

Both diamagnetism and paramagnetism occur only in the presence of an external magnetic field. On the other hand, **ferromagnetic** materials can be magnetized in the absence of an external magnetic field. For ferromagnetic materials, the susceptibility is positive and is much greater than 1, i.e. $\chi \approx 50$ to 10^4. For ferromagnetic material, the spins are aligned parallel due to strong positive interactions. With increasing temperature, this ordered arrangement of

the spins is agitated, resulting in reduction of magnetization up to the Curie temperature θ_c. Above θ_c, the inverse of susceptibility $1/\chi$ increases from zero linearly with temperature according to the Curie-Weiss law, $\chi = C/(T-\theta_c)$. The Curie temperature separates the disordered paramagnetic phase at T > θ_c from the ordered ferromagnetic phase at T < θ_c. Examples of ferromagnetic materials are Cobalt, Iron, Nickel and some of the rare earth metals, along with their alloys.

Figure 1–6 schematically summarizes the characteristics of diamagnetic paramagnetic, ferromagnetic and antiferromagnetic materials.

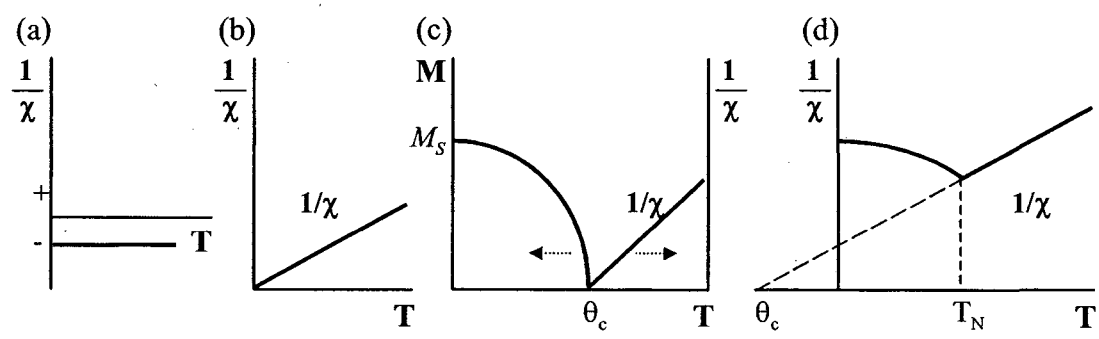

Figure 1–6. A graphical representation of (a) diamagnet (b) paramagnet, (c) ferromagnet and (d) antiferromagnetic powder. T_N is the Néel temperature.

1.4. Ferromagnetism and magnetic domains

As briefly explained in the previous section, a ferromagnetic material may exhibit a spontaneous magnetization **M** in the absence of any external magnetic field [Aharoni - 1996]. The classical way of representing the magnetic properties of a ferromagnetic material is with a **M·H** curve. A **M·H** curve, or a hysteresis loop, represents magnetization **M** as a function of the applied field **H**. The applied

field is ramped to a certain value, reduced to the opposite value and back. A typical **M·H** hysteresis loop, plotted in Figure 1–7, shows all relevant magnetic parameters [Bertotti - 1998].

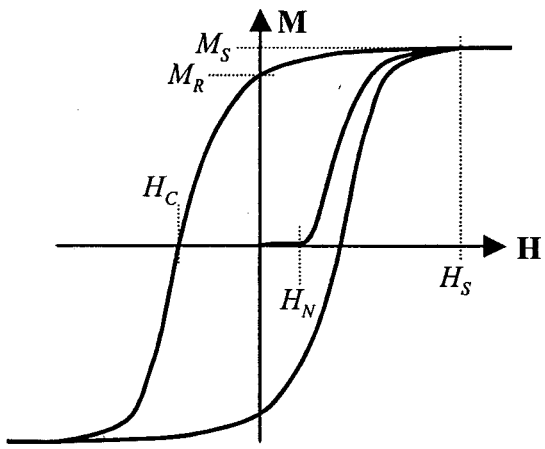

Figure 1–7. A schematic plot of the hysteresis loop of a ferromagnetic material defining the relevant parameters. H_N is the nucleating field, H_S is the saturating field, and H_C is the coercive field. Similarly M_S is the saturation magnetization and M_R is remanent magnetization.

Ferromagnetism is a cooperative phenomenon, which originates from the presence of a magnetic moment (primarily spin **S** of an electron) and the mutual alignment of neighboring moments in the material. The spin alignment is explained quantum-mechanically by the exchange interaction. In the Heisenberg model [Heisenberg - 1928], the exchange interaction of a spin system is given by the exchange interaction energy U:

$$U = -2 \cdot J \cdot \mathbf{S_i} \cdot \mathbf{S_j} \qquad \text{Eq. 1–5}$$

where J is the exchange integral and is related to the overlap of the charge distributions of the atoms i and j. A positive exchange interaction constant J favors parallel spin alignment [Kittel - 1996].

Despite the spontaneous magnetization, ferromagnetic materials can exist in a demagnetized state due to presence of magnetic domains, which were first theoretically postulated by Weiss [Weiss - 1907]. The term *domain*, describing the subdivision of a uniformly magnetized region, was introduced later [Weiss - 1926]. Each magnetic domain is spontaneously magnetized, but the direction of the domain magnetization can vary, and the resulting magnetization for the material can be between zero and the value of spontaneous magnetization. The existence and arrangement of magnetic domains, their size, shape and orientation are a consequence of energy minimization [Landau - 1935].

In the domain theory [Kittel - 1956], the energy terms that dictate magnetic interactions are: exchange energy, magnetostatic energy, external field energy and anisotropy energy.

1.4.1. Exchange energy

Quantum mechanical exchange prevents magnetization from deviating from a straight line. The exchange energy density E_{ex}, arising when the magnetization deviates from complete alignment, is given by:

$$E_{ex} = A \cdot [(\nabla \alpha_1)^2 + (\nabla \alpha_2)^2 + (\nabla \alpha_3)^2] \qquad \text{Eq. 1–6}$$

where A is the exchange constant and α_i are the directional cosines of the $\boldsymbol{M}$ vector. The exchange constant, A, is a property of the material and is proportional to the exchange integral, J.

1.4.2. External field energy

When an external field $\mathbf{H}_A$ is applied to a magnetic body, a torque proportional to $\mathbf{M}\times\mathbf{H}_A$ will try to align $\mathbf{M}$ along $\mathbf{H}_A$. The external field energy density E_H of the system is given by:

$$E_H = -\mu_o \mathbf{H}_A \cdot \mathbf{M}. \qquad \text{Eq. 1–7}$$

The minimum external field energy results when $\mathbf{M}$ and $\mathbf{H}_A$ are parallel.

1.4.3. Magnetostatic energy

Discontinuities and divergences of the magnetization contribute to the magnetostatic energy. The non-vanishing terms $-\nabla\cdot\mathbf{M}$ and $\mathbf{M}\cdot\mathbf{n}$, if treated as magnetic volume and surface charge densities, contribute to the self-demagnetizing magnetic field

$$\mathbf{H}_\mathrm{d}(\mathbf{r}) = \frac{1}{4\pi}\int_V -\frac{\nabla\cdot\mathbf{M}}{r^2}\mathrm{d}V + \frac{1}{4\pi}\int_S -\frac{\mathbf{M}\cdot\mathbf{n}}{r^2}\mathrm{d}S \qquad \text{Eq. 1–8}$$

where S and V are the surface and the volume of the sample respectively and $\boldsymbol{n}$ is the unit vector normal to the surface. The magnetostatic energy density resulting from creation of $\mathbf{H}_\mathrm{d}$ is given by:

$$E_M = -\frac{\mu_o}{2}\mathbf{H}_d \cdot \mathbf{M} \qquad \text{Eq. 1–9}$$

1.4.4. Magnetic anisotropy

The anisotropy density energy considers the orientation of $\mathbf{M}$ with respect to a set of certain axis, fixed with respect to the sample and is given by:

$$E_A = K \cdot f(\alpha_1, \alpha_2, \alpha_3) \qquad \text{Eq. 1–10}$$

In this expression, K is the anisotropy constant and f is a function of the orientation of **M** expressed with directional cosines α_i. The direction for which Eq. 1-10 is minimum is referred to as the easy magnetization axis, and that for which it is maximum is denoted a hard axis.

1.4.5. Magnetic domains

The energy density terms introduced above are all, in general, a function of position in the magnetic body and the orientation of **M** at that position. The total energy of the system is a sum of all such terms. The magnetic domain structure is a consequence of minimization of the total energy. Starting with the uniformly magnetized sample, splitting into several domains reduces the magnetostatic energy by reducing the number of magnetic poles at surfaces where the product $\mathbf{M} \cdot \mathbf{n}$ does not vanish. In general, the magnetostatic energy of the system with n domains is reduced n times as compared to a single domain state. The boundary between two adjacent domains, the domain wall, is not sharp as the magnetization changes direction gradually. Hence, introduction of more than one domain, which implies domain walls, increases exchange and/or anisotropy energy contributions[i]. Thus the resulting domain structure is a result of a delicate balance of all energy terms involved.

---

[i] The balance between exchange and anisotropy energies determines the width of the domain wall. Exchange energy is minimized when the angle between adjacent spins is minimal, favoring wide walls. The anisotropy energy, on the other hand, is minimized when magnetization is aligned along the easy axis, favoring sharp transition and narrow walls.

1.4.6. Ferromagnetic thin film

The one factor that strongly affects the shape of the hysteresis loop of a ferromagnetic material is magnetic anisotropy. Magnetic anisotropy implies that the magnetic properties are not isotropic and depend on the direction in which they are measured, as shown in Figure 1–8. Knowledge of this important parameter is key to the understanding of the behavior of magnetic materials.

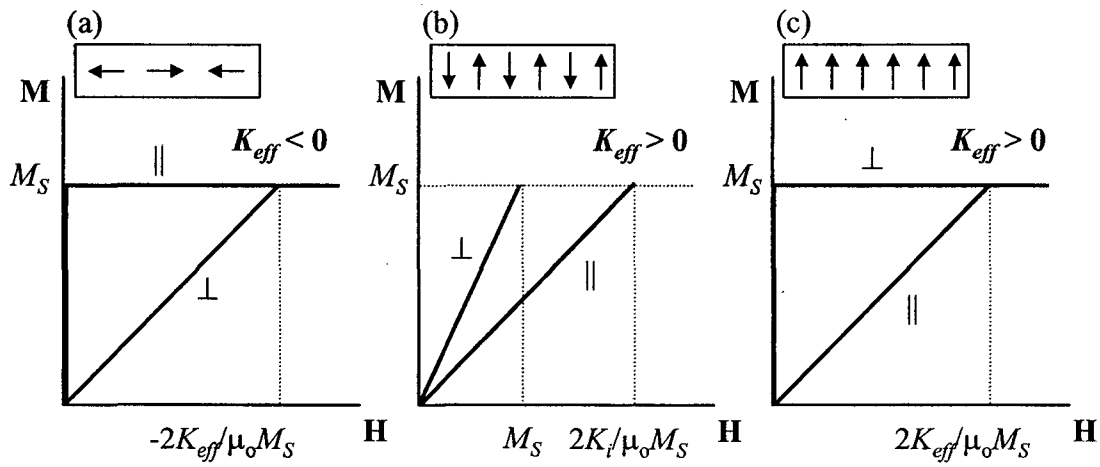

Figure 1–8. Magnetization curves for magnetic thin films having (a) in-plane preferential magnetization, (b) perpendicular magnetization and small domains, (c) perpendicular magnetization with large magnetic domains.

The microscopic origins of anisotropy are poorly understood because of the difficulty in separating various anisotropy contributions and the small size of typical anisotropy energies (10^{-4} to 10^{-5} eV/atom). Historically, anisotropy energies have been grouped into several categories; crystal anisotropy (or magnetocrystalline anisotropy), shape anisotropy due to demagnetization energy, stress anisotropy, exchange anisotropy and induced anisotropy (annealing, plastic

deformation, irradiation, etc.). However, magnetic anisotropy is inherently dependent on only two major, often competing, contributions. The first contribution is due to dipolar coupling between individual spins. This phenomenon, in practice, gives rise to a dependence of anisotropy on the macroscopic shape of the material and, hence, it is called magnetostatic or shape anisotropy. The coupling of the electronic spins to the lattice via spin-orbit coupling provides the second major contribution to the anisotropy. The lattice has the symmetry of the crystal and the anisotropy is called magnetocrystalline anisotropy.

For any magnetic system, the sign of the effective magnetic anisotropy, K_{eff}, which groups all anisotropy contributions, determines the orientation of the easy axis of magnetization. The origin of the preferred magnetic-moment orientation in thin films and multilayers can be very different from the factors contributing to the easy-axis alignment in bulk crystals [Bader - 1990], [Falicov - 1990]. Predominantly, the symmetry braking elements in thin films, such as surfaces and interfaces, can induce anisotropy along directions different from those for bulk materials. For thin film structures, convention dictates that the anisotropy contributions perpendicular to the film's surface are positive and those in the plane of the film are negative. When K_{eff} is positive, the film has perpendicular magnetic anisotropy and assumes a perpendicular easy axis of magnetization. Negative K_{eff} implies an in-plane easy magnetization axis.

For all magnetic thin films, the one term that must always be considered is the magnetostatic shape anisotropy. Due to the plate-like geometry of thin films, this term is governed by the demagnetizing energy. In an attempt to maximize

the separation between the charges, the magnetization aligns in-plane of the film. This contribution is thus negative and is given by:

$$K_{MS} = -2 \cdot \pi \cdot M_S^2 \qquad \text{Eq. 1–11}$$

where M_S is the saturation magnetization. This implies that the perpendicular magnetic anisotropy (PMA) in thin film structures can only be achieved when other contributions to K_{eff} are overall positive and larger in magnitude than K_{MS}.

1.4.7. Systems with perpendicular magnetic anisotropy

Interest in thin film systems with perpendicular anisotropy (PMA) is driven both by scientific curiosity and technical applications. Predominantly interesting is the PMA observed in ultrathin films and certain multilayer structures. The PMA in such systems results from a magnetic anisotropy at the interface, which differs considerably from the magnetic anisotropy in the bulk. Fundamental magnetic properties depend strongly on the local atomic environment. The atomic symmetry of the surface or interface is substantially different from that of the bulk; hence, it is not surprising that the magnetic anisotropy is different at a surface. The first prediction of this so-called interface or surface anisotropy was in 1954 by Néel, who considered a lower symmetry of interface and surface atoms [Néel - 1954]. Later, Gradmann and Muller [Gradmann - 1968] were the first to experimentally show the perpendicular magnetization in ultrathin (1.8 monolayers) NiFe films grown on Cu(111) due to surface PMA. In multilayered systems, consisting of alternating layers of ferromagnetic and nonmagnetic materials, the PMA was first experimentally observed in Co/Pd systems [Carcia - 1985], and later in other Co based systems:

Co/Pt [Carcia - 1988], Co/Au [den Broeder - 1988], Co/Ru [Sakurai - 1992] and Co/Ni [den Broeder - 1992].

In such multilayers, following the nomenclature introduced by Néel, the effective magnetic anisotropy, K_{eff}, is conveniently separated into two terms, a volume contribution [i], K_V (units J/m^3), and an interface or surface contribution K_S (units J/m^2):

$$K_{eff} = K_V + 2 \cdot \frac{K_S}{t_m} \qquad \text{Eq. 1–12}$$

The prefactor 2 in Eq. 1–12 accounts for the magnetic layer, with the thickness, t_m, bounded by two identical interfaces on the top and the bottom. A positive K_{eff} describes a scenario in which a direction perpendicular to the multilayer stack is preferred. In the experimental studies, K_V and K_S contributions are determined by a plot of the $K_{eff} \cdot t_m$ versus t_m. Figure 1–9 shows such a plot for the Co/Pd multilayers [den Boreder - 1991]. The negative slope, which is equal to K_V, indicates a negative volume anisotropy, which favors in-plane magnetization. The intercept at $t_m = 0$, which is equal to K_S, indicates a positive interface anisotropy and favors a perpendicular magnetization. Hence, the perpendicular magnetization is observed only up to a certain thickness. By solving Eq. 1–12, the thickness up to which the K_{eff} remains positive is given by $t_\perp = -2 \cdot K_S / K_V$. For example, for the Co/Pd multilayer, the $K_{eff} \cdot t$ versus t plot presented in Figure 1–9 finds $t_\perp = 13$ Å.

---

[i] In this notation, K_V includes the negative K_{MS} contribution.

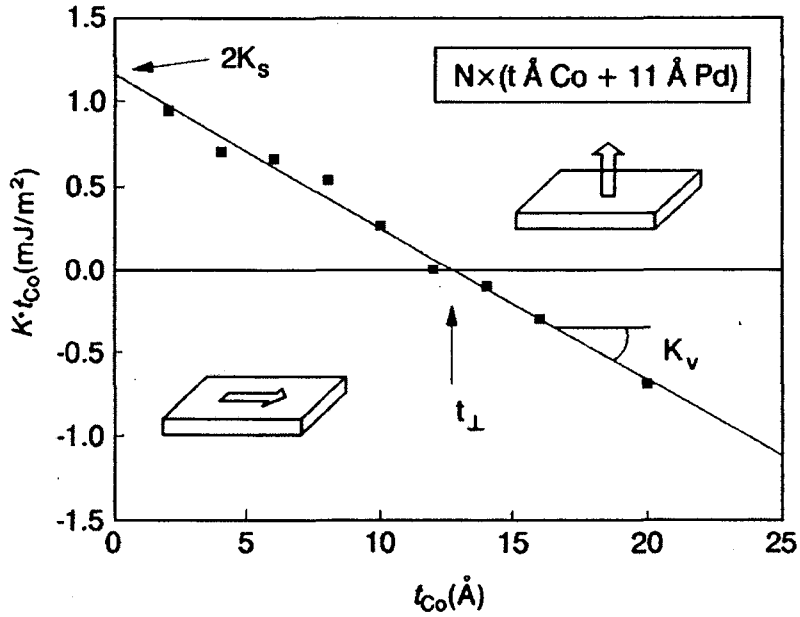

Figure 1–9. Plot of $K_{eff} \cdot t$ versus t for Co/Pd system after [den Boreder - 1991].

Alternatively stated, perpendicular magnetization is observed when there are enough interfacial magnetic atoms per unit volume of the magnetic material. In this case, the interface anisotropy outweighs the volume anisotropy contribution. When the methodology described in Eq. 1–12 and illustrated in Figure 1–9 is applied to estimate interfacial anisotropy, the volume anisotropy contributions, grouped in K_V, are assumed to be independent of the magnetic layer thickness. However, stresses in thin films can induce a $1/t$ dependence of K_V, which can be erroneously associated with a surface contribution. Hence, equation Eq. 1–12 must be used with care, as otherwise it might be very misleading.

It is interesting to note that the order of magnitude of K_S is between 10^{-3} and 10^{-4} J/m^2, which is considerably larger than the value of the regular anisotropy energy constant multiplied by the thickness of one atomic layer

[Gradmann - 1986]. This is attributed to the reduced symmetry of the atomic environment of surface atoms. A review of recent research in magnetic multilayers and superlattices can be found in reference: [Schuller - 1999], where an extensive list of magnetic multilayer materials is provided.

For thin films, which are thick comparing to the $t_{\perp} = -2 \cdot K_S / K_V$ calculated from Eq. 1–12, the surface contributions are negligible and the effective anisotropy contribution reduces to the volume term. The K_{eff}, including most important magnetocrystalline, magnetoelastic and magnetostatic is given by [Brown Jr. - 1966], [Zhang - 1993b]:

$$K_{eff} = K_V = K_u + C \cdot \lambda \cdot \sigma + K_{MS} \qquad \text{Eq. 1–13}$$

where K_u is the magnetocrystalline anisotropy, λ is a magnetostriction coefficient and σ is a film stress.

Based on this equation, the other way to engineer films with PMA is by utilization of magnetocrystalline anisotropy. Taking for example *hcp* Cobalt, where the c-axis is the magnetocrystalline easy direction, depending on the relative orientation of the c-axis with respect to the film surface, the magnetocrystalline anisotropy can have a positive or negative sign. It is positive for out-of-plane orientation and negative for in-plane c-axis alignment. Hence, to achieve PMA, the Co films must be grown with c-axis perpendicular to the plane of the film, and the magnetocrystalline anisotropy constant must be greater than the shape anisotropy constant.

Chapter 2.

EXPERIMENTAL METHODS BACKGROUND

In this chapter, the experimental techniques used to characterize the physical microstructure, physical properties (including magnetic properties) and magnetic domain structure are described. For all techniques used in this research, a description of the measurement is given along with some examples. The extent of the description and detail of the examples varies for each technique, depending on how extensively the technique was used. In particular, magnetic imaging techniques are discussed more thoroughly.

2.1. Magnetic measurements

2.1.1. Magnetic curves and anisotropy

An **M·H** curve, often referred to as a hysteresis loop, represents the measured magnetization of the sample as a function of the applied field **H**, which is changed from a given value (ex. –10 kOe) to the opposite value (+10 kOe) and then back. Usually the applied fields are large enough to saturate the material unless information about the minor loops is desired. As was shown in Figure 1–8, magnetic hysteresis loops can have different shapes depending on the orientation

of the anisotropy axis. Techniques often used to measure such curves are vibrating sample magnetometry (VSM) and magneto optical Kerr effect (MOKE) techniques.

2.1.2. Vibrating sample magnetometer

A vibrating sample magnetometer (VSM) measures sample magnetization, **M**, based on the principle that a moving magnetic sample induces a current in detection coils placed around the sample. The induced current is proportional to the magnetization of the sample.

The basics of the VSM technique were first given by Foner [Foner - 1959], [Foner - 1975], [Foner - 1981] and are briefly summarized below. The sample is positioned between the poles of an electromagnet, which applies the magnetic field and changes the magnetization of the sample. A set of detection coils is placed around the sample. The sample is vibrated between the detection coils and a region of free space in the direction perpendicular to the field direction. The VSM is, hence, a gradiometer, measuring the difference in magnetic induction between the detection coils with and without the sample. When the sample is between the detection coils the magnetic induction linking the coils is:

$$\mathbf{B}_1 = \mathbf{M} + \mu_o \cdot \mathbf{H} \qquad \text{Eq. 2–1}$$

and when the sample is outside the induction is:

$$\mathbf{B}_2 = \mu_o \cdot \mathbf{H}\,. \qquad \text{Eq. 2–2}$$

The change in magnetic induction is thus given by the difference:

$$\Delta \mathbf{B} = \mathbf{B}_1 - \mathbf{B}_2 = \mathbf{M} \qquad \text{Eq. 2–3}$$

From the Faraday law of electromagnetic induction, which states that the voltage induced in an electrical circuit is proportional to the rate of change of magnetic flux linking the circuit, we have:

$$V = -N \cdot A \cdot \frac{\mathrm{d}\mathbf{B}}{\mathrm{d}t}, \qquad \text{Eq. 2–4}$$
$$\int V \mathrm{d}t = -N \cdot A \cdot (\mathbf{B}_1 - \mathbf{B}_2) = -N \cdot A \cdot \mathbf{M}$$

where A is the cross-sectional area of the coil and N is the number of turns. Consequently, the output signal of the VSM detection coils is dependent only on **M** and is independent of **H**.

Due to geometrical constraints, the specimen must be relatively small to fit between poles of the electromagnet, what introduces demagnetization effects. The sensitivity of the method is limited mainly by the mechanical noise transmitted from the vibrator to the pick-up coils.

2.1.3. Magneto-optical Kerr effect

Magneto-optical effects were first discovered by M. Faraday [Faraday - 1846] and by J.C. Kerr [Kerr - 1877]. The Faraday effect is observed in transmission through the material and the Kerr effect is observed on reflection. For both effects, a small rotation of the polarization plane of the light results. The rotation is a linear function of the magnetization is useful for magnetometry applications. The MOKE, especially, is widely applied as a tool to measure magnetization, particularly for ultrathin films [Moog - 1981], [Bader - 1991].

Magneto-optical effects are due to direct interaction of the vector **E** of the incident radiation with **M** (indirectly through the Spin-orbit coupling). At optical frequencies, the vector **H** has no effect. In the case of thin magnetic films it is convenient to refer to three principal orientations: the longitudinal orientation, the polar orientation and the transverse orientation. These orientations are defined in terms of the direction of **M** with respect to the surface of the material and the plane of the incidence of an optical beam. In the *longitudinal case,* **M** is in the plane of the film and parallel to the plane of incidence. In the *polar case,* **M** is along surface normal and in the *transverse case,* **M** is in the plane of the film and perpendicular to the plane of incidence. For a detailed review of the magneto-optical effect the reader is referred to: [Bader - 1991], [Fowler - 1992], [Hubert - 1998].

The magneto-optic effects, in principle, are a consequence of the asymmetry of the dielectric tensor:

$$\epsilon = \varepsilon \begin{bmatrix} 1 & -iQm_3 & iQm_2 \\ iQm_3 & 1 & -iQm_1 \\ -iQm_2 & iQm_1 & 1 \end{bmatrix} \qquad \text{Eq. 2–5}$$

where, m_1, m_2, and m_3 are the directional cosines of **M** and Q is the (Voigt) magneto-optical constant of the magnetic layer.

For systems with perpendicular anisotropy, the polar Kerr configuration is best suited for hysteresis measurements [Visnovsky - 1995]. In this configuration the rotation of the polarization plane of the light is given by:

$$\theta_{K,p} = \left(-4 \cdot \frac{\pi}{\lambda}\right) \cdot \left(\frac{n^2}{1-n_{sub}^2}\right) \cdot Q \cdot d \qquad \text{Eq. 2–6}$$

where λ is the wavelength of the light, n is the index of refraction of the magnetic layer, n_{sub} is the index of refraction of the substrate, and d is the thickness of the magnetic layer.

The magnitude of the output signal in the MOKE is very sensitive to the precise setting of the light polarizer and analyzer, and to surface quality. This makes the determination of the absolute values difficult. For this reason, hysteresis data is usually normalized with the saturation signal.

Both Kerr [Williams - 1951], [Fowler Jr. - 1952], [Rave - 1987] and Faraday [Fowler Jr. - 1956] effects are also widely used for magnetic domain imaging, however, the highest resolution is only up to the limit of the optical microscopy.

2.2. Structural characterization techniques

2.2.1. Transmission electron microscopy

Transmission electron microscopy (TEM) techniques used to elucidate the structure of the analyzed materials are: conventional bright field imaging (BF), dark field imaging (DF), selected area diffraction (SAD), high resolution TEM (HRTEM), and energy filtered imaging (EFI). Most of these techniques are used routinely in materials research and will not be discussed in detail. For in-depth treatments the reader is referred to: [Thomas - 1981], [Edington - 1974], [Belk - 1979], [Reimer - 1984], [Williams - 1996], [Krishnan - in press].

2.2.1.1. Dark-field hollow-cone imaging

For dark field imaging, in addition to standard techniques, a hollow-cone imaging technique was implemented in this research to obtain an image with intensity corresponding to the entire diffracted ring [Krakow - 1976], [Saxton - 1978]. To obtain such hollow cone DF images the beam tilt is first set to bring a particular **g**-vector into the center of the optic axis in the back focal plane. The principles of beam tilting are schematically shown in Figure 2–1 for a crystalline specimen with a spotty diffraction pattern.

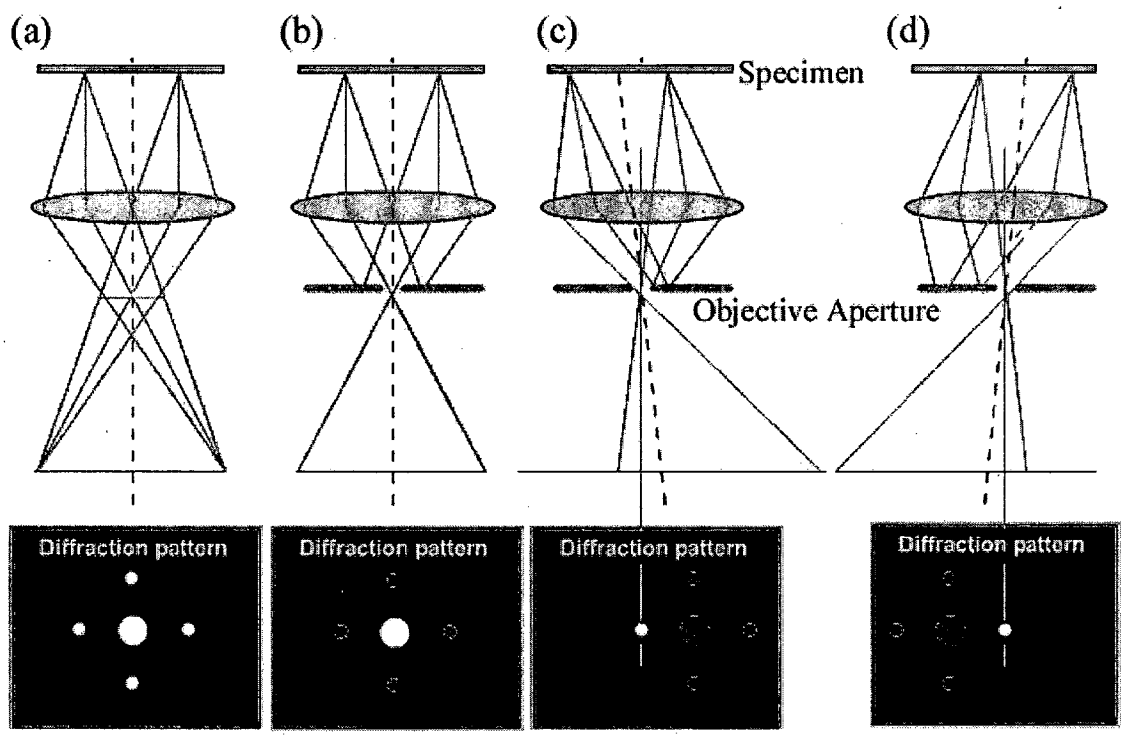

Figure 2–1. Principles of beam tilting in the TEM.

For the polycrystalline specimen, such beam tilt brings part of the diffracted ring onto the center of the back focal-plane. When the beam is then

rocked about the optic axis at a high frequency (much higher than the exposure time) and the magnitude of the beam tilt is kept constant, the entire diffracted ring can be rocked about the objective aperture. This procedure produces a hollow cone of illumination with its apex located at the specimen and a fixed cone azimuthal angle. While the ring of choice is rocking about the objective aperture, an image showing only the sample locations diffracting to this particular ring is recorded. This is particularly useful when texture analysis is desired. For example, hollow-cone imaging about rings, which are forbidden in textured films, can be used to image grains without the desired texture.

In this research, DF hollow-cone imaging was used to investigate the evolution of the quality of the <111> texture for Co/Pt multilayers. The intensity around the (111) ring, which is forbidden for the <111> textured films, was investigated as a function of growth temperature.

2.2.1.2. Energy-filtered imaging

Energy Filtered Imaging (EFI) in the transmission electron microscope (EFTEM) is a relatively new technique and a short introduction is presented below. EFTEM combines imaging techniques with standard analytical techniques, such as energy dispersive X-ray spectrometry (EDXS) or electron energy loss spectrometry (EELS) to image the elemental distribution in the specimen. Recently, EFI using EELS has become very routine, mainly due to the availability of energy filters and, in particular, the post-column filters [Krivanek - 1992], [Gubbens - 1993], [Krivanek - 1994]. Such filters are commercially available from Gatan Inc., Gatan Imaging Filter (GIF). Here, the principles of

EFTEM utilizing the inner-shell ionization edges of the EEL-spectrum are summarized [Egerton - 1996], [Yu - 1997], [Egerton - 1999], [Grogger - 2000].

Elemental mapping requires recording energy-filtered images as shown in Figure 2–2 for the case of Co L_3 edge. For the example presented, three 20 eV energy windows are displayed.

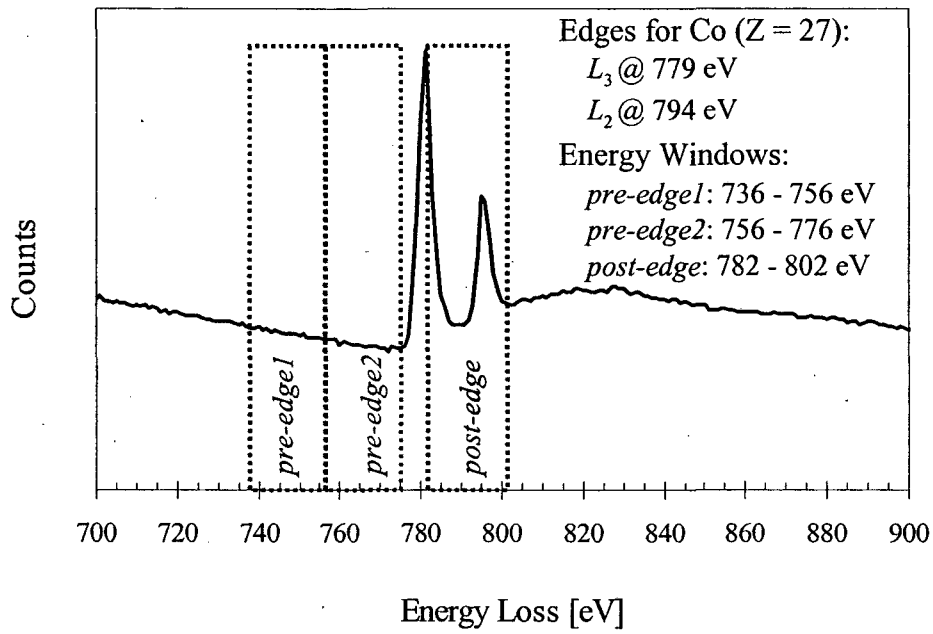

Figure 2–2. Electron energy loss about Co L_3-edge. Rectangular areas show energy ranges used to obtain energy-filtered images with 20 eV slit.

In the simplest procedure, a *pre-edge* image is divided by the *post-edge* image to yield a *jump-ratio* image. The jump-ratio image is, however, sensitive to thickness variation and diffraction condition. In addition, due to plural-scattering background components, it has only qualitative data about an elemental distribution [Hofer - 1995]. To obtain a quantitative *elemental map* image, two pre-edge images must be recorded to model the background contributions to the

post-edge image [Crozier - 1995], [Hofer - 1997]. Such calculations can be performed routinely using Digital Micrograph Software from Gatan Inc. when the images are acquired electronically.

To confirm that diffraction contrast does not contribute to the elemental map, the ratio of the two pre-edge images must be computed and it should yield little contrast. Any contrast on such an image should be different from elemental map contrast to ensure that the latter image represents true elemental concentration. When diffraction contrast introduces difficulties, tilting the sample away from zone axis and obtaining off-axis filtered images was shown to reduce the residual diffraction contributions [Moore - 2002].

Another very useful application of energy-loss spectroscopy is the determination of the local thickness of a TEM specimen. In this method, the filtered image corresponding to the intensity I_0 under the zero-loss peak is recorded as is the unfiltered image corresponding to the total area I_t under the loss spectrum. The thickness t is given by:

$$t = \lambda \cdot \ln\left(\frac{I_t}{I_0}\right) \qquad \text{Eq. 2–7}$$

where λ is a total mean free path for all inelastic scattering, which is typically 50 to 100 nm for 100 keV electron incident energy. It was shown that this technique provides 10% accuracy for $t/\lambda < 5$ [Egerton - 1996].

2.3. Magnetic imaging techniques

The static and dynamic structure of magnetic domains and domain walls is a subject of a number of ongoing scientific investigations. However, the true three-dimensional character of magnetic domains is often far from being resolved. Moreover, understanding the magnetic reversal mechanism in thin films is of both scientific and technological importance. Conventional magnetometry measurements are limited to detecting averaged magnetic properties and cannot give direct information about local nucleation events or reversal mechanisms. Hence, magnetic imaging techniques capable of detecting the onset of isolated nucleation events and also capable of imaging the progress of the magnetic reversal on the local scale are a key to a comprehensive understanding of magnetization phenomena.

Domain observation techniques originated with Bitter magnetic powder methods [Bitter - 1931], [Bitter - 1932]. In this simple technique, the stray fields above a domain pattern are decorated by fine magnetic particles. Since then, many techniques sensitive to the direction of magnetization, directly or indirectly, have been developed. Reviews of domain observation techniques can be found in: [Carey - 1966], [Craik - 1974], [Celotta - 1999], [Freeman - 2001].

In this dissertation research, high-resolution magnetic imaging was utilized to gain a full understanding of dynamic magnetic domain structure. A promising way of approaching this problem utilized the complementary techniques Lorentz Transmission Electron Microscopy (LTEM) and Magnetic Transmission X-

ray Microscopy (MTXM), which are sensitive to in-plane and out-of-plane magnetization, respectively.

2.3.1. Lorentz transmission electron microscopy

In this section, various TEM methods for imaging magnetic domain structure are outlined. Lorentz microscopy is a well-established technique and has been used to study magnetic domain structure in a wide variety of magnetic materials. Some examples are: [Hale - 1959], [Fuller - 1960], [Cohen - 1965], [McKendrick - 1976], [Belli - 1978], [Chapman - 1978], [Hoffmann - 1979], [Nowak - 1979], [Herd - 1979], [Bhatti - 1980], [Chapman - 1981], [Strzeszewski - 1982], [Karamon - 1982], [Hadjipanayis - 1982], [Donovan - 1983], [Taylor - 1983], [Suits - 1986], [Greidanus - 1989b], [Huetten - 1995], [Donnet - 1995], [Portier - 1997], [Verbist - 1998], [PetfordLong - 1998], [Kirk - 1999], [Petford-Long - 1999], [Kusinski - 2000], [Ardhuin - 2000], [Toporov - 2000], [Herrmann - 2000], [Kusinski - 2001a]. The most advanced techniques provide the highest magnetic resolution, with 1 nm achieved in magnetic imaging dedicated instruments. The information achievable includes the geometry of domain structures, the position and often the magnetic structure of domain walls, and the direction of magnetization within individual domains. Usually, the microstructural information is also available at the same or better spatial resolution. A comprehensive review of all magnetic imaging techniques utilizing transmission electron microscopy, which are usually called Lorentz TEM, can be found in [Chapman - 1984], [McFadyen - 1992], [Chapman - 1999]. The basics are summarized below.

When electrons pass through a thin specimen in a TEM, they experience a range of scattering forces. For magnetic specimens, electrons experience, in addition, the Lorentz force, which governs the magnetic deflection:

$$\mathbf{F} = -e(\mathbf{v}\times\mathbf{B}) \qquad \text{Eq. 2–8}$$

where e is electron charge, $\mathbf{v}$ is the velocity of electrons and $\mathbf{B}$ is the magnetic induction. The deflection β of an electron is given by:

$$\beta = \frac{e}{h}\cdot\lambda\cdot B_{\perp}\cdot t \qquad \text{Eq. 2–9}$$

where h is Plank's constant, λ is the electron wavelength, and $B_{\perp}\cdot t$ is the component of magnetic induction perpendicular to the electron path and integrated over the specimen thickness, t. Therefore, the deflection of the beam is perpendicular to both the direction of the magnetization and to the electron propagation direction [Hale - 1959], [Fuller - 1960]. For example, if a specimen contains domains of antiparallel magnetization normal to the electron beam, electrons passing through adjacent domains are deflected in opposite directions. This causes the diffraction spots to split into two sub-spots. Based on Eq. 2–9, using typical values of λ = 3.75 pm, t = 70 nm and $B_{\perp}$ = 1.5 T, the Lorentz deflection of electrons is β = 0.1 mrad. To put this in perspective, the typical values for Bragg angle are θ_B = 10 mrad (Note 10 mrad = 0.573°).

2.3.1.1. Fresnel and Foucault imaging

Fresnel and Foucault imaging are the most widely used and easily implemented modes of magnetic imaging in TEM. Both can be routinely implemented in a conventional TEM. The only constraint is that the sample must

be in the magnetic field-free region to prevent unintentional magnetization. In the conventional electron microscope, the objective lens, which is situated just around the specimen, is a source of a strong (~1 – 2 Tesla) magnetic field along the optic axis. Hence, the lens current must be reduced to prevent sample saturation, which substantially reduces the maximum magnification of the microscope and also introduces spherical aberration. In microscopes designed for Lorentz imaging, the objective lens is modified and consists of two pole-pieces located above and below the sample plane. Such a microscope with a so-called Lorentz lens delivers both the field-free region around the sample and the full magnification of a conventional TEM.

Schematics of how magnetic contrast is formed for Fresnel and Foucault modes are presented in Figure 2–3 and Figure 2–4. All representative images show magnetic domains in 50 nm thick polycrystalline Permalloy film grown on electron-transparent SiN membranes.

For the purpose of illustration, a simple specimen comprising three in-plane domains separated by two 180° domain walls is considered. In Fresnel microscopy, the imaging lens is simply defocused so that the object plane is either above or below the specimen, as shown in Figure 2–3. For the schematic (a), the object plane is fixed below the specimen, which results in narrow dark and bright bands on the image, delineating the positions of the domain walls in an otherwise contrast-free image. When the focus is changed to fix the image plane above the specimen, as illustrated in (b), an opposite contrast is observed, i.e. previously bright bands are dark and vice-versa. Naturally, for a properly focused image such dark and bright band contrast will not be visible. It must be emphasized

that when the defocus values are increased, the widths of the bands also increase. Hence, this technique cannot be used directly to measure the width of the domain wall. As shown on the schematic, the bright band (the convergent domain wall image) consists of interference fringes. Hence, the simple classical ray diagram presented here is only approximate and, in principle, the wave nature of electrons must be considered [Aharonov - 1959].

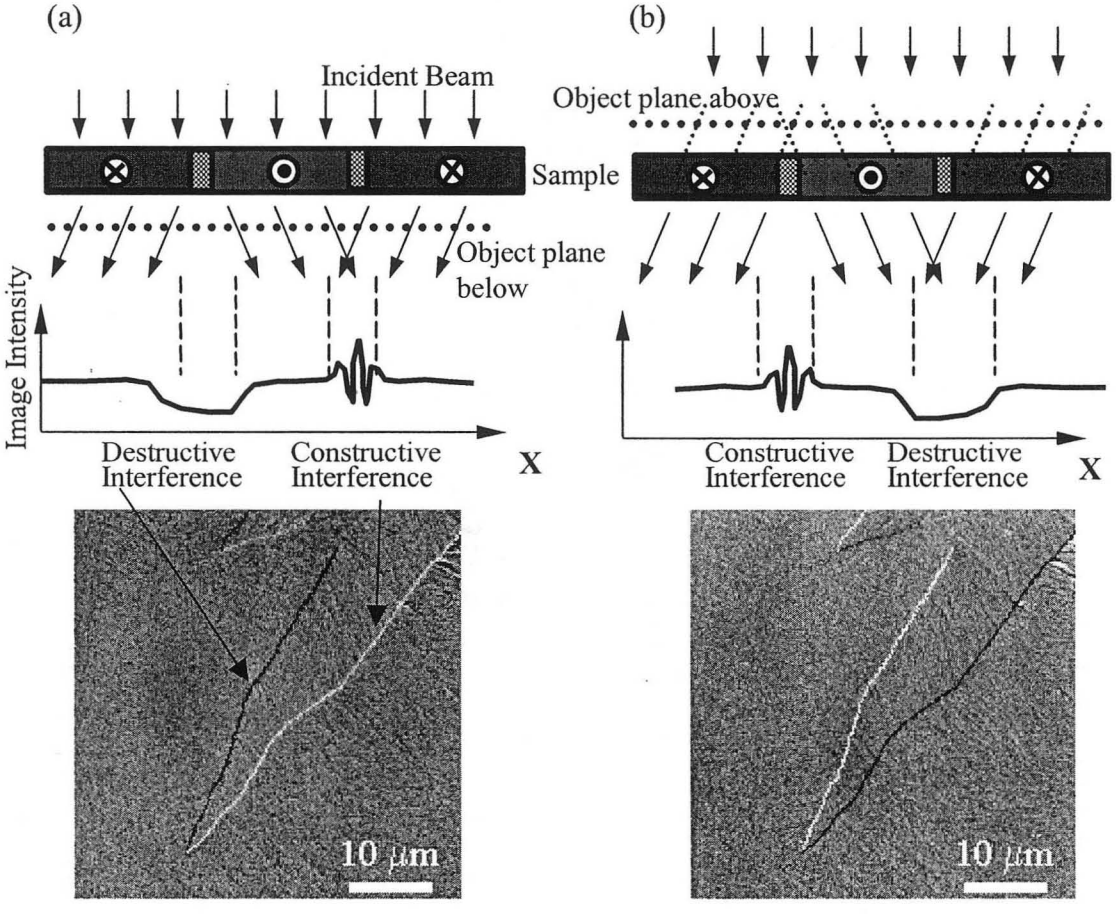

Figure 2–3. The principle of the Fresnel technique of Lorentz TEM. The object plane is fixed (a) below the specimen and (b) above the specimen. Images show domains in a polycrystalline Permalloy (note domain-wall contrast reversal).

Foucault microscopy, technically speaking, is just another form of dark field imaging. A contrast-forming aperture is inserted in the back focal plane (the plane of the diffraction pattern) to obstruct one of the components into which the central diffraction spot is split due to the deflections suffered as the electrons pass through the specimen.

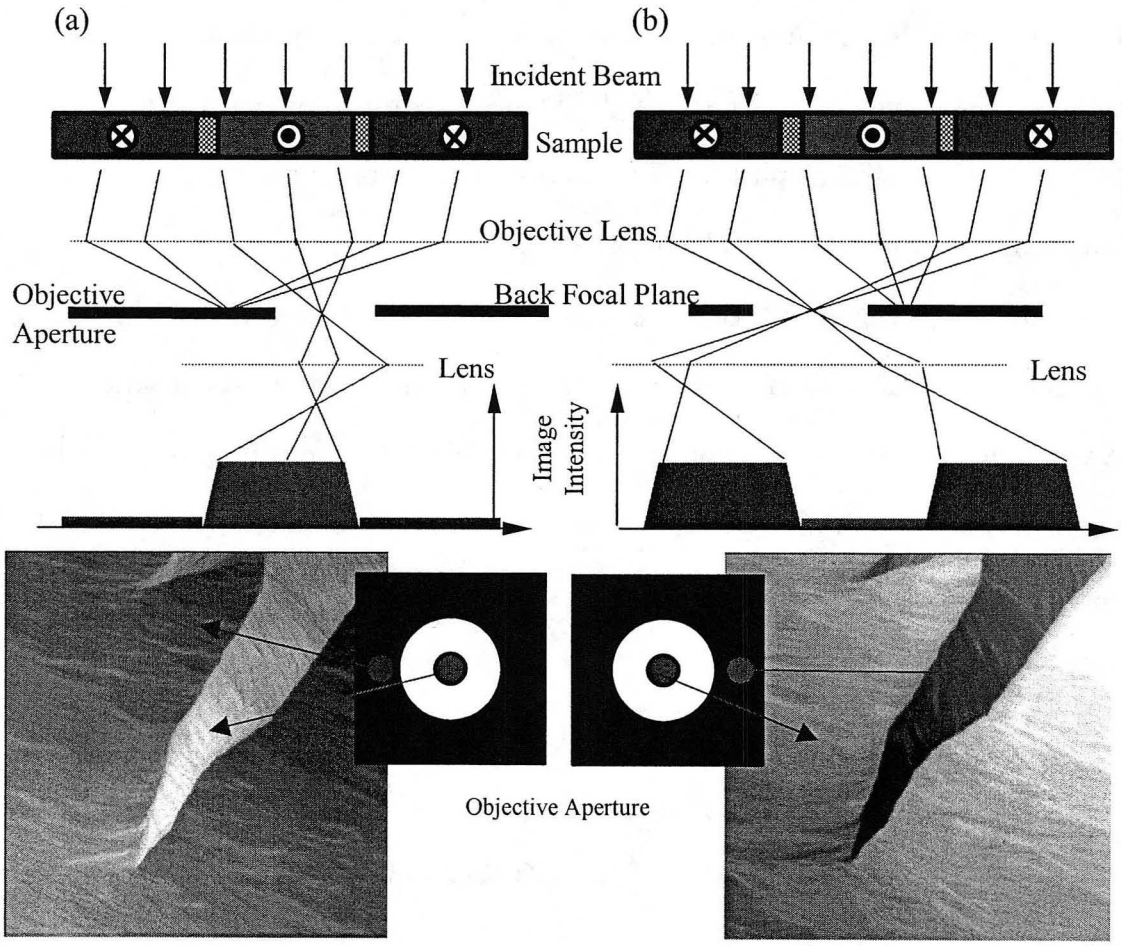

Figure 2–4. The principle of the Foucault imaging mode of Lorentz TEM. Images show the same areas as Figure 2–3. Note contrast-reversal when the objective aperture is moved.

In the simple case illustrated in Figure 2–4, the central spot is split into only two spots. As a result of the obstruction of the first of the diffraction spots, Figure 2–4(a), domain contrast can be seen in the image. Bright areas correspond to domains where the magnetization orientation is such that electrons are deflected into the first spot and through the aperture. Dark areas represent domains for which the orientation of magnetization is oppositely directed, and electrons are deflected into the second spot. When the aperture is shifted to obstruct the second spot, as shown in Figure 2–4(b), complementary contrast results. In general, the splitting of the central spot is more complex than for the simple case of two beams considered here.

Obviously, Foucault contrast can be obtained if electron beam tilt is utilized instead of motion of the aperture. Fixing the aperture position, the diffracted beams can be moved in the back focal plane by controlling the beam tilt magnitude, as shown in Figure 2–1. The advantage of this approach is that the magnitude of the beam tilt can be controlled much more accurately than can the position of the aperture.

The Fresnel and Foucault modes of Lorentz microscopy are generally fairly simple to implement and they provide a clear picture of the overall domain geometry and a useful indication of the directions of magnetization. However, there are many drawbacks.

For Fresnel imaging, no information about the direction of magnetization within a single domain is directly available. For the Foucault mode, reproducible positioning of the contrast-forming aperture is difficult. Moreover, both imaging modes suffer from the disadvantage that the relation between image contrast and

the spatial variation of magnetization is usually non-linear. All these factors make the extraction of quantitative magnetization data problematic.

Differential Phase Contrast (DPC) microscopy in a Scanning Transmission Electron Microscope (STEM) [Chapman - 1978], [Chapman - 1990] is one technique where quantitative maps of the magnetic domains in thin foils can be obtained. DPC requires expensive microscopes equipped with de-scanning coils, a quadrant detector and post-specimen lenses. For this reason, this technique is not generally accessible and is found in relatively few scientific institutions (among them, the University of Glasgow[i]).

2.3.1.2. Quantitative Foucault imaging

Recently, an equivalent technique for the TEM was proposed [Daykin - 1995], [Dooley - 1997a], [Dooley - 1997b], [Verbist - 1998]. It was demonstrated that a relatively standard TEM could be used to obtain maps of the in-plane components of magnetic induction. The technique is equivalent to DPC by the reciprocity theorem; instead of scanning the beam over the sample, the angle of the beam tilt is systematically scanned and the aperture is inserted in the back focal plane. A series of Foucault images are digitally recorded in four quadrants (in two perpendicular directions), as shown schematically in Figure 2–5(a). Four sum images, $\Sigma\{+X\} = B$, $\Sigma\{-X\} = D$, $\Sigma\{+Y\} = A =$ and $\Sigma\{-Y\} = C$ are formed by digitally averaging the respective images.

---

[i] Professor John Chapman, Department of Physics and Astronomy, University of Glasgow, UK.

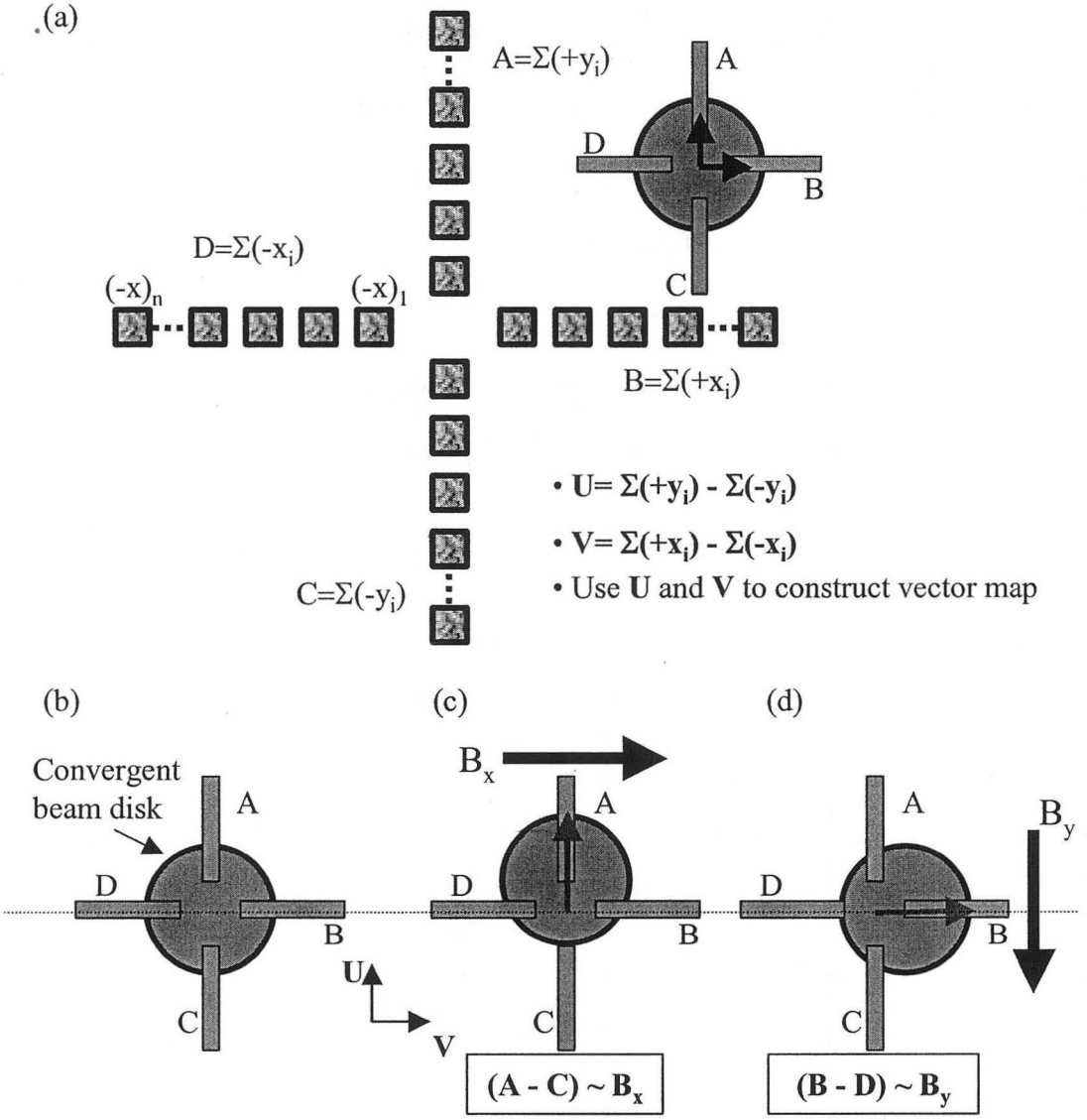

Figure 2–5. Principles of quantitative Foucault imaging in TEM (see text).

The two orthogonal components of the in-plane magnetization vector, **U** and **V** are given by respective differences signals of the before mentioned sum-images:

$$\mathbf{U} = (B - D) = \Sigma\{+X\} - \Sigma\{-X\} \quad \text{and} \quad \mathbf{V} = (A - C) = \Sigma\{+Y\} - \Sigma\{-Y\}$$

Eq. 2–10

When the sample has zero magnetization, Figure 2–5(b), both difference signals, **U** and **V**, are zero. When the sample has a magnetization $\mathbf{B}_x$, Figure 2–5(c), the convergent beam disk is shifted into the +Y direction proportional by an amount to the Lorentz force. The signal (A-C) = **V** is then proportional to $\mathbf{B}_x$ and the signal (B – D) = **U** is zero. By the same argument, with $\mathbf{B}_y$ magnetization, Figure 2–5(d), the signal (A-C) = **V** is zero and (B – D) = **U** is proportional to $\mathbf{B}_y$.

Quantitative Foucault imaging was successfully implemented and fully automated at the Philips CM200 microscope at the National Center for Electron Microscopy (NCEM). The technique was used to obtain detailed magnetization maps of the in-plane component of magnetization in the CoCr system. Results are presented in Chapter 6.

2.3.2. X-ray techniques

All of the X-ray techniques used for imaging of magnetic domains are based on the absorption of photons, a process governed by electronic dipole transitions. The advantage of x-ray techniques is elemental specificity in imaging, which arises from the characteristic binding energies of the atomic core electrons. The transitions are governed by the $\Delta l = \pm 1$ selection rule and the d band transition metals are best studied using $L_{2,3}$ edges ($2p \rightarrow d$). For rare earth metals, $M_{4,5}$ ($3d \rightarrow 4f$) edges are used. Magnetic contrast formation is governed by X-ray Magnetic Circular Dichroism (XMCD).

2.3.3. Magnetic contrast formation by XMCD

The technique known as XMCD spectroscopy was first introduced by Schutz [Schutz - 1987] in the analysis of the absorption of circularly polarized X-rays in iron. An in-depth review of principles of XMCD spectro-microscopy techniques can be found in [Stohr - 1998], [Stohr - 2000]. Figure 2–6 illustrates the concepts of XMCD for a d transition metal. As shown, for a magnetic metal, the d-valence band is split into spin-up and spin-down states with different electron occupation densities. This imbalance in electron occupation can be probed by spin-dependent X-ray absorption, which measures the equivalent, but opposite in sign, difference in spin-up and spin-down holes (states above the Fermi level). When Right Circularly Polarized (RCP) and Left Circularly Polarized (LCP) photons are absorbed by a d transition-metal, they transfer their angular momentum, $+\hbar$ and $-\hbar$, respectively, to the photoelectron. For photoelectrons that originate from a spin-orbit-split level (eg. $p_{3/2}$, L_3 edge), the angular momentum is coupled to the spin through spin-orbit coupling. Hence, photoelectrons with opposite spin, spin-up or spin-down, are created when either RCP or LCP are absorbed, respectively. Moreover, in the X-ray absorption process, which is governed by electric-dipole transitions, spin flips are not allowed. Hence, spin-up photoelectrons from the p core shell can be excited only into spin-up d hole states, and spin-down photoelectrons can be excited only into spin-down d hole states. For this reason, the measured resonance intensity relates directly to the number of empty d-band states of a given spin. Also, the $p_{3/2}$ (L_3) and $p_{1/2}$ (L_2) levels have opposite spin-orbit coupling, l+s and l-s, respectively, and the spin polarization is opposite at these two absorption edges. The applicability of X-ray

absorption process for magnetic imaging stems from the fact that the change in the polarization of photons has the same effect on the absorption as does the change in the magnetization direction. In other words, the change in absorption is equivalent when 1) the photon polarization is changed and the magnetization direction is kept fixed or when 2) magnetization direction is changed and the photon polarization is kept fixed.

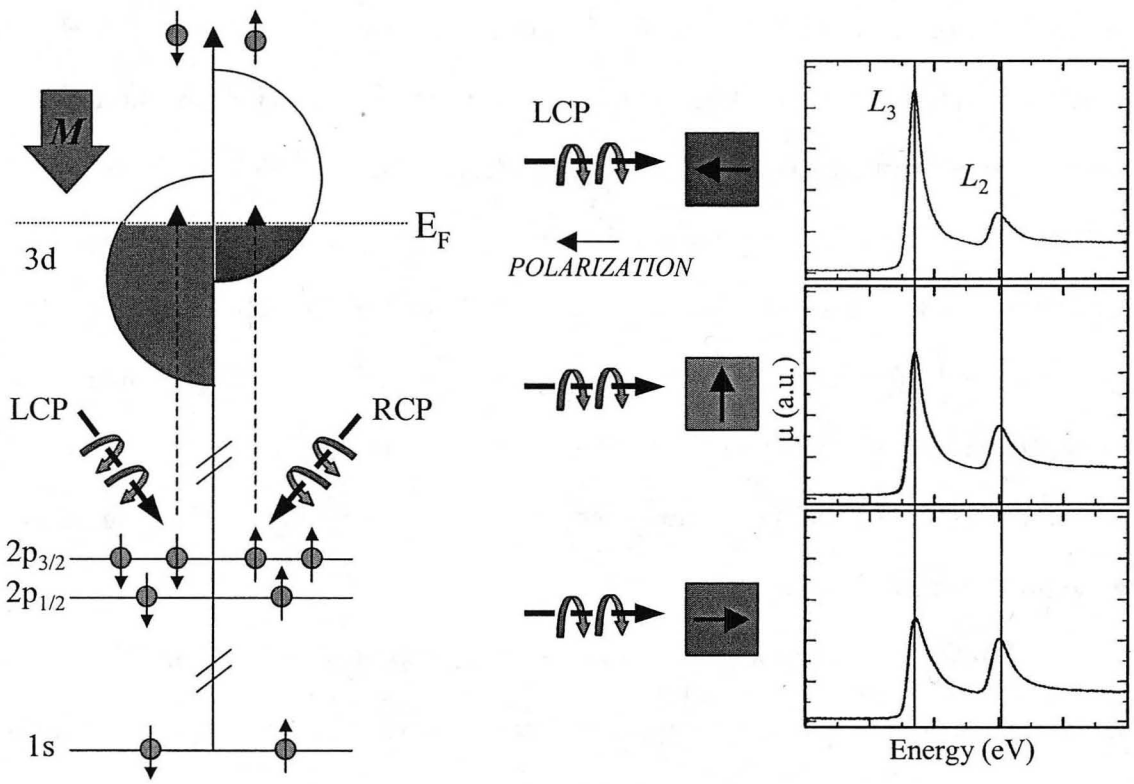

Figure 2–6. Principles of X-ray magnetic circular dichroism, for the case of *L* edge absorption in a *d* band transition metal.

In practice, X-ray absorption studies are carried out with polarized synchrotron radiation. The polarization of the synchrotron radiation emitted from a bending-magnet source depends on the vertical position relative to the plane of

the electron orbit. The center of the beam, which is in the same plane as the electron storage ring, carries linearly polarized X-rays. Radiation below and above the orbit plane of the storage ring has a component of right- or left-hand circular polarization [Stohr - 1998].

2.3.4. Full field magnetic transmission x-ray microscopy

Samples were studied with the full field soft x-ray microscope (The XM-1) located at the Beamline 6.1.2 of the Advanced Light Source at Lawrence Berkeley National Laboratory.[i] Beamline 6.1.2 is a bend-magnet source with illumination energy tunable between 300 – 1500 eV. It is dedicated to a high-resolution transmission x-ray microscope, XM-1, which is used for imaging biological structures, environmental systems and magnetic materials. The microscope is a "conventional" full field transmission microscope, which is able to achieve a resolution of 25 nm by using high-precision zone plates [Anderson - 2000]. A schematic of the optical setup and a scanning electron micrograph of the 25 nm zone plate are shown in Figure 2–7.

XM-1 is a direct-imaging instrument using two Fresnel zone-plate lenses as x-ray lenses. The first one, a condenser, focuses x-rays onto the sample. The large chromatic aberration of this zone-plate, in combination with a small 15 μm pinhole, acts as a monochromator. X-rays of different energy have different focal points along the optic axis; hence, by changing the relative distance between the condenser lens and pinhole, photons with different wavelengths can be selected. The achievable spectral resolution, measured by the ratio $E/\Delta E$, ranges from 500

[i] http://www-cxro.lbl.gov/microscopy/

to 700 depending on the fields of view. The second zone-plate, which is a micro zone-plate, acts as an objective lens and images the transmitted x-rays onto a detector.

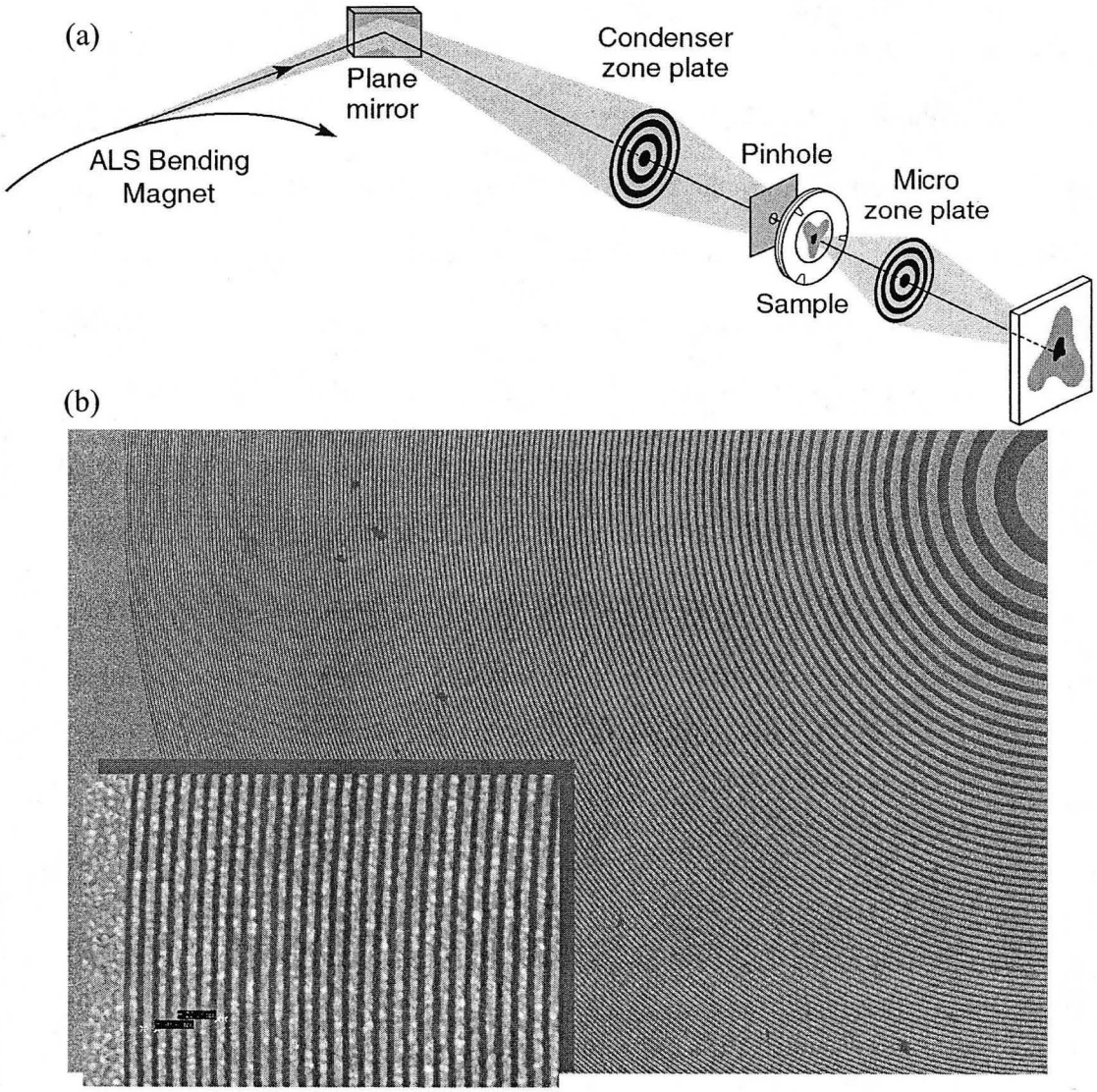

Figure 2–7. (a) The XM-1 Soft X-ray Microscope at the Advanced Light Source, Beam-line 6.1.2. (b) Scanning electron micrograph of the 25 nm zone plates (courtesy G. Denbeaux, E. Anderson [Anderson - 2000]).

This microscope has recently been established as a tool for high-resolution imaging of magnetic domains [Denbeaux - 2001]. It uses off-axis bending-magnet radiation, with the slit placed above the plane of the storage ring, to illuminate samples with elliptically polarized light. When the illumination energy is tuned to the absorption edges of specific elements, it can be used as an element-specific probe of magnetism on a 25 nm scale with a contrast provided by XMCD. If one considers a bilayer system consisting of two ferromagnetic layers, for example 50 nm Fe/50 nm Co, magnetic-domain imaging sensitive to the domain features across a chemical interface can be analyzed. First, magnetic domain structure in the Fe layer can be imaged by tuning to the Fe L_3 absorption edge. Next, tuning to the Co L_3 absorption edge, magnetic domain structure within the Co layer can be studied. Hence, element-specific magnetic imaging is possible.

For the Co/Pt multilayers studied in this dissertation, Co L_3 the absorption edge was used to image magnetic domains.

The studies implementing X-ray microscopy to investigate magnetic domains are referred to as magnetic transmission x-ray microscopy (MTXM). Some examples include: [Fischer - 1996], [Eimuller - 1999], [Fischer - 1999], [Eimuller - 2000], [Kohler - 2000], [Kusinski - 2001a], [Eimuller - 2001], [Fischer - 2001c], [Fischer - 2001b], [Fischer - 2001a], [Denbeaux - 2001].

2.3.4.1. Magnetic contrast at XM-1

The XM-1 is sensitive to the component of the magnetization along the photon propagation direction. Since samples are imaged in transmission, the XM-

1 is suited to study the out-of-plane component of magnetization. The basic principles of contrast formation are shown in Figure 2–8.

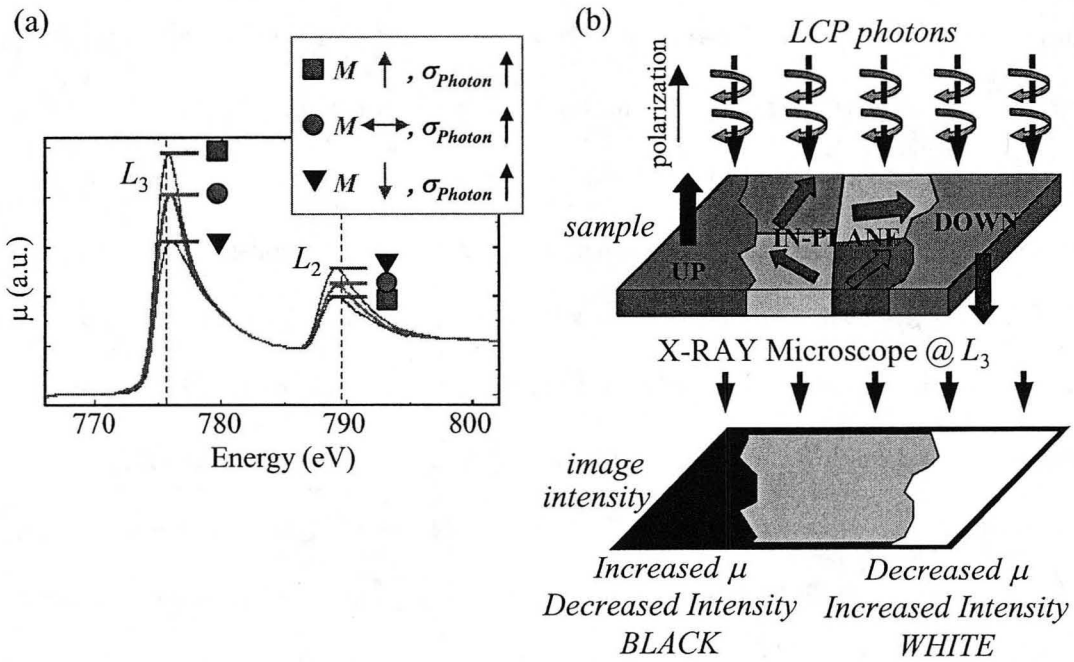

Figure 2–8. Schematic diagrams illustrating the magnetic contrast mechanism in the MTXM. (a) L_3 and L_2 absorption edges with three levels of μ depending on the relative orientation of **M** and σ_{photon}. (b) Magnetic sample with up, down and in-plane domains and a recorded image displaying three intensity levels measured in the X-ray microscope at the L_3 edge.

In the X-ray microscopy setup used in this research, the magnetization of the samples in a positive polar direction is parallel to the x-ray polarization. This parallel alignment of magnetization and photon polarization gives increased absorption of photons at the Co L_3 edge and, hence, lower photon count, seen as dark areas in the image. On the other hand, the negative polar magnetization is anti-parallel to the x-ray polarization. The anti-parallel alignment of

magnetization and polarization results in decreased absorption of photons at the Co L_3 edge and, hence, a higher photon count is measured. On the image, the areas with negative magnetization are thus brighter. For the in-plane magnetized regions, regardless of the in-plane direction, the magnetization has no component along the photon propagation direction. The absorption is not affected by magnetization but gives an intermediate photon count, seen as a uniform gray contrast. Initially, due to experimental limitations, the perpendicular magnetic field, $H_{\perp}$, was applied *ex-situ* in an external VSM magnet and all samples were imaged at remanence. Recently, magnetic coils were installed around the microscope's sample holder, allowing for magnetic imaging with $H_{\perp}$ up to approximately ± 3 kOe applied *in-situ*.[i] This field is still not sufficient to fully reverse and saturate high coercivity samples while imaging. However, it is large enough to reverse parts of the samples, making it possible to image the onsets of magnetic domain nucleation *in-situ*. Such ability is extremely important and essential to complete understanding of the magnetization reversal process. The precise location and the distribution of the nucleation sites can be detected, making it superior over magnetometry techniques. This must be emphasized. Conventional magnetometry measurements, such as VSM or MOKE, can measure the distribution of nucleation fields but always average the information over the

---

[i] The space around the sample is very limited, due to close proximity of two imaging cones. This prevents installing large coils capable of generating significant magnetic fields. However, this purely geometrical constraint can be easily avoided in the x-ray microscope design solely for magnetic imaging. The XM-1 used in this work was initially built primarily for the imaging of biological samples.

investigated volume. This is where magnetic imaging, especially at the relevant length scale at or below about 50 nm, is of great importance.

2.3.4.2. Imaging variables and challenges

As stated in the previous sections, photons are focused onto the sample with a condenser zone plate. However, the intensity projected onto the sample is not uniform. This introduces several difficulties during the interpretation of data. First of all, the CCD counts from two different locations on the sample cannot be directly compared as the incident intensity of photons is not uniform, and is a function of sample position, $I_o = I_o(x,y)$. This requires normalization of recorded intensity with respect to the incident photon count or with respect to the transmitted intensity without magnetic contrast. However, incident intensity distribution changes with time, t, with each storage ring refill or sample loading, $I_o = I_o(x,y,t)$, and a standard background subtraction routine is not possible. For this reason, in order to correct for non-uniform intensity, it is necessary at each time to record images away from the magnetic domain contrast, $I_o(x,y,t)$. Then the image of interest is recorded, $I(x,y,t)$, and it is divided by $I_o(x,y,t)$ to obtain a corrected image.

2.3.5. Magnetic force microscopy

For magnetic force microscopy (MFM) the tip of the atomic force microscope is coated with a ferromagnetic film. The MFM measures the interactions of the magnetic tip and the sample magnetic stray fields in a spatially resolved fashion [Grutter - 1992]. The MFM system is operated in a non-contact mode, and it measures changes in the resonant frequency of the cantilever, which are induced

by the magnetic field's dependence on tip-to-sample separation. This is illustrated in Figure 2–9.

The main advantage of MFM is that the samples do not have to be thinned-down to transparency and, hence, MFM is truly a non-destructive technique. The main limitations of MFM, as compared to both LTEM and MTXM, are lower resolution and sample-tip interactions. When the sample is magnetically softer than the MFM tip, it can be unintentionally switched during the scanning process. Similarly, when the tip is softer, it can be switched by the magnetic field of the sample. In addition, it is often difficult to separate the magnetic signal from the topography of the sample. This introduces ambiguities in interpretation.

MFM was used to study ion-beam patterned Co/Pt ML's during the author's practical training at the IBM Almaden Research Center, in order to study ion-beam patterned Co/Pt multilayers. These results are not presented in this thesis.

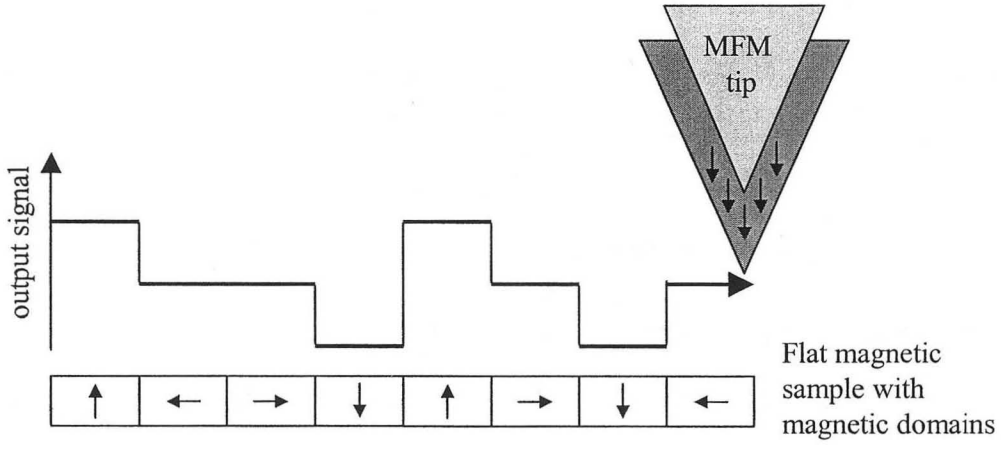

Figure 2–9. Principles of Magnetic Force Microscopy (MFM).

Chapter 3. Experimental:

COBALT-PLATINUM MULTILAYERS

Co/Pt multilayers are one of the most popular and widely studied systems because their magnetic properties can be adjusted and tuned considerably by an appropriate choice of the Co layer thickness, multilayer periodicity, total number of layers, seed layer quality and texture.

The perpendicular magnetic anisotropy in Co-based multilayers (ML's) was first discovered in Co/Pd structures [Carcia - 1985] and later in Co/Pt structures [Carcia - 1988], [Sato - 1988], [Zeper - 1989b]. Initial interest in Co/Pt multilayers was motivated by magneto-optical (MO) recording technology [Kryder - 1993]. It was recognized that the ultra-thin Co/Pt and Co/Pd multilayered films can be prominent material for higher-density MO recording using a shorter-wavelength laser (~400 nm) [Hashimoto - 1989], [Greidanus - 1989c], [Greidanus - 1989a], [Ochiai - 1989], [Zeper - 1989a], [Carcia - 1990b], where conventional rare-earth transition metal media do not operate well. In addition, it was recognized that the Co/Pt ML's are chemically stable and are highly resistive to oxidation and corrosion, which makes them attractive from the processing point of view as well.

Voluminous work has been carried out investigating the origin of perpendicular magnetic anisotropy and the influence of microstructure on the magnetic properties (growth conditions [Zeper - 1991], texture [Li - 1992], sputtering conditions [Carcia - 1993], Co layer thickness [Li - 1993], epitaxy [Cho - 1992b], [Weller - 1993], [Smith - 1994], [Carcia - 1995], and twinning [Cho - 1992a]). It was discovered that Co/Pt ML's show a preferential magnetization perpendicular to the film plane for Co thickness below 12 Å and a 100% perpendicular remanence for Co thickness below 4.5 Å [Zeper - 1989b]. As the Co thickness increases, the Co and Pt layers gradually lose coherency and the magnetic anisotropy goes from perpendicular to planar. This is accompanied by a relaxation of lattice strain in both the Co and Pt layers. The close relationship between magnetic anisotropy and lattice strain can be explained as a magnetoelastic anisotropy or stress anisotropy effect due to lattice mismatch between the adjacent epitaxial layers [Zhang - 1993b], [Zhang - 1993a]. It is now well recognized that the coercivity and perpendicular anisotropy of Co/Pt multilayers are very sensitive to the method of deposition, which leads to different microstructures. In particular, the interface sharpness between layers, the columnar structure and the texture are subject to the fabrication process. Large perpendicular anisotropies are not uncommon for Co/Pt films and are attributed to an interface contribution, K_S. The interface anisotropies reported in the literature for Co/Pt ML's vary greatly (0.2 - 1.2 mJ/m^2) depending on the growth method and texture [Bland - 1994].

The binary Co-Pt system, Figure 3–1, shows complete solid solubility at high temperatures and forms two ordered phases at low temperatures [Massalski -

1990]. These are CoPt-$L1_0$ and CoPt3-$L1_2$ intermetallic phases [Hansen - 1958]. Thus, there is a thermodynamic driving force for interdiffusion in the Co/Pt multilayers. Table 3–1 lists selected data for Co, Pt and their intermetallics.

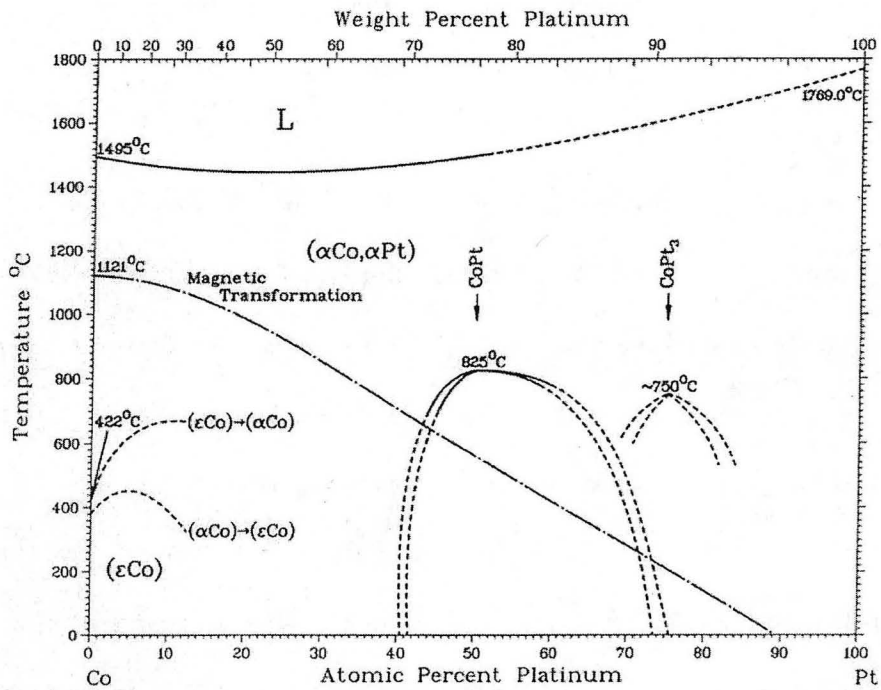

Figure 3–1. Binary Co-Pt phase diagram [Massalski - 1990].

Table 3–1. Selected data for Co-Pt system.

Chemical Formula	Crystal Type	Space Group	Structure Type	a (Å)	c (Å)	Reference
Co	hexagonal	194 $P6_3/mmc$	Mg	2.505	4.070	[Kuznetsov - 1965]
Co	cubic	225 $Fm\underline{3}m$	Cu	3.563		phase stable above 673 K [Kulesko - 1968]
Pt	cubic	225 $Fm\underline{3}m$	Cu	3.923		[Brooksbank - 1968]
Co_3Pt	cubic	225 $Fm\underline{3}m$	Cu	3.668		[Buschow - 1983]
CoPt	tetragonal	123 P4/mmm	AuCu	3.806	3.684	[Woolley - 1964]
$CoPt_3$	cubic	221 $Pm\underline{3}m$	$AuCu_3$	3.831		[Geisler - 1952]

3.1. Objective of the research

Recent interest in Co/Pt was sparked by the discovery that the magnetic properties can be locally modified by ion-beam irradiation. Study of such ion irradiation induced change in magnetic properties was the primary objective of the research reported this thesis.

The key magnetic properties, such as coercivity, H_C, nucleation field, H_N, magnetic remanence, M_R, etc. are structure dependent [Ramesh - 1989] and are tunable via growth conditions and choice of Co/Pt layer periodicity and thickness. Hence, before discussing the modification of magnetic properties and patterning by ion irradiation, proper microstructural characterization of the material at hand was required. In this chapter, research investigating the physical microstructures of Co/Pt multilayers is summarized and these results are correlated with the magnetic properties. The modification of multilayers' magnetic properties by ion-irradiation is discussed in the following chapter.

3.2. Experimental procedures

A number of Co/Pt multilayers have been investigated in an attempt to correlate the microstructure with the measured magnetic properties. For the specific experiments discussed here, Co/Pt multilayers with representative structure:

/ 20 nm Pt seed / N×(t nm Co/1 nm Pt) / 1 nm Pt cap layer /,

were fabricated by electron beam evaporation using a 10^{-8} – 10^{-9} Torr base pressure deposition system. In this notation N indicates number of Co/Pt bilayers,

and t is layer thickness. Samples were grown on SiN_x (40 nm)-coated Si(001) substrates for magnetic and X-ray diffraction (XRD) studies. The SiN_x films were dc-magnetron sputtered at room temperature and annealed at 400°C before Co/Pt growth. For TEM and MTXM imaging, ML's were deposited directly onto commercially available electron-transparent Si_3N_4 windows. The Co/Pt structures were electron beam evaporated at growth rates of ~0.05 nm/s for both the Co and Pt layers with the pressure during evaporation in the low 10^{-7} Torr range. Two sets of multilayers were grown. In the first set, (set A, $N = 10$, $t_{Co} = 0.3$ nm), both the 20 nm Pt seed layer and the multilayer stack were evaporated at roughly the same growth temperature, T_G. These samples were grown at T_G ranging between 200°C and 390°C. In the second set, (set B, $N = 15$, $t_{Co} = 0.5$ nm), the 20 nm Pt seed layer was evaporated at the constant growth temperature $T_{G,seed} \cong 300$°C. As is discussed later, multilayer growth conditions control the grain size and the seed layer growth temperature is fixed to achieve uniform grain size. Subsequently, the multilayers were grown at growth temperatures ranging between 100°C and 250°C in order to control the magnetic coercivity. The thickness, t, of the Co layer was varied between 0.2 and 1.2 nm to control perpendicular anisotropy. The Co/Pt multilayers investigated during this research are listed in Table 3–2. For each sample, seed layer thickness, seed layer growth temperature, multilayer thickness, multilayer growth temperature, Co layer thickness, periodicity, and magnetic coercivity are listed.

Table 3–2. List of Co/Pt multilayers with structure
/ t_{Pt} nm Pt seed layer / N×(t_{Co} nm Co / t_{Pt} nm Pt) / 1 nm Pt cap layer.

Sample ID	Pt seed		Co/Pt Multilayers				
	t_{Pt} (nm)	T_G (°C)	N	t_{Pt} (nm)	t_{Co} (nm)	T_G (°C)	$H_{C\perp}$
EG_108	20	184	10	1	0.2	165	4.5
EG_104	20	243	10	1	0.2	243	7.9
EG_107	20	230	10	1	0.3	190	3.8
EG_103	20	270	10	1	0.3	250	6.8
EG_102	20	300	10	1	0.3	300	7.7
EG_101	20	390	10	1	0.3	390	5.8
EG127 special test	20	200		0.3 to 2.5	0.3 to 2.5	200	NA
EG_173	20	100		1	0.6	100	2.3
EG_169	20	300		1	0.6	300	3.2
EG_D	10	300	15	1	0.5	100	2.5
EG_C	10	300	15	1	0.5	150	2.9
EG_B	10	300	15	1	0.5	200	3.2
EG_A	10	300	15	1	0.5	250	4.3

The multilayers under investigation were all polycrystalline, composed of small grains. It was expected that the magnetic properties of the films are strongly dependent on the microstructural differences. Grain size, grain orientation and texture, grain boundary character and defects in the crystal structure, all of which are related to the deposition processes, play very important roles in the magnetic reversal processes. The electron microscopy techniques used to elucidate the structural information were: bright field (BF), dark field (DF),

high resolution (HRTEM) and energy filtered (EFI) imaging, and selected area diffraction (SAD). All samples investigated in the plan-view were deposited directly on electron-transparent amorphous, sub 50 nm thick Si_3N_4 windows. This procedure removes the ion-mill thinning step and ensures that all samples are examined in the as-grown state (i.e. uniform thickness, no-ion milling damage). For cross-sectional examinations, sandwich-like structures were prepared. These sandwiches were first thinned down by mechanical grinding and then thinned to electron transparency by low angle, low voltage ion-milling in a Technoorg-Linda IV3H/L South Bay Technology ion mill. The ion-milling rate of Co/Pt multilayers is much slower than that of the Si substrate; hence, it was difficult to obtain electron transparency in the multilayer stack before the Si substrate was completely milled out. In addition, Co (atomic number 27) mills faster than Pt (atomic number 78), which results in significant thickness variation. For this reason, a tripod polishing method was first used to thin the sample almost to electron transparency and ion milling was then used for a very short time only to clean the sample. The electron microscopes used were Philips CM 200 FEG and JEOL 3010 LAB6, operated at 200 and 300 kV, respectively. Magnetic measurements were performed using polar and transverse Kerr hysteresis measurements and vibrating sample magnetometry at room temperature in magnetic field, *H,* up to 12 kOe. The magnetic domain structures of the as-grown samples were analyzed by LTEM (explained in section 2.3.1) and by MTXM (described in section 2.3.4). The MTXM is implemented at beam-line 6.1.2 of the Advanced Light Source (ALS) at the Lawrence Berkeley National Laboratory [Denbeaux - 2001]. In particular, high-resolution magnetic imaging

was performed with the MTXM to study the magnetic domain structure as a function of growth temperature and ion irradiation dose (discussed in detail in Chapter 4) with a 25 nm spatial resolution [Kusinski - 2001a]. Moreover, Lorentz TEM, in conjunction with MTXM, was used to study magnetic reversal processes in the patterned multilayers. These results are discussed in Chapter 5.

3.3. Microstructural characterization

The first results discussed concern the evolution of the microstructures of Co/Pt multilayers with the increasing growth temperature, T_G. Before discussing differences in the structure of these multilayers, which strongly influence the magnetic properties, certain characteristic features of the microstructure are first outlined based on the analysis of a multilayer consisting of: 20 nm Pt seed + 10×(3 Å Co and 10 Å Pt), grown at $T_G = 250°C$, sample labeled EG_103 in Table 3–2.

Figure 3–2 shows a plan-view, bright field TEM image and SAD patterns of a Co/Pt multilayer grown at 250°C. The microstructural contrast observed is a projection of the grains through the entire film thickness. The sample was polycrystalline with an average grain size of 50 ± 16 nm. The fine structure visible in some of the grains is attributed to Moiré fringes caused by the small lattice mismatch between Co and Pt planes. The plan-view SAD pattern of the sample presented in Figure 3–2(b) shows typical ring spacing associated with polycrystalline face-centered cubic *(fcc)* Pt structure (except for ring splitting due to the presence of highly strained Co layers, which will be addressed later in this section). All rings allowed by the structure factor for the *fcc* material are present in the diffraction patterns, especially in Figure 3–2(c), which shows SAD at a 30°

sample tilt. The intensity ratios of the rings, however, do not follow those for randomly oriented grains where the intensity of the (111) reflection is usually the strongest.

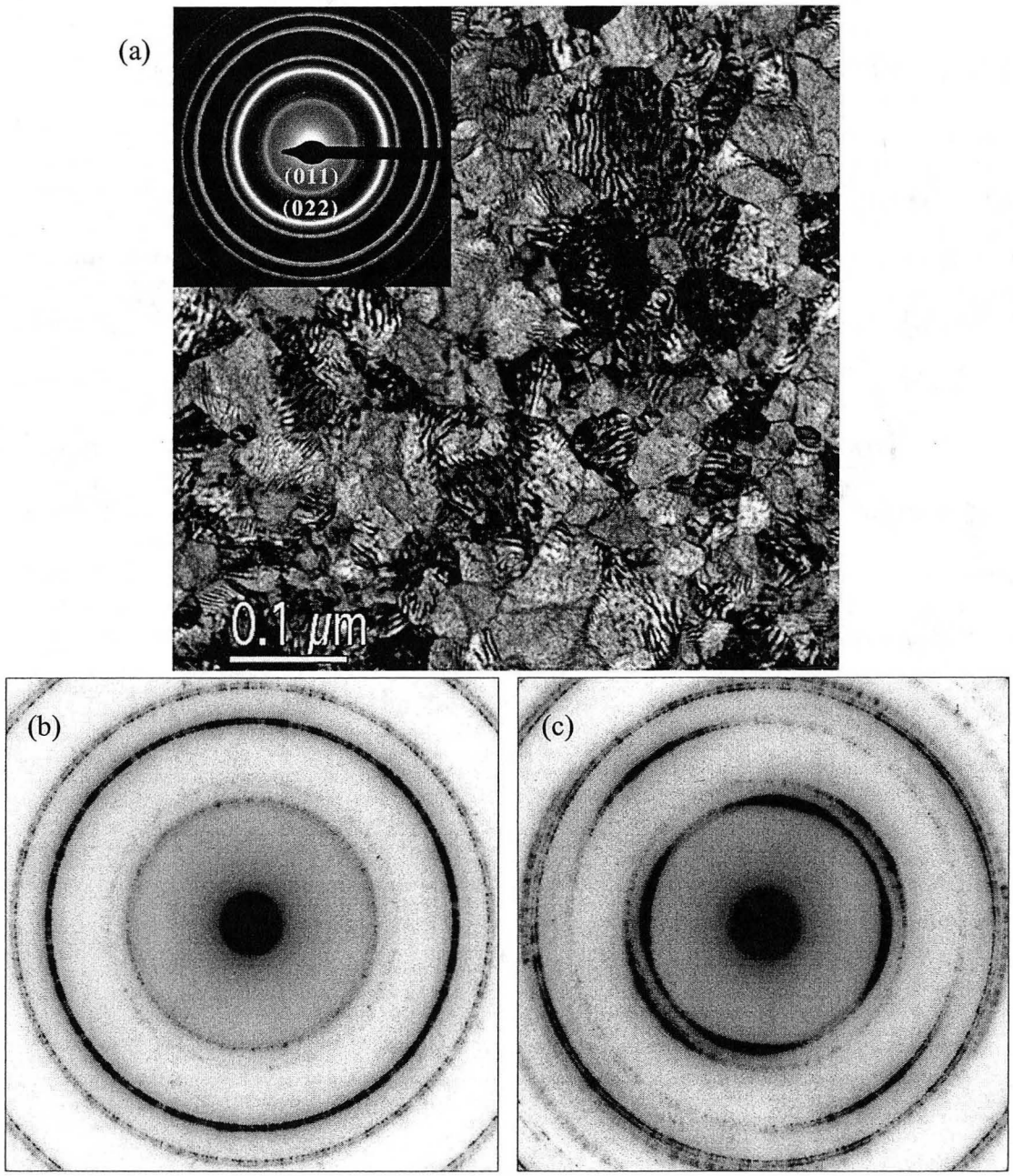

Figure 3–2. (a) Plan-view TEM micrograph and (b) SAD pattern of a 10×(3 Å Co / 10 Å Pt) multilayer grown at T_G = 250°C, (c) SAD with 30° sample tilt showing arcing of the rings.

At room temperature, Pt is a *fcc* metal with lattice parameter a = 3.92 Å. The structure factor, F_{hkl}, which governs the scattering from the unit cell, is given by [Cullity - 1978], [Williams - 1996]:

$$F_{hkl} = \sum_n f_n \exp\{2\pi i(hx_n + ky_n + lz_n)\} \qquad \text{Eq. 3–1}$$

This implies that the indices of the allowed electron diffraction reflections, *(hkl)*, for the *fcc* lattice must be all even or all odd. For mixed, even and odd *h, k, l* values, $F_{hkl} = 0$. For a thin, polycrystalline film, with randomly oriented grains, the reciprocal lattice of the *fcc* unit cell is rotated about all possible axes and the reciprocal lattice is represented by a set of nested concentric spheres of radii corresponding to the respective *(hkl)* reflection. The SAD diffraction pattern of such polycrystalline film, which is a result of the intersection of the reciprocal lattice with an almost flat electron Ewald Sphere, consists of concentric rings. Figure 3–3 shows a simulated diffraction pattern for a *fcc* Pt polycrystalline thin film. As shown for the randomly oriented film, the observed rings correspond to all reflections allowed by the structure factor (i.e.: (111), (200), (220), (311), (220), (400), etc). However, when the film is textured and all grains have one common direction, the spotty reciprocal lattice of the unit cell is now rotated only around the texture axis **T**<*uvw*>, perpendicular to the texture plane. The reciprocal lattice of the textured film is thus reduced and is represented by a set of concentric circles meeting the condition:

$$h \cdot u + k \cdot v + l \cdot w = 0, \pm 1, \ldots, \pm N, \qquad \text{Eq. 3–2}$$

where the integers correspond to consecutive Laue zones.

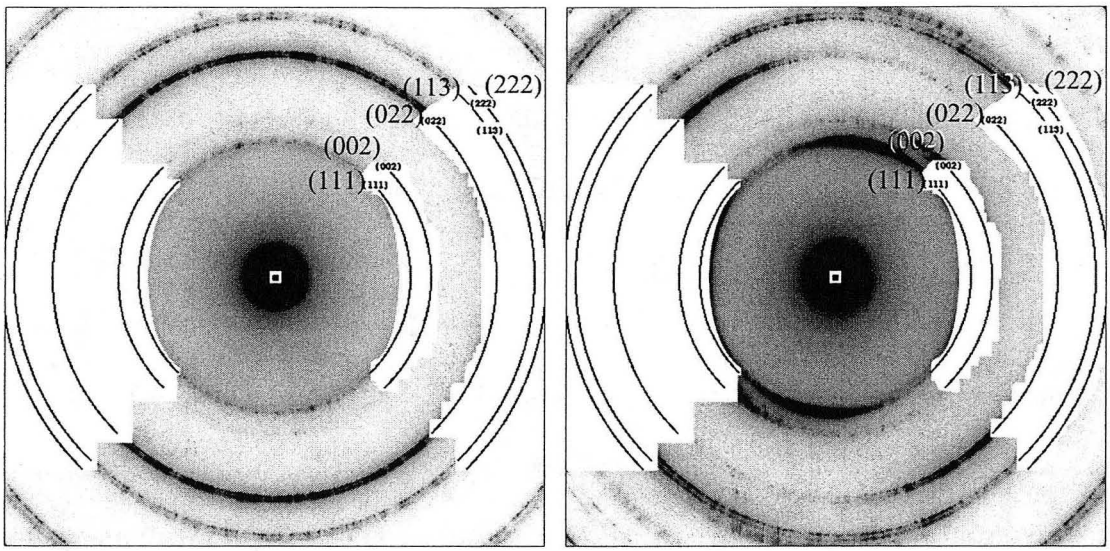

Figure 3–3. Simulated diffraction pattern for polycrystalline *fcc* Pt film overlayed on the recorded SADs from Figure 3–2. (a) 0° sample tilt (b) 30° sample tilt.

The intersection of this reduced and spatially non-symmetric reciprocal lattice with the Ewald Sphere will depend on the relative orientation of the texture axis and the electron-beam incidence. In particular, the electron diffraction pattern taken with the incident beam parallel to the **T**<*uvw*> consists of rings allowed by the structure factor, which, in addition, must satisfy Eq. 3–2 for the zero order Laue zone, that is:

$$h \cdot u + k \cdot v + l \cdot w = 0 \qquad \text{Eq. 3–3}$$

Hence, the intensity ratios of the rings for the textured film are different from those of a film with randomly oriented grains. For example, Eq. 3–3 implies that for the <111> textured film, both (111) and (002) rings are missing and the (022) ring is the first ring present.

Returning to the experimental SAD pattern, it is seen that the intensities of both the (111) and the (002) rings in Figure 3–2(b) are weak, but not zero, and

the (022) reflection is the strongest. This implies a strong <111> texture with only some grains oriented randomly and contributing to the (111) and (002) rings. By utilizing hollow-cone irradiation and DF imaging about the (111) ring, all grains lacking the <111> texture were imaged for samples grown at different temperatures. These results are presented in the following section. Moreover, the SAD pattern recorded when the sample was tilted by 30°, Figure 3–2(c), shows concentric circular arcs. The presence of arcs rather than complete circles is again indicative that the ML's were textured. The presence of strong (111) reflections in Figure 3–2(c), which were very weak in Figure 3–2(b), is due to intersection of the Ewald sphere with the first-order Laue zone. According to Eq. 3–2 in the case of <111> texture, the (111) reflections are allowed for the first Laue zone.

Careful examination of the SAD pattern revealed that all of the rings associated with the *fcc* structure were split, and $\Delta\mathbf{g}$ increased with the diffraction vector $\mathbf{g}$. Figure 3–4 is an enlarged section of the SAD pattern showing two closely spaced (220) rings. For each doublet, the inner ring corresponding to a larger real space parameter is always more intense and the outer ring is weaker. This implies two distinctive lattice parameters through the thickness of the Co/Pt multilayer stack. In addition, the intensity of the two sub rings has the same radial distribution, which demonstrates columnar growth extending throughout the thickness of the multilayer with the columnar grain size determined by the Pt seed layer.

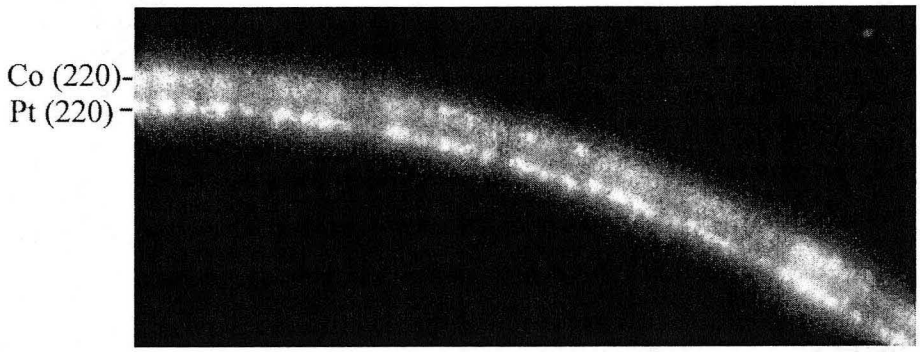

Figure 3–4. Enlarged section of the SAD pattern presented in Figure 3–2, showing closely spaced Pt(220) and Co(220) rings.

When indexing the DP existence of reflections from Pt_{fcc}, Co_{fcc}, Co_{hcp} and $CoPt_3$, were considered. Figure 3–5 shows (a) the SAD pattern for the discussed Co/Pt multilayer and simulated ring diffraction patterns of (b) Pt_{fcc} and $CoPt_3$, (c) Pt_{fcc} and Co_{hcp}, (d) Pt_{fcc} and Co_{fcc}. On all patterns, triangles label Pt rings: (111), (200), (220), (113) and (222). By comparing the simulated SADs to the experimental data shown in Figure 3–5, the only self-consistent way to index the diffraction pattern was to assume *fcc* Pt and *fcc* Co layers. No evidence for ordered compound formation was detected. However, the ratio of the equilibrium Co_{fcc} to Pt_{fcc} spacing in the simulated pattern is not correct. As shown, any two Co and Pt rings on the recorded diffraction pattern, for example Co(220) and Pt(220), are much closer to each other than on the simulated pattern (d). This implies that the Co layers are strained. Figure 3–6 shows simulated diffraction rings as a function of increasing tensile strain of the Co layers. Indeed, the simulated pattern when Co layers are strained in tension by 8.45%, presented in Figure 3–6(g), shows the closest match to the experimental SAD.

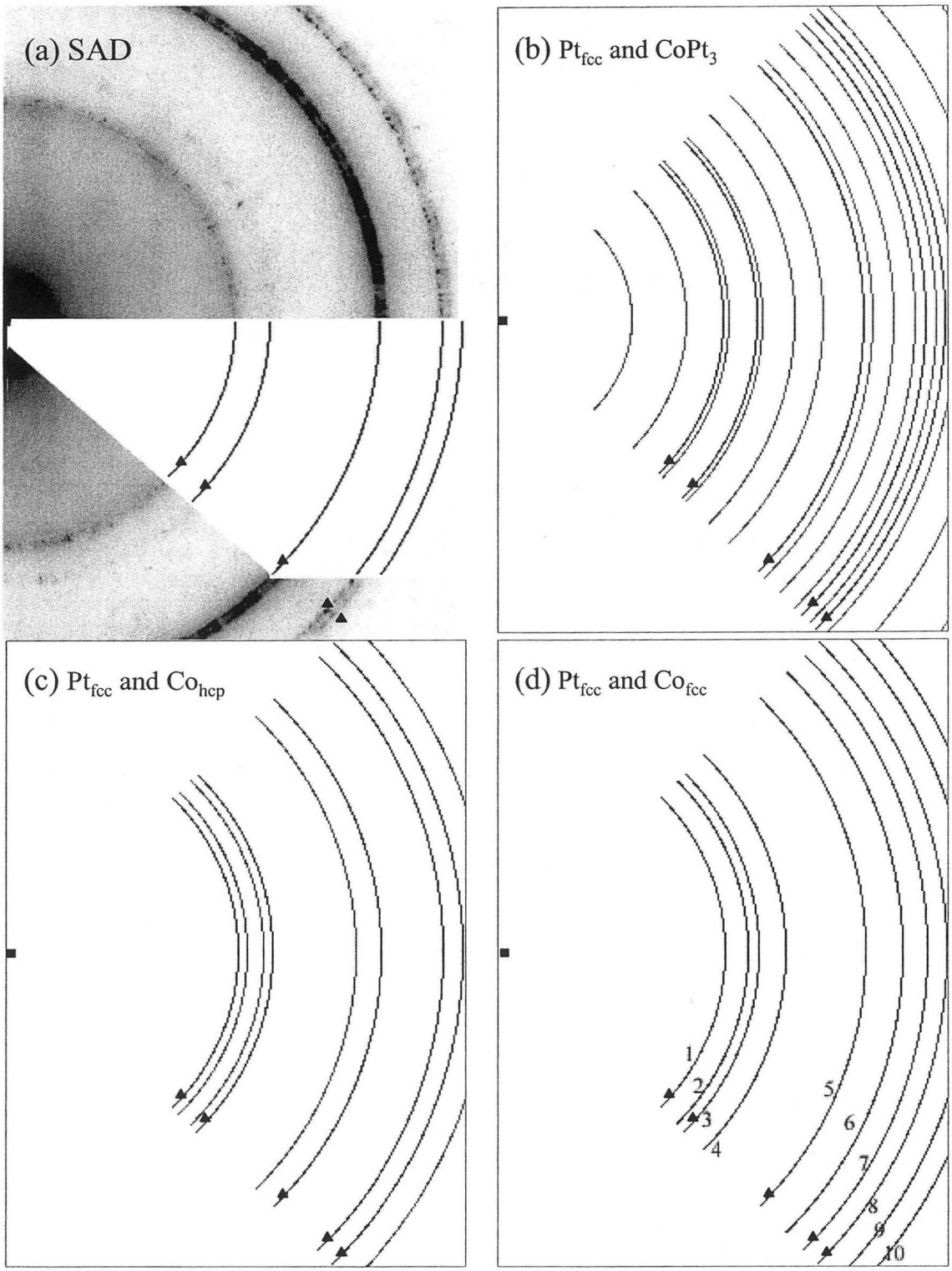

Figure 3–5. (a) SAD pattern for the discussed Co/Pt multilayer and simulated plan-view diffraction patterns for (b) Pt_{fcc} and $CoPt_3$, (c) Pt_{fcc} and Co_{hcp}, and (d) Pt_{fcc} and Co_{fcc}. Triangles label Pt rings (see text)

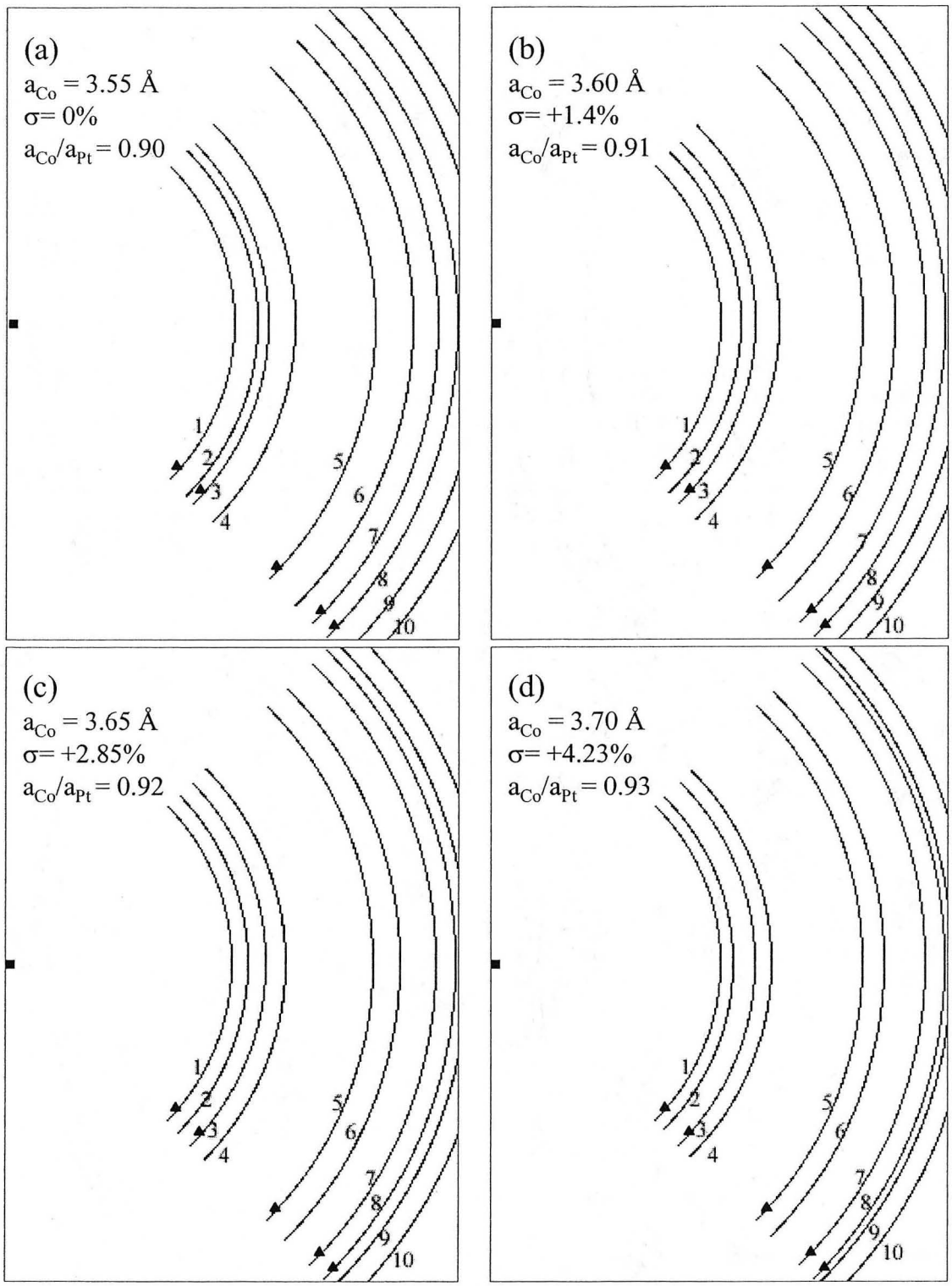

Figure 3–6. Simulated plan-view diffraction patterns of Pt_{fcc} and Co_{fcc} at various strains as indicated on images. Numbers label rings: 1) Pt(111), 2) Co(111), 3) Pt(002), 4) Co(002), 5) Pt(022), 6) Co(022), 7) Pt(113), 8) Pt(222), 9) Co(113), 10) Co(222).

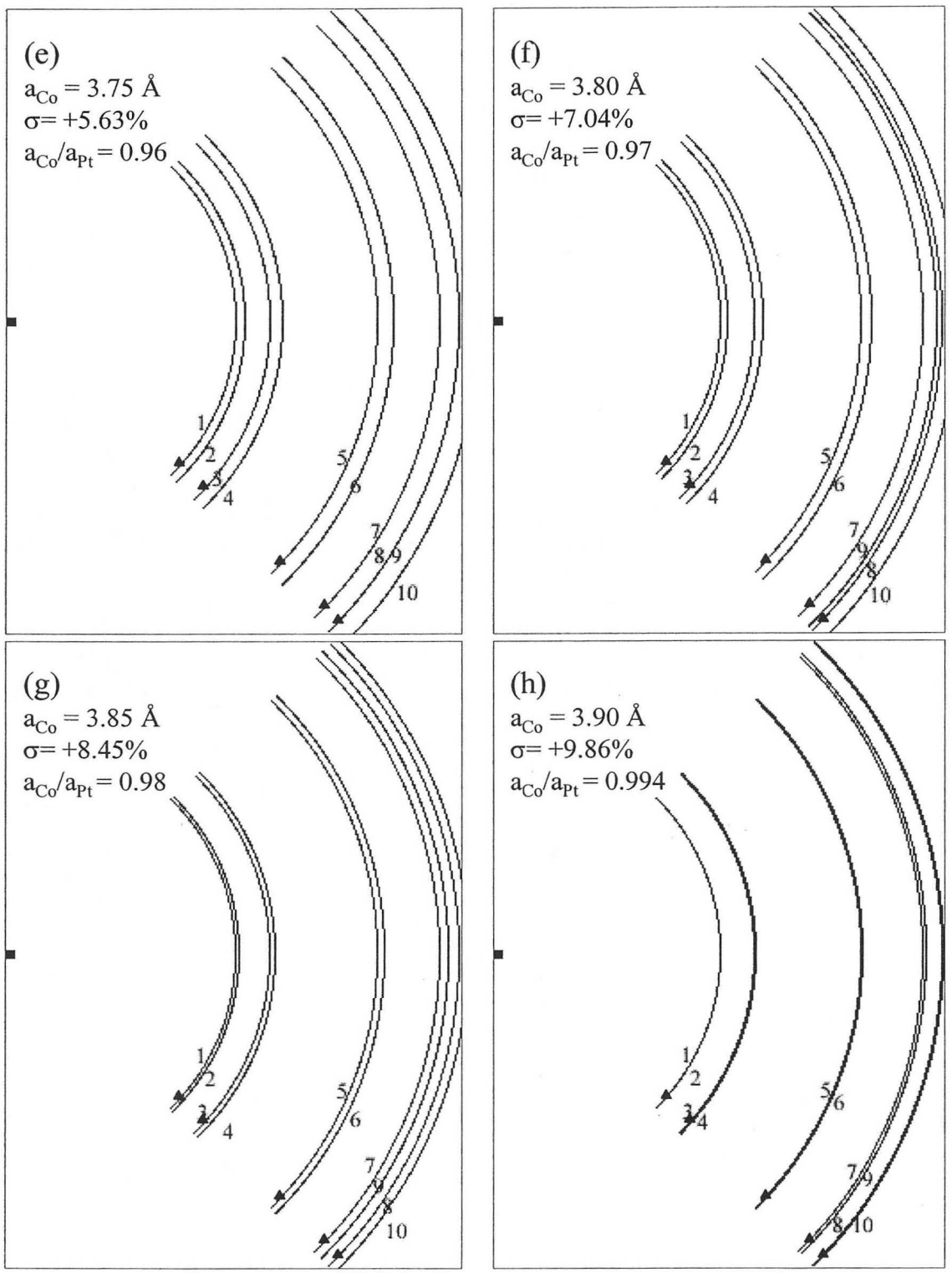

Figure 3–6, cont. Simulated plan-view diffraction patterns of Pt_{fcc} and Co_{fcc} at various strains as indicated on images. Numbers label rings: 1) Pt(111), 2) Co(111), 3) Pt(002), 4) Co(002), 5) Pt(022), 6) Co(022), 7) Pt(113), 8) Pt(222), 9) Co(113), 10) Co(222).

Summarizing the analysis of the SAD pattern, it is concluded that the discussed multilayers grow with <111> texture, which is evident from the weak (111) ring. Starting from the seed Pt layer, the Pt(111) layers are stacked according to the equilibrium *fcc* stacking sequence observed in bulk Pt. The Co layers, which, in bulk are *hcp*, follow the *fcc* stacking sequence of underlaying Pt.[i]

Measuring the diameters of the outer and inner rings in the (220) ring doublet, the ratio of the respective Co and Pt close-pack spacing is approximately equal to $d_{111}(Co)/d_{111}(Pt) = 0.97 - 0.98$. The inner, more intense ring corresponds to *fcc* Pt with a lattice parameter in the expected 3.9 range. The outer, weaker ring is associated with strained Co layers. Assuming a standard Pt lattice parameter $a°(Pt) = 3.9233$ Å, which corresponds to $d_{111}(Pt) = 2.265$ Å, the measured close-packed spacing of the Co layers is $d_{111}(Co) = 2.215$ Å. In bulk, the equilibrium close-packed lattice spacing for *hcp* Co is $a°(Co_{hcp}) = 2.51$ Å and for *fcc* Co with $a°(Co_{fcc}) = 3.544$ Å which gives $d°_{111}(Co) = 2.046$ Å. Hence, Co layers exhibit a 12% compressive strain with respect to *hcp* structure or 8% tensile strain with respect to *fcc* structure.

Figure 3–7 shows cross-sectional images of the Co/Pt multilayer. As concluded from the plan-view TEM analysis, the grain growth is seen to be columnar with grains propagating through the film thickness, Figure 3–7 (a).

---

[i] Note that in the multilayers discussed here, each Co layer is only 3 Å thick, which is less than the thickness of three (111) planes stacked on top of each other.

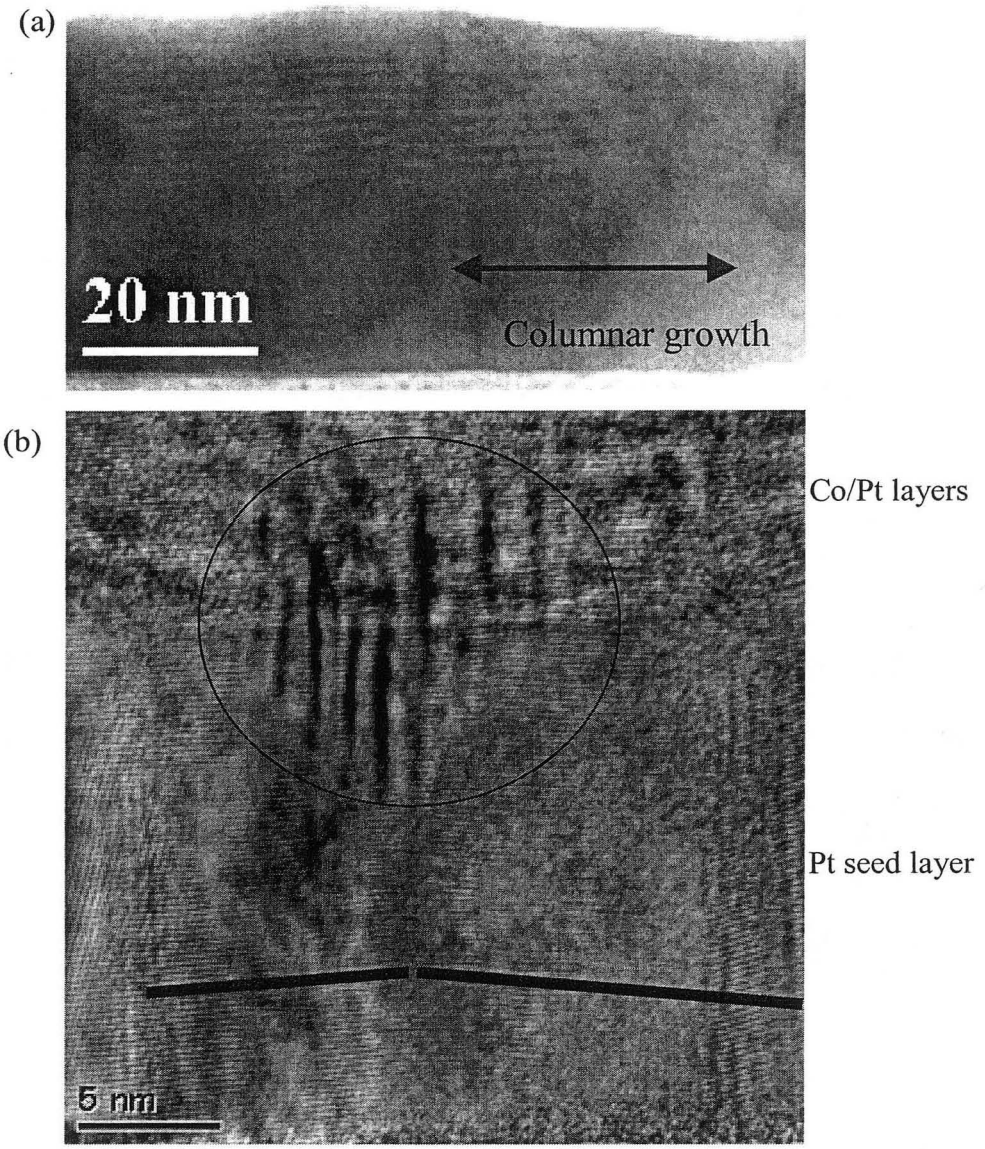

Figure 3–7. Cross-sectional micrographs of a 10×(3 Å Co / 10 Å Pt) multilayer grown at $T_G = 250°C$.

(c)

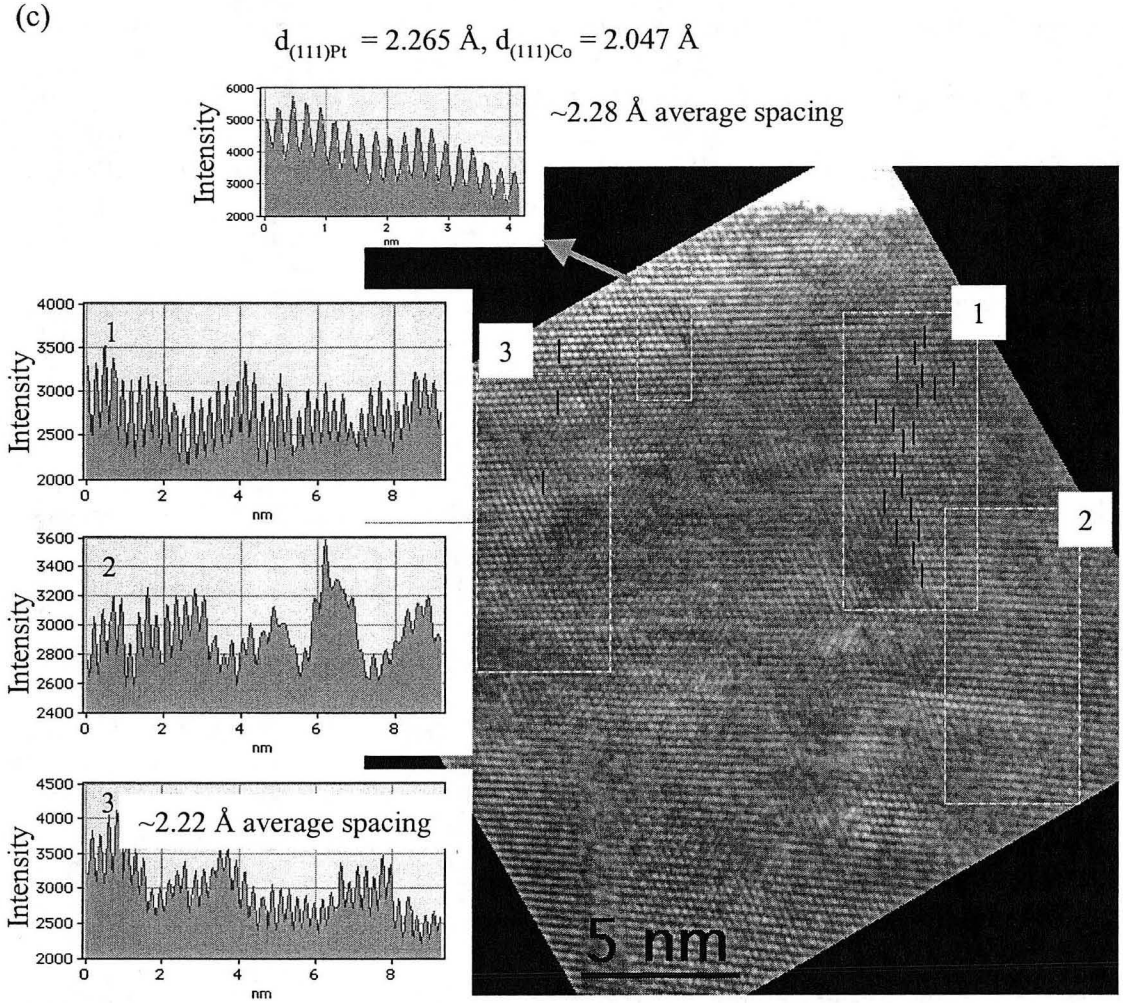

Figure 3–7 cont. (c) Cross-sectional micrograph of a 10×(3 Å Co and 10 Å Pt) multilayer grown at T_G = 250°C.

As shown in Figure 3–7(a), the Pt seed layer determines the size and the orientation of the grains. It should also be pointed out that some of the columnar grains become wider as the thickness increases. As can be seen in the HRTEM image, Figure 3–7 (b), these columnar grains are not perfectly orthogonal to the substrate, and sometimes are misoriented with respect to each other by small angles, less than 5 degrees. This fine misalignment can be seen nicely from the

presence of the rotational Moiré fringes, perpendicular to the misalignment axis. The lattice fringes of 2.28 Å are visible all the way across the multilayer thickness, Figure 3–7 (c). The multilayers have a *fcc* stacking, seen as ABCABC... stacking of (111) planes on HRTEM images. The interface quality between Co and Pt layers is very good, as HRTEM imaging was not sufficient to distinguish between Co and Pt layers. The (111) plane stacking implies a small volume anisotropy of Co. Hence, the perpendicular easy axis of magnetization is attributed to the interface anisotropy and, in particular, is due to strain contributions [Zhang - 1993b]. The very good quality of the interface is believed to contribute to the large perpendicular anisotropy found in these samples. Recently, Jonggeol Kim et al. [Kim - 2001] reported the influence of the substrate roughness on spin reorientation transition (SRT) in ultrathin Co films. A drastically different behavior in SRT of ultrathin Co films grown on smooth versus rough Pd(111) single crystal substrates was reported. On an atomically flat substrate, a smooth transition from perpendicular to in-plane magnetization occurs in a thickness interval of over 1.5 mono-layer, beginning at ~4.5 mono-layer. In contrast, a rough substrate causes the transition to begin much earlier at 3 mono-layer and complete abruptly in less than the 1 mono-layer range. It was reported that on a rough substrate, non-uniform coverage of Co leads to locally thicker regions triggering earlier SRT. In the case of multilayers, the very high coercivity, which scales with the anisotropy constant, is attributed to very smooth interfaces. With increasing temperature, interface quality is improved. These results correlate well with findings presented in this dissertation, and are addressed below.

3.3.1. Analysis of the multilayers as a function of growth temperature

In this section, the structure of the multilayers grown at different temperatures (set A) is discussed. The microstructural evolution of ML's as a function of T_G is presented in Figure 3–8, which shows plan-view BF images, SAD patterns and DF-hollow cone images obtained using (111) rings, (111)DF, of ML's grown at T_G = 190°C, T_G = 250°C and T_G = 390°C. As depicted in the BF images, Figure 3–8(a), (e) and (i), all of the investigated samples were polycrystalline. The average grain size was found to increase with increasing T_G. For samples grown at T_G = 190°C and T_G = 250°C, characteristic Moiré fringe contrast is visible within some of the grains. However, for samples grown at T_G = 390°C, Moiré contrast is not readily found. Magnified BF image of sample grown at T_G = 250°C, along with the line scans across some of the Moiré fringes, is shown in Figure 3–9. As shown on the line scans, the measured Moiré fringe spacing is approximately 6 nm, indicating an interference of two sets of **g**-vectors with nearly common periodicities. This is discussed below, based on the analysis of the DP patterns.

As discussed in the previous section, the SAD patterns, Figure 3–8(d), (h) and (l) showed typical ring spacing associated with the polycrystalline *fcc* Pt structure. For all samples, a strong out-of-plane <111> texture was measured, as seen from very weak (111) and (002) rings and an intense (022) ring. Only some grains oriented randomly contributed to (111) and (002) rings. The SAD patterns from larger areas showed a uniform intensity distribution around all rings, indicating random in-plane orientation and only out-of-plane <111> texture.

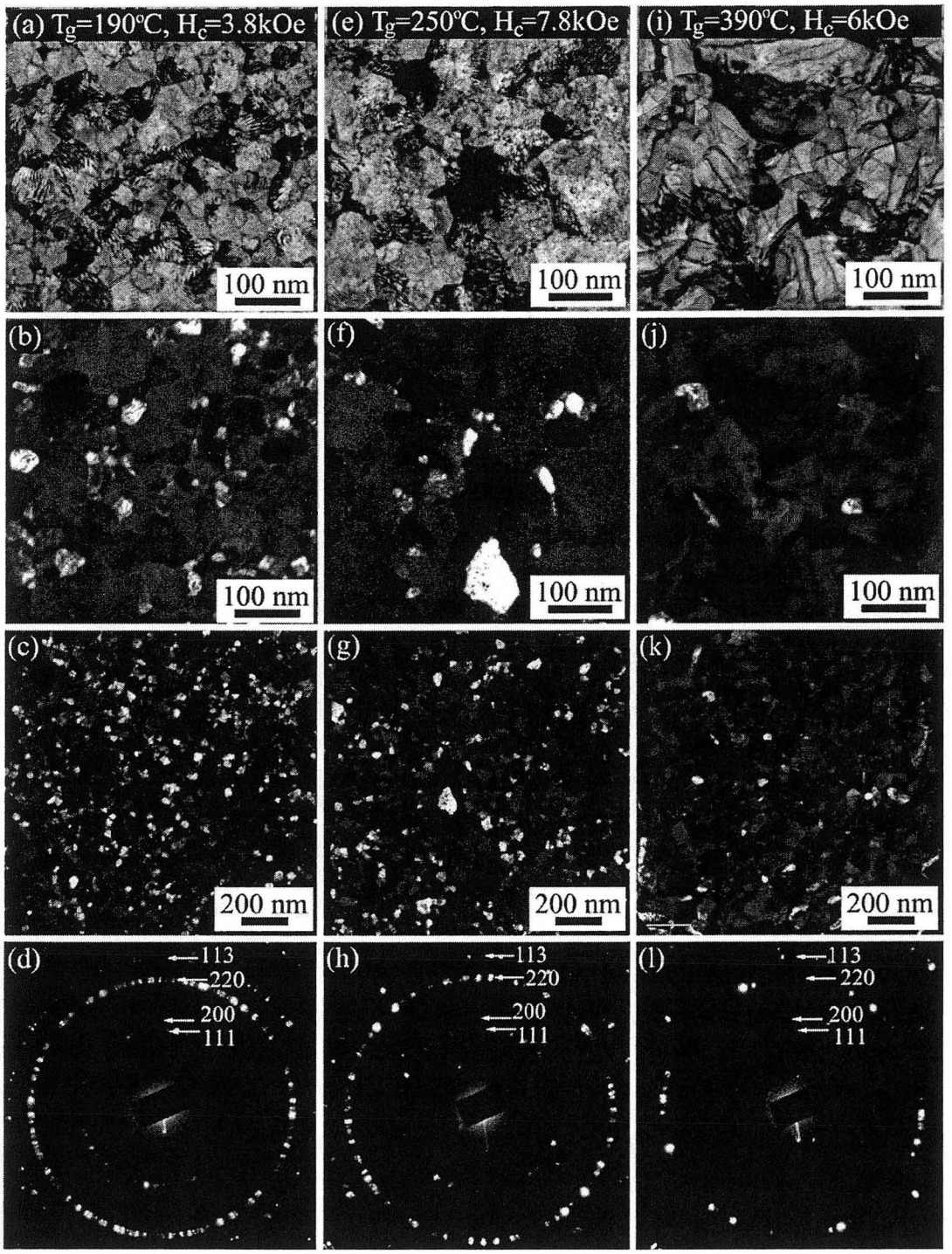

Figure 3–8. Plan-view BF TEM images, SAD patterns and (111)DF images of the Co/Pt ML's grown at T_G = 190°C, T_G = 250°C and T_G = 390°C, displayed in rows. All SAD's were collected with a 5 μm aperture.

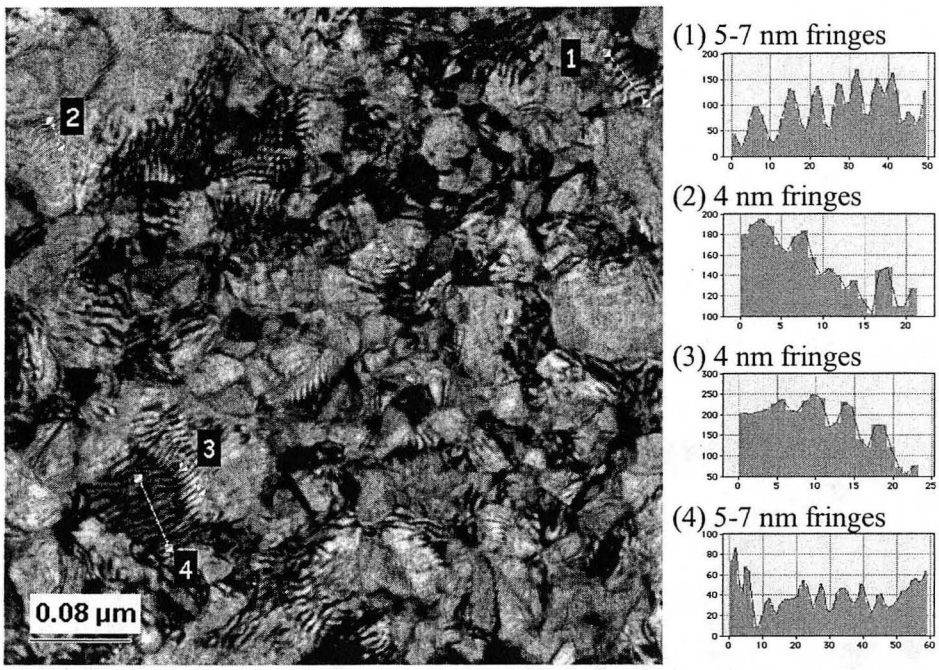

Figure 3–9. BF image of samples grown at T_G = 250°C, and line profiles across some of the Moiré fringe contrast.

The (111)DF images, Figure 3–8(b), (f) and (d), show the same areas as the respective BF images and display only the grains without the <111> texture. Figure 3–8(c), (g) and (k) are lower magnification images showing the distribution of such grains, respectively. As presented, samples grown at the low temperature of 190°C, Figure 3–8(b) and (c), had a large number of grains lacking the <111> texture. The distribution of such grains was very uniform. With increasing T_G, the number of such misoriented grains decreased. For the T_G = 250°C sample, Figure 3–8(f) and (g), the majority of misoriented grains were smaller than the average grain size, although a few, large misoriented grains were also found. For samples grown at 390°C, a good <111> texture was observed, with only very few grains lacking the <111> texture, as shown in Figure 3–8(j) and (k). Moreover, such misoriented grains were much smaller than the <111> textured grains.

Hence, as clearly shown by the set of (111)DF images displayed in Figure 3–8, the <111> texture was found to improve with an increase in sample growth temperature [Shiomi - 1993a].

Figure 3–10(a), (b), (c) and (d) show enlarged sections of SAD patterns for samples grown at 190°C, 250°C, 300°C, and 390°C, respectively.

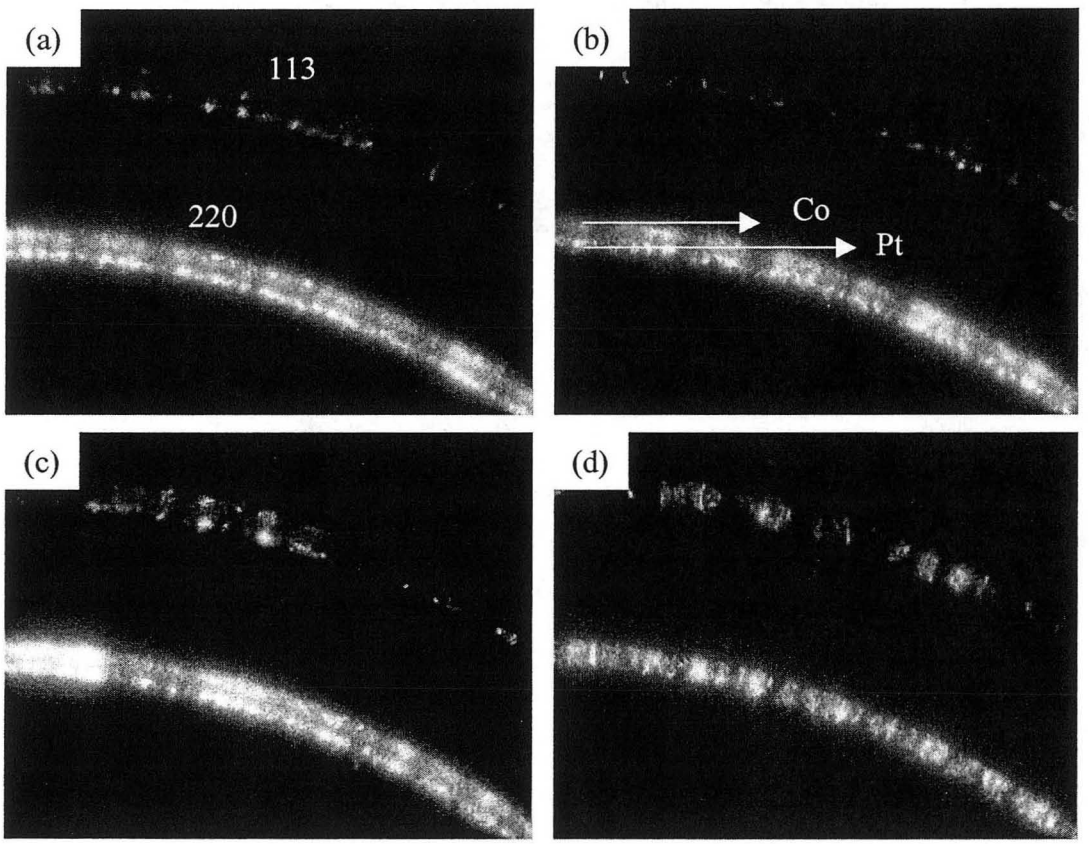

Figure 3–10. Enlarged SAD patterns from (a) T_G = 190°C, (b) T_G = 250°C, (c) T_G = 300°C, and (d) T_G = 390°C samples.

For samples grown at T_G up to 300°C, all diffraction rings were split, indicating two distinctive lattice parameters for the Co and Pt layers. The relative ratio of these rings was 0.97, as compared to $d°_{111}(Co)/d°_{111}(Pt)$ = (2.047 Å/2.265

Å) = 0.904 for equilibrium parameters. Such a high value of 0.97 indicates highly strained Co layers. For samples grown at T_G = 390°C above a critical transition temperature, T_{crit}, the ring splitting attributed to the two separate Pt and Co parameters was not detectable, as shown by one broad ring on Figure 3–10(d), indicating a continuous gradient in lattice parameter between that of strained Co (measured for 190°C and 250°C) and that of Pt. Some of the grains on the BF images of samples grown at T_G = 190°C and 250°C showed a fine Moiré fringe contrast, which was a result of electron interaction with Co and Pt layers. As discussed, the DPs of these samples had two very closely spaced rings from *fcc* Co and *fcc* Pt layers.

In general, Moiré patterns are formed by interference of two sets of lines of close periodicities. Two types of patterns exist: the rotational and the translational (or misfit). Usually, the spacing and the orientation of the fringes is analyzed with respect to the diffraction vectors from the two lattices. In the case of translational Moiré, the two vectors $\mathbf{g}_1$ and $\mathbf{g}_2$, which are reciprocals of respective lattice spacings d_1 and d_2, produce a new translational Moiré vector $\mathbf{g}_{tm}$ given by:

$$\mathbf{g}_{tm} = \mathbf{g}_2 - \mathbf{g}_1 \qquad \text{Eq. 3–4}$$

The vector $\mathbf{g}_{tm}$ will produce a set of fringes with spacing d_{tm} given by:

$$d_{tm} = \frac{1}{\mathbf{g}_{tm}} = \frac{1}{\mathbf{g}_2 - \mathbf{g}_1} = \frac{d_1 \cdot d_2}{d_1 - d_2} \qquad \text{Eq. 3–5}$$

In the more general case where two **g**-vectors of interest can also rotated through a small angle β with respect to each other, the general Moiré spacing d_{gm} is given by:

$$d_{gm} = \frac{d_1 \cdot d_2}{\sqrt{(d_1 - d_2)^2 + d_1 \cdot d_2 \cdot \beta^2}} \qquad \text{Eq. 3–6}$$

The combined results of the analysis of the SAD pattern and the analysis of the Moiré fringe spacing from BF images, presented in Figure 3–9, show good agreement. All films discussed here had a <111> texture with the observed Moiré fringe due to interactions of (110) planes. Table 3–3 shows calculations of both translational and rotational Moiré fringes based on Eq. 3–5 and Eq. 3–6, respectively. The measured Moiré fringe spacing was approximately 6 nm. Assuming a Co to Pt ratio of 0.97, the value measured from the DP patterns shown is Figure 3–10, the calculated (110) translational Morié spacing is 10 nm (see Table 3–3). Assuming a lower value of Co to Pt lattice parameter reduces the Moiré spacing, bringing it closer to the value measured on the images. However, examining the series of simulated diffraction patterns presented in Figure 3–6 and, in particular, the relative positions of Pt(113), Co(113), Pt(222) and Co(222) rings, it can be concluded that the relative ratio of Co/Pt is at least 0.965. For Co/Pt ratios below 0.96, the order of the rings is Pt(113), Pt(222) ,Co(113) and Co(222), as shown in Figure 3–6(a)-(d). When the Co/Pt lattice parameter ratio is above 0.96, the order of these rings switches to Pt(113), Co(113), Pt(222) ,and Co(222), as shown in Figure 3–6(f) and (g). Examining the SAD patterns presented in Figure 3–2 and Figure 3–3, it is concluded that the latter case is relevant. Note that on the 30° tilted SAD, the texture-"forbidden" (222) ring doublet comes after the (113) Pt-Co ring doublet.

The discrepancy between the calculated and the measured Morié spacing can be explained if a small rotation between the layers is assumed. Table 3–3

shows that with increasing rotation between the layers, the fringe spacing decreases. The good agreement between the calculated and measured Morié fringe spacing occurs when ~1.0° - 2.0° misalignment between the Co and Pt layers is considered. Variation in Moiré spacing between different grains and wavy appearance of the fringes indicates that the rotation and/or strain are not uniform.

Table 3–3. Calculated Moiré spacing for Pt and strained Co layers.

	Equilibrium	Strained	Strained	Strained
Pt (Å)	2.27	2.27	2.27	2.27
Co (Å)	2.04	2.17	2.20	2.22
ratio Co/Pt	0.90	0.96	0.97	0.98
	(110) Moiré	(110) Moiré	(110) Moiré	(110) Moiré
angle (deg)	(nm)	(nm)	(nm)	(nm)
0.0	2.88	7.69	10.36	15.70
0.5	2.87	7.52	9.96	14.41
1.0	2.84	7.07	8.99	11.88
1.5	2.80	6.47	7.85	9.59
2.0	2.74	5.84	6.81	7.86
2.5	2.66	5.25	5.93	6.59

For the high T_G = 390°C samples, the Moiré fringe contrast is not observed. In addition, the corresponding DP shows only one set of *fcc* rings, without splitting due to distinct Co and Pt layers. This finding is in agreement with the above discussion.

For all samples, the Co and Pt rings have the same radial distribution in the two sub rings. This can be clearly seen in spotty DPs displayed in Figure 3–8.

This implies that Co and Pt layers share the same orientation within the columnar grain. The growth of the multilayers is columnar, with the columns extending throughout the thickness of the multilayer stack, with the grain size determined by the Pt seed layer. This was also confirmed by cross-sectional HRTEM investigation.

3.3.2. Structure as a function of Co thickness

The structure of Co/Pt multilayers was also investigated as a function of Co layer thickness. In agreement with previously published data [Li - 1993], it was found that the stacking sequence in the Co layers changes with increasing Co thickness. At 0.2 nm – 0.6 nm Co thickness, the (Co/Pt) multilayer structure showed *fcc* stacking with 2.2 Å layer spacing. When the Co thickness increased beyond ~0.6 nm, *hcp* stacking faults (SF) were observed and their density increased with increasing t_{Co}. Above approximately t_{Co} = 15 Å, the Co layer stacking is mainly *hcp*. Co/Pt ML's with Co layer thickness below approximately 6 Å were uniform and relatively defect free. The only indication of the Co vs. Pt layer in the HRTEM image was a slightly higher intensity in the Co layer due to preferential thinning of the Co layer during the ion-milling stage and a lower atomic number. This intensity variation had a periodicity of the analyzed multilayers. With increasing t_{Co}, roughening of the ML's was observed, seen as an increased number of defects in Figure 3–11. As shown, the measured intensity is much higher within the Co layer; however, the precise location of the Co/Pt interface is not known. The (111) stacking sequence in some of the locations is *fcc*,

(same vertical atom position for every third layer, ABCABC), but *hcp* stacking (same vertical atom position for every second layer, ABAB) is also seen.

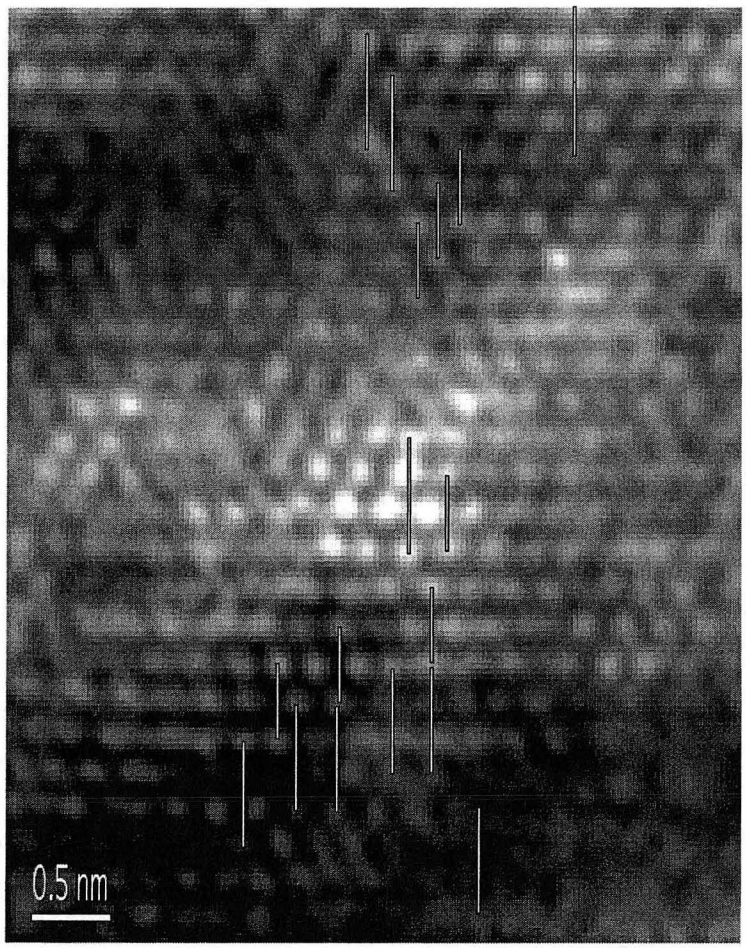

Figure 3–11. HRTEM image of 15 Å, Co layer in the Co/Pt multilayer.

3.4. Magnetic properties

In addition to affecting the grain size and the <111> texture, T_G is also known to influence the magnetic properties. In this section, the magnetic properties of the Co/Pt multilayers as a function of growth temperature are discussed. Subsequently, these results are correlated with the microstructural changes discussed in the previous sections, in particular in section 3.3.1.

3.4.1. Magnetic hysteresis loops

Magnetic hysteresis loops of the Co/Pt multilayers grown at different growth temperatures are shown in Figure 3–12. The square perpendicular hysteresis loops, measured by the polar Kerr rotation [Moog - 1991], [Bader - 1991], [Zak - 1991], indicate that the easy direction of magnetization is out-of-plane. The perpendicular coercivity, H_C values measured from the loops presented in Figure 3–12 are plotted as a function of T_G in Figure 3–13. As shown, and as was reported earlier [Shiomi - 1993a], [Shiomi - 1993b], [Shiomi - 1994], [Weller - 2001], the perpendicular H_C of the Co/Pt ML's was found to increase with increasing T_G. The coercivity increases by almost a factor of two on increasing the T_G from 200°C to 300°C. Moreover, Weller *et al.* [Weller - 2001] (partly this thesis work) first showed that when T_G is increased beyond a critical transition temperature, T_{crit}, a decrease in perpendicular coercivity is observed. As shown, the H_C for samples grown at 390°C is reduced to 5.8 kOe. Further increase in multilayer growth temperature resulted in loss of perpendicular anisotropy. As presented in Figure 3–12, the initial increase in perpendicular coercivity is

accompanied by noticeable changes in the shape of the hysteresis loops. In particular, the nature of the initial magnetization and demagnetization processes in the films is different. For samples grown up to 200°C, square loops were observed with a high hysteresis slope. Moreover, the low T_G films exhibit low initial susceptibility in the as-grown virgin state, consistent with a well-pinned magnetic domain configuration.

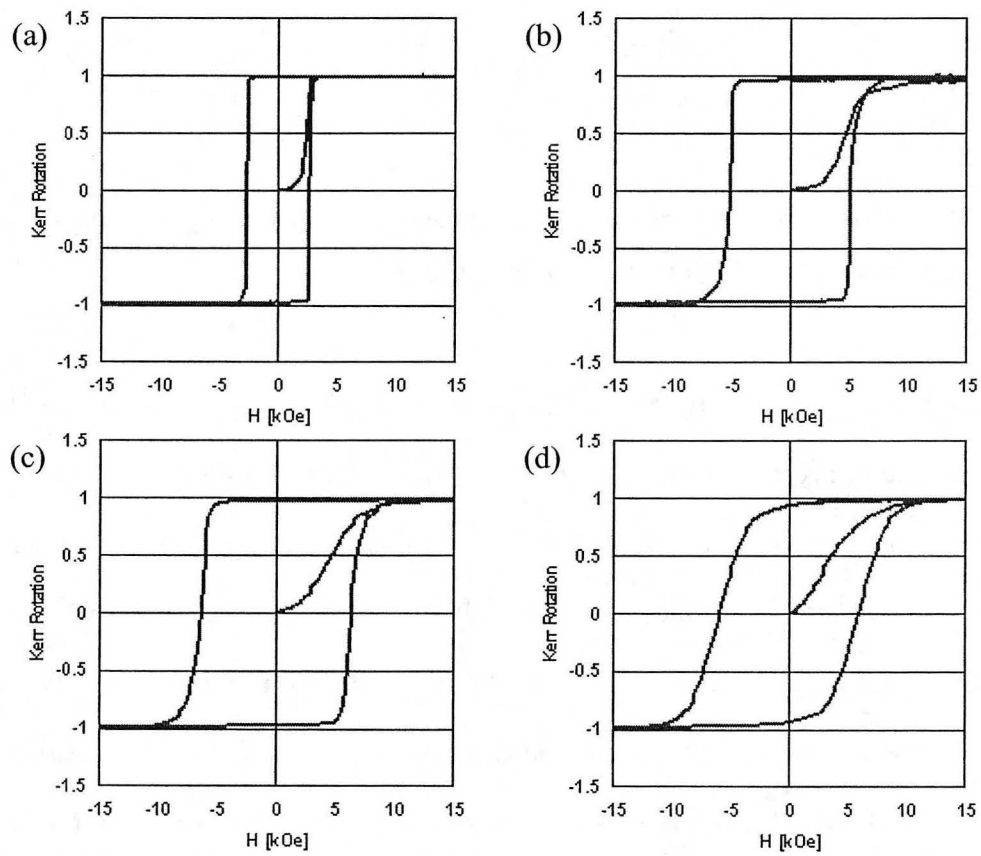

Figure 3–12. Magnetic hysteresis vs. multilayer growth temperature. (a) T_G = 190°C, (b) T_G = 250°C, (c) T_G = 300°C and (d) T_G = 390°C.

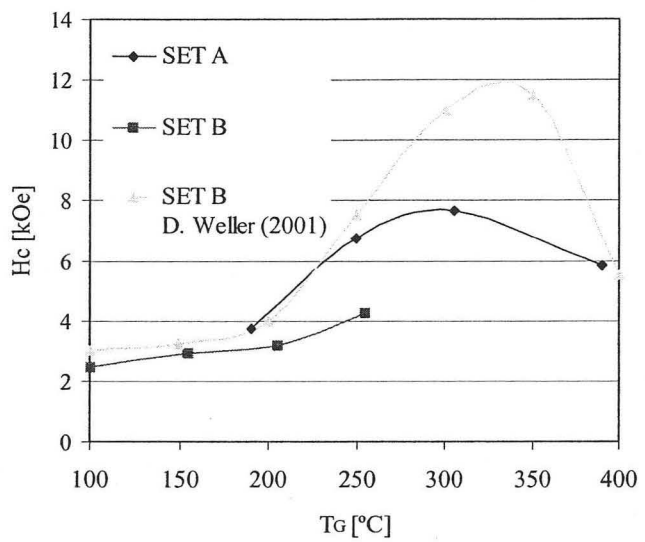

Figure 3–13. Growth-temperature dependence of the room temperature perpendicular coercivity of a series of 10×(3 Å Co / 10 Å Pt) multilayers.

After analyzing the hysteresis loops the following was observed. Starting with the virgin curve of the sample grown at T_G = 190°C, when the applied field, H_A, reaches a critical field for the domain walls to become unpinned, $H_P \sim 0.75 \cdot H_C$, there is a rapid increase in magnetization, M, until all the walls are annihilated and saturation, M_S, is reached. The saturation field, H_S, is approximately twice the pinning field, ($H_S = 2 \cdot H_P$). Following the reversal of the field after saturation, the nucleation field, H_N, required to nucleate a reverse domain is slightly below the pinning field, H_P. Once nucleated, reversal of the entire film occurs very rapidly. As shown in Figure 3–12(a), similar values of H_C and nucleation, H_N, measured for these ML's indicate a magnetic reversal, which is communicated throughout the film via strong exchange-coupling between grains.

The increase in H_C when T_G is increased between 200°C and 300°C, temperatures below T_{crit}, is associated with small shearing of the loops, seen as a small decrease in the hysteresis slope. For the samples shown in Figure 3–12(b) and (c) processes similar to these measured for sample grown at T_G = 190°C are observed in the virgin state. However, there is a broader distribution of the pinning fields. As shown by the virgin curve, the first domain walls become unpinned at $H_P \cong 0.5 \cdot H_C$. Upon further increase in the applied field, the increase in magnetization, M, for these samples is slower, and the saturation is reached only at $H_S \cong 3 \cdot H_P$. Following the reversal of the field after saturation, the H_N required to nucleate a reverse domain is approximately equal to H_C. For the majority of the film, H_N is slightly below H_P and after nucleation, reversal of the majority of the film (~ 80%) occurs rapidly. The increase in magnetization from ~$0.8 \cdot M_S$ to full saturation is slower, indicating presence of a few strong pinning centers, seen as a characteristic magnetization tail. However, as shown in Figure 3–12(b) and (c), similar values of H_C and H_N, indicate magnetic reversal, which is communicated throughout the film via strong exchange-coupling between grains, except for few strongly pinned regions. In addition, for samples grown up to T_{crit}, the remanence, M_R, defined as the magnetization at zero applied field after saturation, is equal or just slightly below M_S. Alternatively stated, $M_R/M_S \cong 1$.

On the other hand, for high T_G films grown above T_{crit}, a decrease in coercivity with an increase in T_G was measured, as shown in Figure 3–13. Moreover, magnetization reversals for these multilayers are drastically different as compared to the low temperature samples. In particular, the virgin curve shows a definitive difference. As shown for the multilayer grown at T_G = 390°C,

Figure 3–12(d), the magnetization was measured to increase almost linearly with the virgin increase in the applied field. The initial susceptibility was higher than for the low T_G films, and was approximately constant in the H_A range from 0 kOe to 5 kOe. After that, a slightly lower and continuously decreasing slope of the magnetization was found. Following the reversal of the field after saturation, first, a remanence lower than saturation was measured with a $M_R/M_S \cong 0.9$. In addition, magnetic reversal takes place over a broad range of H_A, as shown by a significantly sheared hysteresis loop. This broad distribution of switching fields suggests magnetic clusters that reverse rather independently of their neighbors over a range of H_A, implying an exchange-*de*coupled granular system.

3.4.2. Magnetic domain structures

The MTXM was used to investigate the magnetic domain patterns in the as-grown Co/Pt multilayers (virgin state). The investigated samples were T_G = 190°C, T_G = 250°C, T_G = 300°C and T_G = 390°C. These magnetic domain structures are presented in Figure 3–14.

(a) T_G = 190°C, H_C = 3.8 kOe (b) T_G = 250°C, H_C = 7.8 kOe (c) T_G = 390°C, H_C = 6 kOe

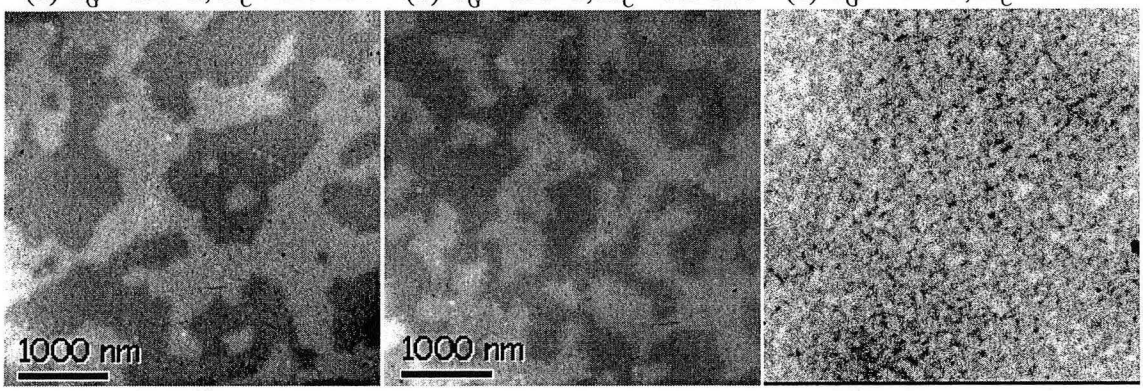

Figure 3–14. MTXM images showing magnetic domains in the as-grown Co/Pt multilayers. Samples grown at different T_G: (a) 190°C, (b) 250°C, (c) 390°C.

All ML's grown below $T_G = T_{crit}$ had irregularly shaped, paisley-like, sub-micrometer magnetic domains, Figure 3–14(a), T_G = 190°C and Figure 3–14(b), T_G = 250°C. As shown, the size of the observed domains decreased with increasing T_G. For all samples grown at $T_G < T_{crit}$, the domain patterns were much larger than the measured grain size (1 μm vs ~ 100 nm), showing that, in general, columnar grains in these Co/Pt multilayers are magnetically coupled. During the magnetic reversal, the magnetic processes are communicated throughout the microstructure, a conclusion consistent with the magnetic hysteresis measurements discussed in section 3.4.1 and shown in Figure 3–12. In addition, the observed decrease in magnetic domain size corresponds to the measured increase in H_C. This correlates with an observed increase in the grain size and an improvement of the <111> texture with an increase in T_G, as discussed in section 3.3.1. However, lack of more ordered magnetic patterns, i.e. regular stripe domains of similar periodicity, implies that these multilayers are not exactly homogeneous. A variation in microstructure and/or in composition causes

irregularity of magnetic properties, which is the cause of nonuniformity of domain shape. Local defects, such as misoriented grains can act as strong pinning centers. For high temperature samples, grown at T_G larger than T_{crit}, a very fine domain structure was observed, with length scales at or below 100 nm. Figure 3–14(c) shows such a domain configuration for the multilayer grown at $T_G = 390°C$. The TEM analysis found the grain size comparable with the domain size. Hence, magnetic domains are confined to individual columnar grains or, at most, small clusters of similarly oriented grains (interaction domains) with length scales below 100 nm. In addition, for samples grown at $T_G = 390°C$, TEM analysis showed one set of CoPt rings indicating diffuse ML interfaces, which correlates with the observed reduction in the perpendicular magnetic anisotropy, measured as lower H_C. As shown in Figure 3–13, the H_C for this multilayer is beyond the previously discussed coercivity peak. Energy filtered TEM revealed Co depleted, Pt rich columnar boundaries in samples grown above T_{crit}. This can explain the magnetic measurements, which indicate grain decoupling, and may help explain the small size of the observed domains.

Figure 3–15 shows a series of MTXM images recorded *in-situ* with the perpendicular field, $H_\perp$, up to ±3.5 kOe. Clearly, no large change in domain size and shape is observed, consistent with the high M_R/M_S ratio measured by MOKE.

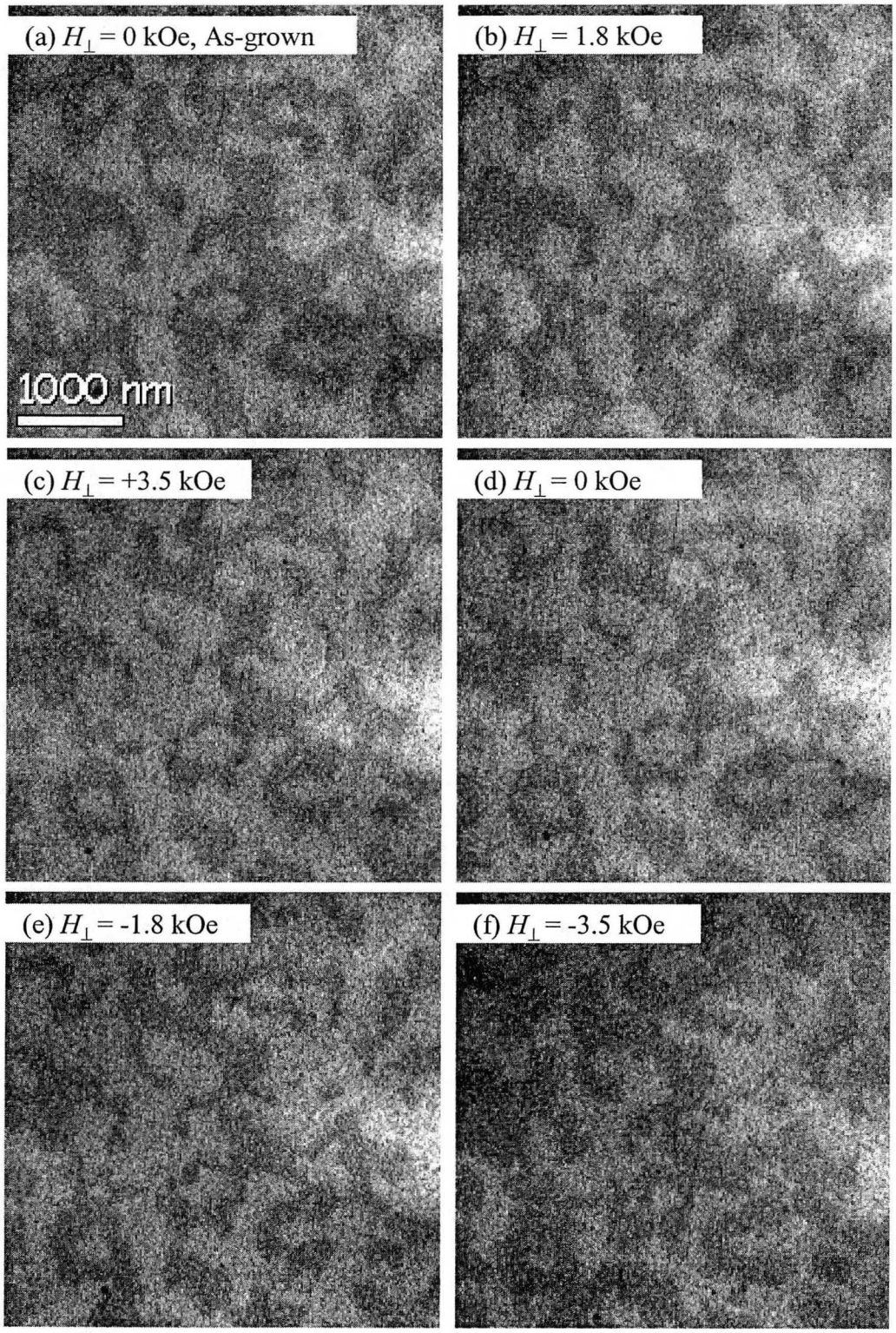

Figure 3–15. Sample T_G = 250°C imaged at (a) As-grown $H_\perp$ = 0 kOe, (b) $H_\perp$ = 1.8 kOe (c) $H_\perp$ = +3.5 kOe (d) $H_\perp$ = 0 kOe, (e) $H_\perp$ = -1.8 kOe and (f) $H_\perp$ = -3.5 kOe.

3.5. Summary

Summarizing and combining the results discussed in sections 3.3 and 3.4, correlation between the microstructure and the magnetic properties was found. With an increase in T_G up to a certain critical temperature, T_{crit}, an increase in grain size and an improved <111> texture were found, both contributing to an increase in H_C. Moreover, a decrease in domain size was observed. For ML's grown at T_G = 390°C > T_{crit}, a decrease in H_C was measured, and small magnetically decoupled domains were observed. The size of these domains was similar to the grain size. This correlates well with Co depletion at the column grain boundaries and with the diffused Co/Pt interfaces, measured as one set of Co-Pt rings. The diffused interfaces are known to reduce the PMA and, hence, reduce H_C. Also with increasing t_{Co}, a decrease in H_C was observed. The coercivity is therefore a function of both the microstructure (grain size and texture) and interface quality, which is strongly influenced by T_G. By appropriate choice of $T_{G,seed}$, $T_{G,ML}$, t_{Co}, and multilayer repetition, structures with desired H_C and domain size can be grown.

Chapter 4.

ION MODIFICATION OF MAGNETIC PROPERTIES

4.1. Motivation

As outlined in the introduction, patterned magnetic media are promising candidates for the future of high-density magnetic recording. Techniques where only the magnetic properties are modified, without affecting the physical topography of the sample, are particularly attractive. In such methods, etching steps, where the magnetic material is physically removed, are not necessary.

Recently, Ferre and Chappert et al. [Ferre - 1999] have discovered that ion irradiation can be used to modify the magnetic properties of Pt/Co/Pt sandwich structures. He^+ irradiation at 30 keV ion energy and $1 \cdot 10^{16}$ ions/cm^2 dose was reported to effectively reduce anisotropy, coercivity and Curie temperature in a Pt/Co/Pt sandwich and multilayer structures. It was also reported that at higher ion fluence the magnetization is reoriented into the film plane. Later, it was shown that the irradiation of Pt/Co/Pt sandwiches and Co/Pt multilayered films by other (heavier) ions (N^+ - [Weller - 2000], Ga^+ - [Aign - 1998], Ar^+, Ga^+ - [Rettner - submitted]) induces similar modification of the magnetic properties. Comparing

the data, it is now known that the fluences necessary to modify the magnetic properties decrease with increasing atomic number of the ions used for irradiation.

Initial work investigating similar phenomena was carried out by Carcia *et al.* [Carcia - 1990a]. Also Bertero and co-workers [Bertero - 1994], [Bertero - 1995], showed that the magnetic properties of the ML'S are strongly dependent on the abruptness of the Co/Pt interfaces. By varying the ambient gas during the sputter deposition of <111> textured Co/Pt ML's, the sharpness of the internal interfaces was controlled. Increasing the interfacial diffuseness caused a substantial decrease in the multilayer's perpendicular magnetization.

Co/Pt multilayers are a good candidate for magnetic media for Terabit/in^2 areal density magnetic recording due to their large, interfacial perpendicular magnetic anisotropy. This, in combination with ion-induced property modification (e.g. spin reorientation transition (SRT) of the easy axis from out-of-plane to in-plane), makes Co/Pt very attractive for patterned media applications.

The precise mechanism of the ion-induced modification of the magnetic properties (reduction in H_C and SRT at higher doses) is currently not well understood, despite its possible technological importance. It is postulated [Ferre - 1999], [Weller - 2000] that irradiation with a suitable dose of energetic ions reduces the interfacial anisotropy, K_S. Based on the discussion from Chapter 2, the effective anisotropy constant for the case of the Co/Pt multilayer system is written as:

$$K_{eff} = K_V + 2 \cdot \frac{K_S}{t_{Co}} \qquad \text{Eq. 4–1}$$

with K_V a total volume anisotropy contribution including the negative demagnetization energy: $-2 \cdot \pi \cdot M_S^2$. The balance of the positive out-of-plane anisotropy energy and the negative demagnetization energy governs the easy axis of magnetization. For Co/Pt multilayers, K_S is the main contribution for out-of-plane magnetization and it must be large enough to overcome the demagnetization energy for the system to support the perpendicular magnetization. When K_S is effectively reduced by ion irradiation, the shape anisotropy dominates, yielding a negative value of K_{eff}, thereby triggering a SRT.

At sufficiently high doses, the easy magnetization axis is rotated from out-of-plane to in-plane [Ferre - 1999], [Weller - 2000]. It has been shown that using resist [Chappert - 1998] or stencil masks [Terris - 1999] to spatially vary the fluence of ions incident on the film, or by utilizing focused ion beam (FIB) writing [Aign - 1998], [Hyndman - 2001], [Warin - 2001], patterns of in-plane and out-of-plane magnetization can be produced. Such direct modification of magnetic properties on a local nanometer scale may be useful for future high-density patterned magnetic data storage.

The basics of ion matter interactions are reviewed in Appendix C on page 207.

4.2. Modification of magnetic properties by ion irradiation

4.2.1. Experimental procedures

As reported earlier, ion irradiation can be used to reduce the perpendicular anisotropy of the Co/Pt multilayers. For all the data presented in this

dissertation, 700 keV N^+ or 30 keV Ga^+ ions were used to modify the magnetic properties and to study the irradiation effects. The 700 keV N^+ ions were obtained from a NEC 3UH Pelletron accelerator. The 30 keV Ga^+ ions were obtained from a commercial FEI, 830XL focused ion-beam (FIB) instrument[i]. When irradiating larger areas with FIB, a quasi-uniform dose was obtained. A beam with a 15 nm full-width-half-maximum (FWHM) was scanned in a regular raster using a 5 nm step size.

For the irradiation study, five identical samples were grown at $T_G = 300°C$ in a single run, as described in Chapter 3 (sample ~EG_102). These samples had nearly identical polar Kerr loops, which indicated coercivities of ~8 kOe. Samples were exposed to increasing doses of 700 keV N^+/cm^2 between $1 \cdot 10^{14}$ N^+/cm^2 and $5 \cdot 10^{15}$ N^+/cm^2. After exposure, polar Kerr hysteresis loops were measured and analyzed to yield coercivities.

4.2.2. Results and discussion

Figure 4–1 shows perpendicular hysteresis loops of 3Co/10Pt ML with $H°_C$ = 8.5 kOe before and after irradiation with an increasingly larger dose of 700 keV N^+ ions [Weller - 2000]. As shown, a strong sensitivity of H_C to ion dose was observed. Doses of 700 keV N^+ as low as $1 \cdot 10^{14}$ N^+/cm^2 were found to reduce H_C substantially without, however, affecting the square loop shape. For example, after a dose of ~$5 \cdot 10^{14}$ N^+/cm^2, H_C of the sample was reduced to half its initial value. A substantial decrease in the perpendicular remanence (i.e. $M_R/M_S < 1$) was observed only for doses above ~10^{15} N^+/cm^2. Such doses cause H_C to drop

[i] Both instruments are located at the IBM Almaden Research Center.

below about 10% of H°_C of the unexposed film. With further increase in the irradiation dose, the transition from out-of-plane to in-plane easy magnetization axis was measured. Depending on the initial anisotropy and coercivity of the sample, doses of ~$5 \cdot 10^{15}$ - $1 \cdot 10^{16}$ N^+/cm^2, were required. Ion irradiation with increasing doses is associated with a gradual decrease in the perpendicular magnetic anisotropy, which causes a decrease in H_C and, finally, a SRT to in-plane.

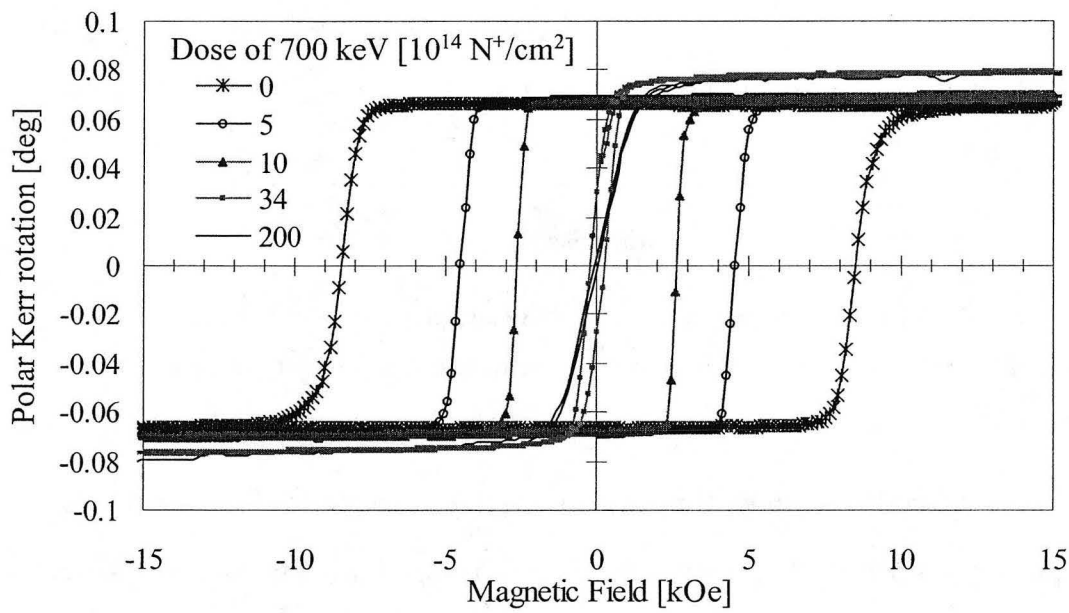

Figure 4–1. Polar Kerr hysteresis loops of a Co/Pt multilayer subjected to N^+ ion irradiation at various doses.

Figure 4–2 plots coercivity and remanence normalized to the zero-dose values as a function of 700 keV N^+ ion dose for two samples with different initial coercivity. The first sample, Sample I, had H°_C = 8.5 kOe and Sample II had H°_C = 3.9 kOe. As shown, coercivity was found to decay exponentially with increasing

ion dose. The perpendicular remanence on the other hand was constant up to ~5 ·10^{15} N^{+}/cm^{2} and then decreased rapidly with increase in ion fluence.

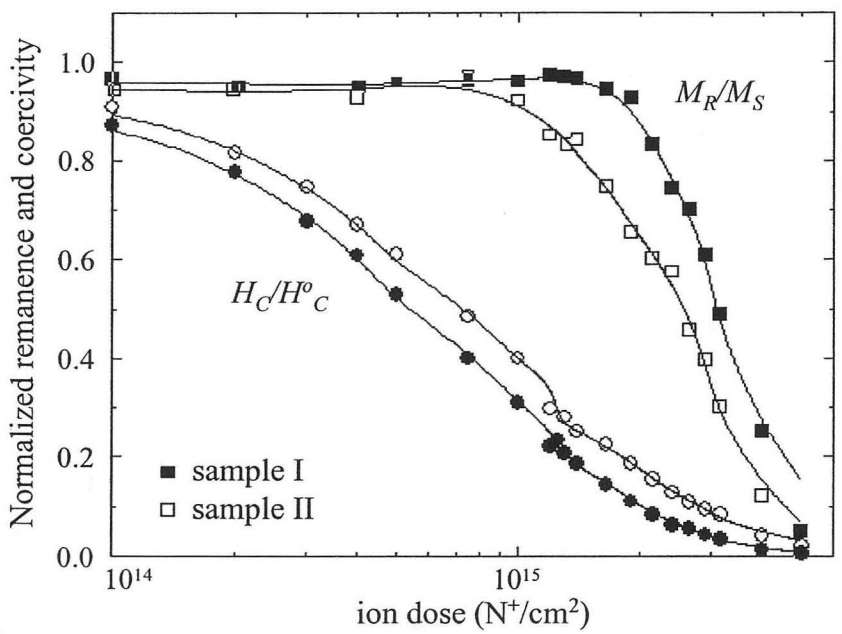

Figure 4–2. Normalized perpendicular coercivity and perpendicular remanence as a function of N^{+} ion dose for two samples with different initial coercivity (see text).

It is interesting to note that the Co interface density in these multilayers is approximately 1.5 ·10^{15} atoms/cm^{2}. Comparing this value with the ion fluences, it is concluded that the doses at which noticeable magnetic changes are measured are about 10 times lower than the Co monolayer density. The full SRT requires 1 ·10^{16} N^{+}/cm^{2}, which is less then 10 monolayers.

Recently, a group from the IBM Almaden Research Center conducted a systematic study characterizing the dependence of coercivity of Co/Pt multilayers on exposure for various ion species (He^{+}, Ar^{+}, Ga^{+}), energies (20 keV – 2 MeV), and doses (10^{11}-10^{17} ions/cm^{2}) in order to better understand the nature of the magnetic

changes [Rettner - submitted]. The data is displayed in Figure 4–3, which shows coercivities, measured by MOKE, for samples that were exposed to beams of 30 keV Ga^+, 20 keV Ar^+, 2 MeV Ar^+, 700 keV N^+, 20 keV He^+, and 2 MeV He^+, respectively.

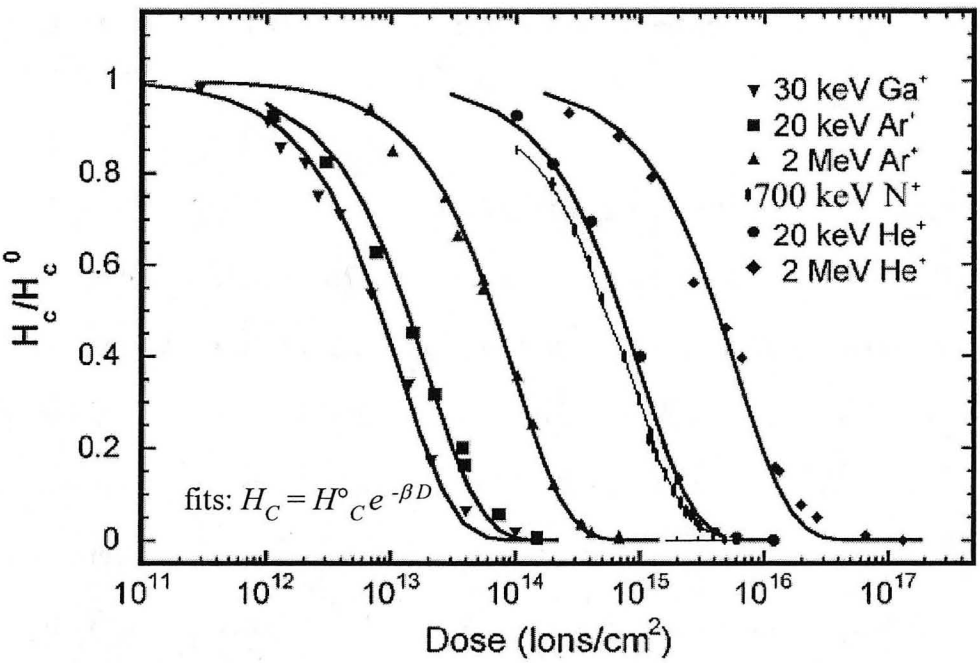

Figure 4–3 Dependence of coercivity on ion-beam exposure for Co/Pt multilayer sample. Coercivities are normalized to zero-dose values. The curves are a fit to exponential decay. Data courtesy of C. Rettner [Rettner - submitted].

Coercivity values are plotted as a function of exposure, relative to the coercivities of the unexposed films, H°_C, which ranged from 11.7 to 13.4 kOe. As shown, essentially any energetic species can be used to reduce the perpendicular coercivity. The sensitivity of H_C to different species scales with the number of displacements created per incident ion. Heavy Ar^+ or Ga^+ ions cause more damage

than lighter He^+ or N^+ ions, hence, the former influence the magnetic properties at much lower doses. However, for all species a similar exponential decay of the form $H_C = H^\circ_C e^{-\beta D}$ was found, where D is the dose in units of ions/cm^2 and β is a fitted constant. In Figure 4–3, the lines are fits to such an exponential decay. The data for 700 keV N^+ and 30 keV Ga^+ is of particular relevance for the rest of this thesis, as these were the sources used for modification and patterning of the Co/Pt multilayers.

4.3. Physical modification, mechanism

Despite the potential technological importance, the physical mechanism of ion-matter interaction, by which the magnetic properties of multilayers can be tailored, is not well understood. The motivation behind this research was to investigate and model the mechanism of ion modifying process. The results presented in this section are not conclusive, due to current resolution limitations of the experimental techniques. However, the approach taken along with the experimental results will be presented here, as they offer an improved insight by eliminating some possible mechanisms.

4.3.1. Results and discussion

The structural mechanism of the spin reorientation transition (SRT) associated with ion irradiation was studied with TEM. The goal was to correlate the ion-induced microstructural changes with the changes in magnetic properties. As was presented in Figure 4–1 and Figure 4–2 for the case of 700 keV N^+ ion irradiation, the SRT from perpendicular to in-plane magnetization is observed at a

dose of approximately $5 \cdot 10^{15}$ N^+/cm^2. Figure 4–4 shows plan-view TEM images of the 10×(3 Å Co / 10 Å Pt) multilayers grown at T_G = 250°C in the as-grown state and after irradiation[i] with $5 \cdot 10^{16}$ N^+/cm^2, a dose 10 times the SRT threshold dose. On average, the examination revealed no detectable changes in microstructure even at such large doses (same grain size, <111> texture, similar Moiré fringes).

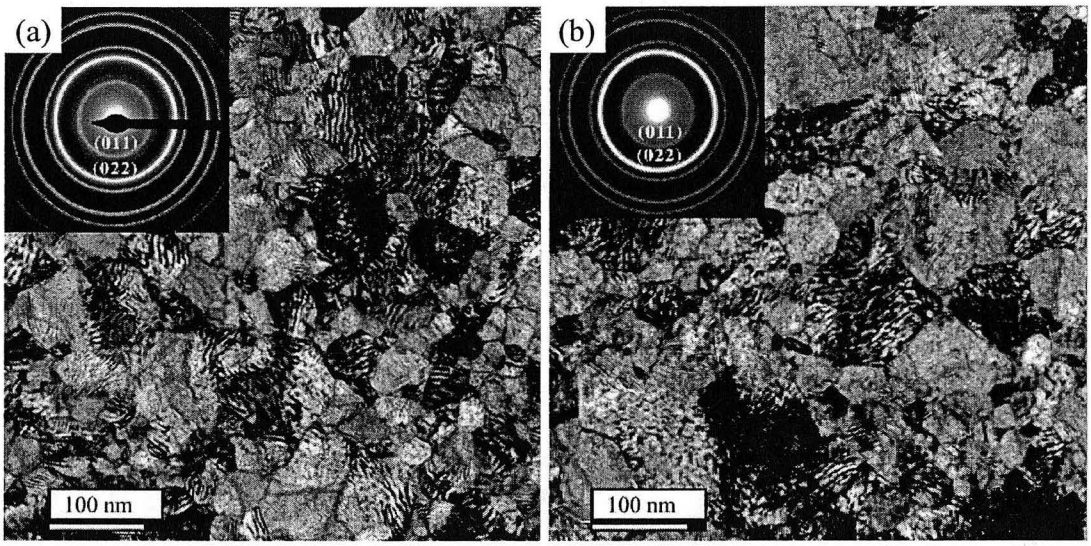

Figure 4–4. Bright field TEM images of Co/Pt multilayer T_G = 250°C (a) as grown (b) irradiated with $5 \cdot 10^{16}$ N^+/cm^2.

Figure 4–5 shows a side-by-side comparison of the SAD patterns of the as-grown and irradiated samples. Indexing the rings and comparing their relative intensities revealed virtually identical DPs. Based on the analysis presented in detail in Section 3.3, a strong <111> texture was confirmed for both patterns. The SAD for the irradiated sample has rings present only in the as-grown SAD. No evidence of rings from ordered $CoPt_3$ compound formation was detected for the

[i] Due to experimental limitations and difficulties it was not possible to image the very same sample location.

irradiated sample. This result is not unexpected considering the very slow $CoPt_3$ ordering kinetics reported by Berg and Cohen in $Co_{0.25}Pt_{0.75}$ single crystals [Berg - 1972], [Berg - 1973a], [Berg - 1973b]. Also, McIntyre *et al.* have systematically investigated interdiffusion in epitaxial Co/Pt ML's [McIntyre - 1997]. Similarly, no evidence was found for ordered compounds.

As presented in Figure 4–5, the SAD patterns before and after irradiation are almost identical. The only difference is, perhaps, in the splitting of the (022) ring. The Pt and Co (002) rings for the ion-irradiated sample appear more diffuse. In addition, for the ion-irradiated sample the Co (002) ring is further from the Pt (002) ring by approximately 0.49% as compared to the as-grown sample.

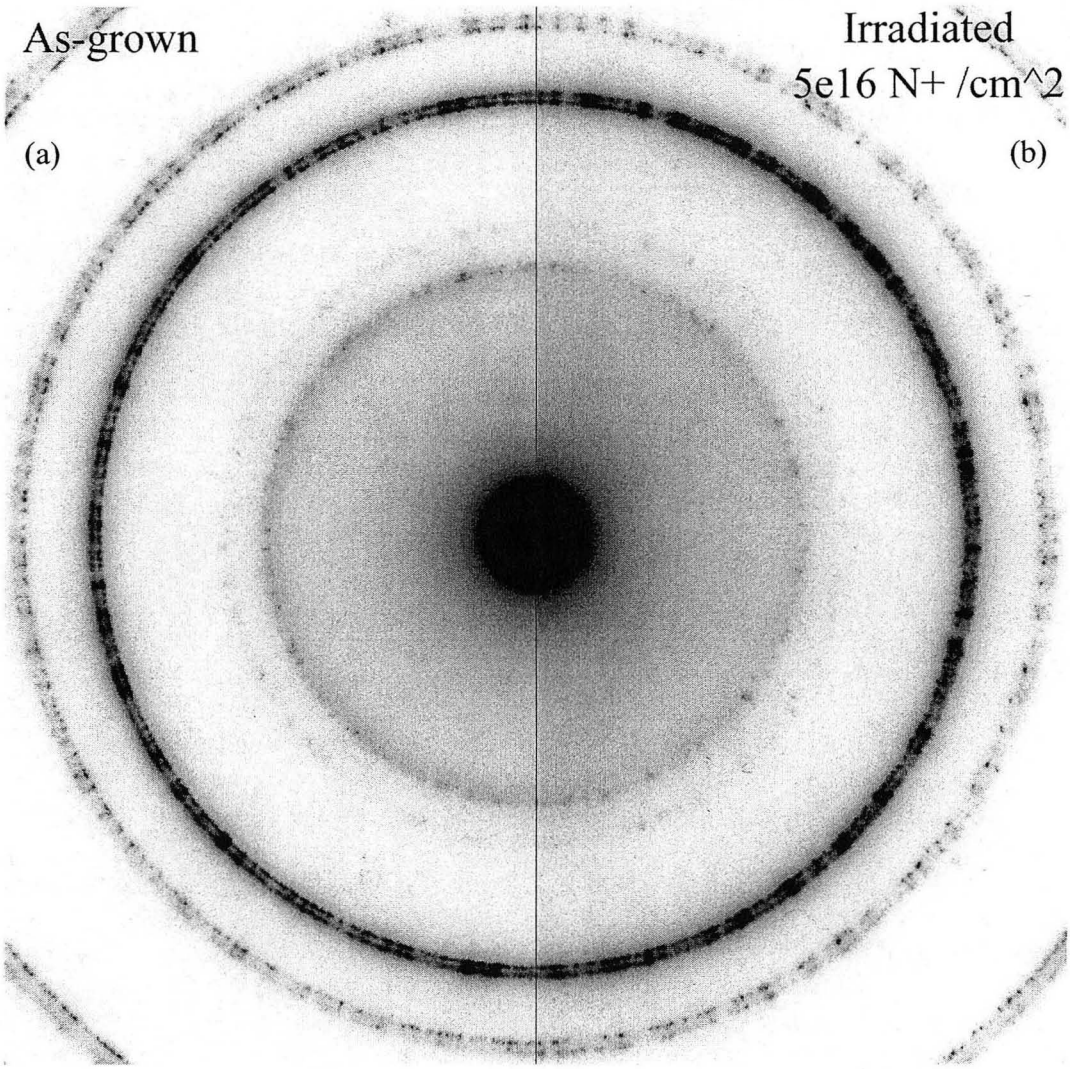

Figure 4–5. SAD patterns of Co/Pt multilayer $T_G = 250°C$ (a) as grown (b) irradiated with $5 \cdot 10^{16}$ N^+/cm^2.

In addition, FIB was also used to irradiate the same sample. Square 2 μm regions were exposed to increasingly larger fluences of 30 keV Ga^+, ranging from $1 \cdot 10^{12}$ to $1 \cdot 10^{17}$ ions/cm^2. For doses that yield full in-plane SRT no noticeable change in microstructure was observed, similar to N^+ ion irradiation data. Figure 4–6 shows BF TEM images of the sample EG_102 irradiated with $2 \cdot 10^{16}$ of 30 keV Ga^+/cm^2 in the vicinity of the irradiated region boundary. This fluence was over 200 times greater than needed to yield in-plane magnetization. As shown, the irradiated region appeared to be brighter in transmission than the non-irradiated region. The reduction of absorption in the irradiated areas indicates local etching due to sputtering. Note, however, that the grain sizes in the ion irradiated and non-irradiated regions were approximately the same. The main difference is lack of the Moiré contrast in the irradiated region.[i] This, however, is not surprising, as probably the entire 13 nm Co/Pt multilayer stack was sputtered away, and the presented image shows mainly the Pt seed layer. However, as was previously stated, the ML grain size is the same as the grain size of the seed layer. Hence, even for this very large ion dose no grain growth was observed.

These results are very different from the data published recently by the Universite Paris-Sud, Orsay group [Hyndman - 2001], [Warin - 2001]. It was reported that under low irradiation fluences both the grain size and the <111> texture of the Co/Pt multilayers increased. After fluences of $1 \cdot 10^{15}$ 30 keV Ga^+/cm^2, more than doubling of grain diameters was reported. The discrepancy

---

[i] The black dot contrast in BF image in Figure 4–6(b) in the ion irradiated region has not been elucidated. However, it could be due to cluster-point defects from ion irradiation.

between the data presented in this dissertation and the data of Hyndman *et al.*, showing significant grain growth, is not clear. However, as shown in Figure 4–6, the diffraction contrast in the irradiated region is substantially reduced. It is possible that this can mistakenly be interpreted as a larger grain size.

Based on the presented results showing no change in microstructure, it is concluded that irradiation effects, which contribute to drastic magnetic property changes, are on a much finer scale.

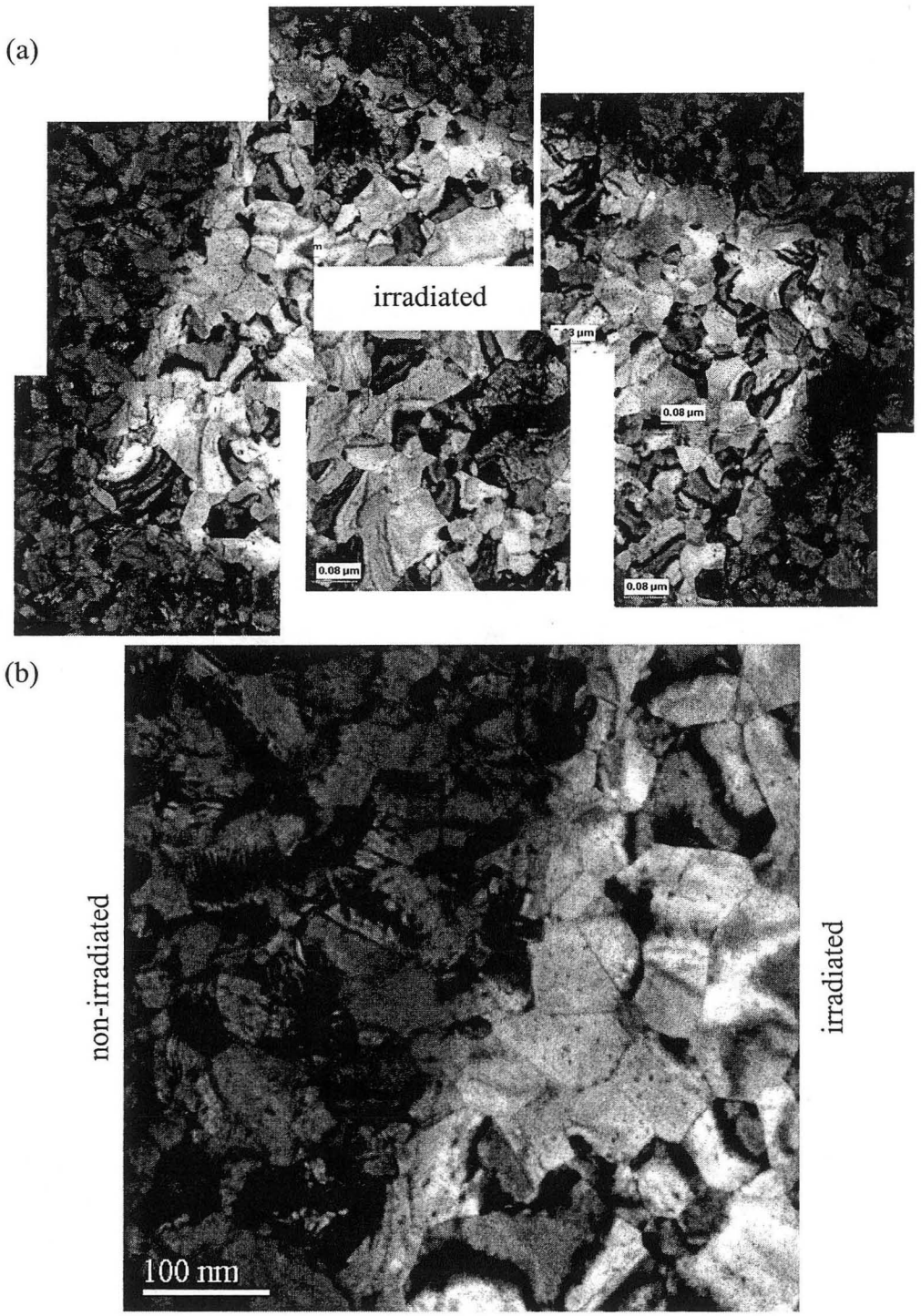

Figure 4–6. TEM bright field images in the vicinity of the boundary between irradiated and non-irradiated areas. Irradiation fluence was $2 \cdot 10^{16}$ of 30 keV Ga^{+}/cm^{2} (b) larger magnification.

4.3.2. Cross-sectional investigation

Currently, HRTEM imaging is capable of obtaining structural information at 1 Ångstrom level [O'Keefe - 1992], or even at a resolution better than 1 Å when image reconstruction techniques and astigmatism corrections are implemented [O'Keefe - 2001a]. This very high resolution was only demonstrated for well-known and perfect Si or diamond structures [O'Keefe - 2001b]. Moreover, for imaging at the 1 Å level, very strict requirements are imposed on the specimen thickness, t. Typically, depending on the chemical composition (and kV), $t < 100$ Å is required. Specimen preparation to $t < 100$ Å is very difficult, especially in hetero-structures of the Co/Pt ML's. Hence, structural information is in the 2 Å range, but it cannot distinguish between individual Co or Pt atoms. In addition, for magnetic samples such as Co/Pt multilayers, resolution is limited due to astigmatism. For these reasons, the HRTEM imaging of cross-sections to study the irradiation effects was found not to be practical for use in this investigation, as it was difficult to distinguish between Pt and highly strained Co layers.

Electron energy loss imaging in TEM, also know as energy filtered imaging (EFI), was used to image the ML's in cross-section. Compositional imaging does not exist at the level of HRTEM and part of this research investigated the resolution limits of the EFTEM imaging. The approach was to grow a test multilayer structure, shown schematically in Figure 4–7.

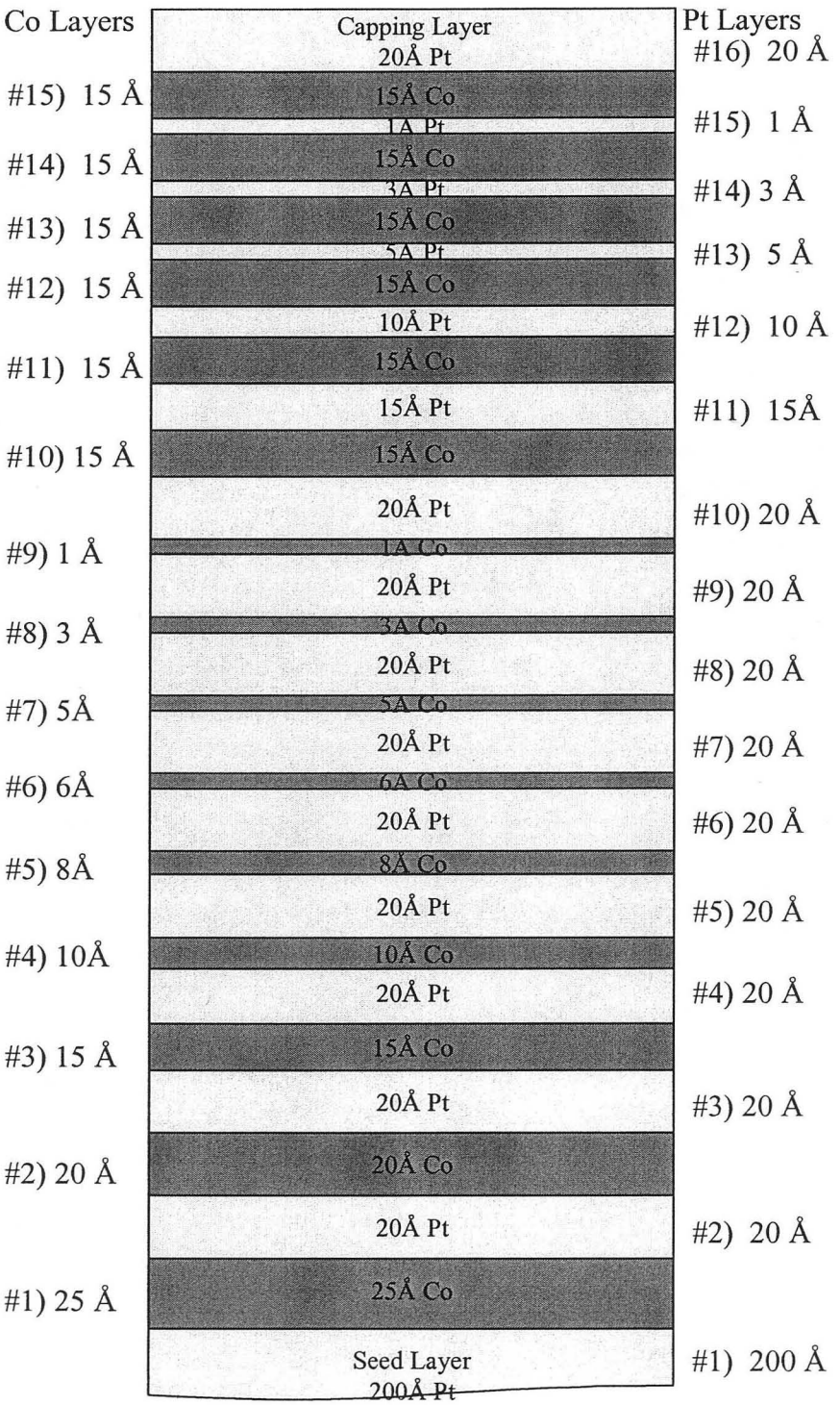

Figure 4–7. Schematic of the Co/Pt multilayer structure used to study resolution limits of electron energy loss TEM imaging.

The sample consisted of alternating layers of Pt and Co. In the bottom part of the sample, the Pt layer thickness was kept constant at 20 Å, and Co thickness was decreased from 25 Å down to 1 Å. This part of the sample was used to find the minimum detectable Co thickness and the resolution. On the other hand, in the upper half of the sample shown in Figure 4–7, the Co layer thickness was kept constant at 15 Å and the Pt thickness was decreased from 20 Å down to 1 Å. This part of the sample was used to check the minimum Pt separation at which two separate Co layers are still resolvable. Figure 4–8 shows a series of energy-filtered images obtained around the Co L absorption edge with 20 eV slit (Edges for Co, Z = 27 are: $M_{2,3}$ at 60 eV, L_3 at 779 eV, L_2 at 794 eV). Figure 4–8(a) is a pre-edge1 image, recorded with electrons between 736-756 eV energy loss, (b) pre-edge2: 756-776 eV and (c) post-edge: 782-802 eV. All three images (a), (b) and (c) show stripe contrast corresponding to Co layers. Image (d) is the ratios of the two pre-edge images and image (e) is the Co jump-ratio image obtained by dividing image (c) by (b). Image (f) is the Co elemental map. Any diffraction or elastic contributions, are expected to show up in the ratio image (d). The uniform intensity of image (d) ensures that the stripe contrast shown on both the Co jump-ratio and the Co elemental map is truly an elemental Co contrast. The line profiles perpendicular to the layering sequence of the multilayer in the jump ratio image, from areas labeled with lines in Figure 4–8(e) are presented in Figure 4–8(g) and (h).

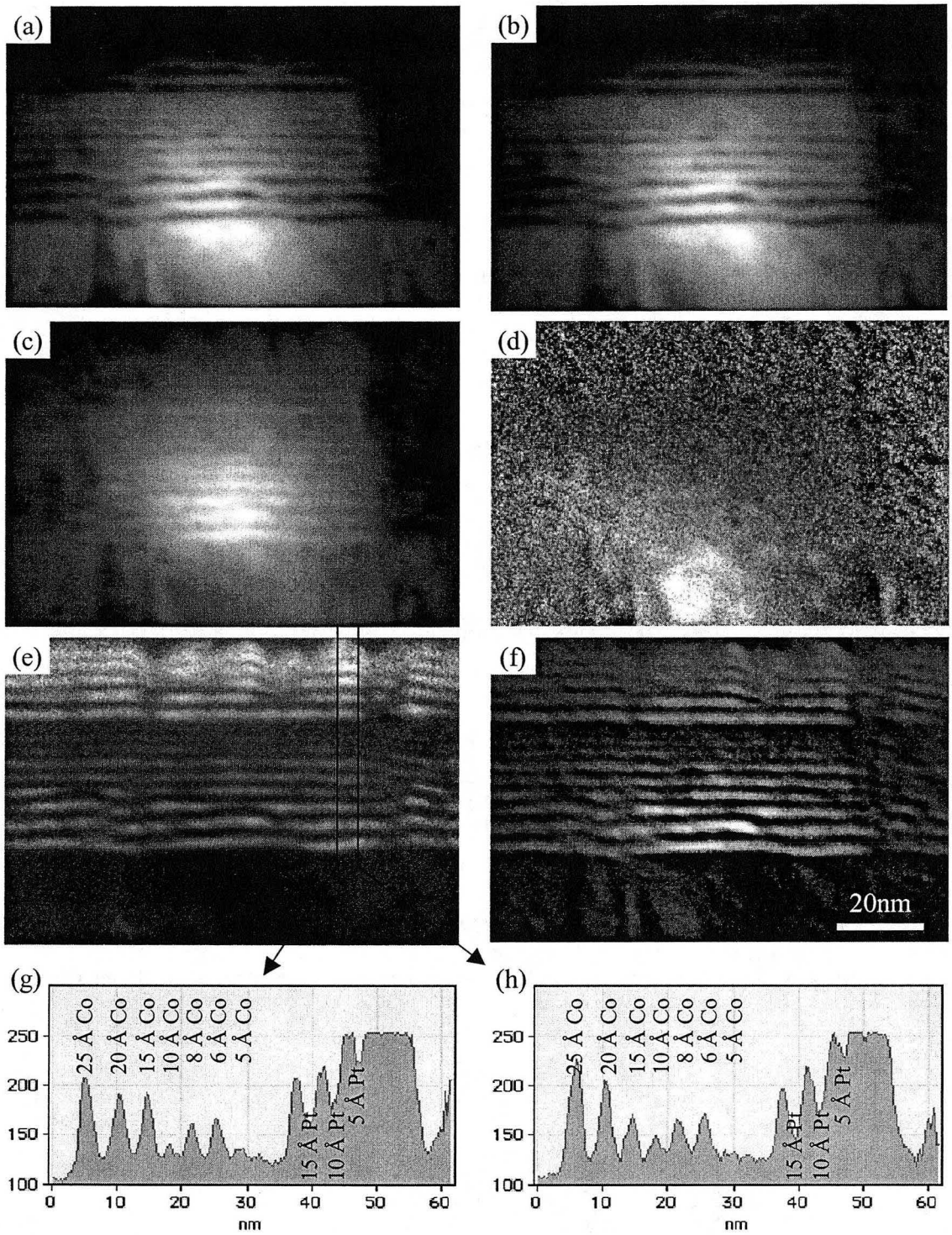

Figure 4–8. Energy filtered imaging of the Co/Pt resolution test sample from Figure 4–7. Images show: (a) pre-edge 1, (b) pre-edge2, (c) post-edge, (d) pre-edge1/pre-edge2, (e) Co jump-ratio, (f) Co elemental map. (g) and (h) Line profiles across image (e).

All peaks are present down to the 3 Å thick Co layer, but below that any peaks associated with 2 Å and 1 Å are not easily detectable. Layers down to about 6 Å are resolved clearly, with the full-width half maximum (FWHM) of the corresponding peak equal to approximately 10 Å. When the Co layer is reduced below 10 Å, the FWHM of the corresponding peak measured on the EFI profile is found to remain approximately constant, but the intensity of the measured peak decreases. On the other end of the test Co/Pt multilayer structure, decreasing Pt thickness is measured as dips between Co peaks. Separation of two Co layers by 15 Å and 10 Å of Pt are clearly resolvable. At a 5 Å Pt separation, a significant Co peaks overlap is measured. In most locations, Co layers separated by 5 Å Pt or less appear as one layer, with small intensity modulation. Hence, if the Pt spacer is reduced to below 10 Å, two layers of Co are imaged as one and below 5 Å the dip is no longer detectable. The test of the EFI resolution showed that Co layers down to 6 Å (but with approximately 10 Å FWHM) were detectable. The thinnest Pt layer at which two Co layers were resolved was 10 Å.

Based on these results, a 10×(6 Å Co/10 Å Pt) ML was grown to investigate the irradiation effects. However, no convincing results were obtained. It was hard to distinguish between ion mixing (if any) and instrumental resolution. To further understand the ion irradiation processes, simulation of ion matter interactions was carried out.

4.3.3. TRIM simulation of ion irradiation

A dynamic version (T-DYN 4.0) of the Monte-Carlo based TRIM program [Biersack - 1980] was used to simulate ballistic mixing of the Co/Pt multilayers. Figure 4–9 plots Co concentration for a 2×(6 Å Co/10 Å Pt) structure as a function of 700 keV N^+ ion irradiation.

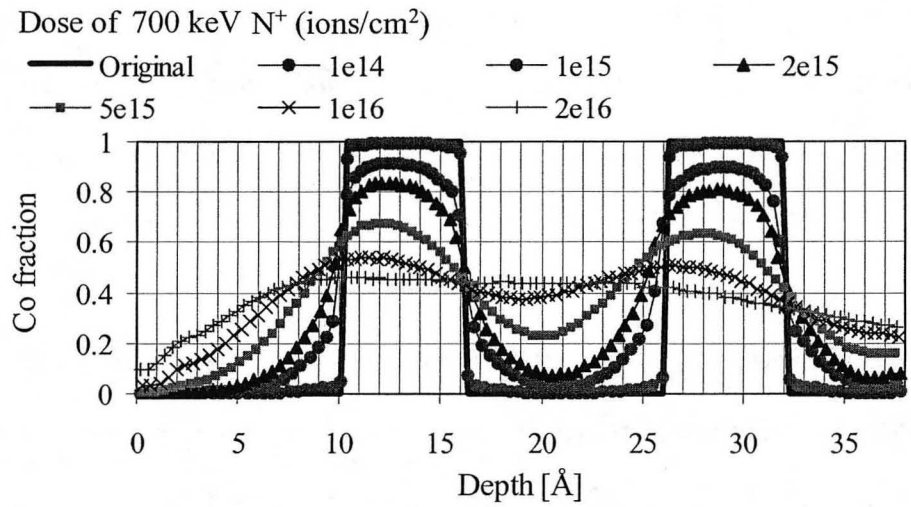

Figure 4–9. Profiles of Co versus ion dose, calculated with TRIM (T-DYN 4.0), see text.

As shown, doses that are responsible for the magnetic property change (as presented in Figure 4–2 and Figure 4–3), induce only small "mixing" at the Co/Pt interfaces. According to the simulated data the full-width-half-maximum (FWHM) of the Co profile at a dose of $5 \cdot 10^{15}$ N^+/cm^2, which causes SRT is only 6.97 Å, (see Table 4–1), indicating roughening rather than real intermixing. According to the EFI resolution study presented in Figure 4–8, such a small increase in Co profile width (from 6 Å to 6.97 Å) is not easily detectable. EFTEM does not exist

at the resolution level necessary to tackle the problem at hand, where effects of ion-irradiation on 1 Å Co layers must be understood.

4.3.4. Modeling

Ab initio electronic structure calculations for a variety of Co/X multilayers have indicated that the variation in magnetic anisotropy energy is controlled by the quality of internal interfaces [Daalderop - 1994a], [Daalderop - 1994b]. Also, experimental data available in the literature shows that multilayers with more ideal abrupt interfaces, such as those grown by molecular beam epitaxy, exhibit significantly larger anisotropies than those grown by sputtering with more diffuse interfaces [Maclaren - 1995], [Draaisma - 1988]. Based on the Néel symmetry model [Néel - 1954] and on first principle electronic structure calculations, MacLaren and Victora [Victora - 1994], [Maclaren - 1994], [Maclaren - 1995] have shown that the magnetic anisotropy energy in the case of multilayers with imperfect interfaces is reduced as compared to the perfect interface case. They showed that the anisotropy of a disordered superlattice (K_i) is related to that of the perfect superlattice (K_p) by:

$$K_i = \frac{1}{2} \cdot K_p \cdot \sum_{j=1}^{n} (P_j - P_{j+1})^2$$

Eq. 4–2

where P_j is the probability of a magnetic atom existing on layer j. Such a model explains well the irradiation data presented here. With increasing disorder induced by ion irradiation, the interface anisotropy is effectively reduced.

The Co/Pt profiles calculated from the TRIM simulations, shown in Figure 4–9, were used calculate the ratio of K_i/K_p from Eq. 4–2 at different ion-induced

disorder. This data is summarized in Table 4–1. The calculated data suggest that even very small ion-induced changes of the interface roughness reduces K_i significantly. Moreover, comparing the K_i/K_p calculated ratios with the measured $H_C/H°_C$ ratios, it can be concluded than the profiles calculated from TRIM, even perhaps, overestimate the ion-induced roughening of the Co/Pt interfaces. This is a reasonable conclusion as TRIM code assumes an amorphous target.

Table 4–1. Summary of data from TRIM calculations and data calculated from Eq. 4–2.

Dose (700 keV N^+/cm^2)	FWHM (Å)	K_i/K_p top interface	K_i/K_p bottom interface	$\sim H_C/H°_C$
	from TRIM	*From* Eq. 4–2 *based on profiles from TRIM* Figure 4–9		*measured see* Figure 4–3
0	6	1	1	1
$1\cdot10^{14}$	6.07	0.7762	0.7731	0.87
$1\cdot10^{15}$	6.42	0.1453	0.1162	0.30
$2\cdot10^{15}$	6.97	0.0583	0.0453	0.10
$5\cdot10^{15}$	9.86	0.0180	0.0125	in-plane
$1\cdot10^{16}$	13.73	0.0050	0.0033	in-plane
$2\cdot10^{16}$	NA	0.0011	0.0007	in-plane

Combining the results from the TRIM simulations, Eq. 4–2, and the "lack" of clear intermixing data from SAD patterns and EFI analysis, it is concluded that ion-irradiation modifies the local arrangement of Co and Pt atoms at an atomic level.

4.4. Magnetic domain-structure as a function of ion dose.

In Chapter 3, the effect of ML growth temperature on H_C was presented, and correlation between H_C and the magnetic domain structure was found. It is thus expected that ion irradiation, which reduces H_C will also change the magnetic domain structure [Kusinski - 2002].

4.4.1. Experimental Procedures

The domain structure was studied as a function of 700 keV N^+ and 30 keV Ga^+ irradiation. The doses were chosen to reduce the perpendicular magnetic anisotropy (PMA) and coercivity, but were lower than necessary to render in-plane magnetization.

Sample EG_103 (see Table 3–2 on page 68 for sample specifics) was irradiated with 700 keV N^+ ions. The dose was $5 \cdot 10^{14}$ N^+/cm^2, which was sufficient to reduce H_C by half, from 6.8 kOe to approximately 3.5 kOe.

Sample EG_A was irradiated with 30 keV Ga^+ ions. Two side-by-side 3 μm by 3 μm regions were irradiated. In the first region, the dose was $3 \cdot 10^{12}$ Ga^+/cm^2, which reduces H_C from 4.3 kOe to approximately 3.0 kOe. In the second region, the dose was $3 \cdot 10^{14}$ Ga^+/cm^2. According to the data presented in Figure 4–3 for 30 keV Ga^+, this dose was large enough to reduce PMA sufficiently below demagnetization and give in-plane magnetization.

For both samples magnetic domains in the demagnetized state (max ±20 kOe with 0.5% reduction step) were investigated in the MTXM for the as-grown and irradiated regions.

4.4.2. Results and discussion

Figure 4–10 shows magnetic transmission x-ray microscopy (MTXM) images of magnetic domains for sample EG_103 grown at T_G = 250°C in (a) as-grown state and (b) after irradiation with 700 keV $5 \cdot 10^{14}$ N^+/cm^2. A substantial decrease in domain size after ion-irradiation is evident. However, the domains still had similar irregular appearance and only a smaller feature size.

Figure 4–11 shows one sample where 2 doses of the 30 keV Ga^+ irradiation were used. In region (b) a reduction in domain size was observed, similar to the data for the N^+ ions. Again, in the irradiated region the domains had a similar irregular appearance as in the non-irradiated region and only a smaller feature size. Region (c) was exposed to 30 keV $5 \cdot 10^{14}$ Ga^+/cm^2, what according to data shown in Figure 4–3 gives in-plane magnetization. As expected, no out-of-plane magnetic domains were observed and only a uniform gray contrast was found corresponding to in-plane magnetization. The photon count in this region is between up and down domains.

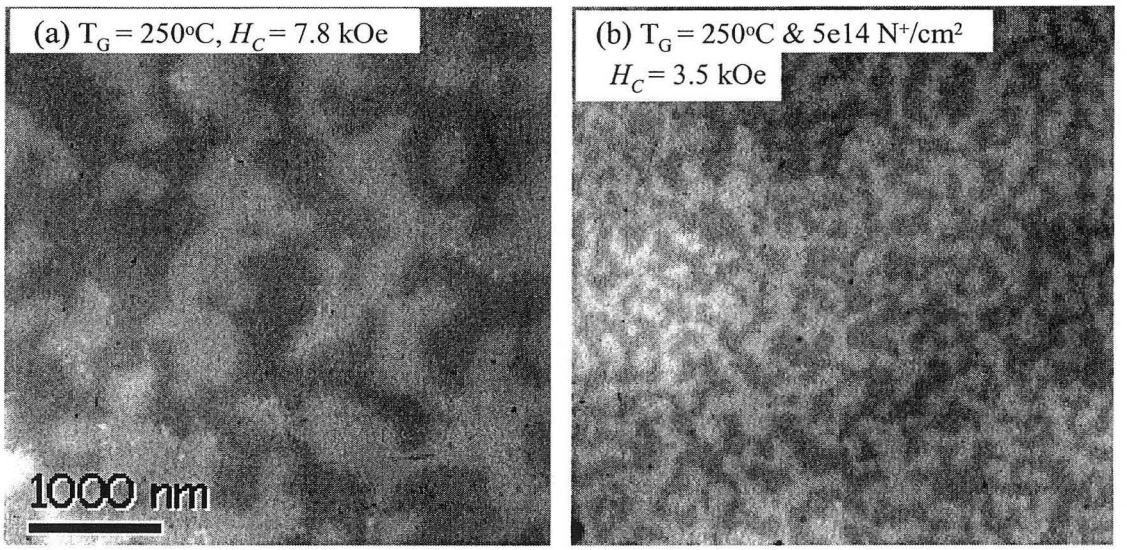

Figure 4–10. Magnetic domain structure in Co/Pt multilayers (a) as-grown (b) after ion irradiation with 700 keV $5 \cdot 10^{14}$ N^+/cm^2.

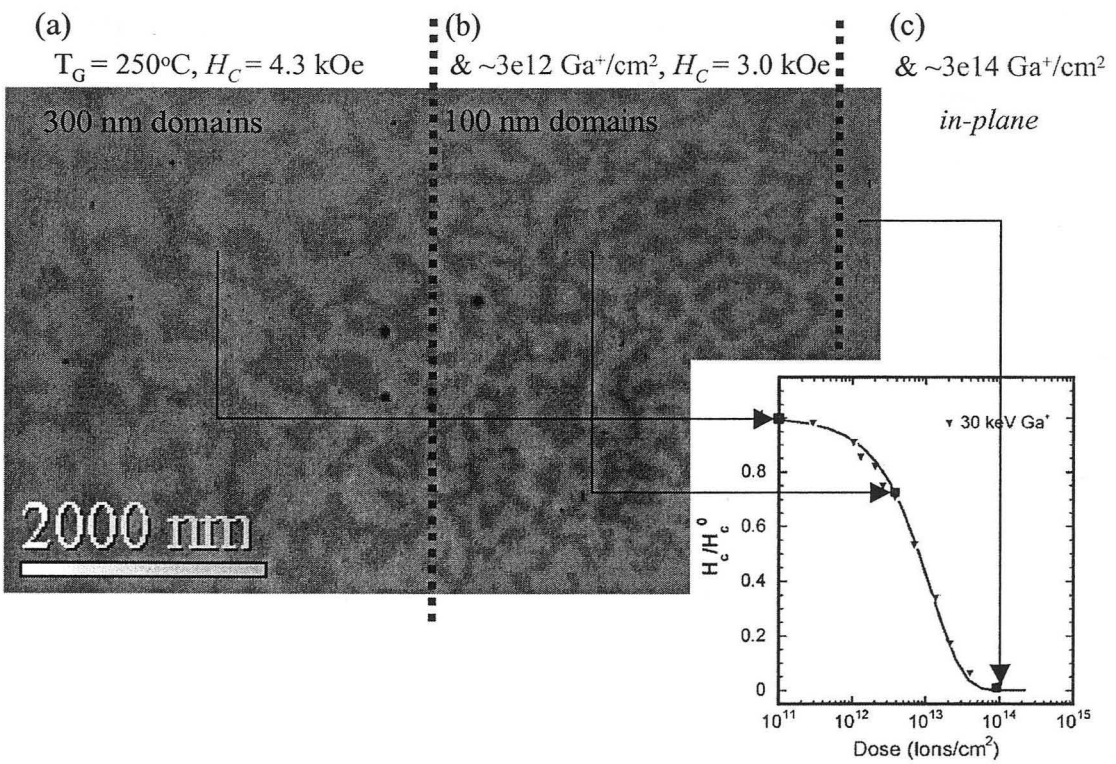

Figure 4–11. Magnetic domain structure in Co/Pt multilayers (a) as-grown (b) after ion irradiation with 30 keV $3 \cdot 10^{12}$ Ga^+/cm^2, (c) 30 keV $3 \cdot 10^{14}$ Ga^+/cm^2.

As stated before, the TEM investigations of the ion-irradiated samples revealed no noticeable microstructural changes from the as-grown samples (i.e. same grain size and <111> texture) even at the doses of 700 keV $5 \cdot 10^{16}$ N^+/cm^2 or was exposed to 30keV $1 \cdot 10^{16}$ Ga^+/cm^2. Hence, for these multilayers, ion induced decrease in H_C is associated with reduction in the PMA and not the microstructure, which gives a decrease in the magnetic domain size. Moreover, combining and reemphasizing the results presented in Figure 3–14 and Figure 4–10, an important conclusion is made. For the ease of presentation, the data is replotted in Figure 4–12. The domain sizes, D, are not directly determined by H_C and are governed in a complex way by both the PMA and the microstructure. Using the following nomenclature:

D1 = D(T_G = 190°C, H_C = 3.8 kOe)

D2 = D(T_G = 250°C, H_C = 7.8 kOe)

D3 = D(T_G = 250°C and $5 \cdot 10^{14}$ N^+/cm^2, H_C = 3.5 kOe),

an interesting observation is made. As shown, D1 > D2 yet D2 > D3. Hence clearly, coercivity alone cannot be used to predict the domain size.

When T_G is increased from 190°C-Figure 4–12(a) to 250°C-Figure 4–12(b), H_C increases and domain size decreases. The increase in T_G results in improved <111> texture what gives increased anisotropy resulting in increase of H_C from 3.8 kOe to 7.8 kOe, corresponding to smaller D. When the T_G = 250°C sample was then irradiated, which reduced H_C back down to 3.5 kOe, the smallest domain size was observed, Figure 4–12(d). In the latter step, however, the grain structure was not changed, and only the PMA was reduced due to local intermixing of the ML's.

Hence, the ion irradiation reduces the domain size, similar to the increase in T_G in the high temperature regime, above T_{crit}, Figure 4–12(c).

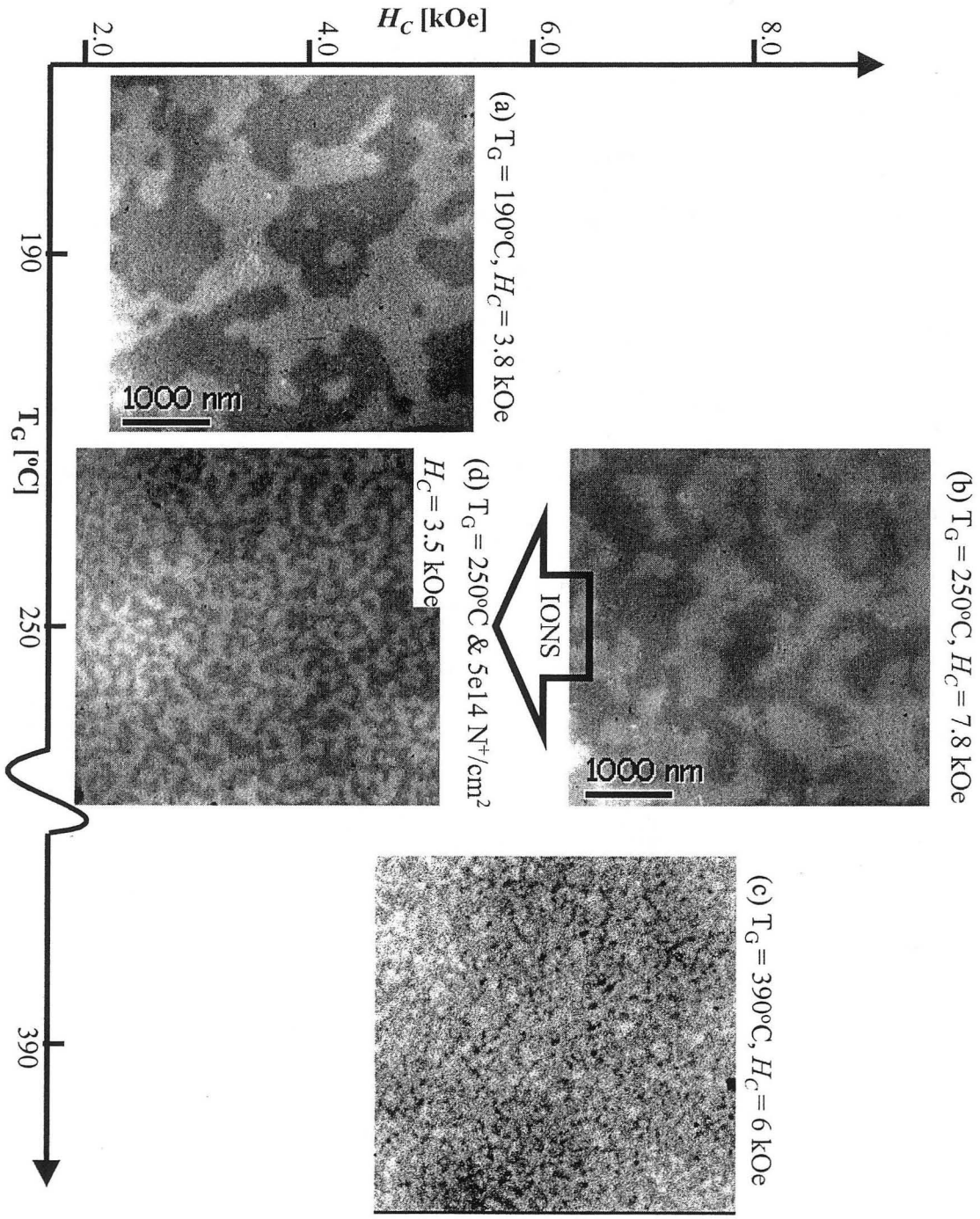

Figure 4–12. Magnetic domain structure and H_C versus T_G and the ion dose.

4.5. Summary

It is concluded that the changes in magnetic properties with exposure to ion irradiation are associated with decrease in interfacial anisotropy K_S. The rotation of the magnetization to in-plane at high dose supports this conclusion. With increasing doses of ions, K_S is reduced primarily due to localized ion-beam induced atomic disordering at the interfaces and becomes comparable to the shape anisotropy. At high enough doses this is seen as a transition to in-plane magnetization. At roughly the same point, the coercivity falls to zero. The fact that the loop shapes remain similar as the coercivity falls is evidence against an alternative softening mechanism based on the creation of soft defects.

Even though it was not possible to directly correlate the structural changes induced by ion-irradiation with magnetic properties, the following conclusion can be drown. The change is clearly not microstructural,[i] as TEM investigation showed the same features before and after irradiation. Ion irradiation displaces Co and Pt atoms near Co/Pt interfaces, which leads to local roughening and reduction in K_i.

For all ML's, ion irradiation, which reduces H_C by decreasing the perpendicular interface anisotropy, was found to decrease the size of the magnetic domains.

---

[i] The change is not related to the grain size. The interface roughness is a microstructural feature albeit at a very local Å length scale.

Chapter 5.

MAGNETIZING EXPERIMENTS IN PATTERNED CO/PT MULTILAYERS

5.1. Magnetic patterning by selective ion-irradiation

In Chapter 4, the ion dose was shown to influence the magnetic properties and magnetic domain structure of Co/Pt multilayers. Applying those principles, two techniques to locally modify the magnetic properties of the Co/Pt multilayers were utilized by applying a spatially varying ion dose. These techniques were ion-irradiation through a stencil mask and direct writing with focused ion beams.

The magnetic reversal processes of magnetic arrays fabricated by such ion beam irradiation are reported in this Chapter. One important aspect of the patterning technique is the nature of the magnetic interaction between the ion irradiated and the non-irradiated matrix regions, where the irradiated regions have in-plane anisotropy and the non-irradiated matrix has perpendicular anisotropy. Particularly important is how the switching fields and the reversal mechanisms in one of the regions influence the reversal processes in the adjacent region. To be more specific, the question is how the presence of the ion-irradiated in-plane regions influences the reversal of the non-irradiated regions with

perpendicular anisotropy. In order to study such effects, it is essential to investigate the three dimensional magnetic structure using high-resolution magnetic imaging techniques. Two complementary magnetic imaging techniques, Lorentz transmission electron microscopy (LTEM) [Chapman - 1999], which is sensitive to in-plane magnetization and magnetic transmission x-ray microscopy (MTXM) [Denbeaux - 2001], which measures perpendicular magnetization[i], were used to understand the three-dimensional magnetic domain structure.

Numerous patterns were investigated, with importance placed on the correlation between resulting magnetic domain structure and irradiation parameters (i.e. dose, spatial distribution of the dose—dimensions of the applied patterns).

5.2. Experimental procedures

5.2.1. Choice of the multilayers system for patterning

The multilayers selected for pattering were the ones characterized by perpendicular anisotropy and square loops with $M_R/M_S \cong 1$. These included:

/ 20 nm Pt seed / 10×(0.3 nm Co/1 nm Pt) / 1 nm Pt cap layer /,

grown at 250°C according to procedures detailed in Chapter 3. These multilayers were grown directly on electron and x-ray transparent 50 nm thick SiN membranes. The dimensions of the transparent region were 100 μm by 100 μm.

---

[i] M-TXM is implemented at the beam line 6.1.2 of the Advanced Light Source at the Lawrence Berkeley National Laboratory.

5.2.2. Irradiation through a stencil mask

In the first patterning method, a uniform intensity large beam was used to irradiate the samples through a stencil mask. The silicon stencil mask was fabricated from commercial silicon-on-insulator (SOI) wafers with a 10 μm thick top-side Si layer, 0.5 μm of SOI oxide, and a 500 μm thick Si carrier substrate. The stencil holes were first patterned by optical lithography and then transferred into the 10 μm Si layer by SF_6-based, high aspect ration reactive ion etching. The SOI oxide was used as an etch stop. Following this step, windows were etched from the backside through the carrier substrate, using a similar reactive ion etching, and the remaining SOI oxide was removed with a wet HF etch. The resulting silicon mask consisted of 10 μm thick Si membranes with 1 – 1.5 μm regularly spaced arrays of circular holes. Depending on the location of the mask, the spacing of the holes was between 1 μm and 10 μm. For the results discussed here, areas with 1.3 μm holes spaced at 2 μm or 3 μm were used.

During the patterning process, the mask was placed directly on the film and the sample was bombarded with 700 keV N^+ ions from a NEC 3UH Pelletron accelerator. According to the TRIM[i] calculations [Biersack - 1980], shown in Figure 5–1, the 700 keV N^+ ions are completely stopped within 1 μm of Si layer. Hence, such a Si mask provides a perfect shadowing of ions in the masked areas and only the un-masked areas are exposed to ion-irradiation, creating a sharp interface between magnetically virgin and magnetically modified regions, respectively.

---

[i] TRIM program for PC available from J.F. Ziegler (jfz@us.ibm.com) and J.P. Biersack, http://www.research.ibm.com/ionbeams/(2000)

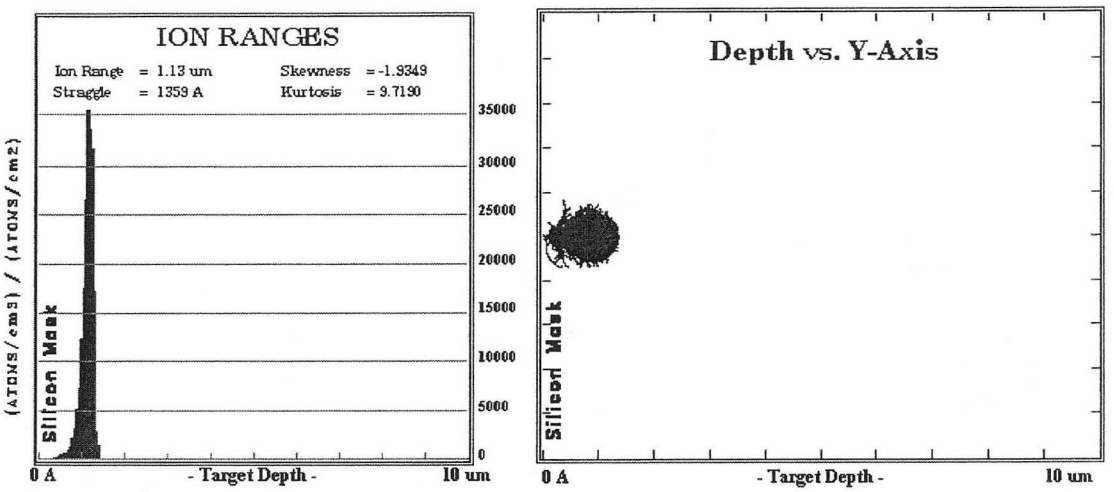

Figure 5–1. TRIM simulation of absorption of 700 keV N^+ ions in Si.

The dose and ion species were selected to create a variety of patterns. Table 5–1 lists all samples that were modified by ion irradiation through a Si mask. Their magnetic domain structure was subsequently analyzed. The logic behind the selected parameters will become more evident in the discussion.

Table 5–1. List of samples patterned by irradiation through a Si stencil mask.

Pattern ID	Sample ID see Table 3–2	Ion species	Dose through the mask (ions/cm^2)	Uniform irradiation dose (ions/cm^2)
#I	EG_103-C6	700 keV N^+	1) $5\cdot10^{16}$	
#II	EG_103-C6-2	700 keV N^+	1) $5\cdot10^{16}$	2) $5\cdot10^{14}$
#III	EG_103-H	700 keV N^+	1) $5\cdot10^{14}$	2) $5\cdot10^{14}$

For the first sample, #I, the irradiation dose and the ion species were selected to give in-plane magnetization in the irradiated regions. By using such a well-defined magnetic pattern, the interactions between the irradiated and non-

irradiated regions, could be investigated. For the second sample, #II, sample #I was irradiated with 700 keV $5 \cdot 10^{14}$ N^+/cm^2 to reduce the coercivity. For the third sample, #III, the pattern used for sample #I was applied (different dose) and then the entire sample was irradiated with 700 keV $5 \cdot 10^{14}$ N^+/cm^2 to reduce the coercivity. The first dose was set to reduce the coercivity in the irradiated regions, but to keep the perpendicular easy axis. Then, the coercivity of the entire matrix was reduced by a uniform ion irradiation. The doses were such that in single irradiated regions $H_C \cong 60\%\ H^\circ_C$ and in twice irradiated matrix $H_C \cong 80\%\ H^\circ_C$.

5.2.3. Patterning with a focused ion beam

In the second patterning approach, a 30 keV Ga^+ Focused Ion Beam (FIB), with 20nm beam size and 1 pA current was used. A variety of patterns were created by directly "writing" features by rastering the beam across the sample. To create continuous lines, pixel separation was set at 5 nm to achieve 75% spot overlap. For this technique, varying exposures were used to study the effects of different irradiation doses for a given pattern. Table 5–2 lists samples modified by selective ion irradiation with FIB, and discussed in this thesis.

Table 5–2. List of FIB patterned samples

Pattern ID	Sample ID Table 3–2	$H_{C\perp}$ (kOe)	Pattern
FIB#1	EG_103	6.8	140 nm lines, 450 nm period => 310 nm bits
FIB#2	EG_107	3.8	320 nm × 80 nm rectangles
FIB#3	EG_A	4.3	40 nm lines, 140 nm period => 100 nm bits
FIB#4	EG_A	4.3	100 nm squares

5.3. Experimental results and discussion

First, detailed analysis of patterns formed by irradiation of a Co/Pt multilayer (sample #I in Table 5–1, grown at 250°C with H°_{C} = 6.8 kOe) through a stencil mask with $1 \cdot 10^{16}$ 700 keV N^{+}/cm^{2} is discussed. For this sample, both LTEM and MTXM techniques were utilized to fully understand the reversal processes. As is explained in section 5.3.1, the LTEM analysis was crucial to the interpretation of the magnetic orientation in the ion-irradiated regions and especially to understanding the contrast formation in MTXM. However, for the subsequent samples, only results from MTXM imaging will be reported as this technique was found to be more suitable for the investigation of samples with perpendicular magnetic anisotropy.

5.3.1. Sample # I, mask irradiation $1 \cdot 10^{16}$ 700 keV N^{+}/cm^{2}

5.3.1.1. Magnetic imaging with Lorentz TEM (LTEM)

As explained in the introductory section, LTEM is sensitive only to the component of magnetization that is perpendicular to the optic axis. The investigated Co/Pt multilayer samples exhibit a perpendicular easy axis of magnetization and, in the as-grown state, are known to break up into patterns of up and down magnetic domains to minimize the overall magnetostatic energy. For this configuration, only domain walls are expected to have in-plane magnetization, which could contribute to magnetic contrast in LTEM images. In earlier research, investigating domain structures in similar Co/Pt multilayers by LTEM, Plossl [Plossl - 1993] estimated that the transition from up to down

magnetization takes place over a distance smaller than 20 nm (approximate resolution of the LTEM dedicated TEM at the University of Glasgow) [Chapman - 1999]. In our experimental setup, no magnetic domain contrast was recorded when imaging the as-grown samples in the Fresnel and Foucault modes of LTEM. This indicates that the domain wall regions are below the sensitivity of the LTEM technique. As shown by Plossl [Plossl - 1993], sample tilting can be utilized to obtain information about the perpendicular component of magnetization. This, however, introduces ambiguities in image interpretation and multiple tilt axes must be used. For this reason, no attempt was made to use LTEM to study the perpendicular domain configuration. However, LTEM is ideally suited to analyze the in-plane magnetic domain configuration. Hence, for the samples irradiated through a stencil mask with 700 keV $1 \cdot 10^{16}$ N^+/cm^2, LTEM was used to elucidate the magnetization orientation in the ion-irradiated regions, and in particular, to verify whether the irradiated regions are paramagnetic or have an in-plane magnetization.

In the first studies investigating ion irradiation effects on Pt/Co/Pt structures, Chappert, Ferre et al. [Chappert - 1998], [Ferre - 1999] found the irradiated regions to be paramagnetic. However, later studies, similar to those discussed in this dissertation and shown in Figure 4–2 on Co/Pt multilayers, were found at the IBM Almaden Research Center to exhibit ferromagnetic irradiated regions but with an in-plane easy axis of magnetization.

Prior to LTEM imaging, the sample was saturated in a perpendicular field of +14 kOe, and was imaged at remanence. This ensures that only differences in

magnetization between irradiated and non-irradiated regions contribute to LTEM contrast.[i]

Figure 5–2 shows Fresnel images of the Co/Pt multilayer irradiated through a stencil mask with a dose of $1 \cdot 10^{16}$ N^+/cm^2 and the schematic showing the mask. As shown, both images had magnetic contrast consistent with the irradiation pattern. Periodic circular regions equal to the size of the holes in the stencil mask are shown. The black and white lines running across the irradiated regions visible in the Fresnel LTEM images, Figure 5–2(a) and magnified in (b), correspond to domain walls between in-plane domains. The non-irradiated matrix shows small contrast variations, which are due to the physical microstructure. The analyzed multilayers consisted of 10 periods of (3 Å Co / 10 Å Pt). Hence, the total magnetic thickness of the film was only 3 nm. This resulted in weak magnetic contrast as compared to the strong microstructure contrast arising from diffraction of the individual columnar grains. The physical microstructure in this film is on a significantly smaller scale than the magnetic pattern size (50 nm grain size vs. 1 μm pattern size). Large defocus values, $\Delta f > 100$ μm, were used to minimize the contributions of high spatial frequency components, corresponding to smaller real space dimensions. The use of large Δf, however, increases the apparent width of the domain walls (see Figure 2–3), and reduces the magnetic imaging resolution, which makes estimation of the real domain wall thickness impossible.

---

[i] As shown before, Figure 3–12, the hysteresis loop of this sample shows an M_R/M_S ratio of 1. Hence, at remanence after perpendicular saturation, areas with perpendicular anisotropy remain magnetized along the saturation direction, without splitting into up and down multi-domain states.

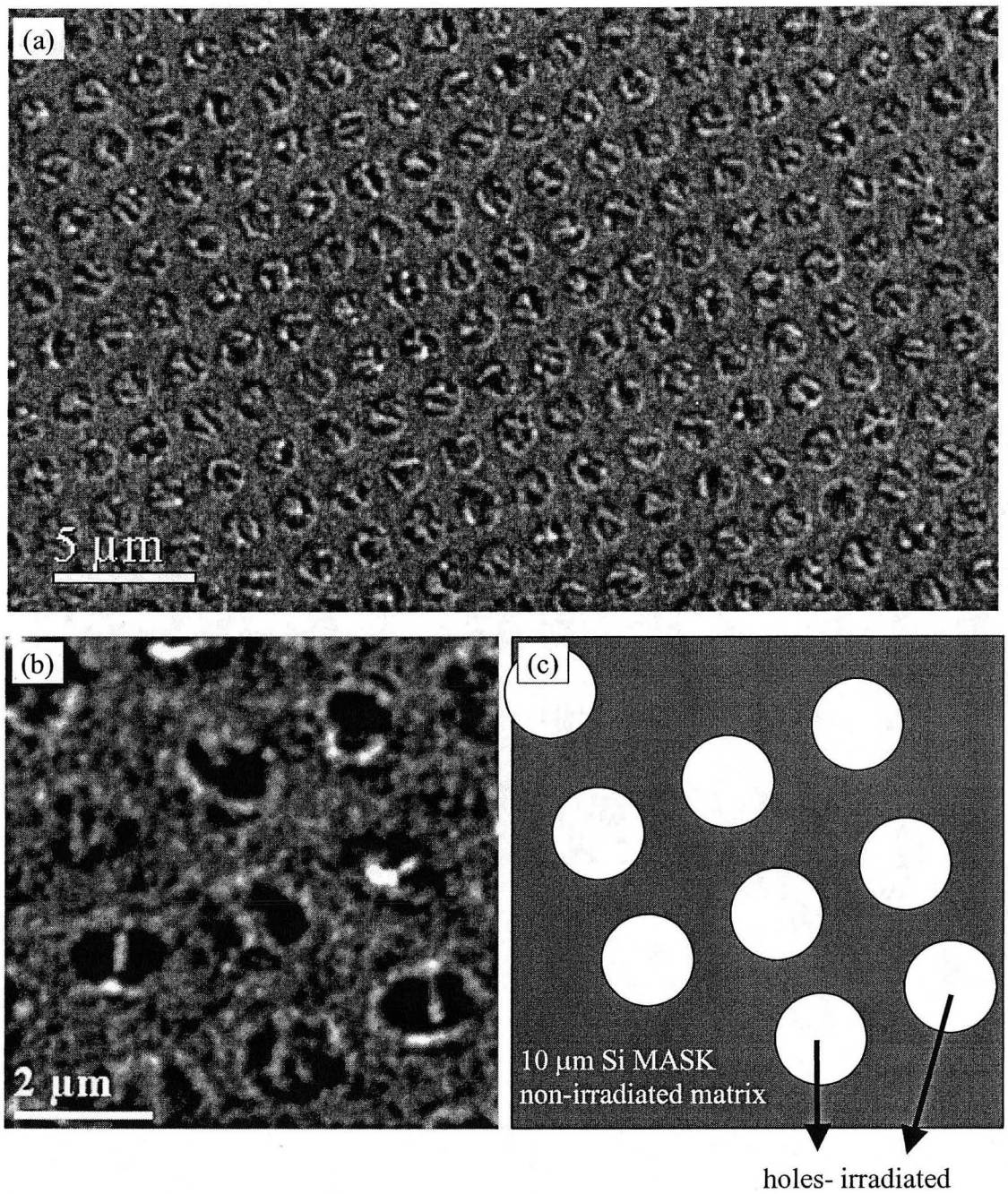

Figure 5–2. (a) Fresnel LTEM image of the Co/Pt multilayer patterned by ion-irradiation through a stencil mask with a dose of $1 \cdot 10^{16}$ N^{+}/cm^{2}, (b) magnified image, (c) schematic of the patterning geometry.

Two Foucault images obtained with +X and –X beam tilts are presented in Figure 5–3. For both images, all irradiated regions showed both black and white domains on the gray matrix background, indicative of a multi-domain configuration. Moreover, with change in the beam tilt from +X to –X a complementary contrast was seen. For example, the region in the top left corner of the image labeled with a white circle is mainly black with white edges in image (a) and switches to white center and black outlines in image (b).

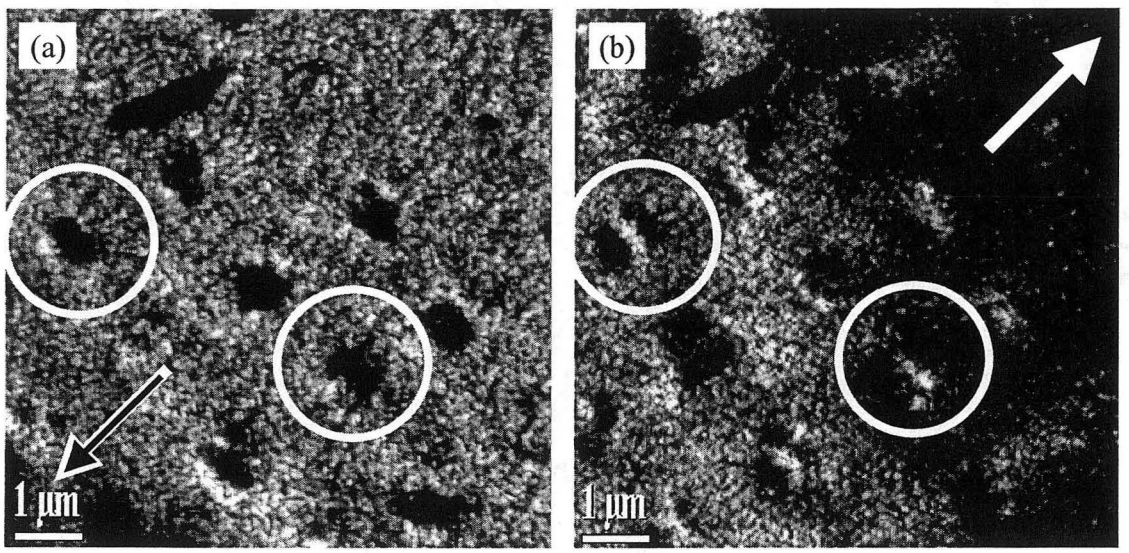

Figure 5–3. Foucault images of the Co/Pt multilayer patterned by ion-irradiation through a stencil mask with a dose of $1 \cdot 10^{16}$ N^+/cm^2. Arrows show the direction of the beam tilt (a) +X, (b) –X. Two circles indicate same sample locations.

The presence of magnetic contrast for both Fresnel and Foucault images indicates that the irradiated regions went through a SRT from out-of-plane to in-plane easy axis of magnetization. At remanence, the ion-irradiated regions cannot support perpendicular magnetization. The shape anisotropy renders in-plane magnetization, which is consistent with magnetic measurements of large areas

exposed to similar irradiation doses. As explained above, the SRT in the ion-irradiated areas is associated with a decrease of the interface anisotropy upon ion-irradiation.

To understand the magnetic properties in the irradiated areas further, Fresnel imaging during *in-situ* magnetizing experiments was performed [Kusinski - 2001b]. The objective lens of the microscope, which is a source of vertical magnetic field, was used to apply a perpendicular magnetic field by adjusting the objective lens current [Verbist - 1998]. In addition, a magnetic field along the in-plane direction of the sample was applied utilizing sample tilting, as shown schematically in Figure 5–4. When the objective lens current was increased to apply a perpendicular field above $H_{\perp}$ = 2000 Oe, the magnetic contrast shown in Figure 5–2 was observed to disappear and uniform contrast for the entire sample was observed. This was a result of perpendicular alignment of the magnetization in the irradiated areas in the direction of the applied field. When the objective lens current was reduced to decrease the applied perpendicular magnetic field, the contrast corresponding to the irradiated regions with the in-plane magnetization and the perpendicular matrix was observed again.

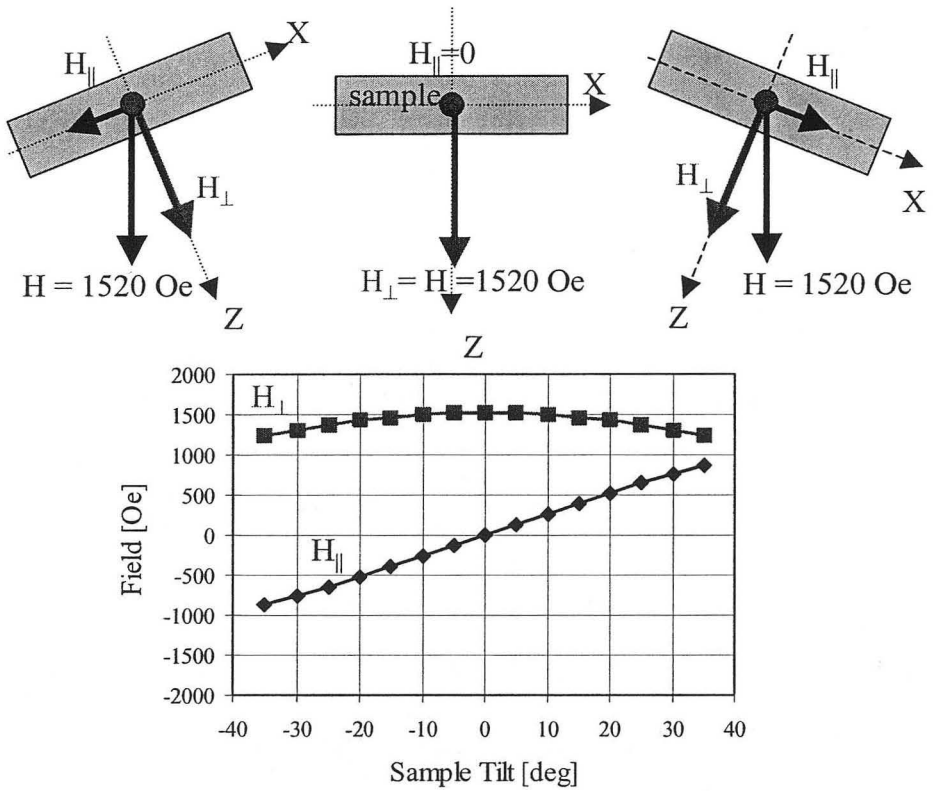

Figure 5–4. Schematic diagram illustrating the tilting in TEM. Chart shows the perpendicular and in-plane components of the magnetic field as a function of the sample tilt angle.

To measure the nucleation fields and the statistics of magnetic reversal processes in the ion-irradiated regions, a constant $H_{\perp}$ = 1500 Oe vertical field was set, and sample tilt was varied between ±35°. By adjusting the specimen tilt angle, an in-plane field in the range $H_{||}$ = ±850 Oe, was applied. The sample was taken through the hysteresis loop and Fresnel images were recorded *in-situ*. As explained in section 2.3.1.1, a spatially varying component of the in-plane magnetic induction contributes to the Fresnel imaging contrast. The domain walls appear as dark or bright fringes [Fuller - 1960], [Chapman - 1984], [Chapman - 1999]. The deflection of electrons governed by the Lorentz force is perpendicular

to both the direction of the magnetization and to the electron propagation direction. Based on this, the uniformly magnetized in-plane region yields an increased intensity, seen as a bright fringe at one end and decreased intensity, indicated by a dark fringe at the other end. When the magnetization is reversed, the contrast is opposite. A multi-domain configuration yields contrast consisting of bright and dark lines running through the region indicating the locations of the domain walls.

Figure 5–5 shows two Fresnel images of the sample with $H_{||}$ = 264 Oe applied in the two opposite in-plane directions and the schematics explaining the recorded contrast. Clearly, the magnetic domain contrast across the patterns, seen in Figure 5–2, is not present. At the in-plane field of $H_{||}$ = +264 Oe, Figure 5–5(a), the recorded Fresnel contrast consisted of respective dark and bright fringes at the top and bottom of each irradiated pattern.

As shown schematically in Figure 5–5(c), the contrast is consistent with the irradiated areas magnetized in-plane and to the right, along the applied field. When the in-plane field was reversed to $H_{||}$ = -264 Oe, an opposite Fresnel contrast was observed. Figure 5–5(b) shows bright and dark fringes at the top and bottom of each irradiated pattern, respectively, which was opposite to the contrast shown in Figure 5–5(a). As shown schematically in Figure 5–5(d), the contrast in image (b) is consistent with the irradiated areas magnetized in-the-plane, and to the left.

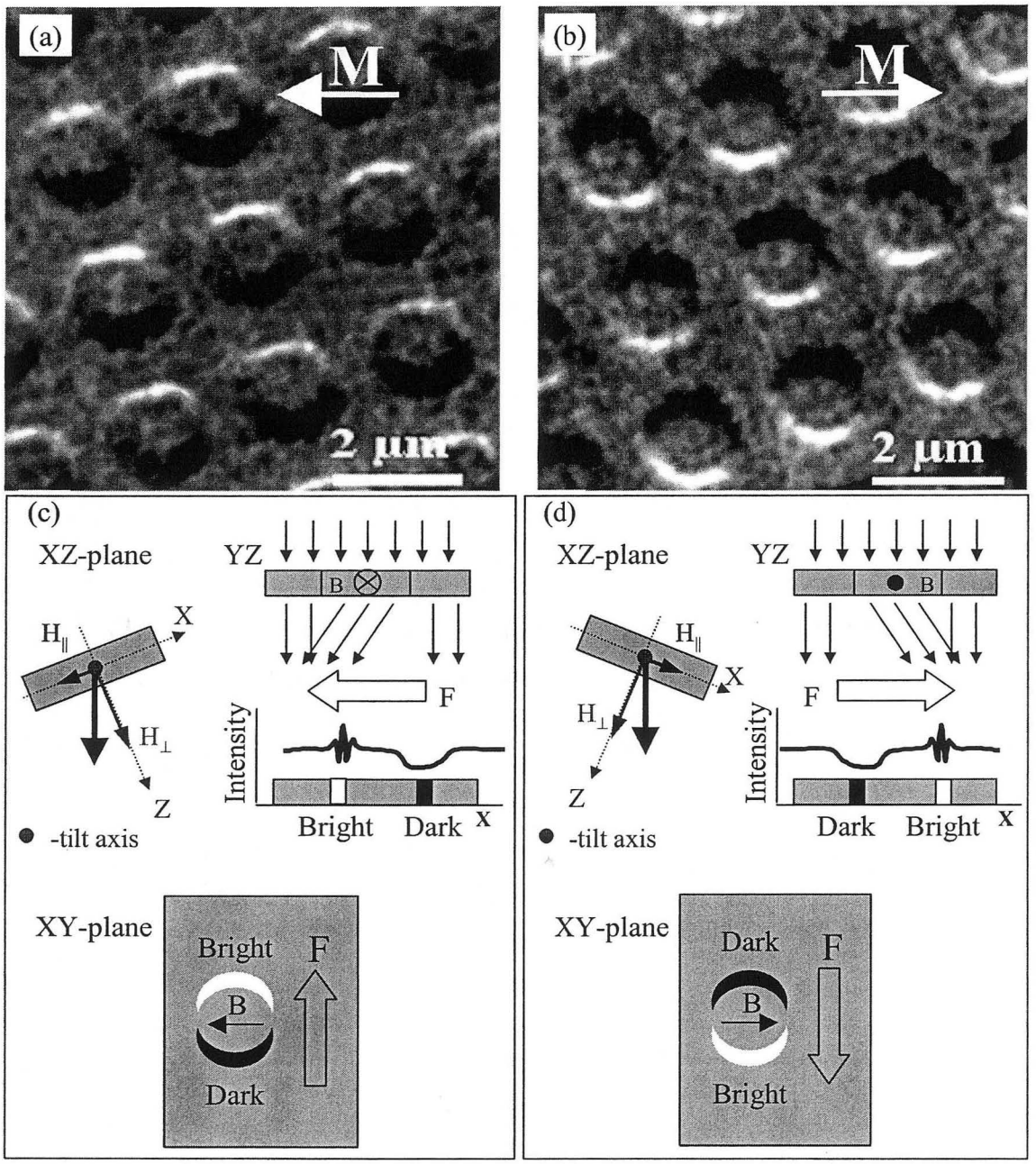

Figure 5–5. Fresnel images of the patterned sample with in-plane field of: (a) $H_{||}$ = +264 Oe and (b) $H_{||}$ = -264 Oe. (c) and (d) Respective schematics explaining the contrast.

Figure 5–6 shows a series of Fresnel images of the patterned multilayers recorded at different sample tilts and, hence, at a different in-plane magnetic field. For each image, the sample tilt and the applied in-plane magnetic field are indicated. Figure 5–6(a) is an image recorded at a 10° tilt ($H_{||}$ = 264 Oe). As explained in the discussion of Figure 5–5, this field was sufficient to magnetize (align) all the in-plane patterned areas along the applied field direction as indicated by the arrow. When the in-plane field was decreased, the sample remained magnetized in the same direction. Figure 5–6(b) shows the area with the field reduced to $H_{||}$ = ~7 Oe. Patterned areas still have a white fringe at the bottom but some develop a split contrast. This contrast stays approximately constant with reduction of the field to $H_{||}$ = 0 Oe. When the field was applied in the negative direction, reversal of the in-plane regions was observed by domain wall motion. The reversal for some of the patterns started at the relatively low field of $H_{||}$ = -54 Oe, Figure 5–6(c). However, patterns magnetized in the positive direction were still present. At this field, for some of the patterns, the contrast changed to bright fringes at the top and at the bottom of the patterns with a dark center. A reversed contrast, namely dark boundaries and bright middle, was also found. Such patterns supported a multi-domain state and the Lorentz deflection was in two directions: either to the top and bottom, or both to the middle of the pattern. When the field was further increased in the negative direction, (Figure 5–6(d), $H_{||}$ = -82 Oe), the multi-domain contrast was observed for most of the patterns. As the field was further increased, (Figure 5–6(e), $H_{||}$ = -135 Oe), the observed contrast was similar to that shown in Figure 5–6(d). However, notice that the bright fringes are less continuous and are brighter at the top of the

patterns. This implies a multi-domain state with the majority of the area already magnetized in the negative direction to the left on the image. Finally, when $H_{||}$ = -264 Oe was applied, further domain wall motion was observed. This resulted in the complete alignment of the patterns with the direction of the applied field, (to the left), as shown in Figure 5–6(f). The Fresnel contrast consisted of only dark and bright fringes at the bottom and top, respectively, which is opposite to the contrast shown on Figure 5–6(a).

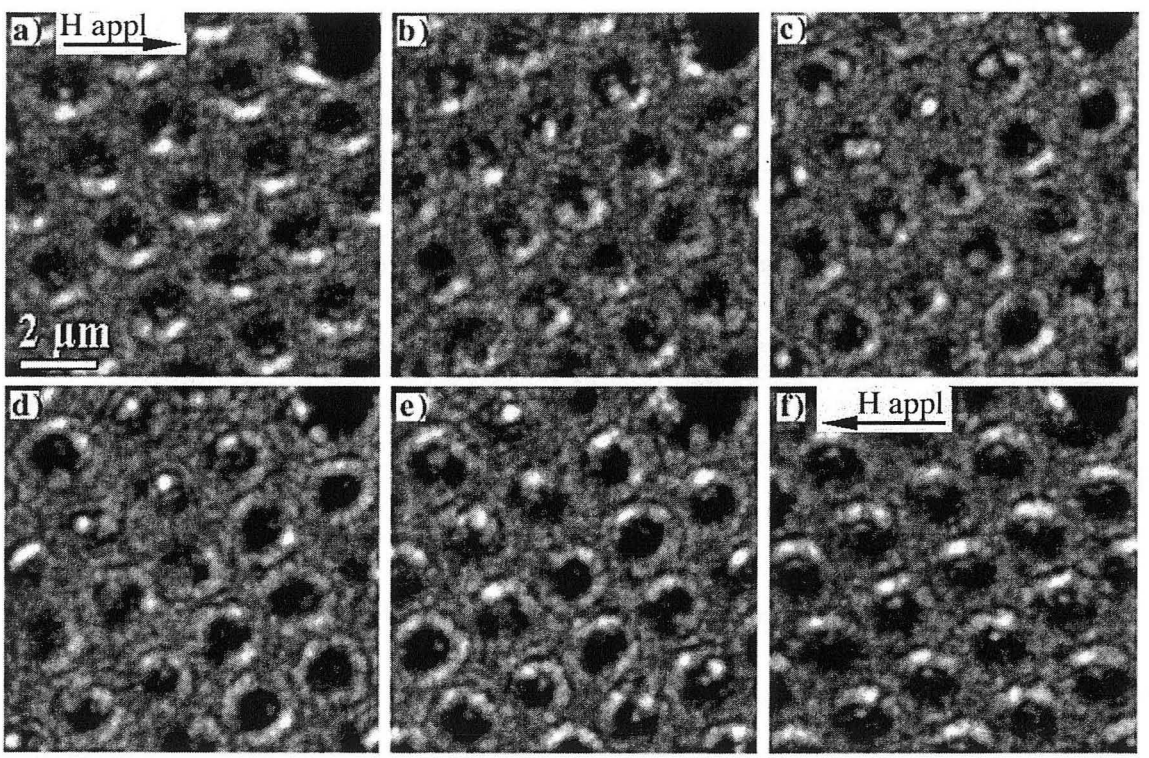

Figure 5–6. A series of Fresnel images of patterned multilayers recorded at different sample tilts. a) tilt =10°; $H_{||}$ = 264 Oe, b) tilt = 0.3°; $H_{||}$ = 7 Oe, c) tilt = -2°; $H_{||}$ = -54 Oe, d) tilt = -3.1°; $H_{||}$ = -82 Oe, e) tilt = -5.1°; $H_{||}$ = -135 Oe, f) tilt = -10°; $H_{||}$ = -264 Oe.

The results presented in Figure 5–6 proved the ion-irradiated regions to have an in-plane easy axis of magnetization and to be relatively soft as compared to the non-irradiated sample. Foucault LTEM imaging was carried out to confirm these findings. A series of Foucault images recorded with in-plane magnetic field are presented in Figure 5–7. At remanence, with no magnetic field applied, the irradiated patterns showed split dark-and-white contrast within each of the bits, as presented in Figure 5–7(a) and (b). These two images were recorded at opposite +X and –X beam tilts, respectively, and indeed they had a complementary contrast. For example, two bits highlighted with circular fiducial marks are dark in the middle and bright on the outside in image (a) and are bright in the middle and dark on the outside in image (b). This means that, at remanence, these ion-irradiated regions are split into multiple in-plane magnetic domains. When the field $H_{||} = \pm 400$ was applied, the irradiated regions showed a uniform dark or white uniform contrast as presented in Figure 5–7 (c), (d) and (e). Moreover, images (c) and (d), both recorded at $H_{||} = -400$ Oe, with +X and –X beam tilt, show black and white contrast for the irradiated patterns, respectively. Hence, a field of 400 Oe was sufficient to saturate these regions, yielding uniformly magnetized regions with single in-plane magnetic domains.[i] In addition, image (e) which was recorded at $H_{||} = +400$ Oe with a –X beam tilt had the same contrast as image (c), which was recorded at $H_{||} = -400$ Oe with a +X beam tilt. Reversing the in-plane magnetic field at a set beam tilt, or switching the beam tilt direction at constant

[i] If these regions were not uniformly magnetized and had a mulidomain configuration, black and white contrast would have been observed just as for images presented in Figure 5–7(a) or (b).

field, has same effect. This proves that the irradiated patterns have in-plane easy direction of magnetization and are magnetically soft as compared to the non-irradiated matrix.

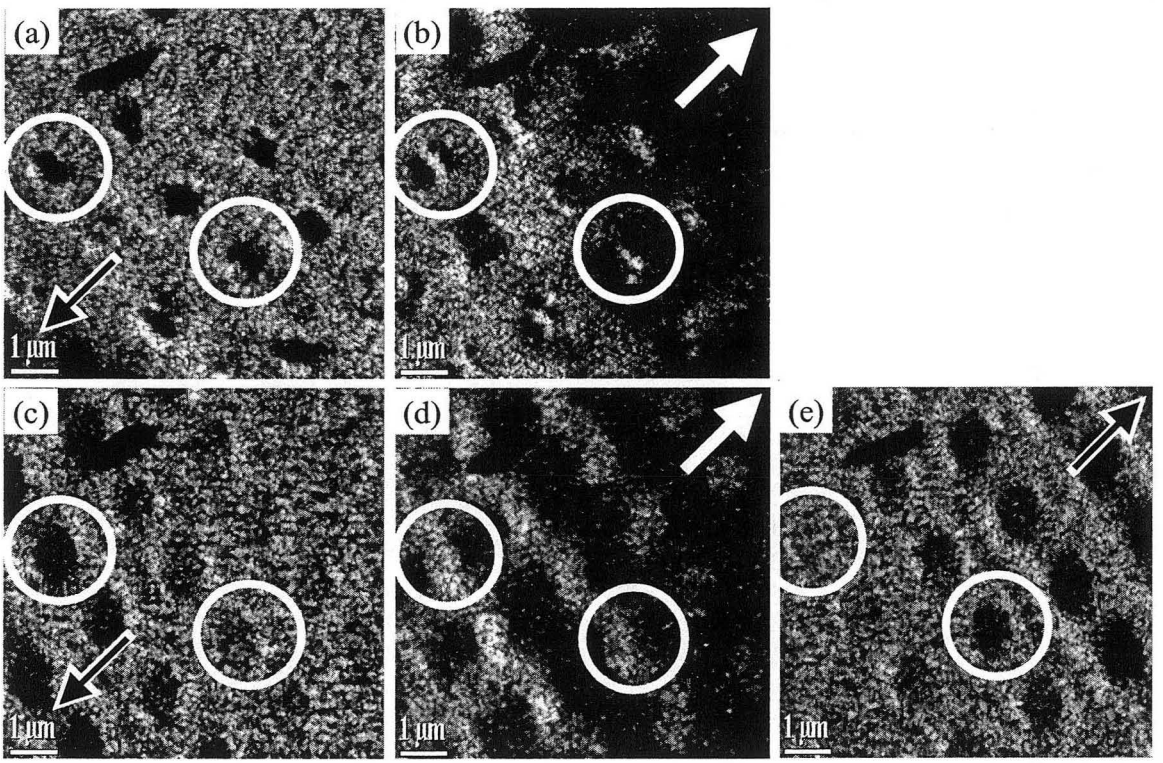

Figure 5–7. Foucault images of the Co/Pt multilayer patterned by ion-irradiation through a stencil mask with a dose of $1 \cdot 10^{16}$ N^{+}/cm^{2}. Arrows show the direction of the beam tilt. Two circles indicate same sample locations. (a) $H_{||} = 0$, +X, (b) $H_{||} = 0$, -X, (c) $H_{||} = -400$ Oe, +X, (d) $H_{||} = -400$ Oe, -X, (e) $H_{||} = +400$ Oe, -X.

5.3.1.2. Magnetic transmission x-ray microscopy (MTXM)

On the other hand, MTXM is sensitive to the out-of-plane component of the magnetization. The basic principles of contrast formation were shown in Figure 2–8. The results of an *ex-situ* magnetization of the sample EG103C6 ($T_g \cong 250°C$, $H_{C\perp}$ = 6.8 kOe, patterned by irradiation with $1 \cdot 10^{16}$ 700 keV N^+/cm^2 through a stencil mask) are discussed first.

To understand the magnetic contrast in such a patterned sample, the MTXM images obtained at remanence after saturation into opposite perpendicular directions are presented in Figure 5–8. The sample imaged at remanence after saturation with $H_\perp$ = +14 kOe showed contrast consistent with the irradiation pattern, as shown in Figure 5–8(a). The non-irradiated matrix had uniform dark contrast and the un-masked irradiated circular regions were brighter—gray. After saturation in the opposite, direction with $H_\perp$ = -14 kOe, the sample showed an opposite contrast, as presented in Figure 5–8(b), which is complementary to the one seen in Figure 5–8(a). The unirradiated matrix was brighter than the gray irradiated regions. The LTEM results, unambiguously showing the irradiated regions to have in-plane magnetization at remanence, were used to interpret these MTXM images. For this reason, the intensity of the gray contrast was assigned to correspond to the in-plane magnetization. Based on this, the dark contrast corresponds to perpendicular up, positive magnetization, and bright contrast to perpendicular down, negative magnetization, in accordance with Figure 2–8. Line profiles obtained from the areas labeled with rectangles in Figure 5–8(a) and (b) are shown in Figure 5–8(c) and (d), respectively. The normalized intensity levels

across the ion-irradiated circles were the same and were equal to the average between that of positive—dark and negative—bright perpendicular magnetization. This confirms the interpretation of the observed contrast.

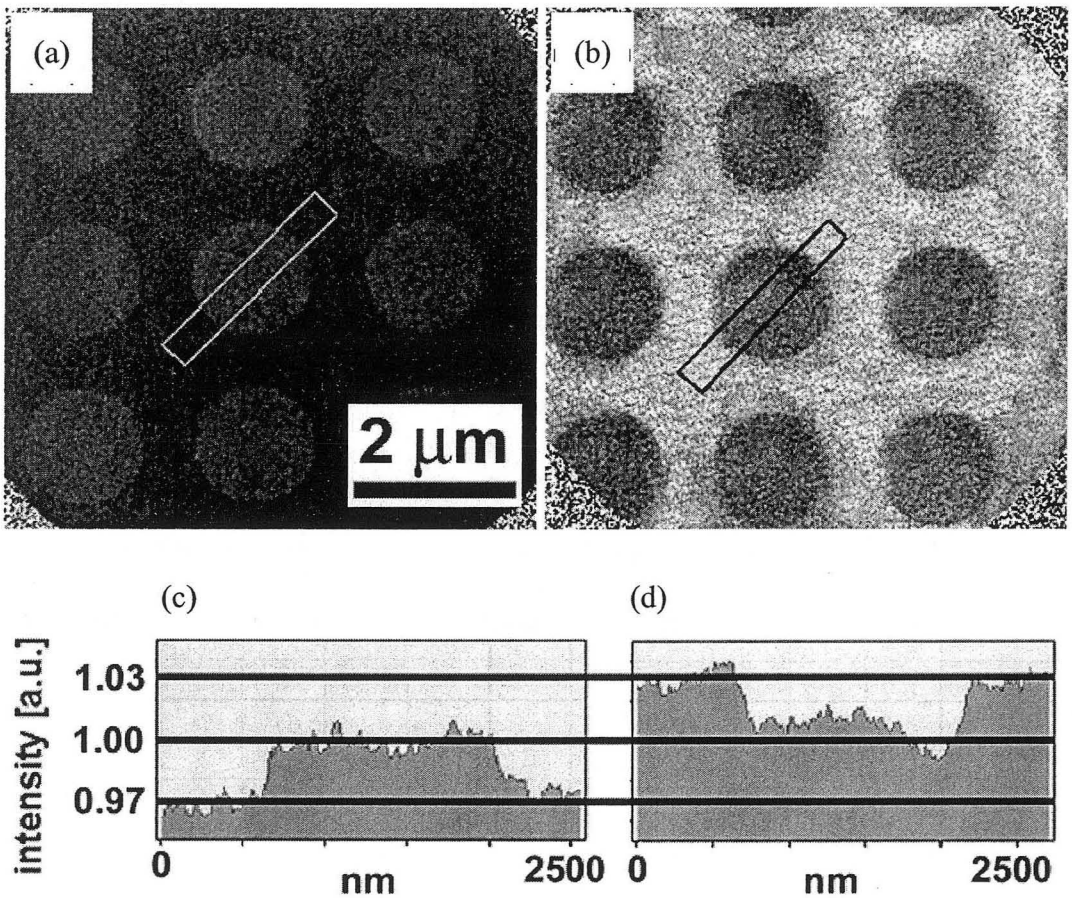

Figure 5–8. MXTM images of the patterned Co/Pt multilayers recorded at the Co L_3 absorption edge. Both images recorded at remanence after saturation with (a) $H_\perp = +14$ kOe, and (b) $H_\perp = -14$ kOe. (c), (d) normalized line profiles obtained from the areas labeled with rectangles on images (a) and (b) respectively.

The Lorentz TEM results discussed in section 5.3.1.1, clearly show that at remanence after perpendicular saturation, the ion-irradiated regions had in-plane

magnetization and, in addition, supported a multi-domain configuration (i.e. different orientations of in-plane magnetization). The MTXM images, however, have no sensitivity to the direction of in-plane magnetization, as shown schematically in Figure 2–8. Hence, all in-plane magnetic domains must show the same intensity and the observed uniform contrast within each irradiated area is expected. Theoretically, however, a black or white contrast of Bloch domain walls, which separate the in-plane domains, should be present. The magnetization in the Bloch wall is normal to the plane of the film and, hence, it is either parallel or anti-parallel to the spin polarization. However, the lack of such contrast on the images in Figure 5–8 is due to resolution and sensitivity limitations of the imaging technique. In fact, Bloch domain walls separating in-plane domains were never resolved using MTXM.

When the same sample location was imaged with photons off the Co absorption edge (for example only 4 eV off the Co L_3 edge), a uniform contrast was recorded. For this case, there is no dichroic contribution to the absorption. This proves that the ion-irradiation patterned samples had uniform thickness and the contrast observed in image Figure 5–8 is only magnetic without any topographic contribution. The absence of thickness variations was also confirmed by TEM investigation.

In order to fully understand the perpendicular reversal process, various *ex-situ* magnetizing experiments were conducted. Each time, the sample was removed from the microscope, magnetized in the external magnet, remounted in the microscope and imaged at remanence. The magnetic field was always applied in a perpendicular direction ($H_{\perp}$) with the magnitudes set between +14 kOe and –

14 kOe. In the first experiment, the successive magnetizing steps were as follows: (1) saturation with $H_\perp$ = +14 kOe, (2) saturation with $H_\perp$ = -14 kOe, (3) application of $H_\perp$ = +1 kOe, (4) application of $H_\perp$ = +2 kOe, (5) application of $H_\perp$ = +2 kOe, (6) application of $H_\perp$ = +3 kOe, (7) application of $H_\perp$ = +4 kOe, (8) application of $H_\perp$ = +5 kOe, (9) application of $H_\perp$ = +6 kOe, (10) application of $H_\perp$ = +6.5 kOe, (11) application of $H_\perp$ = +7 kOe, (12) application of $H_\perp$ = +8 kOe, (13) application of $H_\perp$ = +10 kOe.

A summary of this *ex-situ* magnetizing experiment is shown by a series of images in Figure 5–9. It must be reemphasized that each image was recorded at remanence. Figure 5–9(j) shows the MOKE hysteresis loop of the same sample measured in the as-grown state, before patterning. As shown, the MOKE loop is square, characteristic of PMA with $H^\circ_{N\perp} \cong 4.5$ kOe, $H_{C\perp}$ = 6.8 kOe and $H_S > 10$ kOe. The first image, Figure 5–9(a), recorded at remanence after saturation with $H_\perp$ = -14 kOe, showed perpendicular areas magnetized uniformly along the negative polar direction. In agreement with the hysteresis loop, which showed a magnetic remanence to saturation ratio $M_R/M_S \approx 1$, no dark contrast corresponding to positive-polar magnetization was observed. For this and all consecutive images in Figure 5–9, the irradiated circular regions show gray contrast, consistent with the in-plane magnetization. These areas cannot support perpendicular magnetization and, at remanence, magnetization collapses to in-plane. At remanence, after application of $H_\perp$ = +1 kOe, Figure 5–9(b), initial stages of the nucleation of positive domains were recorded near the edges of the irradiated patterns, as shown by the black contrast.

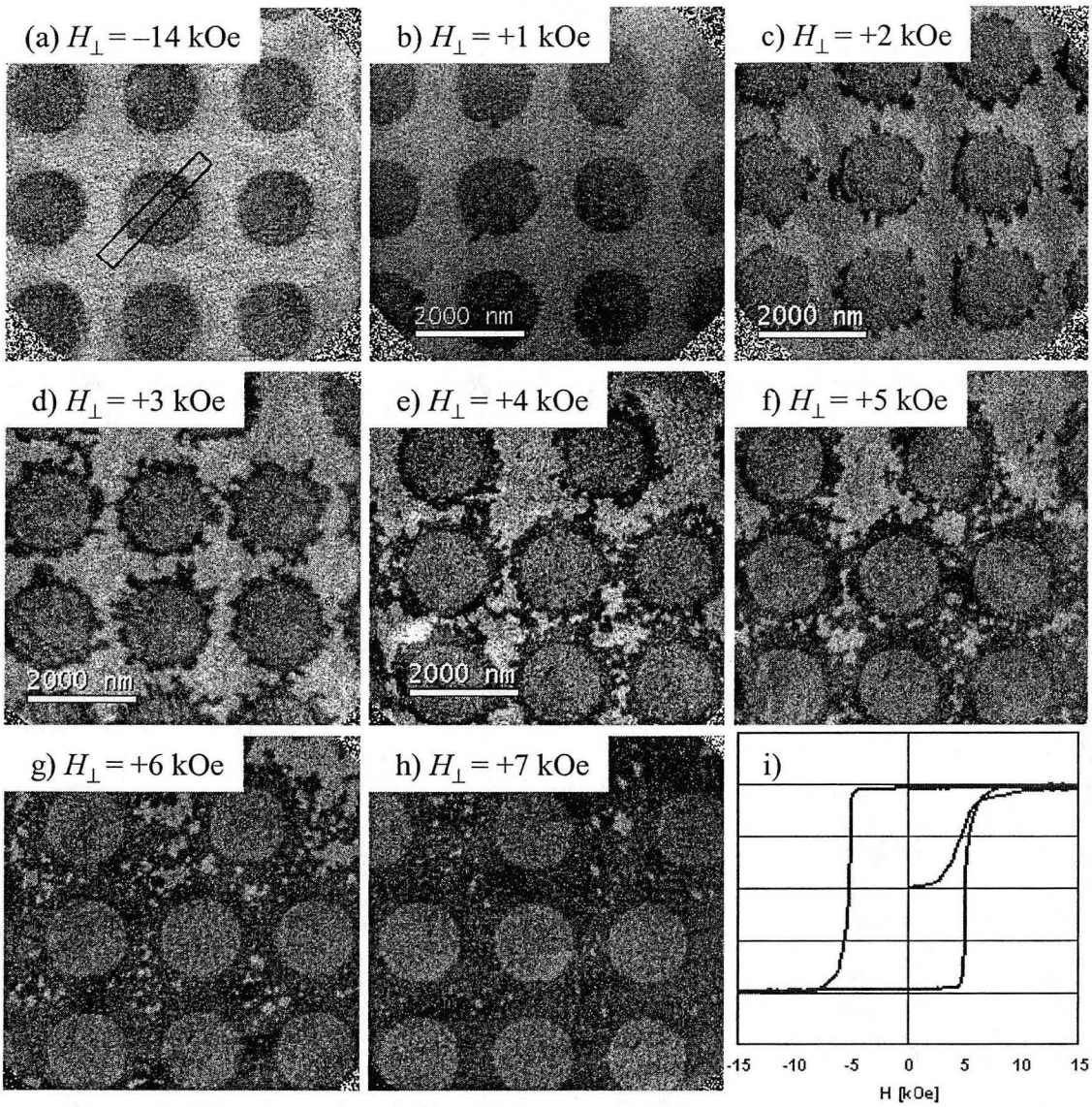

Figure 5–9. MTXM images showing a progress of an *ex-situ* magnetizing experiment. (a) $H_\perp = -14$ kOe, (b) Onset of nucleation at the edges of irradiated patterns, $H_\perp = +1$ kOe (c) $H_\perp = +2$ kOe, (d) $H_\perp = +3$ kOe, (e) $H_\perp = +4$ kOe, (f) $H_\perp = +5$ kOe, (g) $H_\perp = +6$ kOe, (h) $H_\perp = +7$ kOe, (i) Normalized MOKE hysteresis loop of an as-grown Co/Pt multilayer.

These positive—black domains were reversed when $H_{\perp} \leq +1$ kOe was applied, and remained magnetized in the reverse direction at remanence. Referring to the MOKE loop in Figure 5–9(j), this nucleation is well below $H^{\circ}_{N\perp} \cong 4.5$ kOe. When increasingly larger, positive fields were applied [Figure 5–9(c-d), $H_{\perp} = +2$ kOe and +3 kOe] the interface regions reversed first, and a continuous reversed area was observed around the circumference of each circle before the domain wall propagated substantially into the matrix. Moreover, at applied fields up to $H_{\perp} < 4$ kOe, no nucleation of reversed, black domains, isolated from the pattern boundaries was observed. The only black reversed domains were those that nucleated at the irradiation pattern boundaries. The nucleation field within the non-irradiated matrix is larger than the nucleation field at the irradiation boundaries, and also larger than the propagation field into such a matrix. Application of larger fields (Figure 5–9(e), $H_{\perp} = +4$ kOe), resulted in a radial growth of the reversed domains away from the irradiated areas. The propagation of the domain-wall into the unirradiated matrix was characterized by a jagged structure. Only after application of $H_{\perp}$ between +4 kOe and +5 kOe, was nucleation of the reversed black domains away from the edge of the irradiated pattern first observed. This observation is consistent with the nucleation field $H^{\circ}_{N\perp} \cong 4$ to 5 kOe measured from the magnetic hysteresis loop of the as-grown non-patterned film. Figure 5–9(f), recorded at remanence after $H_{\perp} = +5$ kOe was applied, shows a few such isolated reversed domains. These domains were approximately 100 nm in size and, more importantly, they remained pinned after nucleation. This directly shows that the local pinning fields, H_P, are larger than $H^{\circ}_{N\perp}$. At this point, that is at remanence after $H_{\perp} = +5$ kOe was applied, the

domains nucleated at the pattern boundaries extend up to 200 nm away from the pattern edges.

This sequence of images suggests that ion irradiation introduces low-field nucleation centers at the irradiation pattern boundaries. Similar effects, showing low nucleation centers at the irradiation pattern boundaries were observed by Ferre *et.al.* [Ferre - 1999], [Aign - 1998]. In their work, the Pt/Co/Pt sandwich structures were magnetically patterned by ion-irradiation through a resist layer, which was patterned by selective etching directly on the sample surface.

Returning to Figure 5–9, further nucleation events away from the boundaries and growth of all reversed domains were observed above $H_{\perp}$ = +5 kOe. At $H_{\perp}$ = +7 kOe, which was higher than the coercive field of the non-irradiated sample ($H_{C\perp}$ = 6.8 kOe), the majority of the matrix was reversed; however, small unreversed, bright areas were still observed, as shown in Figure 5–9(h). The importance of this image is that it shows the size and distribution of the magnetically hardest regions, which contribute to the tail of the magnetization loop. In agreement with the magnetic measurements, fields of +10 kOe were necessary to fully saturate the matrix.

Figure 5–10 shows images of larger areas recorded during the same reversal sequence. The roughness of the observed black domains is suggestive of microstructure-governed perpendicular reversal. It is postulated that the motion of domain walls is hindered by the columnar boundaries. To verify this, a series of magnetizing experiments were conducted.

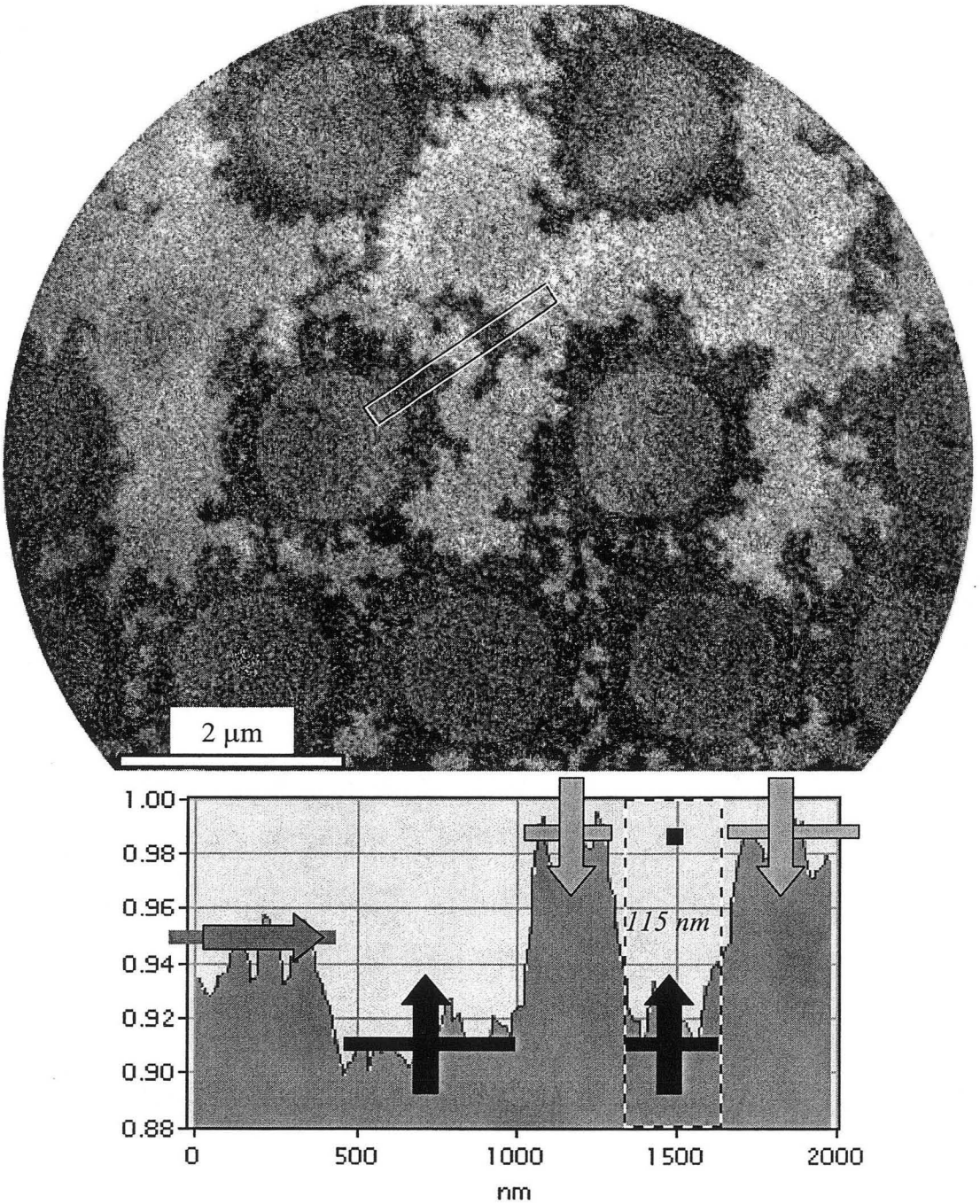

Figure 5–10. Larger area MTXM images showing tree-like rough growth. Image recorded after saturation at $H_{\perp}$ = -14 kOe and subsequent application of $H_{\perp}$ = +5 kOe to nucleate black domains. A normalized line profile is obtained from the area labeled with the rectangle.

In the first experiment, the sample was saturated in a positive or negative direction and subsequently an opposite field of 4 kOe was applied to nucleate reversed domains at the irradiation boundaries. Two images of the same sample location collected after (1) saturation with $H_{\perp}$ = -14 kOe followed by application of a reversed field $H_{\perp}$ = +4 kOe, and (2) saturation with $H_{\perp}$ = +14 kOe and application of $H_{\perp}$ = -4 kOe, are shown in Figure 5–11. These images show exactly complementary contrast. The extent of the reversed domains, black areas in Figure 5–11(a) and white areas in Figure 5–11(b), is identical. The reversed domains are pinned in exactly the same locations, indicating a return point memory. This provides clear evidence that the magnetic reversal in these Co/Pt multilayers is not random but is governed by the under-lying physical microstructure and interactions at mask interfaces.

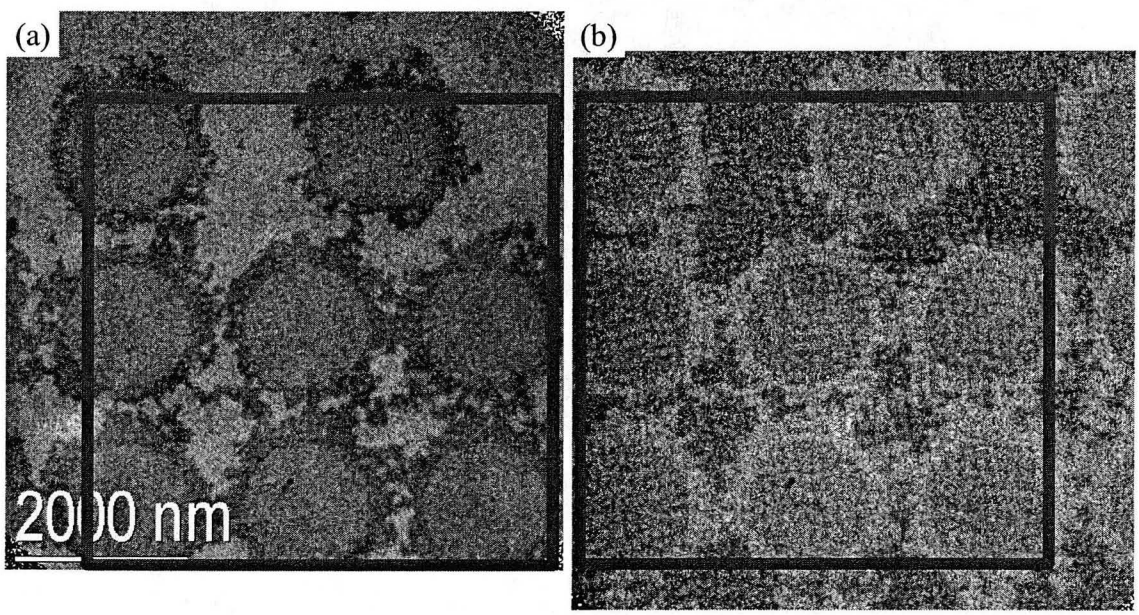

Figure 5–11. Same location and opposite contrast. (a) $H_{\perp}$ = -14 kOe and $H_{\perp}$ = +4 kOe (b) $H_{\perp}$ = +14 kOe and $H_{\perp}$ = -4 kOe.

A magnetic image, recorded at remanence (after $H_{\perp}$= -14 kOe then $H_{\perp}$ = +4 kOe), superimposed on the TEM image, which shows the physical microstructure at the same magnification, is displayed in Figure 5–12. The length scale associated with the roughness of the reversed domains is clearly comparable with the physical dimensions of the columnar grains. This suggests that the microstructure and, in particular, the columnar grain size influences the domain-wall pinning and the reversal processes [Weller - 2001], consistent with theoretical modeling of Lemerle et al. for Pt/Co/Pt sandwich-like structures [Lemerle - 1998].

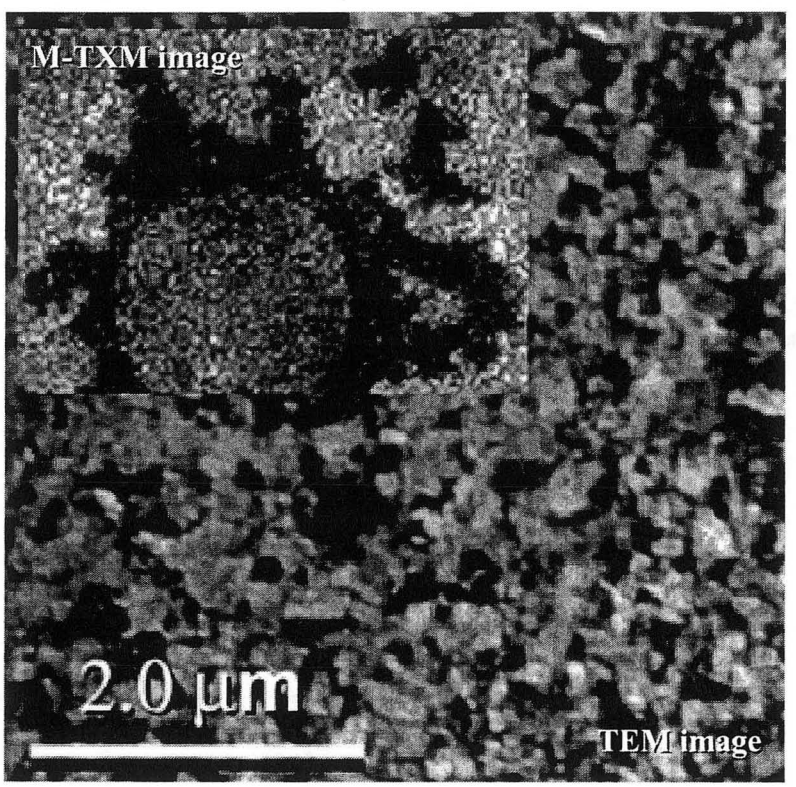

Figure 5–12. MTXM image, showing magnetic reversal, superimposed onto the TEM image, detailing the microstructure. Both images are shown at the same magnification.

The main characteristic of perpendicular reversal in such ion-beam patterned multilayers is the presence of the low nucleation centers at the irradiation pattern boundaries. The series of images presented in Figure 5–9 clearly showed that magnetic reversal always starts at the pattern boundaries; *however, the pinning fields, H_p, of the non-irradiated matrix are not affected.*

Figure 5–13 shows an image recorded at remanence after the following magnetizing sequence: 1) saturation with $H_\perp$ = +14 kOe then 2) application of $H_\perp$ = -5 kOe followed by 3) application of $H_\perp$ = +3 kOe. As shown, a double ring of reversed white and black domains around the irradiation patterns was recorded. The progress of this magnetic process is illustrated schematically in the same figure. After the first step, the matrix was uniformly magnetized up as shown by the black contrast. When –5 kOe was applied, step 2, down—white domains nucleated at the patterns boundaries and propagated outwards, approximately 350 nm into the matrix. Since the growth of the reversed domains is not exactly radial but rather rough in some areas, the reversed domain extended further. When the field was reversed again, but only to +3 kOe (step 3), new up—black domains were nucleated at the pattern boundaries. These black domains propagated outwards and partially consumed the previously nucleated white domains. However, the new black domains extend only up to approximately 180 nm away from the boundary. The previously nucleated white domains are still present between approximately 180 nm and 350 nm away from the boundary. This magnetizing experiment confirms that the nucleation of reversed domains always starts at the pattern boundaries, as shown by the double rings of black and white domains, and proceeds outwards. The extent of the reversed domains is

consistent with values measured on images (d) and (f) shown in Figure 5–9. What, however, is very important to note from Figure 5–13 is that after step 3, the domain walls between the original black matrix and the white domains are pinned at the same location as they were after step 2, (i.e. ~ 350 nm). The pinning strength at that location is higher than the field applied during step 3, which was 3 kOe. The reversal process is limited by the pinning strength, as the existing domains did not move. During the irradiation patterning process, both the pinning strength and the coercivity are decreased in the vicinity of the irradiation boundary. The fields H_C and H_P increase gradually from the lowest value at the irradiation boundaries up to the original values of the as-grown samples away from the boundary.

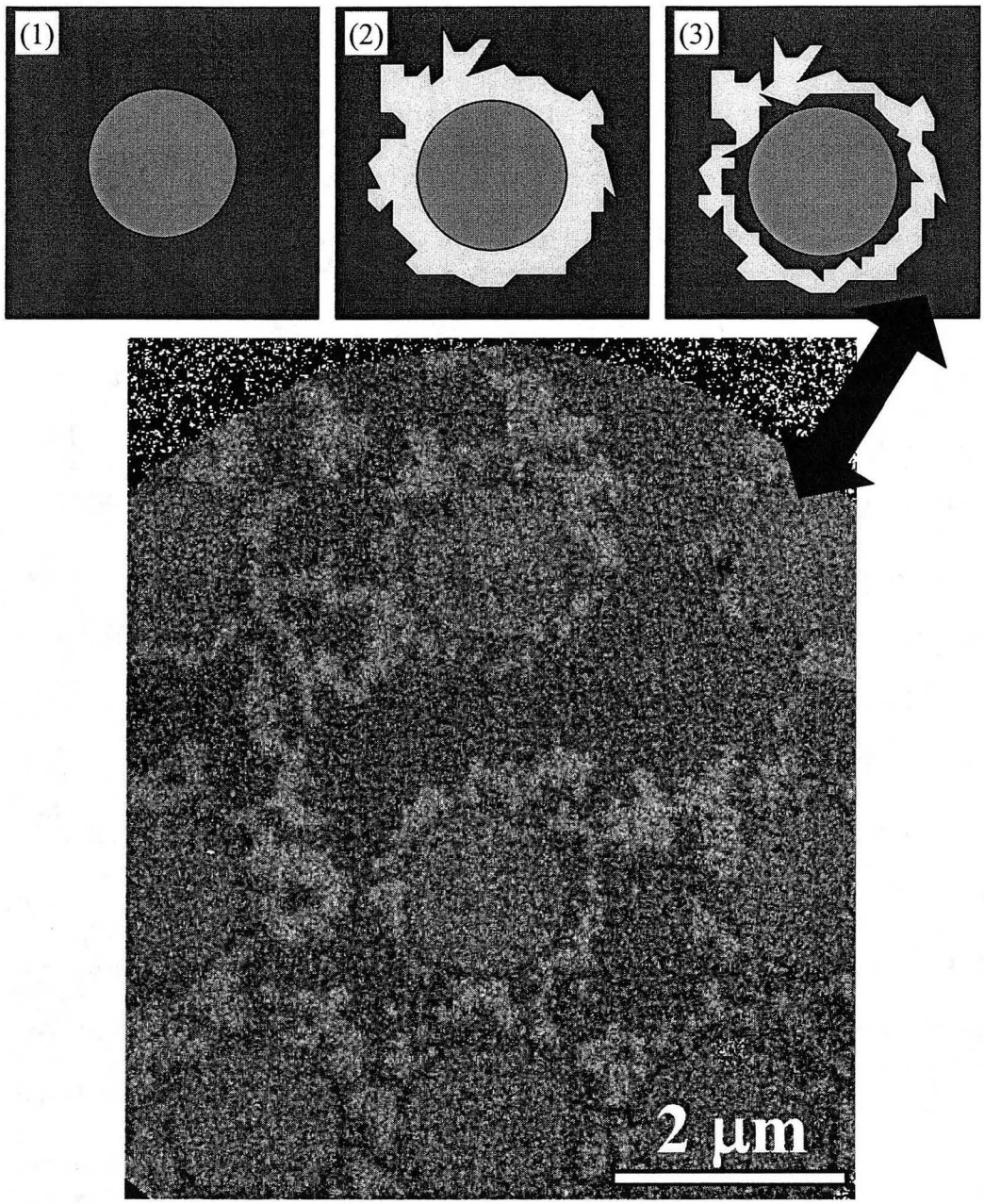

Figure 5–13. MTXM image recorded at remanence after a following magnetizing sequence: (1) saturation with $H_{\perp}$ = +14 kOe, (2) application of $H_{\perp}$ = -5 kOe, (3) application of $H_{\perp}$ = +3 kOe. Schematic shows the domain evolution during these three magnetizing steps.

To further elucidate the information about details of the reversal process, *in-situ* magnetizing experiments were conducted.

The progress of the *in-situ* magnetizing experiment of the sample patterned by ion-irradiation through the stencil mask with a dose of $1 \cdot 10^{16}$ N^+/cm^2 is presented in Figure 5–14 [i]. Before starting, the sample was saturated with +14 kOe field. When imaged at remanence, the sample had a uniform black—up magnetized matrix and a gray irradiated disk indicating in-plane magnetization, as was shown in Figure 5–8(a). When $H_\perp$ = -3 kOe was applied, rotation of the magnetization in the irradiated regions and reversal of the adjacent areas was observed first, as shown by image Figure 5–14(a). Note that the contrast associated with reversed irregular white domains is the same as for the irradiated regions. Only two levels of photon intensity were measured, black and white, corresponding to up and down domains, respectively. The intermediate gray level, corresponding to in-plane domains, is not present. When the perpendicular field was turned off and an image was recorded at remanence, again three levels of photon intensity were measured, as shown in Figure 5–14(b). The magnetization in the ion-irradiated regions collapsed to in-plane, which is seen as gray contrast. When $H_\perp$ = +3 kOe was applied, Figure 5–14(c), the entire sample had black contrast, indicating a uniform up magnetization except for small white—negative,

---

[i] The quality of the MTXM images shown in Figure 5–14 is not as good as for images presented in the previous section for the *ex-situ* experiments. The overall contrast is lower. This is due to decreased acquisition time, which increases photon noise and makes it unfortunately comparable with the magnetic signal. The background correction is also compromised resulting in non uniform background intensity.

unreversed areas. Then, when the perpendicular field was reduced to zero, the ion-irradiated regions again collapsed to in-plane, which is seen as gray contrast in Figure 5–14(d).

The sequence clearly shows that the reversal process in not precisely associated with the irradiation boundary alone. The reversal starts by rotation of the in-plane regions and subsequent propagation of magnetic domains into the perpendicular matrix.

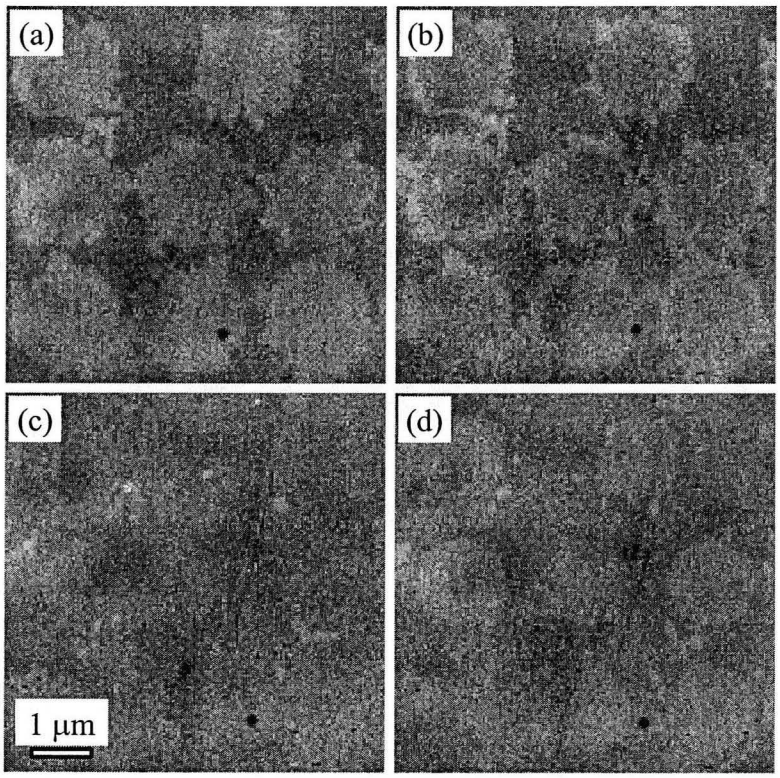

Figure 5–14. Progress of the in-situ magnetizing experiment. Images were acquired with the applied magnetic field. (a) $H_{\perp}$ = -3 kOe, (b) $H_{\perp}$ = 0, (c) $H_{\perp}$ = +3 kOe and (d) $H_{\perp}$ = 0.

Figure 5–15 schematically illustrates this process. As increasingly larger reverse, down fields are applied, the magnetization of the irradiated regions is

rotated. At some point, in step 3 in the schematic, before the irradiation regions are completely aligned with the applied field, the down magnetization extends into the non-irradiated matrix. With further increase in the downward field, both the rotation of the in-plane magnetization continues and the grown of the down domains occurs. At a certain field, as show in step 5, the irradiated regions are completely rotated and have the same contrast as the reversed down regions. However, when the field is removed, the irradiated regions collapse back to in-plane, but the newly reversed down regions remain, as shown in step #.

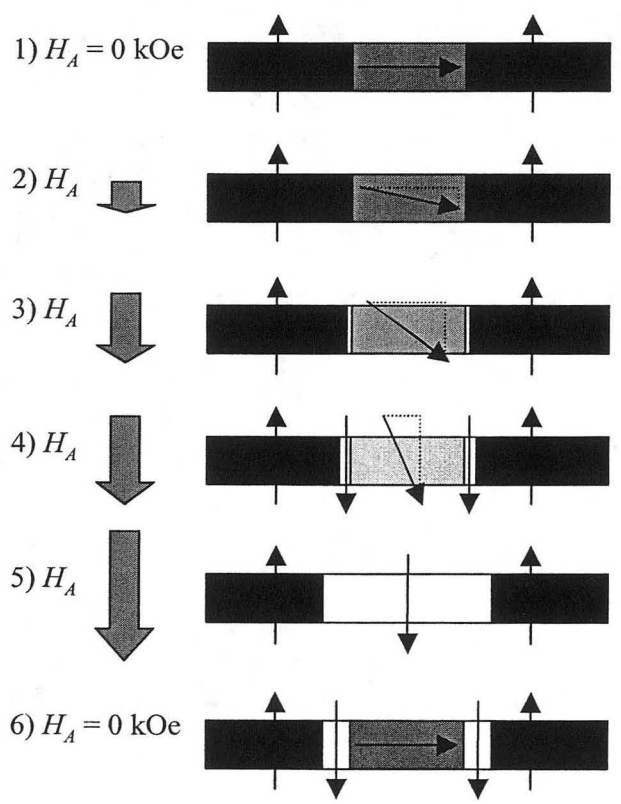

Figure 5–15. Schematic of the reversal process in the ion-irradiation patterned Co/Pt multilayers. Sample colors indicate the orientation of magnetization: black – up, white – down, gray – in-plane. Large arrows show magnitude and direction of the applied field H_A.

5.3.2. Sample # II, mask $1 \cdot 10^{16}$ and plain $5 \cdot 10^{14}$ 700 keV N^+/cm^2

As discussed previously, the largest field, which can be applied *in-situ* during MTXM imaging is limited to 3 kOe. To observe a full reversal process, sample #I was additionally irradiated with a uniform dose of $\sim 5 \cdot 10^{14}$ 700 keV N^+/cm^2 to soften the matrix by reducing H_C. The results of the experiment are summarized in Figure 5–16. As expected, the reversal of the perpendicular matrix was found to start at the irradiation pattern boundaries, as it did in sample #I. However, nucleation away from the pattern boundaries started at a much lower field as compared to sample #I. This field was lower both in absolute value and relative to the nucleation field at the pattern boundaries. Also, at such fields the domains nucleated at the pattern boundaries propagated shorter distances as compared with sample #I.

In the case of sample #I, reversal was dominated by the growth of domains, which nucleated/reversed at the irradiation boundaries. For sample #II, the irradiation boundaries were still significant, but their overall contribution was reduced. Ion irradiation reduced H_N and H_P of the matrix, bringing them closer to the respective values in the vicinity of the irradiation boundary.

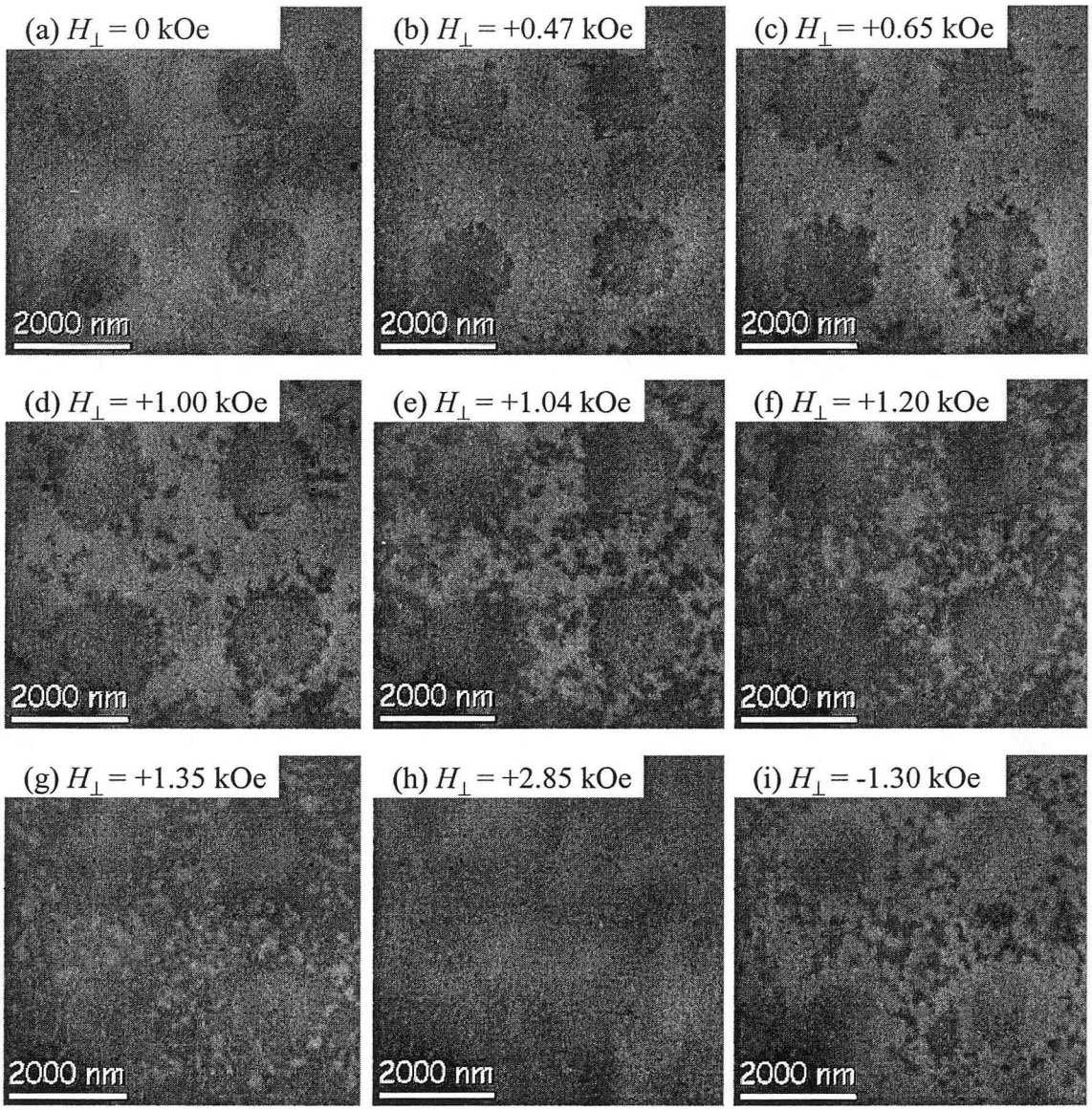

Figure 5–16. Sample #II, progress of an *in-situ* MTXM experiment. (a) $H_\perp = 0$, (b) $H_\perp = +0.47$ kOe, (c) $H_\perp = +0.67$ kOe, (d) $H_\perp = +1.00$ kOe, (e) $H_\perp = +1.04$ kOe, (f) $H_\perp = +1.20$ kOe, (g) $H_\perp = +1.35$ kOe, (h) $H_\perp = +2.85$ kOe and (i) $H_\perp = -1.30$ kOe.

5.3.3. Sample # III, mask $5 \cdot 10^{14}$ and plain $5 \cdot 10^{14}$ 700 keV N^+/cm^2

Patterning by ion-irradiation was first done by Ferre et. al. [Ferre - 1999], [Aign - 1998] in Pt/Co/Pt sandwich structures. Perpendicular reversal was observed to nucleate in the vicinity of the irradiation boundary. Later, Devolder [Devolder - 2000b], [Devolder - 2000a] postulated that this phenomenon is associated with radiation over-shoot at the pattern boundary due to ion scattering at the mask edges. Increased doses of ions at the irradiation boundaries make these areas magnetically softest and, hence, nucleation always starts there.

To determine whether the nucleation at the irradiation boundaries is due to irradiation over-shoot or due to rotation of in-plane areas, as outlined in Figure 5–15, a different pattern was prepared. First the entire sample was irradiated with a dose of $5 \cdot 10^{14}$ N^+/cm^2 to reduce the coercivity of the matrix from $H^\circ_C = 6.8$ kOe to below 3 kOe. In the next step the Si stencil mask was used and a second dose of $5 \cdot 10^{14}$ N^+/cm^2 was selectively applied. Such irradiation produced a pattern where the entire sample had perpendicular anisotropy but locally different coercivity, as shown schematically in Figure 5–17(a). The magnetically softer region will be referred to as A, and the harder one as B.

Figure 5–17 shows a series of MTXM images recorded during the *in-situ* reversal process. Figure 5–17(b) is an image recorded at $H_\perp = -2.6$ kOe. This field was strong enough to saturate the sample. Uniform white contrast was recorded in both areas A and B. The next images show progress of reversal into a positive—dark direction. When the reversed field $H_\perp = +0.65$ kOe, Figure 5–17(c), was applied, the double-dose region A was almost completely reversed. At this

field, small reversed domains were also recorded within region B. However, it is interesting to note that in this case, the reversed domains did not nucleate at the boundary between A and B and then propagate into region B. Nucleation of small black—positive domains was observed throughout region B. When increasingly larger fields were applied, $H_{\perp}$ = +0.85 kOe, Figure 5–17(d) and $H_{\perp}$ = +1.2 kOe, Figure 5–17(e), further growth and nucleation of black domains within region B was recorded. Finally, $H_{\perp}$ = +1.5 kOe, Figure 5–17(f), was strong enough to saturate the entire sample. A uniform black contrast was recorded in both areas A and B.

This experiment suggests that the previously discussed nucleation at the irradiation pattern boundary is only relevant for in-plane/out-of-plane cases.

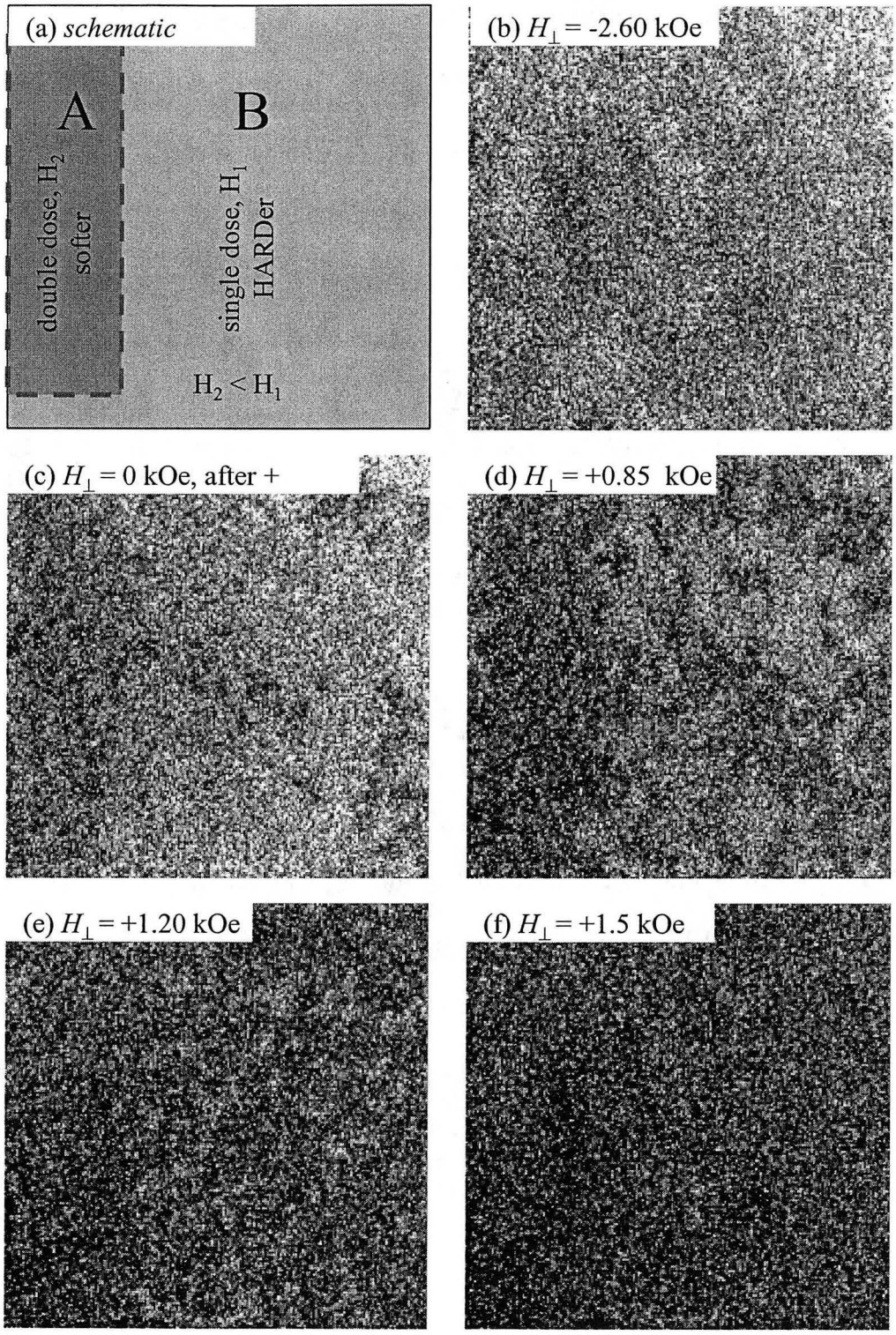

Figure 5–17. Sample #III, progress of an *in-situ* MTXM experiment.

5.3.4. Focused ion-beam patterning

In this section, results from focused ion-beam patterning (FIB) of Co/Pt ML's are summarized. Selected patterns are discussed to illustrate that ion beams can be used to pattern magnetic domains down to 40 nm (or perhaps lower, but data interpretation is compromised by magnetic imaging resolution). As for stencil-mask irradiation, the reversal processes are shown to originate at the irradiation pattern boundaries.

For comparison, the pattern prepared by irradiation through a stencil mask and the FIB patterns, detailed in Table 5–2, are displayed at the same magnification in Figure 5–18. These images show:

- Figure 5–18(a) sample #I with 1.3 μm in-plane regions patterned by irradiation through the stencil mask.
- Figure 5–18(b) sample FIB#1 with 140 nm in-plane lines defining 310 nm squares with PMA;
- Figure 5–18(c) sample FIB#2 with 80 nm × 320 nm in-plane rectangles;
- Figure 5–18(d) sample FIB#3 with 100nm in-plane squares; and
- Figure 5–18(e) sample FIB#4 with 40 nm in-plane lines defining 100 nm squares with PMA.

Referring back to Chapter 3, the grain size in the discussed multilayers was approximately 50 – 100 nm. Hence, pattering across individual grains was obtained in all cases.

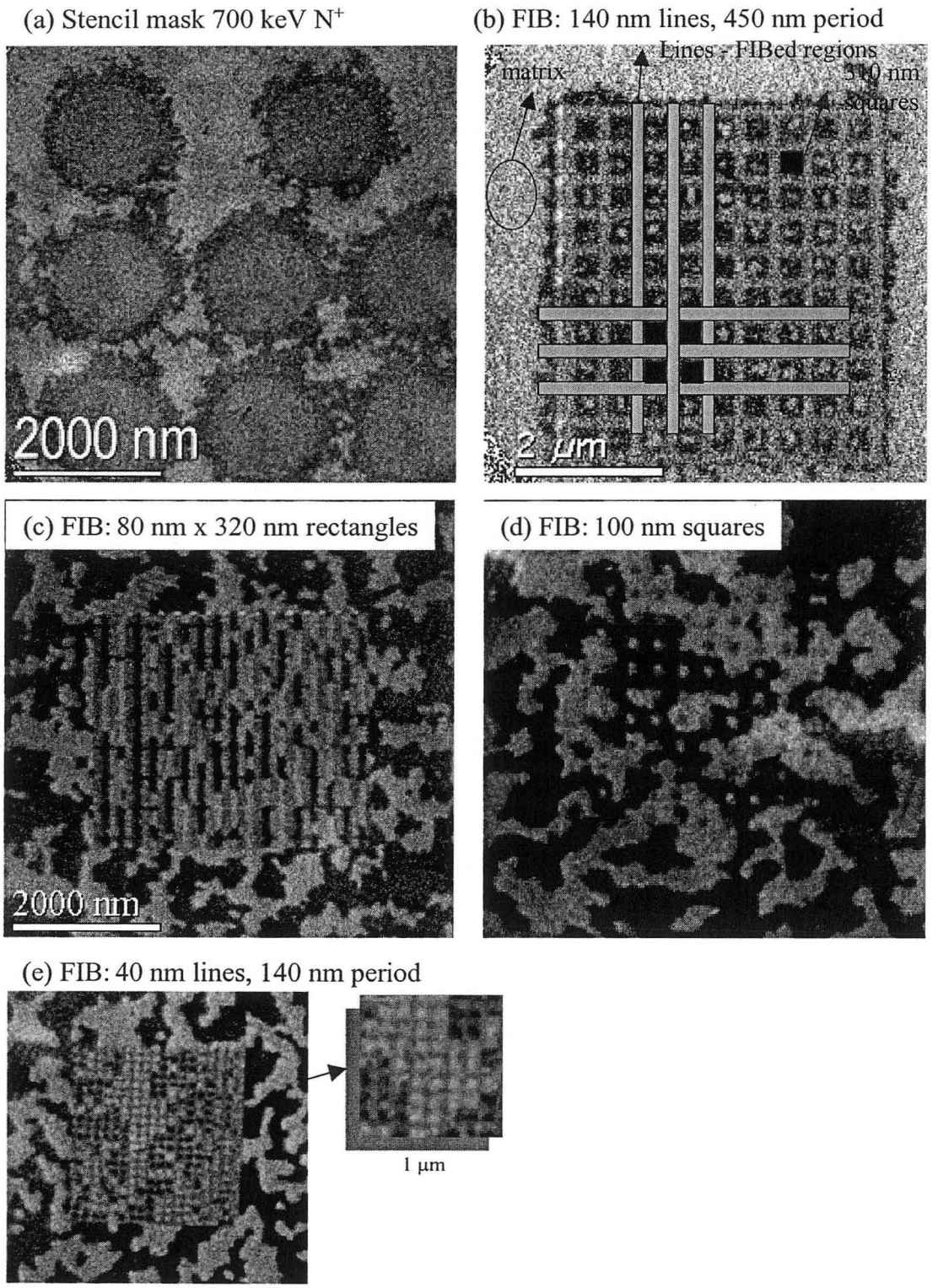

Figure 5–18. Comparison of the stencil mask patterns with the FIB patterns. All images are displayed at same magnification, except for insert in (e). See text for details.

5.3.4.1. Pattern FIB# 1

Figure 5–19 shows four patterns prepared by identical FIB raster, except for the dose of the 30 keV Ga^+ ions. Sets of 140 nm wide, orthogonal lines were written with FIB to create 310 nm square bits. For all patterns, the ion fluence was sufficient to give in-plane magnetization in the FIBed lines. The patterning features are very precise and regular (perfectly straight magnetic lines, 90° corners). Interestingly, the in-plane lines have same widths, which are equal to the width of the irradiation pattern regardless of the ion dose. This implies that the irradiation profile is very sharp. As shown, very small features can be written. Clearly, the under-laying microstructure does not affect the profile of the SRT. The patterning process is shown to be capable of defining very small features, with straight edges, much better than the grain boundary roughness.

The images in Figure 5–19 were recorded at remanence after saturation with –14 kOe and application of +3 kOe to nucleate black domains. (For reference, the coercivity of the as-grown sample is 6.8 kOe.) The reversal extends further into the non-irradiated squares for patterns where the irradiation dose on the line was highest. For all doses, the perpendicular magnetic reversal was found to start at the FIB boundary and propagate gradually outward toward the center of the squares. When the lines were exposed to higher fluences, the same degree of magnetic reversal was found at lower fields. As shown, the lines are gray, the edges of the squares are black (indicating reversed areas) and the centers of the squares and the matrix are white. This effect is believed to be associated with the tails of the FIB profile. The fluence of the FIB-tail is not sufficient to cause SRT

but it reduces the perpendicular coercivity. With increasing ion dose on the line, the dose in the FIB-tail increases, making the adjacent areas softer. The images presented show that the individual 310 nm squares support a multi-domain configuration.

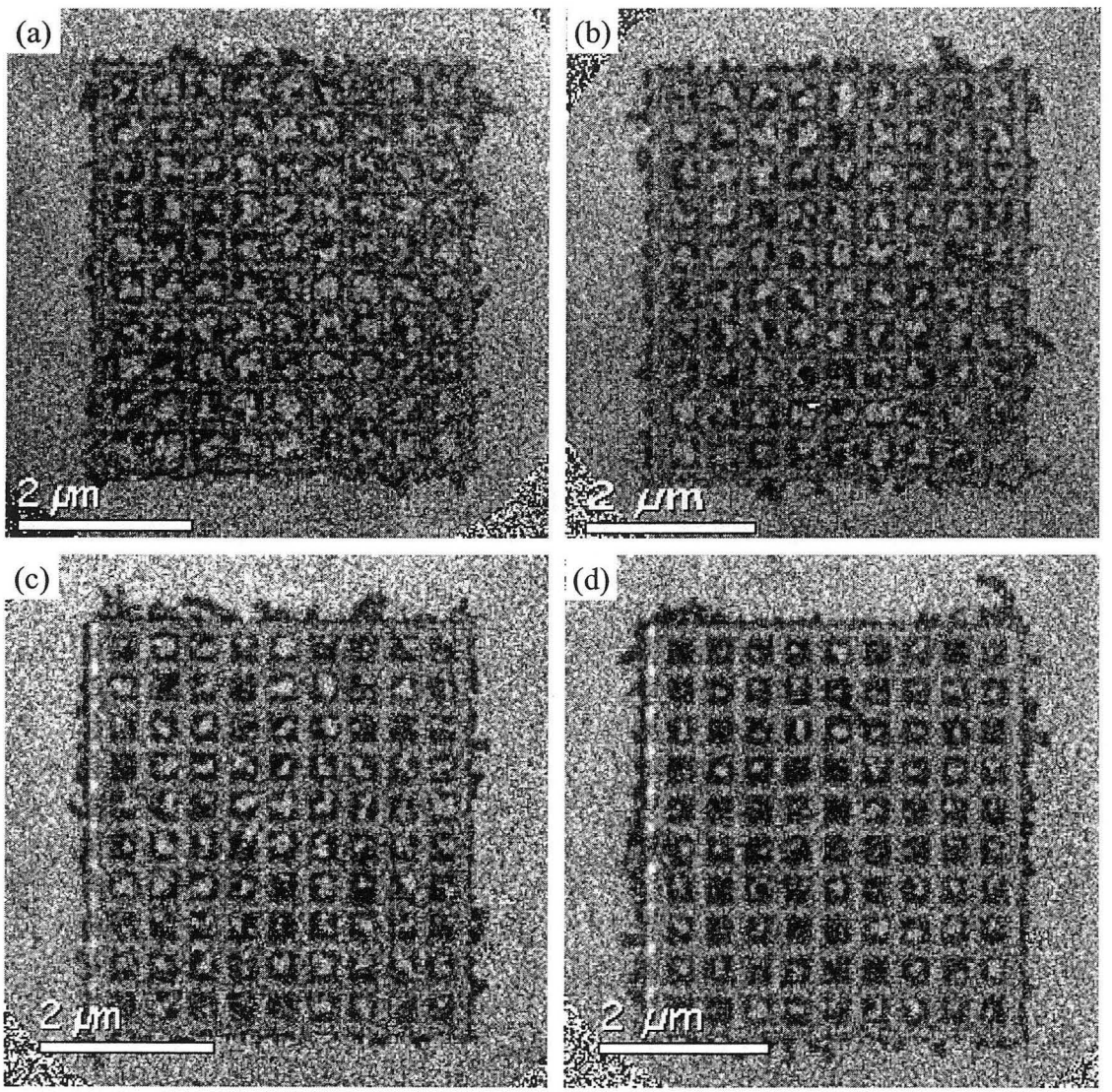

Figure 5–19. MTXM images of pattern FIB#1 with a period of 450 nm for different doses of 1 pA 30 keV Ga^+ beam. The exposures were (a) 3 s, (b) 6 s, (c) 12 s and (d) 14 s. Images were recorded after 1)-14 kOe and then 2) +3 kOe.

5.3.4.2. Pattern FIB# 2

This sample is used to illustrate that the reversal process in the FIB-patterned samples is governed by the irradiation boundaries, similar to the samples irradiated through the stencil mask. Figure 5–20 shows a series of MTXM images recorded during the *in-situ* reversal process. The starting image, Figure 5–20(a), shows the sample at $H_{\perp}$ = +2.8 kOe. The field was not strong enough to saturate the sample and small white—down domains were still present. When the field was turned off, Figure 5–20(b), the irradiation pattern was observed. The ion-irradiated regions collapsed to in-plane, which is seen as a gray contrast. The next images show progress of reversal into a negative-white direction. At $H_{\perp}$ = -1.0 kOe, Figure 5–20(c), no noticeable growth of the white domains was seen in images (a) and (b). However, the gray irradiated region appears to be slightly wider and brighter, indicating partial rotation from in-plane to negative—white perpendicular direction (recall the schematic in Figure 5–15, steps #3 and #4. At $H_{\perp}$ = -2.1 kOe, Figure 5–20(d), the irradiated rectangular regions were fully down—white, while the other white domains remained pinned and did not grow. This indicates that for this particular sample, the H_P of the matrix is higher than the field required to rotate the in-plane areas. When a larger field was applied, $H_{\perp}$ = -2.6 kOe, Figure 5–20(e), growth of all white domains was recorded. Finally, when the field was turned off, Figure 5–20(f), gray in-plane contrast in the irradiated regions was seen again. However, except for the rectangles, the size of the white domains was the same as on image (e).

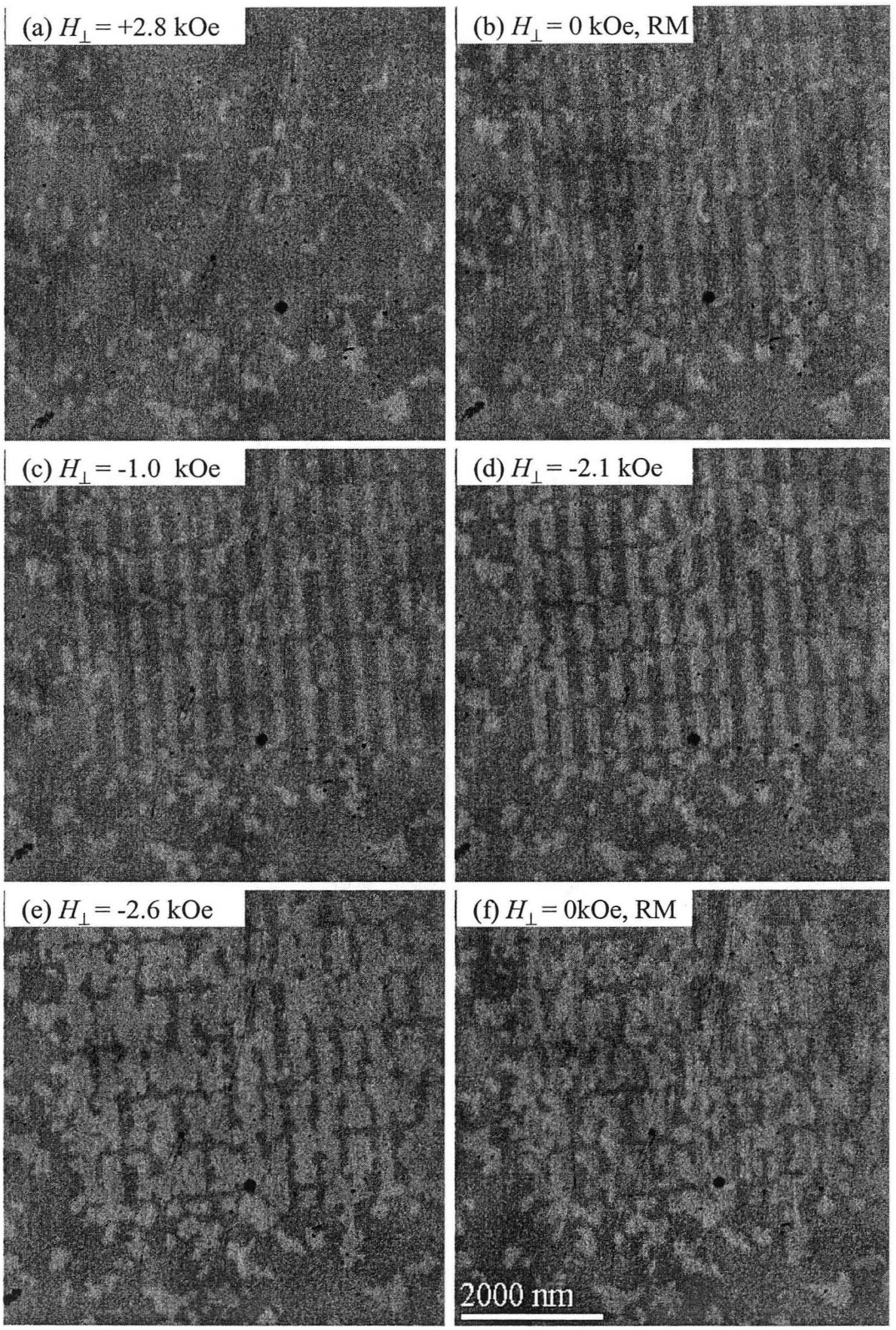

Figure 5–20. Sample FIB#2, progress of an *in-situ* MTXM experiment.

5.4. Summary

In summary, the unique combination of LTEM and MTXM made it possible to image the three-dimensional magnetization structure of the patterned film. For stencil mask irradiation, the boundaries of the patterns, defined by the transition from out-of-plane to in-plane magnetization, were found to be determined by the mask, while the scale of the magnetic reversal was governed by the microstructure. LTEM imaging of the patterns confirmed the irradiated regions to have in-plane easy axis of magnetization. Moreover, these regions were magnetically soft, saturating at or below $H_{||} \cong 300$ Oe. Reversal in the non-irradiated matrix, exhibiting perpendicular anisotropy, was by nucleation of reversed domains at the pattern boundaries followed by domain wall motion into the non-irradiated region. These nucleation fields, $H_{N\perp} = 1$ kOe, were significantly lower than nucleation fields for the as-grown film $H^{\circ}_{N\perp} \cong 4$ to 5 kOe. *In-situ* data showed that the perpendicular reversal process starts by rotation of the in-plane regions, followed by propagation into the matrix.

FIB pattering was used to create features down to and below 100 nm periodicities. Bit patterns with large 300 nm islands were found to support more than one domain. For smaller 100 nm patterns, single-domain bits were recorded. Similar to patterning through the mask, perpendicular reversal was found to start at the ion irradiation boundaries.

Ion irradiation is a new technique for patterning magnetic properties without changing the planarity of the sample. Patterned magnetic media with a feature size below 30 nm can be fabricated.

Chapter 6.

SPIN REORIENTATION STUDIES IN C-AXIS ORIENTED CO-CR FILMS

6.1. Introduction

This Chapter moves away from the Co/Pt system discussed so far and summarizes domain investigations in c-axis Co thin films.

As discussed in the background section, one of the ways to obtain Co thin films with perpendicular magnetic anisotropy is to utilize magnetocrystalline anisotropy to overcome the magnetostatic demagnetization energy. For hexagonally close-packed (*hcp*) Co, the c-axis, is the easy direction of magnetization.[i] Hence, c-axis growth is desirable for obtaining Co films with perpendicular anisotropy.

---

[i] Note that in the case of *hcp* Co thin films the magnetocrystalline anisotropy could have positive or negative sign depending on the orientation of the c-axis. (positive for c-axis growth).

6.2. C-axis oriented Co-based thin films

Krishnan *et al.* [Krishnan - 1994] investigated the feasibility of MgO(001), NaCl(001), GaAs(001) and cleaved mica (0001) substrates for growth of c-axis oriented Co films, utilizing Ti or Ru under-layers. For MgO(001), not surprisingly, only in-plane epitaxy was achievable and for NaCl(100) weak c-axis growth was observed. For the case of mica (0001), where *hcp* geometry was utilized, highly c-axis oriented growth of both Ru and Co was possible. However, due to high cost, this growth system is not practical for industrial applications.

In this research, a new method for achieving highly oriented perpendicular Co-alloy films by utilizing epitaxial growth on <111> oriented single crystal Si substrates, was developed. Enormous effort has been applied to the growth of Si single-crystals because of their importance in the semiconductor industry and, as result, these substrates are readily available at low cost.

Epitaxy implies that the crystallographic order of the thin film is significantly influenced by that of the substrate as a result of lattice parameter matching along the film-substrate interface. When the film is deposited on a single-crystal substrate, the interface energy, γ_i, is minimized in an attempt to minimize the overall energy of the system. Any interruption of crystal symmetry across the interface increases the potential energy of the system. The symmetries of the two crystals are merged by maximizing the density of bonds with appropriate length and angles across the interface. For this reason, epitaxial growth is readily achievable for a thin film—substrate combination having some degree of lattice parameter matching. The temperature of deposition must be high

enough to allow the depositing atoms to rearrange themselves into equilibrium positions before subsequent burial by incoming atoms.

The feasibility of epitaxial growth is measured by the fractional mismatch parameter, *f*, which assesses the difference in the atomic parameters across the interface, and is given by:

$$f = \frac{(a_f - a_s)}{(a_f + a_s)/2} \approx \frac{(a_f - a_s)}{a_s} \qquad \text{Eq. 6–1}$$

where a_f and a_s are the atomic spacings along some specific crystallographic direction in the film and the substrate respectively [Smith - 1995]. In general, to obtain epitaxial growth, the fractional mismatch must be

$$f \leq 0.1. \qquad \text{Eq. 6–2}$$

For larger misfit, too few interfacial bonds are well enough aligned to achieve reduction in the interfacial energy due to epitaxy. When the fractional mismatch is below 0.2, highly textured growth is attainable.

The lattice parameters of Si and Co are listed in Table 6–1. As calculated, the lattice mismatch between Co and Si atoms along the close-pack planes is above 50%. Based on the condition given in Eq. 6–2, epitaxial growth of c-axis Co on Si(111) is not possible. In order to minimize the lattice mismatch between Si(111) and Co(0001) planes, *fcc* Ag was utilized as a buffer-layer. The mismatch is still substantial and strict epitaxy was not expected. Figure 6–1 shows the lattice planes and the architecture of the discussed structure.

Figure 6–2 shows a binary Co-Cr phase diagram [Massalski - 1990].

Table 6–1. Lattice parameters and lattice misfit for Si, Ag and Co films.

	a (Å)	c (Å)	(111) (Å)	Lattice mismatch *f* from Eq. 6–1
Si	5.43		3.84	Si & Co = 0.53
Ag	4.09		2.89	Si & Ag = 0.34
Co	2.507	4.069	2.507	Ag &Co = 0.15

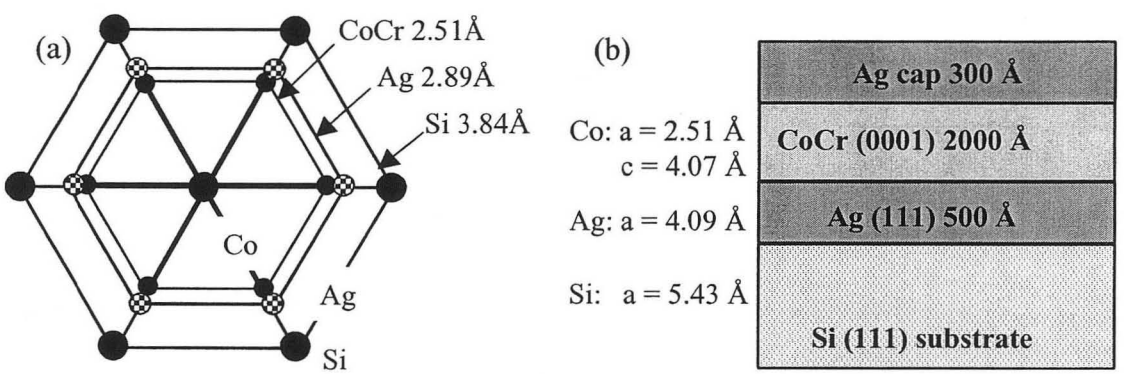

Figure 6–1. (a) Schematic drawing of the lattice planes of Si(111), Ag(111) and Co (0001), and their lattice parameters. (b) Schematic of the cross-section of the designed structure.

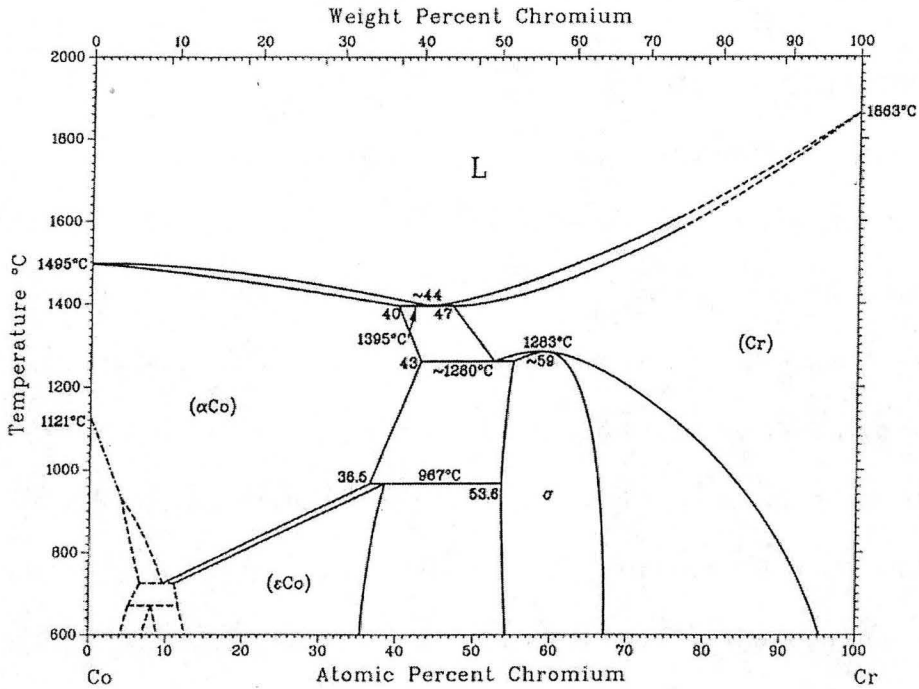

Figure 6–2. CoCr phase diagram [Massalski - 1990].

6.3. Experimental procedures

First, Si(111) wafers were ultrasonically cleaned in organic solvents. Subsequently, they were submersed in a HF:H_2O (1:10) solution for 3-4 minutes to remove the native SiO_2 and to obtain a hydrogen-terminated surface. Upon etching, wafers were blown dry and immediately loaded into a vacuum chamber.

For optimum growth, a 500 Å Ag buffer-layer was evaporated at 300°C to completely cover the Si substrate. It was reported previously by W. Yang *et al.* [Yang - 1997] that the growth of Ag on Si(001) is by the Stranski-Krastanov, or layer-plus-island, mode. After the formation of several 2D monolayers, 3D island growth begins. When the Ag film thickness is increased, neighboring islands coalesce and above 250 Å a more continuous-like film forms. The surface root-mean-square roughness, R_{rms}, reaches a maximum at 50 Å Ag thickness, with the value equal to the film thickness R_{rms} = 50 Å. When the Ag thickness is increased to above 250 Å, the R_{rms} drops to 15 Å, and stays roughly constant for thicker films. Hence, in this investigation, a 500 Å Ag layer was chosen to accomplish complete surface coverage and minimal R_{rms}.

The 2000 Å Co-Cr layer was deposited at a substrate temperature of 300°C by evaporation from the $Co_{95}Cr_5$ source. The choice of 5% Cr was to reduce magnetic saturation as compared with pure Co. Finally, a 300 Å Ag capping layer was evaporated to prevent oxidation of the magnetic layer. The vacuum achieved during evaporation was in low 10^{-6} Torr range. The film structure (θ-2θ diffraction scans), c-axis dispersion (rocking curves - θ-scans) were characterized by x-ray diffraction. The microstructure (grain size, orientation relationship between

substrate—underlayer—film) of the film was evaluated by TEM. The composition of the film was verified by quantitative energy dispersive x-ray spectroscopy (EDS) in TEM. Rutherford back-scattering (RBS) was also used to analyze the composition and structure of the film. The magnetic hysteresis loops, with an external field (≤ 1.4 T) applied both parallel and perpendicular to the thin film sample, were measured by VSM. The magnetic domain structures of these films were investigated by Lorentz TEM as a function of thickness t and temperature in a Philips CM200FEG TEM using Fresnel, Foucault and differential phase contrast (DPC) imaging methods [Chapman - 1984], [Daykin - 1995]. The influence of thickness on the magnetic domain pattern was studied using a wedge-shaped sample prepared by low angle ion-milling. Local thickness of the sample was obtained from measurements of inelastic mean-free path lengths in transmission electron energy-loss spectroscopy (EELS) [Egerton - 1996]. Temperature dependence of the domain pattern in the investigated thickness range was *in-situ* during resistance heating in TEM.

6.4. Experimental results

6.4.1. Co-Cr microstructure and magnetic properties

A representative θ-2θ X-ray diffraction scan, Figure 6–3(a), shows only Si(111), Ag(111) and Co-Cr(0002) peaks, indicating epitaxial growth and a hexagonal closed-pack structure of Co-Cr layer, with the c-axis oriented normal to the film plane. The corresponding rocking curves, Figure 6–3(b) for the Ag (111) and Co-Cr (0002), show a very narrow full-width at half-maximum (FWHM) widths of 0.59° and 1.14°, implying a narrow dispersion of the (111) and (0002) orientations through the grains of the Ag and Co-Cr layers, respectively. Figure 6–4 shows the RBS spectrum of the sample. The measured data are plotted along with an overlaid simulated fit, where layers of $Co_{95}Cr_5$ were simulated as pure Co. Contributions to the simulation from Ag and Co have been plotted separately, as shown. Note that the bottom Ag layer is partially overlapped with the Co signal. Both Ag peaks are about the same size indicating their similar thickness. A 20 nm roughness in the Co layer was assumed when modeling the fit. This indicates that the bottom Ag layer is non-wetting on the Si substrate and it appears almost as spherical beads rather than a continuous layer parallel to the substrate. The roughness of the Ag buffer layer was much larger than the R_{rms} of 15 Å reported in the work of W. Yang *et al.* [Yang - 1997]. The RBS data confirmed the following film stacking from the bottom up:

$$Si_{substrate} / 400 \pm 200 \text{ Å } Ag_{under\text{-}layer} / 2100 \pm 200 \text{ Å } Co_{95}Cr_5 / 300 \pm 30 \text{ Å } Ag_{cap}.$$

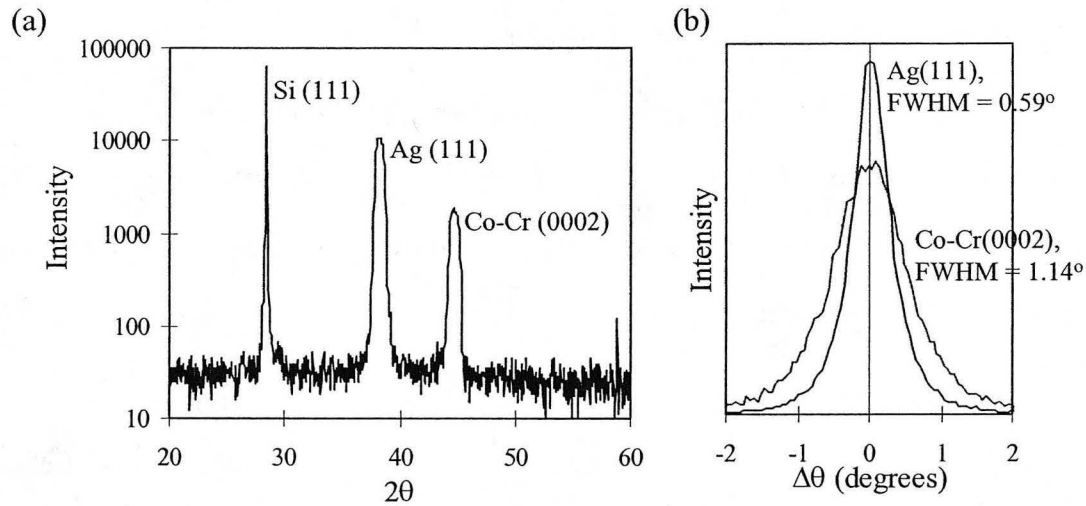

Figure 6–3. (a) θ-2θ X-ray diffraction spectra of a $Co_{95}Cr_5$ 100nm/Ag 500nm/Si(111) film (b) rocking curves (θ-scans) for the Ag (111) and $Co_{95}Cr_5$ (0002) peaks.

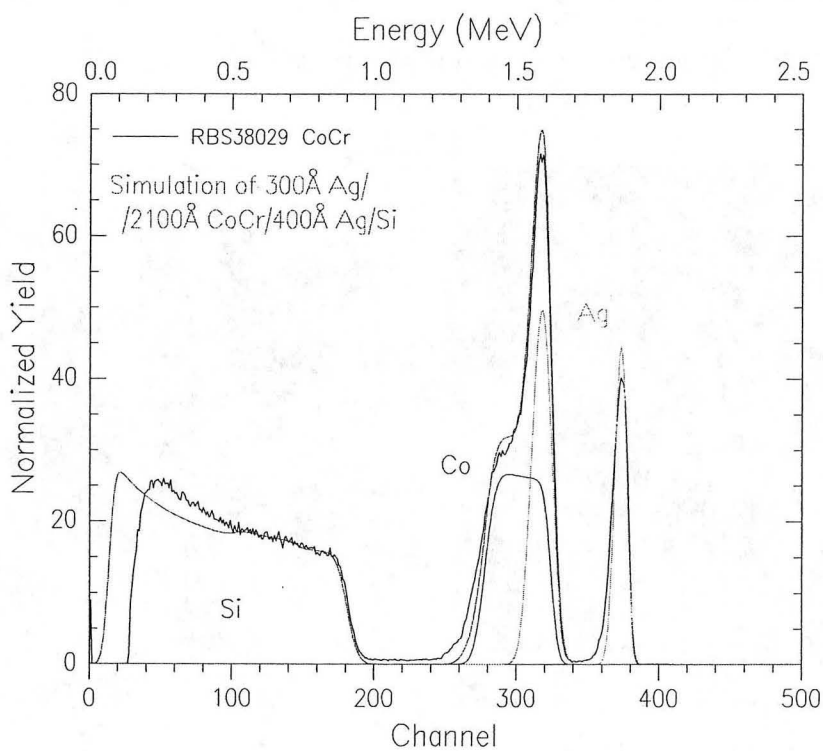

Figure 6–4. Rutherford back-scattering analysis data.

Bright field TEM imaging revealed small grains with an average size of 30 to 50nm. However, the SAD pattern of the plan-view sample, obtained from an area much larger than the observed grain size, had a single crystal appearance, Figure 6–5(b). After indexing this diffraction pattern, the following epitaxial relationship was confirmed:

$$(111)_{Si} \,||\, (111)_{Ag} \,||\, (0001)_{CoCr}\,;\ [-220]_{Si} \,||\, [-220]_{Ag} \,||\, [-1100]_{CoCr} \qquad \text{Eq. 6–3}$$

However, the Ag and Co-Cr spots exhibit small arcing ($\leq 3°$), indicating a small variation of in-plane alignment about the $<111>_{Ag}$ and $<0001>_{CoCr}$ out-of-plane axes. Hence, the analyzed film is not exactly epitaxial, but has 30-50 nm sub-grain structure. The EDS analysis confirmed the composition ratio of the film to be Co/Cr = 95/5, which was the elemental ratio of the evaporation source used.

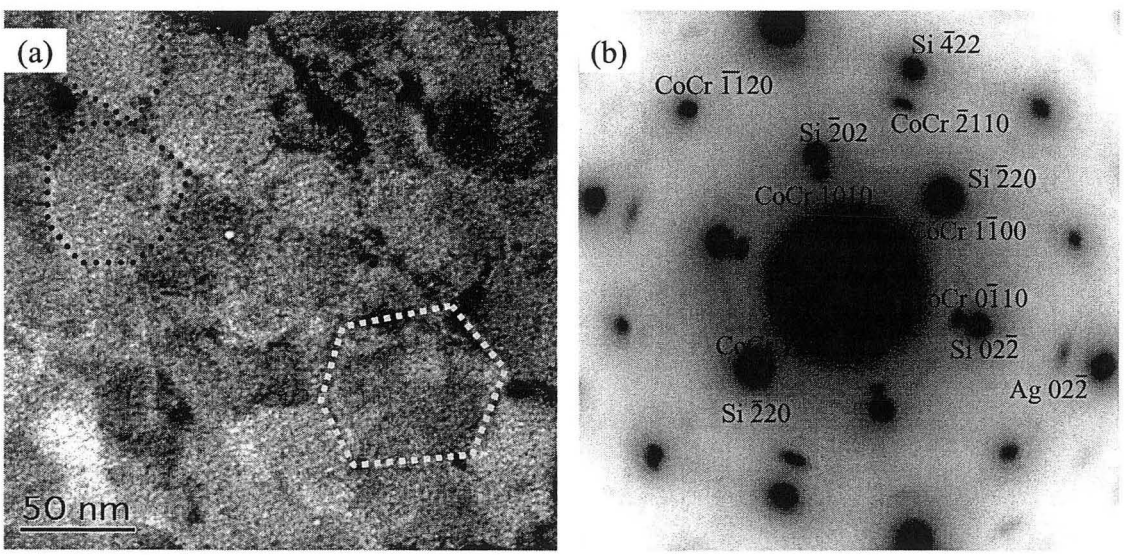

Figure 6–5. (a) Bright field TEM image of the $Co_{95}Cr_5$, (b) SAD pattern.

Typical hysteresis loops (VSM) with the external field applied parallel ($H_{C||} \cong 455$ Öe, $M_R \cong 0.15 \cdot M_S$) and perpendicular ($H_{C\perp} \cong 230$ Öe) to the thin-film sample are shown in Figure 6–6. As shown, the in-plane and perpendicular coercivities are comparable. This indicates a tilted easy axis of magnetization, which is a result of competition between perpendicular magnetocrystalline anisotropy and in-plane shape anisotropy. Based on the wasp-like shape of the perpendicular hysteresis loop, enlarged in Figure 6–6 (b), it can be concluded that the sample is not uniformly magnetized, but is divided into magnetic domains with up and down magnetization components [Gehanno - 1997].

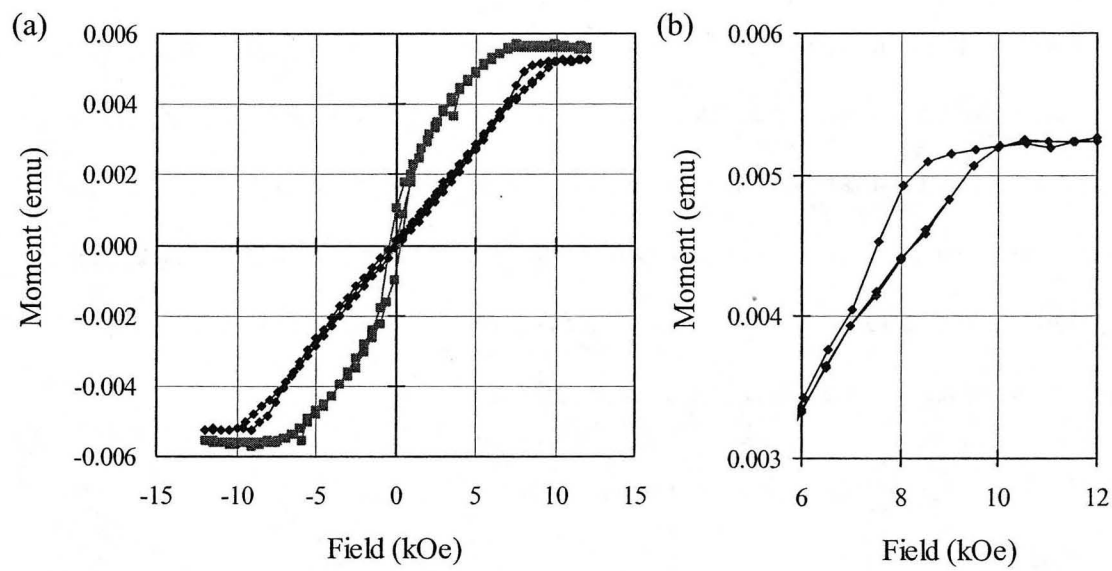

Figure 6–6. (a) Magnetic hysteresis loops for both in-plane and perpendicular field directions, measured with VSM. (b) Enlarged portion of the perpendicular loop.

Figure 6–7 shows a Fresnel image of the wedge shape TEM sample, with the thickness varying from approximately 150 Å near the perforation to above 700 Å in the thickest areas. As shown, the domain pattern changes drastically at the

critical transition thickness, $t_c \cong 300$Å. Below t_c the magnetization is in-plane and the film supports large domains with size in the range 0.6 - 1μm. Above t_c a regular stripe like pattern is observed with stripe period, L, increasing gradually with thickness, t, from approximately L = 90nm at t = 300 Å to L = 110 nm at t = 700 Å. Figure 6–8 shows a bright field TEM image and two Fresnel images taken at small defocus, $\Delta f = \pm 15$ μm. The faint bright and dark lines, which reverse contrast with the change in defocus, are the domain walls separating areas of opposite in-plane magnetization. The distribution of the in-plane magnetization vector was studied in detail by utilizing a quantitative Foucault imaging technique, which is equivalent to the modified TEM DPC imaging mode. Figure 6–9 shows the quantitative Foucault analysis of the in-plane magnetization component of the stripe like domains. Figure 6–9(a), (b), (c) and (d) are the sums of the series of 15 images recorded at incremental beam tilts in +X, -X, +Y, and –Y directions, respectively. As explained in the background section 2.3.1.2, the two orthogonal components of the in-plane magnetization vector, **U** and **V** are given by respective differences of the aforementioned sum-images:

$$\mathbf{U} = \Sigma\{+X\} - \Sigma\{-X\} = \text{Figure 6–9(a)} - \text{Figure 6–9(b)}$$

$$\mathbf{V} = \Sigma\{+Y\} - \Sigma\{-Y\} = \text{Figure 6–9(c)} - \text{Figure 6–9(d)} \qquad \text{Eq.6–4}$$

The resulting images are shown in Figure 6–9(e) and (f), respectively.

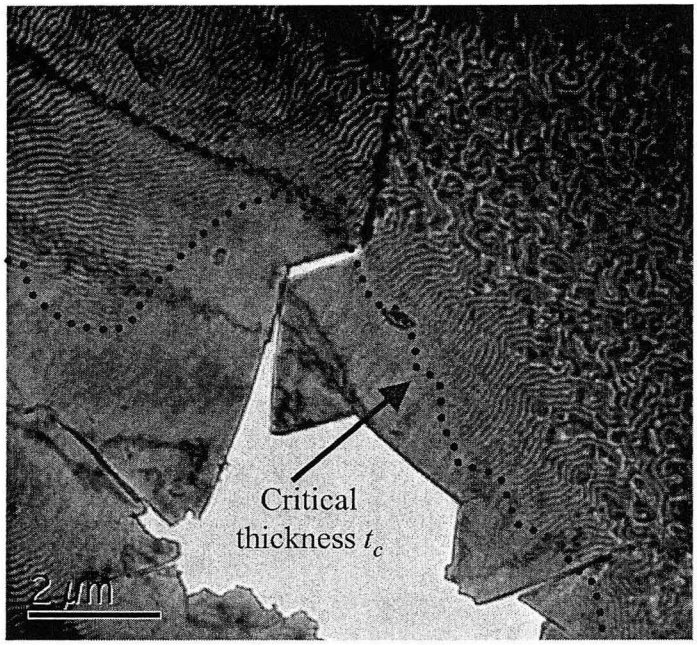

Figure 6–7. Fresnel image showing change of the magnetic domain pattern with increasing sample thickness.

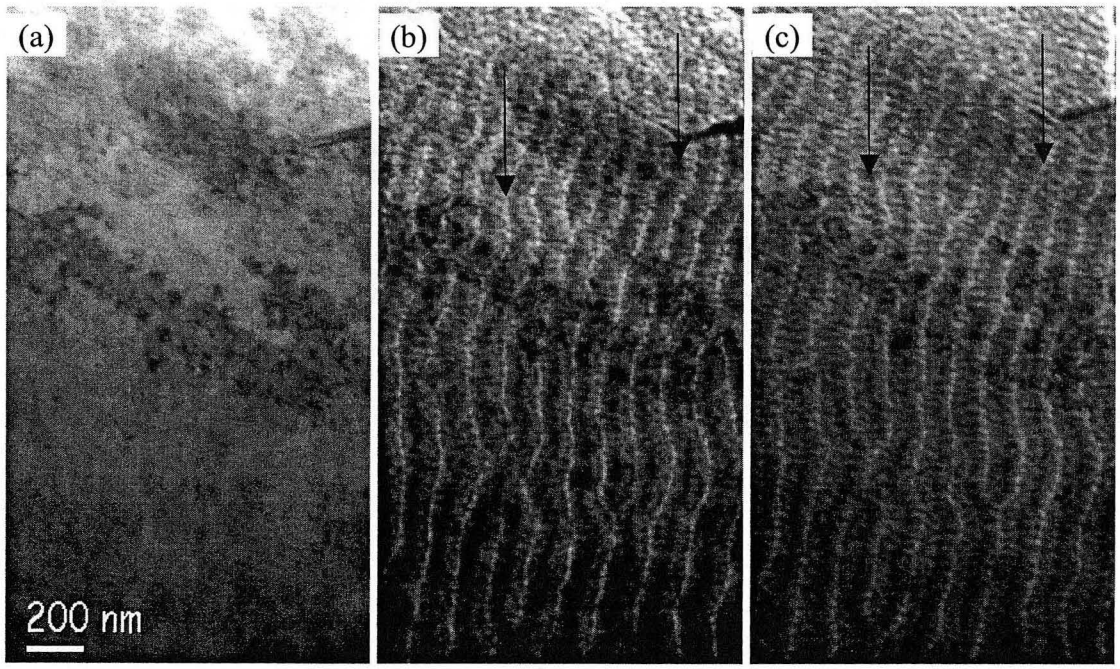

Figure 6–8. Series of images taken at different defocus above t_c (a) Bright field TEM image, (b) Fresnel image of the same area, defocus f = -15 um (c) f = +15um.

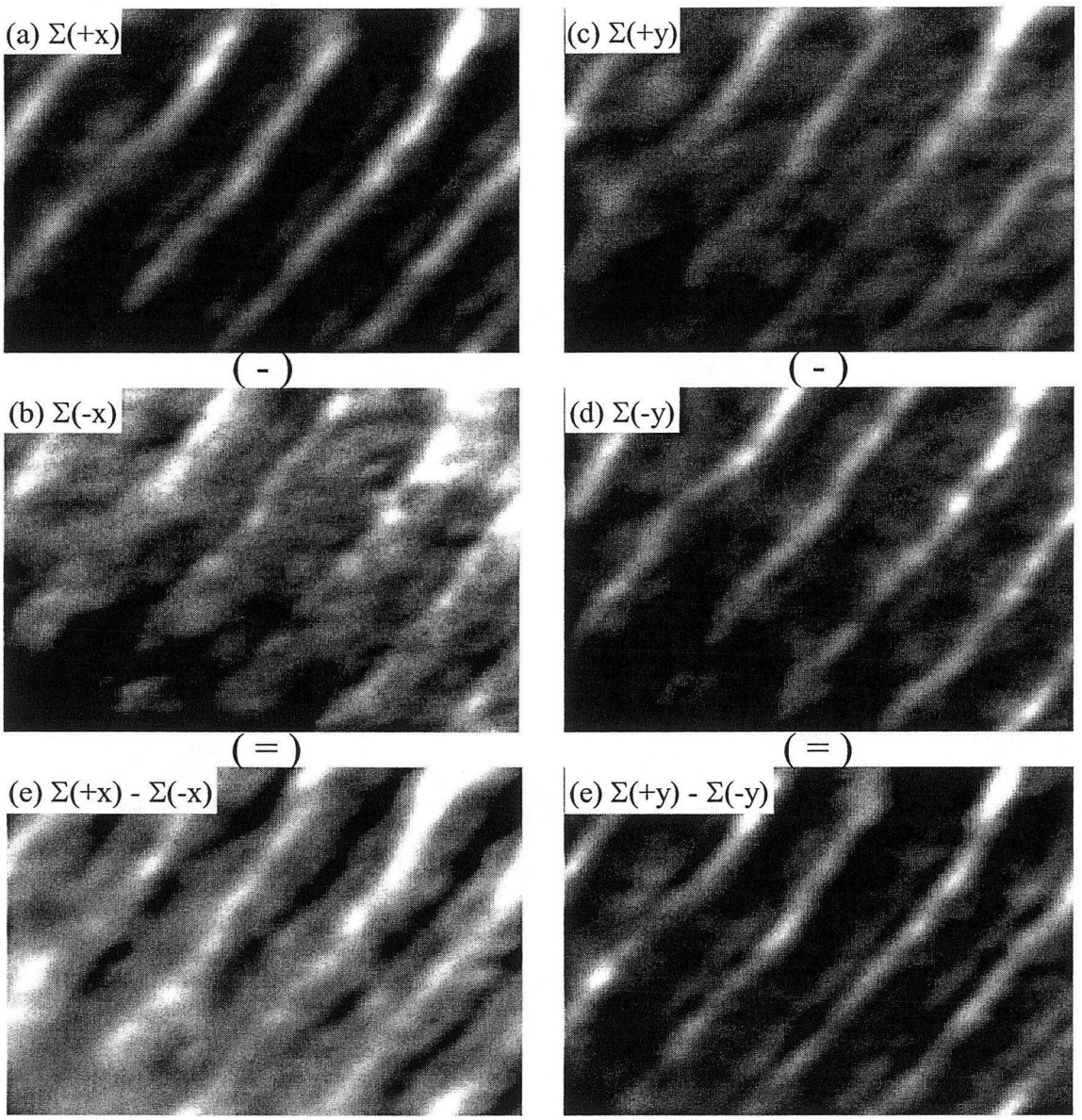

Figure 6–9. Images obtained by summing series of images according to the quantitative Foucault technique: (a) Σ(+x), (b) Σ(-x), (c) Σ(+y), (d) Σ(-y). The differential signal images, which are proportional to in-plane magnetization (e) Σ(+x) -Σ(-x), (f) Σ(+y) - Σ(-y).

A vector plot combining the **U** and **V** components is presented in Figure 6–10. Regions with no arrows indicate areas where the magnetization has no in-plane component and is completely out-of-plane. Lengths of the arrows correspond to the magnitude of the in-plane component of the magnetic induction. It can be concluded that the stripe domains arise from alternating out-of-plane magnetic components, with a significant in-plane component in the transition regions. This conclusion is in agreement with perpendicular hysteresis measurements, which showed a wasp-like structure characteristic for the up and down stripe patterns, Figure 6–6(b) [Gehanno - 1997].

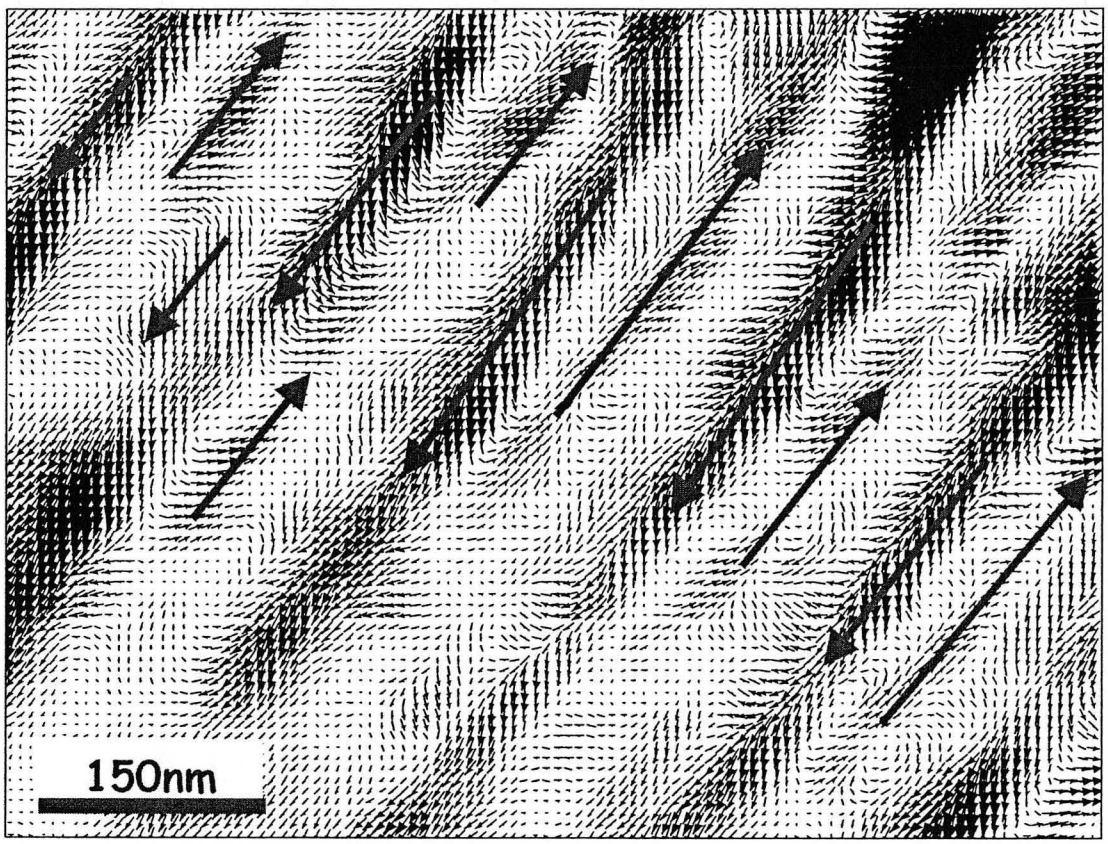

Figure 6–10. Vector plot of the U and V components from Figure 6–9 (e) and (f). The length of the arrows corresponds to the magnitude of the in-plane component of magnetization.

6.4.2. Stripe domain patterns and spin reorientation.

In this section, the nature of the observed stripe domain pattern is discussed in detail. The stripe patterns observed above $t_c \cong 300$ Å arise from the competition between magnetostatic and magnetocrystalline energy.

The stripe-like magnetic domain patterns in these films are similar to the patterns observed by Kooy and Enz [Kooy - 1960] in thin layers of garnet material. Using their model for the total energy of the film with stripe domains, one can estimate the t_c at which this configuration will be energetically favorable over the in-plane magnetization. The model assumes straight domains with the preferential direction of magnetization normal to the surface of the plate and a large anisotropy as compared with the demagnetization field. This implies no closure domains. Moreover, the magnetization is allowed to depart from the c-axis (the μ-effect), which was observed in the studied CoCr films. Energy terms included in the model are: the magnetocrystalline energy E_{MC}; the wall energy E_γ; and the magnetostatic or demagnetizing energy E_{MS}. When the magnetization is in-plane, the only contribution to the total energy of the layer is given by:

$$E_{T(1)} = E_{MC} = K_u \cdot t \qquad \text{Eq. 6–5}$$

where K_u is the uniaxial anisotropy energy and t is the thickness of the film. When the film assumes an out-of-plane magnetization with the stripe pattern, the total energy of the layer is given by:

$$E_{T(2)} = E_{MS} + E_\gamma = 1.7M_S^2 + \gamma \cdot {}^{t}\!/_{D} \qquad \text{Eq. 6–6}$$

where M_S is the saturation magnetization of the material, D is the stripe domain period, $\gamma = (4 \cdot A \cdot K_u)^{1/2}$ is the wall surface energy and A is the exchange constant.

Solving for the optimal domain period D, and substituting into Eq. 6–6 the minimum total energy is given by:

$$E_{T(2)\min} = 2M_S \cdot \sqrt{1.7 \cdot \gamma \cdot t} \qquad \text{Eq. 6–7}$$

Comparing the energy terms for the two configurations Eq. 6–5 and Eq. 6–7, the transition thickness can be approximated by:

$$t_c = 13.6 \cdot M_S^2 \cdot \frac{\sqrt{A}}{K_u^{3/2}} \qquad \text{Eq. 6–8}$$

For the 5% Cr film composition, M_S is approximately constant in the (0°C - 400°C) temperature range [Song - 1993]. However, K_u decreases with increasing temperature as shown in Figure 6–11 [Cullity - 1972].

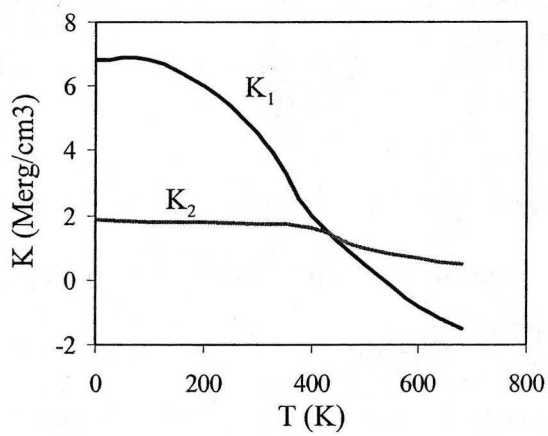

Figure 6–11. Anisotropy constant versus temperature [Cullity - 1972].

For a given composition, considering only the temperature as a variable, Eq. 6–8 can be simplified to:

$$t_c \propto \frac{1}{f(K_u)} = \frac{1}{f\left(\frac{1}{T}\right)} = f(T) \qquad \text{Eq. 6–9}$$

Hence, the critical thickness is shown to be a function of temperature, and it is expected to increase with increasing temperature.

The spin reorientation transition (SRT) of the stripe domains with decreasing value of the anisotropy constant, K_u, was studied dynamically by observing the domains as a function of temperature by *in-situ* heating up to 350°C. The thickness of the sample was measured by EELS, according to Eq. 2–7 and is displayed in Figure 6–12(a). Image (b) displays a Fresnel image of the same area. The progress of the *in-situ* heating of the same area is shown in Figure 6–13. As predicted, the critical transition thickness, t_c, was found to increase with increasing temperature. Upon heating, the stripe domain contrasts shift to larger thickness. The experimental values of t_c as a function of temperature are plotted in Figure 6–14.

Upon cooling, the stripe pattern was found to return, Figure 6–13(e) and (f), and t_c was found to be similar for both heating and cooling directions. The stripe period was measured to be the same after cooling and no hysteresis was observed. However, the direction of the stripes was changed, as can be see by comparing Figure 6–13(a) and (l).

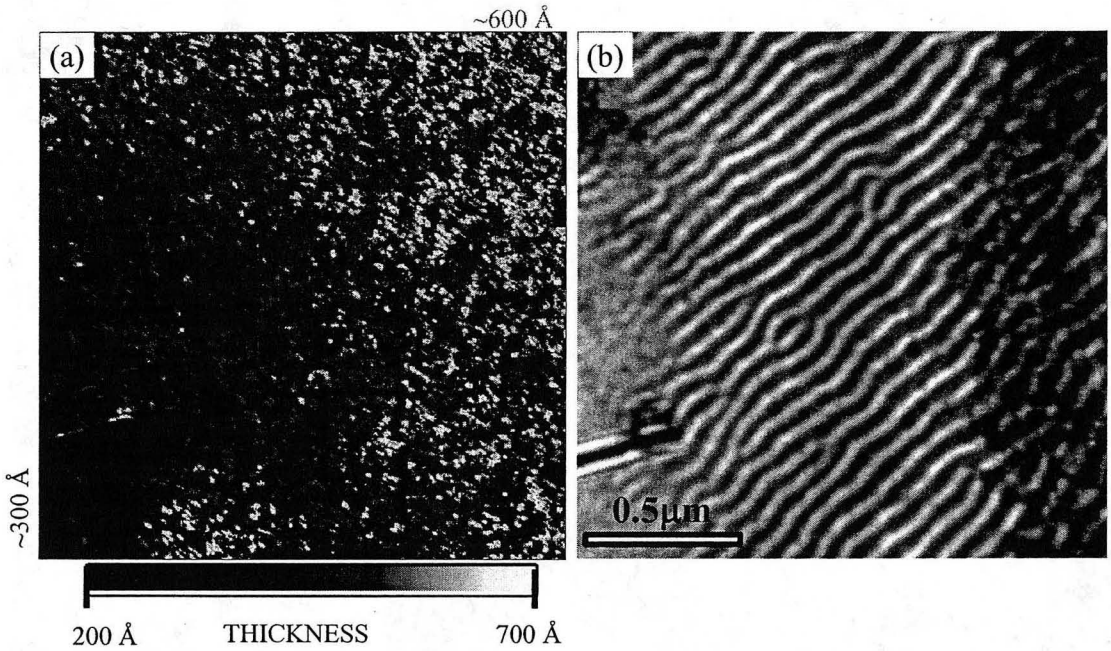

Figure 6–12. (a) EELS thickness map. (b) Fresnel image of the area where *in-situ* heating was done, see Figure 6–13.

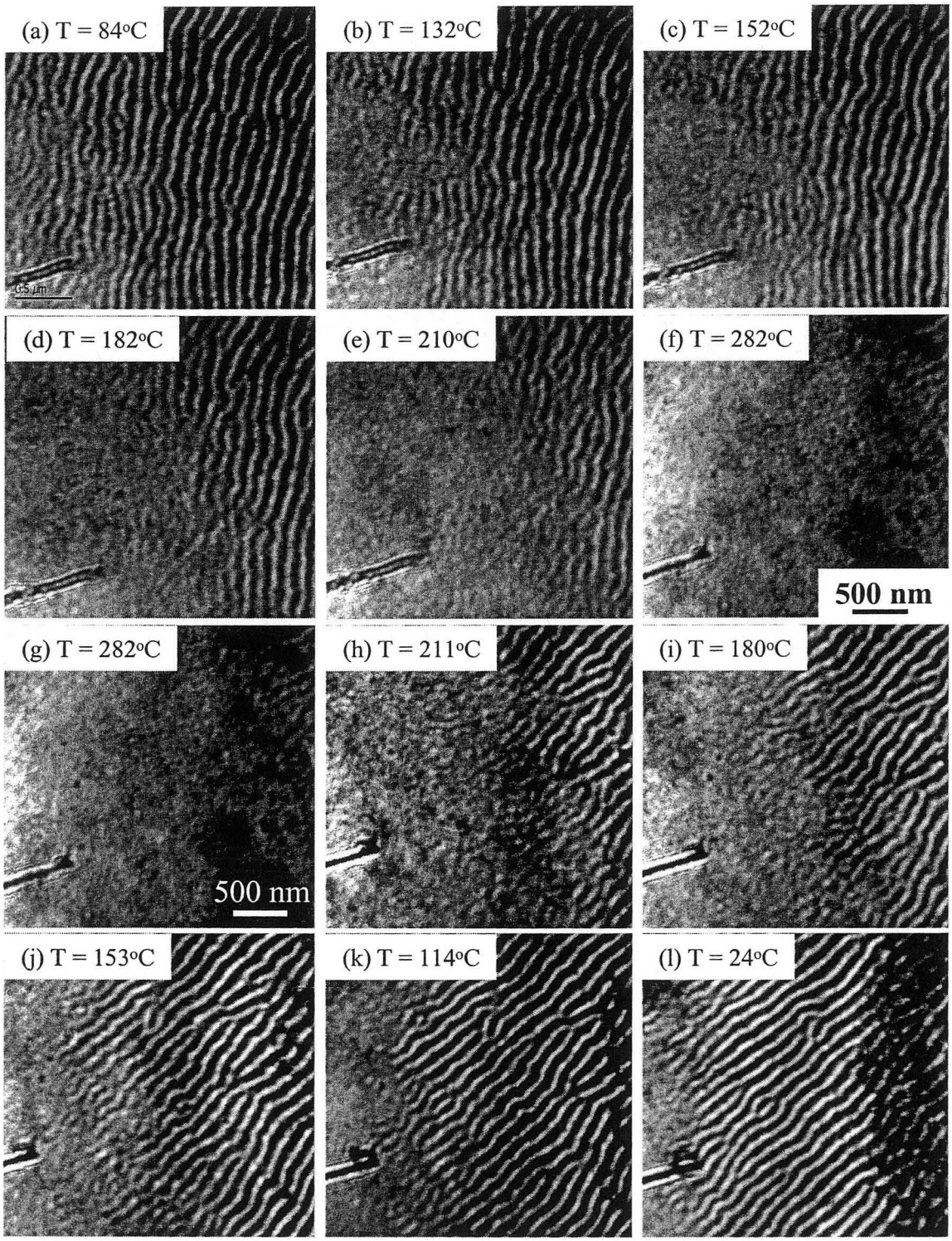

Figure 6–13. Fresnel images summarizing the temperature-dependent domain patterns. (a) – (f) Heating, (g) – (l) cooling.

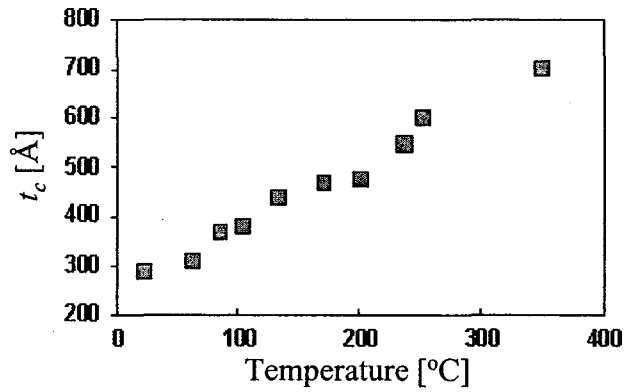

Figure 6–14. Plot of the critical transition thickness $t_c = 13.6\, M_S^2 \cdot (A)^{1/2}/(K_u)^{3/2}$, as a function of temperature measured during an *in-situ* TEM experiment.

6.5. Summary

As shown by the experimental work, the magnetic orientation in c-axis $Co_{95}Cr_5$ depends on the thickness of the investigated film. Below 300 Å, magnetization is in-plane, and above 300 Å it has a perpendicular component. However, for this alloy the magnetocrystalline anisotropy is not large enough to fully overcome the demagnetization energy $2 \cdot \pi \cdot M_S^2$. In order to achieve a system with complete perpendicular axis, further Cr alloying would be necessary to lower M_S and decrease the demagnetization energy contribution.

Two types of domain patterns were observed. Below t_c, magnetization is in-plane, and the film supports large ~ 1 μm domains. Above t_c, the magnetization has both in-plane and out-of-plane components, and a regular stripe pattern is observed. The SRT observed as a disappearance of the stripe pattern upon heating is associated with the loss of the out-of-plane component, rendering the magnetization strictly in-plane. This novel *in-situ* experiment has made it possible to track the SRT in a spatially varying fashion.

Chapter 7.

CONCLUSIONS

Certainly, methods discussed in this dissertation are not exhaustive and further research is required for a full understanding of ion-irradiation phenomena in Co/Pt multilayers.

Summarizing the results for Co/Pt multilayers, a correlation between the microstructure and magnetic properties was found. An increase in grain size and an improved <111> texture were found, with an increase in T_G up to a certain critical temperature, T_{crit}, both grain size and texture contributing to an increase in H_C. Moreover, a decrease in domain size was observed. For ML's grown at T_G = 390°C > T_{crit}, a decrease in H_C was measured, and small magnetically decoupled domains were observed. The size of these domains was similar to the grain size. This correlates well with Co depletion at the column grain boundaries and diffused Co/Pt interfaces, measured as one set of Co-Pt rings. The latter is known to reduce the PMA and, hence, reduce H_C. Also, a decrease in H_C was observed with increasing t_{Co}. The coercivity is therefore a function of both the microstructure (grain size and texture) and interface quality, which is strongly

influenced by T_G. Appropriate choice of $T_{G,seed}$, $T_{G,ML}$, t_{Co}, and multilayer repetition, can produce structures with desired H_C and domain size.

The ion dose was shown to influence the magnetic properties and the magnetic domain structure of Co/Pt multilayers. The changes in magnetic properties with exposure to ion irradiation are associated with a decrease in interfacial anisotropy, K_S. The rotation of the magnetization to in-plane at high doses supports this conclusion. With increasing doses of ions, K_S is reduced primarily due to localized ion-beam induced atomic disordering at the interfaces and becomes comparable to the shape anisotropy. At high enough doses, this is seen as a transition to in-plane magnetization. At roughly the same point, the coercivity falls to zero.

Transmission electron microscopy, ion-irradiation simulations and calculations of interface anisotropy found the ion-induced changes of magnetic properties not to be due to the large microstructural grain-size changes, but to be associated with localized ion-beam induced atomic disordering at the Co/Pt interfaces. Ion irradiation displaces Co and Pt atoms near Co/Pt interfaces, which leads to local roughening and reduction in K_S. To further study irradiation effects, techniques capable of elucidating the symmetry of the local environment of Co atoms must be used. One such technique is X-ray Absorption Fine Structure analysis. This synchrotron-based technique is capable of finding statistical information on the number of Co-Co bonds versus Co-Pt bonds before and after irradiation. In addition, HRTEM analysis, including extensive image simulation, should be carried out on Molecular Beam Epitaxy grown single crystal Co/Pt multilayers. The effect of tensile strain relaxation after ion irradiation within Co

layers should be investigated. Relaxation of Co layers during ion irradiation could be responsible for a decrease in perpendicular anisotropy. As reported in this dissertation, a small shift in Co rings in the selected area diffraction was measured after irradiation. This is indicative of strain relaxation.

For all ML's, ion irradiation, which reduces H_C by decreasing the perpendicular interface anisotropy, was found to decrease the size of magnetic domains.

The principles of ion modification were applied to spatially pattern the magnetic properties of the Co/Pt multilayers. Two techniques were utilized to apply a spatially varying ion dose. These techniques were ion-irradiation through a stencil mask and direct writing with FIB.

The magnetic reversal processes of magnetic arrays fabricated by ion beam irradiation were studied. A unique combination of two complementary magnetic imaging techniques, LTEM (in-plane) and MTXM (out-of-plane), was used to study the three-dimensional magnetic structure of the patterned films. For the stencil mask irradiation, the boundaries of the patterns, defined by the transition from out-of-plane to in-plane magnetization, were found to be determined by the mask, while the scale of magnetic reversal was governed by the microstructure. LTEM imaging of the patterns confirmed that the irradiated regions have in-plane easy axes of magnetization. MTXM imaging found nucleation of domains at the irradiation pattern boundaries at $H_{N\perp}$ = 1 kOe, which is significantly lower than nucleation fields for the as-grown film, $H^{o}_{N\perp} \cong$ 4 to 5 kOe. *In-situ* data showed that the perpendicular reversal process starts by rotation of in-plane regions and propagation into the matrix. FIB pattering was used to create features below 100

nm periodicity. Bit patterns with large 300 nm islands were found to support more than one domain. For smaller 100 nm patterns, a single-domain bits were recorded. Similar to the patterning through the mask, the perpendicular reversal was found to start at ion irradiation boundaries.

Ion irradiation is a new technique for patterning magnetic properties without changing the planarity of the sample. Patterned magnetic media with a feature size below 30 nm can be fabricated. The important finding was that ion-patterning is independent of the microstructure.

Often, the patterned media are plagued by wide a distribution of switching fields. The reversal of individual bits is governed by local nucleation fields. For the case of ion-beam patterns, Co/Pt multilayer reversal starts at the irradiation boundary and the nucleation fields are more uniform. Provided that single-domain bits can be achieved, this can be very attractive. Hence, ion-irradiation patterning is promising for the development of new magnetic architectures, comprising areas with patterned perpendicular anisotropies, alternating areas with perpendicular and in-plane magnetization, or a combination of the two.

Another important conclusion from the magnetic imaging point of view was that element-specific magnetic imaging with x-ray magnetic circular dichroism contrast has been demonstrated to have a high sensitivity, which allows imaging of magnetic layers as thin as 3 nm.

The results of this dissertation show that Co/Pt multilayers patterned by ion-irradiation are am attractive candidate for future magnetic recording media. Further experiments to optimize the magnetic performance by this method would be appropriate.

Appendix A. VALUES OF SELECTED PHYSICAL CONSTANTS

For full list see: www.physics.nist.gov/constants

Quantity	Symbol	Value	SI
Avogardo's number	N_o	6.022	$\times 10^{26}$ atoms/(kg·mole)
Boltzman constant	k_B	1.381	$\times 10^{-23}$ J/K
Gas constant	R	8.314	J/(mole·K)
Velocity of light	c	2.998	$\times 10^{8}$ m/s
Permittivity of free space	ε_o	8.854	$\times 10^{-12}$ F/m
Permeability of free space	μ_o	1.257	$\times 10^{-6}$ H/m
Atomic mass unit	$a.m.u$	1.661	$\times 10^{-27}$ kg
Electron charge	e	-1.602	$\times 10^{-19}$ C
Electron rest mass	m_e	9.109	$\times 10^{-31}$ kg
Electron volt	eV	1.602	$\times 10^{-19}$ J
Planck's constant	h	6.626	$\times 10^{-34}$ J·s
Bohr magneton	μ_B	9.274 1.165	$\times 10^{-24}$ A·m^2 (=J/T) $\times 10^{-29}$ J·m/A
Nuclear magneton	μ_N	5.051	$\times 10^{-27}$ A·m^2 (=J/T)
Magnetic flux quantum	Φ_o	2.067	$\times 10^{-15}$ Wb

Appendix B. UNITS CGS AND SI.

Quantity	Symbol	Gausian & cgs emu[a]	Conversion Factor, C[b]	SI & rationalized mks[c]
Magnetic flux density, magnetic induction	B	gauss (G) [d]	10^{-4}	tesla (T), Wb/m^2
Magnetic flux	Φ	Maxwell (Mx), $G\text{-}cm^2$	10^{-8}	weber (Wb), volt second (V·s)
Magnetic potential difference, magnetomotive force	U, F	gilbert (Gb)	$10/4\pi$	ampere (A)
Magnetic field strength, magnetizing force	H	oersted (Oe), [e] Gb/cm	$10^3/4\pi$	A/m [f]
(Volume) magnetization [g]	M	emu/cm^3 [h]	10^3	A/m
(Volume) magnetization	$4\pi M$	G	$10^3/4\pi$	A/m
Magnetic polarization, intensity of magnetization	J, I	emu/cm^3	$4\pi\times10^{-4}$	T, Wb/m^2 [i]
(Mass) magnetization	σ, M	emu/g	1 $4\pi\times10^{-4}$	$A\cdot m^2/kg$ Wb·m/kg
Magnetic moment	m	emu, erg/G	10^{-3}	$A\cdot m^2$, jule per tesla (J/T)
Magnetic dipole moment	j	emu, erg/G	$4\pi\times10^{-10}$	Wb·m [j]
(Volume) susceptibility	χ, κ	dimensionless, emu/cm^3	4π $(4\pi)^2\times10^{-7}$	dimensionless henry per meter (H/m), Wb/(A·m)
(Mass) susceptibility	χ_p, κ_p	cm^3/g emu/g	$4\pi\times10^{-3}$ $(4\pi)^2\times10^{-10}$	m3/kg $H\cdot m^2/kg$
(Molar) susceptibility	χ_{mol}, κ_{mol}	cm^3/mol emu/mol	$4\pi\times10^{-6}$ $(4\pi)^2\times10^{-13}$	m3/mol $H\cdot m^2/mol$
Permeability	μ	dimensionless	$4\pi\times10^{-7}$	H/m, Wb/(A·m)
Relative permeability [j]	μ_r	not defined		dimensionless
(Volume) energy density, energy product [k]	W	erg/cm^3	10^{-1}	J/m^3
Demagnetization factor	D, N	dimensionless	$1/4\pi$	dimensionless

[a] Gaussian units and cgs are the same for magnetic properties. The defining relation is $\mathbf{B} = \mathbf{H} + 4\pi\mathbf{M}$.

[b] Multiply a number in Gausian units by C to convert it to SI (e.g. $1\ G \times 10^{-4}\ T/G = 10^{-4}\ T$).

[c] SI (Systeme International d'Unites) has been adopted by the National Bureau of Standards. There tow conversion factors are given, the upper one is recognized under, or consistent with, SI and is based on the definition $\mathbf{B} = \mu_o(\mathbf{H} + \mathbf{M})$, where $\mu_o = 4\pi\times10^{-7}$ H/m. The lower one is not recognized under SI and is based on definition $\mathbf{B} = \mu_o\mathbf{H} + \mathbf{J}$, where the symbol **I** is often used in place of **J**.

[d] 1 gauss = 10^5 gamma (γ).

[e] Both oersted and gauss are expressed as $cm^{-1/2}\cdot g^{1/2}\cdot s^{-1}$ in terms of base units.

[f] A/m was often expressed as "ampere-turn per meter" when used for magnetic field strength.

[g] Magnetic moment per unit volume

[h] The designation "emu" is not a unit

[i] Recognized under SI, even though based on the definition $\mathbf{B} = \mu_o\mathbf{H} + \mathbf{J}$. See footnote C

[j] $\mu_r = \mu/\mu_o = 1 + \chi$, all in SI. μ_r is equal to Gaussian μ.

[k] $\mathbf{B}\cdot\mathbf{H}$ and $\mu_o\mathbf{M}\cdot\mathbf{H}$ have SI units J/m^3, $\mathbf{M}\cdot\mathbf{H}$ and $\mathbf{B}\cdot\mathbf{H}/4\pi$ have Gaussian units erg/cm^3.

R.B. Goldfarb and F.R. Fickett, U.S. Department of Commerce, National Bureau of Standards, Boulder, Co 80303 March 1985 NBS Special Publication 696

Appendix C. BACKGROUND OF ION-MATTER INTERACTION.

This appendix reviews the basics of the fundamental physics associated with the penetration of energetic ions into solids [Ziegler - 1985], [Ziegler - 1992], [Averback - 1994].

Studies of radiation damage were initiated in the 1940's as part of the research and development program on nuclear weapons. In the 1970's, ion implantation and ion-beam modification of materials became a wide-scale commercial process, mainly in the electronics industry. Today, ion beams are employed widely. Some examples are: implantation of electrically active elements into Si semiconductor devices; fabrication of oxidation and corrosion-resistant layers on metal; implantation of Nitrogen into various metals for improved wear resistance; focused ion beam cutting and removal of materials used for TEM sample preparation, etc. Essentially, any ion species can be implanted into the solid. The depth distribution of the implanted ions can be controlled with high precision. In addition, ion implantation is suitable for lateral patterning with submicron resolution using either masks or focused ion-beams.

When energetic ions penetrate a solid, they lose energy by interaction with atomic nuclei and electrons. The total stopping cross-section of ions in solids is thus divided into two parts, the nuclear stopping cross-section and the electronic stopping cross-section. These two components are usually considered separately from each other, ignoring the possible correlation between hard nuclear collisions and large inelastic losses to electronic excitation.

Nuclear stopping

The heavy target nucleus is assumed to be unconnected to the lattice and the elastic recoil energy transferred from the passing ion is treated simply as the kinetic scattering of two heavy, screened particles. Due to Coulombic repulsion, the target atom recoils and absorbs energy resulting in the deflection of the incoming ion. The loss of projectile energy due to such nuclear collisions is given by:

$$\left(\frac{\mathrm{d}E}{\mathrm{d}x}\right)_n = -N \cdot S_n(E) = -N \cdot \int_0^{T_{\max}} T \cdot \frac{\mathrm{d}\sigma(E,T)}{\mathrm{d}T}\mathrm{d}T, \qquad \text{Eq. C–1}$$

where E is the projectile energy, x is the distance along the ion trajectory, $S_n(E)$ is the nuclear stopping cross-section in units of energy-area, N is the atomic density, and $\mathrm{d}\sigma(E,T)$ is the differential cross-section for an ion of energy E to transfer an energy between T and $T + \mathrm{d}T$ to a target atom [Averback - 1994].

Based on the conservation of energy and momentum, the energy transfer between ion and target is:

$$T = 4 \cdot \frac{A_1 \cdot A_2}{(A_1 + A_2)^2} \cdot E \cdot \sin^2 \frac{\theta}{2} \qquad \text{Eq. C–2}$$

where A_1 and A_2 are the atomic masses of the implanted ion and target atoms, respectively, and θ is the scattering angle. The maximum energy transfer occurs in a head-on collision, and it is largest when the ion and substrate atoms have similar masses[i].

---

[i] This is why energetic electrons, even with energies in MeV range, cause little structural damage in thin foils during TEM investigations.

The scattering angle of deflection, θ, can be derived in the single central force-field approximation if it is assumed that the two potentials are spherically symmetric and do not vary with time or with particle velocity [Ziegler - 1992]. Based on the laws of conservation of energy and momentum,

$$\theta = \pi - 2 \cdot p \cdot \int_{r_{min}}^{\infty} \frac{\mathrm{d}r}{r^2 \cdot \left[1 - \frac{V(r)}{E_c} - \frac{p^2}{r^2}\right]^{1/2}} \qquad \text{Eq. C–3}$$

where p is the impact parameter defined as the distance between the center of the target atom and the projectile trajectory, r_{min} is the distance of the closest approach during the collision and E_c is the center of mass energy given by:

$$E_c = \frac{A_2 \cdot E_o}{A_1 + A_2} \qquad \text{Eq. C–4}$$

In this model, it is assumed that any projectile passing within the cross-section $\sigma = \pi \cdot p^2$ is deflected by nuclear scattering.

Electronic stopping

When the projectile passes near the target atom, it looses energy by electron ionization and/or generation of plasmons. Early models by Fermi and Teller [Fermi - 1947] found the electron energy loss proportional to the ion velocity:

$$\left(\frac{\mathrm{d}E}{\mathrm{d}x}\right)_e = v \cdot \rho^{1/3} \qquad \text{Eq. C–5}$$

where v is the particle velocity and ρ is the electron density. A later model by Firsov [Firsov - 1959] assumed the ion velocity to be slow relative to the electron orbital velocities. During projectile motion, target electrons are able to fully

readjust their electronic states to the projectile position. Consequently, electrons are free to exchange between projectile and target atom during collision. During the electron exchange, the ion loses energy by performing work in accelerating target electrons up to its velocity. By considering the electron currents flowing between the moving ion and the target atom, the electron stopping power is described by the expression:

$$\left(\frac{\mathrm{d}E}{\mathrm{d}x}\right)_e = -N \cdot S_e(E) = -N \cdot \{(0.336eV^{1/2}\text{Å}^2) \cdot [Z_1 + Z_2] \cdot \left(\frac{E}{A_1}\right)^{1/2}\} \qquad \text{Eq. C–6}$$

where $S_e(E)$ is the electronic stopping cross-section in units of energy-area, N is the atomic density, Z_1 and Z_2 are the atomic numbers of the implanted ion and target atoms, respectively, A_1 is the atomic mass of the ion, E is the projectile energy and x is the distance along the ion trajectory. Based on Eq. C–6, the electronic stopping power increases with increasing ion energy (velocity) and atomic number.

Damage-physics of recoil cascades

An ion penetrating a target constantly loses energy to the electron sea. This may proceed for many monlayers into the target, before collision with a target atom. Upon such a collision, an energetic ion might transfer sufficient energy to displace the target atom from its lattice site. The energy required for a target atom to be displaced (the recoil atom) and to create a vacancy is called the displacement energy, E_d. Typical values are 10 to 60 eV and Table C–1 lists values for Co and Pt.

Table C–1. Minimum and average displacement energies for Co and Pt.

Atomic Number	Element	E_d minimum (eV)	E_d average (eV)
27	Co (*hcp*)	22	34
78	Pt	33	44

Depending on the magnitude of the transferred energy, T, different processes occur. For $T < E_d$, the target atom experiences large amplitude vibrations and generation of phonons, which may lead to localized heating. For $T > E_d$, a target atom is displaced; such an atom is referred to as the primary knock-on atom. For $T >> 2 \cdot E_d$ after the collision, the recoil target atom may acquire adequate energy to start a collision cascade, hitting other atoms, which in turn may recoil into subsequent target atoms. Collision cascades usually involve displacement collisions, vacancy production, replacement collisions, interstitial atoms and other forms of lattice disruption. High-energy particles produce such collision cascades. However, since the cross-section for atomic collisions increases with decreasing energy, a projectile, which slows down in the target, produces recoils closer and closer to each other.

After several collisions, the momentum of the implanted ion and the momenta of the recoil atoms become randomized and the location of the displacement atoms is a stochastic process. For interfaces between two different materials, this significant atomic rearrangement can lead to local intermixing and perhaps alloying. The intermixing can be due to ballistic effects, enhancement of chemical driving forces, thermal spike phenomenon, and transformation to metastable or equilibrium phases.

In recent years, computer simulations have become the main means for calculating the ion range distribution, damage events and the depth distribution of defects and electronic excitations. The most widely used simulation code, ***TRIM*** (The ***TR***ansport of ***I***ons in ***M***atter) was first developed by Biersack and Haggmark [Biersack - 1980] and later by Ziegler [Ziegler - 1985], ["J.F. Ziegler and J.P. Biersack" -]. TRIM is a Monte-Carlo computer program that simulates scattering and slowing-down processes of energetic ions in matter. It follows a large number of individual ions or particles in a target (histories). For the purpose of the calculation, the target is considered amorphous, ignoring directional properties of the crystal. Each history begins with a given energy, position and direction. The particle is assumed to change direction as a result of binary nuclear collisions, and to travel in a straight free-flight-path between such collisions. During each collision, the energy of the particle is reduced as a result of nuclear or electronic (inelastic) processes. When the energy of the particle is reduced below a pre-specified value, the history is terminated.

In this research TRIM calculations were used to study and understand the irradiation processes. In addition, a dynamic version of the program (T-DYN 4.0)[Biersack - 1980] was used to simulate ballistic mixing of the Co/Pt multilayers.

REFERENCES:

[Aharoni - 1996] A. Aharoni, *Introduction to the Theory of Ferromagnetism*, Clarendon Press, Oxford (1996).

[Aharonov - 1959] Y. Aharonov and D. Bohm, *"Significance of Electromagnetic Potentials in the Quantum Theory"*, Physical Review **115**(3), 485 (1959).

[Aign - 1998] T. Aign, P. Meyer, S. Lemerle, J.P. Jamet, J. Ferre, V. Mathet, C. Chappert, J. Gierak, C. Vieu, F. Rousseaux, H. Launois, and H. Bernas, *"Magnetization reversal in arrays of perpendicularly magnetized ultrathin dots coupled by dipolar interaction"*, Physical Review Letters **81**, 5656 (1998).

[Anderson - 2000] E.H. Anderson, D.L. Olynick, B. Harteneck, E. Veklerov, G. Denbeaux, W. Chao, A. Lucero, L. Johnson, and D. Attwood, *"Nanofabrication and diffractive optics for high-resolution X-ray applications"*, Journal of Vacuum Science & Technology B **18**(6), 2970 (2000).

[Ardhuin - 2000] H. Ardhuin, J.N. Chapman, P.R. Aitchison, M.F. Gillies, K.J. Kirk, and C.D.W. Wilkinson, *"Magnetization reversal of patterned spin-tunnel junction material: A transmission electron microscopy study"*, Journal of Applied Physics **88**(5), 2760 (2000).

[Averback - 1994] R.S. Averback, *"Ion-beam modification of materials"*, in: Encyclopedia of Applied Physics ed. by (VCH Publishers, Inc., **8**, 173 (1994)

[Bader - 1990] S.D. Bader, *"Thin film magnetism"*, Proceedings of the IEEE **78**(6), 909 (1990).

[Bader - 1991] S.D. Bader, *"SMOKE"*, Journal of Magnetism and Magnetic Materials **100**(1-3), 440 (1991).

[Belk - 1979] J.A. Belk, *Electron microscopy and microanalysis of crystalline materials*, Applied Science Publishers LTD, (1979).

[Belli - 1978] Y. Belli, M. Okada, G. Thomas, M. Homma, and H. Kaneko, *"Microstructure and magnetic properties of Fe-Cr-Co-V alloys"*, Journal of Applied Physics **49**(3), 2049 (1978).

[Berg - 1972] H. Berg, Jr. and J.B. Cohen, Metallurgical Transactions **3**, 1797 (1972).

[Berg - 1973a] H. Berg, Jr. and J.B. Cohen, *"Local atomic arrangements in partially ordered CoPt/sub 3/. I. Studies of diffuse X-ray scattering"*, Acta Metallurgica **21**(12), 1579 (1973a).

[Berg - 1973b] H. Berg, Jr., T.T. Tsong, and J.B. Cohen, *"Local atomic arrangements in partially ordered CoPt/sub 3/ II. Field-ion microscopy"*, Acta Metallurgica **21**(12), 1589 (1973b).

[Bertero - 1994] G.A. Bertero and R. Sinclair, *"Structure-property correlations in Pt/Co multilayers for magneto-optic recording"*, Journal of Magnetism and Magnetic Materials **134**(1), 173 (1994).

[Bertero - 1995] G.A. Bertero, R. Sinclair, C.H. Park, and Z.X. Shen, *"Interface structure and perpendicular magnetic anisotropy in Pt/Co multilayers"*, Journal of Applied Physics **77**(8), 3953 (1995).

[Bertotti - 1998] G. Bertotti, *Hysteresis in Magnetism*, Academic Press, New York (1998).

[Bertram - 1994] H.N. Bertram, *Theory of magnetic recording*, Cambridge University Press, Cambridge (1994).

[Bhatti - 1980] A.R. Bhatti, P.J. Grundy, G.A. Jones, D.A. Scarsbrook, and R.S. Tebble, *"Lorentz electron microscopy of some amorphous and annealed FeB alloys"*, IEEE Transactions on Magnetics **MAG-16**(6), 1437 (1980).

[Biersack - 1980] J.P. Biersack and L. Haggmark, *"A Monte Carlo computer program for the transport of energetic ions in amorphous targets"*, Nuclear Instruments & Methods in Physics Research Section B-Beam Interactions with Materials and Atoms **174**(1-2), 257 (1980).

[Bitter - 1931] F. Bitter, *"On the inhomogeneities in the magnetization of ferromagnetic materials"*, Physical Review **38**, 1903 (1931).

[Bitter - 1932] F. Bitter, *"Experiments on the nature of ferromagnetism"*, Physical Review **41**, 507 (1932).

[Bland - 1994] *Ultarthin Magnetic Structures I: an introduction to the electronic, magnetic, and structural properties*, ed. by J.A.C. Bland and B. Heinrich, Springer-Verlag, Berlin, Heidelberg (1994)

[Brooksbank - 1968] D. Brooksbank and K.W. Andrews, *"Thermal expansion of some inclusions found in steels and relation to tessellated stress"*, Journal of the Iron and Steel Institute, London **206**, 595 (1968).

[Brown Jr. - 1966] W.F. Brown Jr., *Magnetoelastic Interactions*, Springer, Berlin, Heidelberg, New York (1966).

[Brown - 1984] W.F. Brown, *"Tutorial Paper on Dimensions and Units"*, IEEE Transactions on Magnetics **MAG-20**(1), 112 (1984).

[Buschow - 1983] K.H.J. Buschow, P.G. van Engen, and R. Jongebreur, *"Magneto-optical properties of metallic ferromagnetic materials"*, Journal of Magnetism and Magnetic Materials **38**, 1 (1983).

[Carcia - 1985] P.F. Carcia, A.D. Meinhaldt, and A. Suna, *"Perpendicular magnetic anisotropy in Pd/Co thin film layered structures"*, Applied Physics Letters **47**(2), 178 (1985).

[Carcia - 1988] P.F. Carcia, *"Perpendicular magnetic anisotropy in Pd/Co and Pt/Co thin-film layered structures"*, Journal of Applied Physics **63**(10), 5066 (1988).

[Carcia - 1990a] P.F. Carcia, S.I. Shah, and W.B. Zeper, *"Effect of energetic bombardment on the magnetic coercivity of sputtered Pt/Co thin-film multilayers"*, Applied Physics Letters **56**(23), 2345 (1990a).

[Carcia - 1990b] P.F. Carcia and W.B. Zeper, *"Sputtered Pt Co Multilayers for Magneto-Optical Recording"*, IEEE Transactions on Magnetics **26**(5), 1703 (1990b).

[Carcia - 1993] P.F. Carcia, Z.G. Li, and W.B. Zeper, *"Effect of Sputter-Deposition Processes on the Microstructure and Magnetic Properties of Pt/Co Multilayers"*, Journal of Magnetism and Magnetic Materials **121**(1-3), 452 (1993).

[Carcia - 1995] P.F. Carcia, Z.G. Li, H.W. Vankesteren, and M.T. Johnson, *"Heteroepitaxial Growth of Pt/Co Multilayers on Single Crystal ZnO"*, Journal of Magnetism and Magnetic Materials **145**(1-2), 231 (1995).

[Carey - 1966] R. Carey and E.D. Isaac, *Magnetic Domains and Techniques for their Observation*, Academic Press, New York (1966).

[Celotta - 1999] R.J. Celotta, J. Unguris, M.H. Kelley, and D.T. Pierce, *Techniques to measure magnetic domain structures*, Wiley, New York (1999).

[Chapman - 1978] J.N. Chapman, P.E. Batson, E.M. Waddell, and R.P. Ferrier, *"The direct determination of magnetic domain wall profiles by differential phase contrast electron microscopy"*, Ultramicroscopy **3**(2), 203 (1978).

[Chapman - 1981] J.N. Chapman, G.R. Morrison, D. Fort, and D.W. Jones, *"An electron microscope investigation of domain structures in thin terbium foils"*, Journal of Magnetism and Magnetic Materials **22**(3), 212 (1981).

[Chapman - 1984] J.N. Chapman, *"The investigation of magnetic domain structures in thin foils by electron microscopy"*, Journal of Physics D (Applied Physics) **17**(4), 623 (1984).

[Chapman - 1990] J.N. Chapman, I.R. McFadyen, and S. McVitie, *"Modified differential phase contrast Lorentz microscopy for improved imaging of magnetic structures"*, IEEE Transactions of Magnetics **26**(5), 1506 (1990).

[Chapman - 1999] J.N. Chapman and M.R. Scheinfein, *"Transmission electron microscopies of magnetic microstructures"*, Journal of Magnetism and Magnetic Materials **200**, 729 (1999).

[Chappert - 1998] C. Chappert, H. Bernas, J. Ferre, V. Kottler, J.-P. Jamet, Y. Chen, E. Cambril, T. Devolder, F. Rousseaux, V. Mathet, and H. Launois, *"Planar patterned magnetic media obtained by ion irradiation"*, Science **280**(5371), 1919 (1998).

[Charap - 1997] S.H. Charap, L. Pu-Ling, and H. Yanjun, *"Thermal stability of recorded information at high densities"*, IEEE Transactions on Magnetics **33**(1.2), 978 (1997).

[Chikazumi - 1965] S. Chikazumi, *Physics of Magnetism*, Wiley, New York (1965).

[Cho - 1992a] N.H. Cho, K.M. Krishnan, and R.F.C. Farrow, *"Twin formation in seeded Co/Pt superlattices grown by MBE"*, Applied Physics Letters **60**(19), 2371 (1992a).

[Cho - 1992b] N.H. Cho, K.M. Krishnan, C.A. Lucas, and R.F.C. Farrow, *"Microstructure and Magnetic Anisotropy of Ultrathin Co/Pt Multilayers Grown on GaAs (111) by Molecular-Beam Epitaxy"*, Journal of Applied Physics **72**(12), 5799 (1992b).

[Cohen - 1965] M.S. Cohen, *"Magnetic measurements with Lorentz microscopy"*, IEEE Transactions of Magnetics 1, 156 (1965).

[Comstock - 1999] R.L. Comstock, *Introduction to magnetism and magnetic recording*, Wiley, New York (1999).

[Craik - 1974] D.J. Craik, *"The observation of magnetic domains"*, in: Methods of Experimental Physics ed. by R.V. Coleman (Academic Press, New York) **11**, 675 (1974)

[Crozier - 1995] P.A. Crozier, *"Quantitative elemental mapping of materials by energy-filtered imaging"*, Ultramicroscopy **58**(2), 157 (1995).

[Cullity - 1972] B.D. Cullity, *Introduction to magnetic materials*, Addison-Wesley Publishing Company, Inc., Reading, MA (1972).

[Cullity - 1978] B.D. Cullity, *Elements of x-ray diffraction*, Addison-Wesley, Reading, MA (1978).

[Daalderop - 1994a] G.H.O. Daalderop, P.J. Kelly, and M.F.H. Schuurmans, *"Magnetic anisotropy of a free-standing Co monolayer and of multilayers which contain Co monolayers"*, Physical Review B-Condensed Matter **50**(14), 9989 (1994a).

[Daalderop - 1994b] G.H.O. Daalderop, P.J. Kelly, and M.F.H. Schuurmans, *"Magnetic Anisotropy from First Principle"*, in: Ultrathin Magnetic Structures I ed. by J. A. C. Bland and B. Heinrich (Springer-Verlag, Berlin) 40 (1994b)

[Daniel - 1998] *Magnetic Recording: The First 100 Years*, ed. by E.D. Daniel, C.D. Mee, and M.H. Clark, IEEE Press, New York (1998)

[Daykin - 1995] A.C. Daykin and A.K. Petford-Long, *"Quantitative mapping of the magnetic induction distribution using Foucault images formed in a transmission electron microscope"*, Ultramicroscopy **58**(3-4), 365 (1995).

[den Boreder - 1991] F.J.A. den Boreder, W. Hoving, and P.J.H. Bloemen, Journal of Magnetism and Magnetic Materials **93**, 562 (1991).

[den Broeder - 1988] F.J.A. den Broeder, D. Kuiper, A.P. van de Mosselaer, and W. Hoving, *"Perpendicular magnetic anisotropy of Co-Au multilayers induced by interface sharpening"*, Physical Review Letters **60**(26), 2769 (1988).

[den Broeder - 1992] F.J.A. den Broeder, H.W. van Kesteren, W. Hoving, and W.B. Zeper, *"Co/Ni multilayers with perpendicular magnetic anisotropy: Kerr effect and thermomagnetic writing"*, Applied Physics Letters **61**(12), 1468 (1992).

[Denbeaux - 2001] G. Denbeaux, P. Fischer, G. Kusinski, M.L. Gros, A. Pearson, and D. Attwood, *"A Full Field Transmission X-ray Microscope as a tool for High-Resolution Magnetic Imaging"*, IEEE Transactions on Magnetics **37**(4.1), 2764 (2001).

[Devolder - 1999] T. Devolder, C. Chappert, Y. Chen, E. Cambril, H. Bernas, J.-P. Jamet, and J. Ferré, *"Sub-50 nm planar magnetic nanostructures fabricated by ion irradiation"*, Appl. Phys. Lett. **74**, 3383 (1999).

[Devolder - 2000a] T. Devolder, *"Light ion irradiation of Co/Pt systems: Structural origin of the decrease in magnetic anisotropy"*, Physical Review B **62**(9), 5794 (2000a).

[Devolder - 2000b] T. Devolder, C. Chappert, V. Mathet, H. Bernas, Y. Chen, J.P. Jamet, and J. Ferre, *"Magnetization reversal in irradiation-fabricated nanostructures"*, Journal of Applied Physics **87**(12), 8671 (2000b).

[Doerner - 2001] M. Doerner, X.P. Bian, M. Madison, K. Tang, Q.Z. Peng, A. Polcyn, T. Arnoldussen, M.F. Toney, M. Mirzamaani, K. Takano, E. Fullerton, D. Margulies, M. Schabes, K. Rubin, M. Pinarbasi, S. Yuan, M. Parker, and D. Weller, *"Demonstration of 35 Gbits/in(2) in media on glass*

substrates", IEEE Transactions on Magnetics **37**(2.2), 1052 (2001).

[Donnet - 1995] D. Donnet and K.M. Krishnan, *"Domain structutes in epitaxially grown cobalt thin films"*, Journal of Physics D (Applied Physics) **28**, 1942 (1995).

[Donovan - 1983] P.E. Donovan and W.M. Stobbs, *"Magnetic domain structures in deformed and undeformed foils of a metallic glass"*, Journal of Magnetism and Magnetic Materials **37**(3), 257 (1983).

[Dooley - 1997a] J. Dooley and M. De Graef, *"Energy filtered Lorentz microscopy"*, Ultramicroscopy **67**, 113 (1997a).

[Dooley - 1997b] J. Dooley and M. De Graef, *"Energy Filtered Magnetic Induction Mapping"*, Micron **28**(5), 371 (1997b).

[Draaisma - 1988] H.J.G. Draaisma, F.J.A. den Boreder, and W.J.M. de Jonge, *"Perpendicular anisotropy in Pd/Co multilayers"*, Journal of Applied Physics **63**(8), 3479 (1988).

[Edington - 1974] J.W. Edington, *The operation and calibration of the electron microscope*, The MacMillan Press LTD, (1974).

[Egerton - 1996] R.F. Egerton, *Electron Energy-Loss Spectroscopy in the Electron Microscope*, Plenum Press, (1996).

[Egerton - 1999] R.F. Egerton, *"Spatial resolution of nanostructural analysis by electron energy-loss spectroscopy and energy filtered imaging"*, Journal of Electron Microscopy **48**(6), 711 (1999).

[Eimuller - 1999] T. Eimuller, P. Fischer, G. Schutz, P. Guttmann, G. Schmahl, K. Pruegl, and G. Bayreuther, *"Magnetic transmission X-ray microscopy: imaging magnetic domains via the X-ray magnetic circular dichroism"*, Journal of Alloys and Compounds **286**(1-2), 20 (1999).

[Eimuller - 2000] T. Eimuller, R. Kalchgruber, P. Fischer, G. Schutz, P. Guttmann, G. Schmahl, M. Kohler, K. Prugl, M. Scholz, F. Bammes, and G. Bayreuther, *"Quantitative imaging of magnetization reversal in FeGd multilayers by magnetic transmission x-ray microscopy"*, Journal of Applied Physics **87**(9.3), 6478 (2000).

[Eimuller - 2001] T. Eimuller, P. Fischer, G. Schutz, M. Scholz, G. Bayreuther, P. Guttmann, G. Schmahl, and M. Kohler, *"Magnetization reversal of a multilayered FeGd dot array imaged by transmission x-ray microscopy"*, Journal of Applied Physics **89**(11.2), 7162 (2001).

[Falicov - 1990] L.M. Falicov, D.T. Pierce, S.D. Bader, R. Gronsky, K.B. Hathaway, H.J. Hopster, D.N. Lambeth, S.S.P. Parkin, G. Prinz, M. Salamon, I.K. Schuller, and R.H. Victora, *"Surface, interface, and thin-film magnetism"*, Journal of Materials Research **5**(6), 1299 (1990).

[Faraday - 1846] M. Faraday, *"On the magnetization of light and the illumination of magnetic lines of force"*, Philosophical Transactions of the Royal Society (London) **136**, 1 (1846).

[Farhoud - 1998] M. Farhoud, M. Hwang, H.I. Smith, M.L. Schattenburg, J.M. Bae, K. Youcef-Toumi, and C.A. Ross, *"Fabrication of large area nanostructured magnets by interferometric lithography"*, IEEE Transactions on Magnetics **34**, 1087 (1998).

[Fermi - 1947] E. Fermi and E. Teller, Physical Review **72**, 399 (1947).

[Ferre - 1999] J. Ferre, C. Chappert, H. Bernas, J.-P. Jamet, P. Meyer, O. Kaitasov, S. Lemerle, V. Mathet, F. Rousseaux, and H. Launois, *"Irradiation Induced Effects on Magnetic Properties of Pt/Co/Pt Ultrathin Films"*, Journal of Magnetism and Magnetic Materials **191**, 198 (1999).

[Firsov - 1959] O.B. Firsov, Soviet Physics JETP **36**, 1076 (1959).

[Fischer - 1996] P. Fischer, G. Schutz, G. Schmahl, P. Guttmann, and D. Raasch, *"Imaging of Magnetic Domains with the X-Ray Microscope at Bessy Using X-Ray Magnetic Circular Dichroism"*, Zeitschrift Fur Physik B-Condensed Matter **101**(3), 313 (1996).

[Fischer - 1999] P. Fischer, T. Eimuller, R. Kalchgruber, G. Schutz, G. Schmahl, P. Guttmann, and G. Bayreuther, *"X-ray magnetic circular dichroism used to image magnetic domains"*, Journal of Synchrotron Radiation **6**(3), 688 (1999).

[Fischer - 2001a] P. Fischer, T. Eimuller, G. Schutz, G. Bayreuther, S. Tsunashima, N. Takagi, G. Denbeaux, and D. Attwood,

"Magnetic domains in nanostructured media studied with M-TXM", Journal of Synchrotron Radiation **8**(T2), 325 (2001a).

[Fischer - 2001b] P. Fischer, T. Eimuller, G. Schutz, G. Denbeaux, A. Pearson, L. Johnson, D. Attwood, S. Tsunashima, M. Kumazawa, N. Takagi, M. Kohler, and G. Bayreuther, *"Element-specific imaging of magnetic domains at 25 nm spatial resolution using soft x-ray microscopy"*, Review of Scientific Instruments **72**(5), 2322 (2001b).

[Fischer - 2001c] P. Fischer, T. Eimuller, G. Schutz, M. Kohler, G. Bayreuther, G. Denbeaux, and D. Attwood, *"Study of in-plane magnetic domains with magnetic transmission x-ray microscopy"*, Journal of Applied Physics **89**(11.2), 7159 (2001c).

[Foner - 1959] S. Foner, *"Versatile and sensitive vibrating-sample magnetometer"*, The Review of Scientific Instruments **30**(7), 548 (1959).

[Foner - 1975] S. Foner, *"Further improvements in vibrating sample magnetometer sensitivity"*, Review of Scientific Instruments **46**, 1425 (1975).

[Foner - 1981] S. Foner, *"Review of magnetometry"*, IEEE Transactions of Magnetics **17**, 3358 (1981).

[Fowler - 1992] D.E. Fowler, *"Magneto-optic Kerr rotation"*, in: Encyclopedia of Materials Characterization ed. by C.R. Brundle (Butterworth-Heinemann, Boston, MA) **Sec. 12.3**, (1992)

[Fowler Jr. - 1952] C.A. Fowler Jr. and E.M. Fryer, *"Magnetic domains on silicon iron by the longitudinal Kerr effect"*, Physical Review **86**, 426 (1952).

[Fowler Jr. - 1956] C.A. Fowler Jr. and E.M. Fryer, *"Magnetic domains in thin films by the Faraday effect"*, Physical Review **104**, 552 (1956).

[Freeman - 2001] M.R. Freeman and B.C. Choi, *"Advances in Magnetic Microscopy"*, Science **294**(5546), 1484 (2001).

[Fuller - 1960] H.W. Fuller and M.E. Hale, *"Determination of magnetization distribution in thin foils using electron microscopy"*, Journal of Applied Physics **31**, 238 (1960).

[Futamoto - 1999] M. Futamoto, N. Inaba, Y. Hirayama, K. Ito, and Y. Honda, *"Microstructure and micromagnetics of future thin-film media"*, Journal of Magnetism and Magnetic Materials **193**, 36 (1999).

[Ganesan - 2000] S. Ganesan, C.M. Park, K. Hattori, H.C. Park, R.L. White, H. Koo, and R.D. Gomez, *"Properties of lithographically formed cobalt and cobalt alloy single crystal patterned media"*, IEEE Transactions on Magnetics **36**(5.1), 2987 (2000).

[Gass - 1993] I.G. Gass and H.M. Prichard, *Magmatic processes and plate tectonics*, Geological Society, London (1993).

[Gehanno - 1997] V. Gehanno, A. Marty, B. Gilles, and Y. Samson, *"Magnetic domains in epitaxial ordered FePd(001) thin films with perpendicular magnetic anisotropy"*, Physical Review B **55**, 12552 (1997).

[Geisler - 1952] A.H. Geisler and D.L. Martin, *"A New Superlattice in Co-Pt Alloys"*, Journal of Applied Physics **23**(3), 375 (1952).

[Gradmann - 1968] U. Gradmann and J. Muller, Phys. Status Solidi **27**, 313 (1968).

[Gradmann - 1986] U. Gradmann, *"Magnetis surface anisotropies"*, Journal of Magnetism and Magnetic Materials **54**, 733 (1986).

[Greidanus - 1989a] F. Greidanus, W.B. Zeper, B.A.J. Jacobs, J.H.M. Spruit, and P.F. Carcia, *"Magneto-Optical Recording in Co/Pt Multilayers"*, Japanese Journal of Applied Physics Part 1-Regular Papers & Short Notes **V28**(S28-3), 37 (1989a).

[Greidanus - 1989b] F.J.A.M. Greidanus, B.A.J. Jacobs, F.J.A. den Broeder, J.H.M. Spruit, and M. Rosenkranz, *"Lorentz microscopy on dynamically written domains in GdTbFe"*, Applied Physics Letters **54**(10), 963 (1989b).

[Greidanus - 1989c] F.J.A.M. Greidanus, W.B. Zeper, F.J.A. den Broeder, W.F. Godlieb, and P.F. Carcia, *"Thermomagnetic writing in thin Co/Pt layered structures"*, Applied Physics Letters **54**(24), 2481 (1989c).

[Grogger - 2000] W. Grogger, F. Hofer, P. Warbichler, and G. Kothleitner, *"Quantitative energy-filtering transmission electron*

microscopy in materials science", Microscopy and Microanalysis **6**(2), 161 (2000).

[Grogger - 2001] W. Grogger and K.M. Krishnan, *"Scatter diagram analysis of Cr segregation in Co-Cr based recording media"*, IEEE Transactions on Magnetics **37**(4.1), 1465 (2001).

[Grutter - 1992] P. Grutter, H.J. Mamin, and D. Rugar, *"Magnetic force microscopy (MFM)"*, in: Scanning Tunneling Microscopy ed. by H.-J. Guntherodt and R. Wiesendanger (Springer, Berlin, Heidelberg, New York) **Vol. II**, 151 (1992)

[Gubbens - 1993] A.J. Gubbens and O.L. Krivanek, *"Applications of a Post-Column Imaging Filter in Biology and Materials Science"*, Ultramicroscopy **51**(1-4), 146 (1993).

[Guruswamy - 1998] S. Guruswamy, J.E. Shield, and M. Tarakci, *"Control of crystallographic texture in magnetic thin films for ultra-high density storage media"*, Scripta Materialia **39**(4-5), 647 (1998).

[Hadjipanayis - 1982] G.C. Hadjipanayis, R.C. Hazelton, K.R. Lawless, and L.S. Horton, "Magnetic domains in rare-earth cobalt permanent magnets," presented at the Third Joint INTERMAG-Magnetism and Magnetic Materials Conference, Montreal, Que., Canada 20-23 July 1982, 1982 (unpublished).

[Hale - 1959] M.E. Hale, H.W. Fuller, and H. Rubinstein, *"Magnetic domain observation by electron microscopy"*, Journal of Applied Physics **30**, 789 (1959).

[Hansen - 1958] M. Hansen, *Constitution of Binary Alloys*, 2nd ed., MCGraw-Hill, New-York (1958).

[Hashimoto - 1989] S. Hashimoto, Y. Ochiai, and K. Aso, *"Light wavelength dependence of magneto-optical properties in ultrathin Co/Pt and Co/Pd multilayered films"*, Japanese Journal of Applied Physics, Part 1 (Regular Papers & Short Notes) **28**(10), L1824 (1989).

[Heisenberg - 1928] W. Heisenberg, *"Zur Theorie des Ferromagnetismus (On the theory of ferromagnetism)"*, Zeitschrift Fur Physik B-Condensed Matter **49**, 619 (1928).

[Herd - 1979] S.R. Herd, K.Y. Ahn, and S.M. Kane, "Magnetization reversal in narrow strips of NiFe thin films," presented at the Joint INTERMAG-MMM Conference, New York, NY, USA 17-20 July 1979, 1979 (unpublished).

[Herrmann - 2000] M. Herrmann, S. McVitie, and J.N. Chapman, *"Investigation of the influence of edge structure on the micromagnetic behavior of small magnetic elements"*, Journal of Applied Physics **87**(6), 2994 (2000).

[Hofer - 1995] F. Hofer, P. Warbichler, and W. Grogger, *"Characterization of nanometer sized precipitates in solids by electron spectroscopic imaging"*, Ultramicroscopy **59**, 15 (1995).

[Hofer - 1997] F. Hofer, W. Grogger, G. Kothleitner, and P. Warbichler, *"Quantitative analysis of EFTEM elemental distribution images"*, Ultramicroscopy **67**(1-4), 83 (1997).

[Hoffmann - 1979] H. Hoffmann, A.J. Owen, and F. Schrope, *"Electron microscopy of evaporated and sputtered Gd/Co and Ho/Co films"*, Physica Status Solidi A **52**(1), 161 (1979).

[Hubert - 1998] A. Hubert and R. Schafer, *Magnetic Domains: the analysis of magnetic microstructures*, Springer-Verlag, Berlin (1998).

[Huetten - 1995] A. Huetten, J. Bernardi, C. Nelson, and G. Thomas, *"Lorentz microscopy of giant magnetoresistive Au-Co alloys"*, Physica Status Solidi A **150**(1), 171 (1995).

[Hyndman - 2001] R. Hyndman, P. Warin, J. Gierak, J. Ferre, J.N. Chapman, J.P. Jamet, V. Mathet, and C. Chappert, *"Modification of Co/Pt multilayers by gallium irradiation - Part 1: The effect on structural and magnetic properties"*, Journal of Applied Physics **90**(8), 3843 (2001).

[Inaba - 1997] N. Inaba, T. Yamamoto, Y. Hosoe, and M. Futamoto, *"Microstructural segregation in CoCrTa and CoCrPt longitudinal magnetic recording media"*, Journal of Magnetism and Magnetic Materials **168**(1-2), 222 (1997).

[Inaba - 2000] N. Inaba and M. Futamoto, *"Effects of Pt and Ta addition on compositional microstructure of CoCr-alloy thin film media"*, Journal of Applied Physics **87**(9.3), 6863 (2000).

[Iwasaki - 1975] S.I. Iwasaki and K. Takemura, *"An analysis for the circular mode of magnetization in short wavelength recording"*, IEEE Transactions on Magnetics **MAG-11**, 1173 (1975).

[Iwasaki - 1977] S.I. Iwasaki and Y. Nakamura, IEEE Transactions on Magnetics **MAG-13**, 1272 (1977).

["J.F. Ziegler and J.P. Biersack" -] http://www.research.ibm.com/ionbeams/(2000)

[Jakubovics - 1994] J.P. Jakubovics, *Magnetism and Magnetic Materials*, The Institute of Materials, London (1994).

[Jiles - 1995] D. Jiles, *Introduction to Magnetism and Magnetic Materials*, Chapman & Hall, London (1995).

[Johnson - 1996] K.E. Johnson, C.M. Mate, J.A. Merz, R.L. White, and A.W. Wu, *"Thin-Film Media - Current and Future Technology"*, IBM Journal of Research and Development **40**(5), 511 (1996).

[Jorgensen - 1999] F. Jorgensen, *"The inventor Valdemar Poulsen"*, Journal of Magnetism and Magnetic Materials **193**, 1 (1999).

[Karamon - 1982] H. Karamon, G.F. Rempfer, J. Dash, and M. Takeo, *"Electrostatic TEM studies of twisted domains in thin iron films"*, Journal of Applied Physics **53**(3), 2774 (1982).

[Kemner - 1996] K.M. Kemner, V.G. Harris, V. Chakarian, Y.U. Idzerda, W.T. Elam, C.C. Kao, Y.C. Feng, D.E. Laughlin, and J.C. Woicik, *"The Role of Ta and Pt in Segregation within Co-Cr-Ta and Co-Cr-Pt Thin Film Magnetic Recording Media"*, Journal of Applied Physics **79**(8), 5345 (1996).

[Kerr - 1877] J.C. Kerr, *"On rotation of the plane of polarization by reflection from the pole of a magnet"*, Philosophical Magazine B **3**, 321 (1877).

[Kim - 2001] J. Kim, J.-W. Lee, J.-R. Jeong, S.-K. Kim, and S.-C. Shin, *"Influence of substrate roughness on spin reorientation transition of ultrathin Co films on Pd(111)"*, Applied Physics Letters **79**(1), 93 (2001).

[Kirk - 1999] K.J. Kirk, J.N. Chapman, S. McVitie, P.R. Aitchison, and C.D.W. Wilkinson, *"Switching of nanoscale magnetic elements"*, Applied Physics Letters **75**(23), 3683 (1999).

[Kittel - 1956] C. Kittel and J.K. Galt, *"Ferromagnetic domain theory"*, Solid State Physics **3**, 437 (1956).

[Kittel - 1996] C. Kittel, *Introduction to Solid State Physics*, 7th ed., John Wiley & Sons, Inc., New York (1996).

[Kohler - 2000] M. Kohler, T. Schweinbock, T. Schmidt, J. Zweck, G. Bayreuther, P. Fischer, G. Schutz, T. Eimuller, P. Guttmann, and G. Schmahl, *"Imaging of sub-100-nm magnetic domains in atomically stacked Fe(001)/Au(001) multilayers"*, Journal of Applied Physics **87**(9.3), 6481 (2000).

[Kooy - 1960] C. Kooy and U. Enz, *"Experimental and theoretical study of the domain configuration in thin layers of BaFe12O19"*, Philips Research Reports **15**, 7 (1960).

[Krakow - 1976] W. Krakow and L.A. Howland, *"A method for producing hollow cone illumination electronically in the conventional transmission microscope"*, Ultramicroscopy **2**(1), 53 (1976).

[Krishnan - 1994] K.M. Krishnan, Y. Honda, Y. Hirayama, and M. Futamoto, *"Microstructure and epitaxy of c-axis oriented single crystal cobalt films grown on rigid underlayers"*, Applied Physics Letters **64**, 1499 (1994).

[Krishnan - in press] K.M. Krishnan, *"Magnetism and Microstructure: Imaging Techniques and Structure - Property Correlations in Information Storage Materials"*, in: NATO/ASI, Magnetic Storage Systems Beyond 2000 ed. by G. Hadjipanayis (Kluwer Academic Publishers, 12-23 June 2000, Rhodes, Greece) (in press)

[Krivanek - 1992] O.L. Krivanek, A.J. Gubbens, N. Dellby, and C.E. Meyer, *"Design and first applications of a post-column imaging filter"*, Microscopy, Microanalysis, Microstructures **3**(2-3), 187 (1992).

[Krivanek - 1994] O.L. Krivanek, M.K. Kundmann, and X. Bourrat, "Elemental mapping by energy-filtered electron microscopy," 1994 (unpublished).

[Kryder - 1993] M.H. Kryder, *"Magneto-optical storage materials"*, Annual Review of Materials Science **23**, 411 (1993).

[Kulesko - 1968] G.I. Kulesko and A.L. Seryugin, *"Geometrical Shape of Martensitic Plates in Cobalt"*, Physics of Metals and Metallography, Translated from Fizika Metallov, Metallovedenie **26**(2), 140 (1968).

[Kusinski - 2000] G.J. Kusinski, K.M. Krishnan, G. Thomas, and E.C. Nelson, *"Domain structures and temperature-dependent spin reorientation transitions in c-axis oriented Co-Cr thin films"*, Journal of Applied Physics **87**(9.3), 6376 (2000).

[Kusinski - 2001a] G.J. Kusinski, K.M. Krishnan, G. Denbeaux, G. Thomas, D. Weller, and B.D. Terris, *"Magnetic imaging of ion-irradiation patterned Co/Pt multilayers using complementary electron and photon probes"*, Applied Physics Letters **79**(14), 2211 (2001a).

[Kusinski - 2001b] G.J. Kusinski, K.M. Krishnan, D. Weller, B.D. Terris, L. Folks, A.J. Kellock, J.E.E. Baglin, and G. Thomas, *"Lorentz transmission electron microscopy investigation of magnetically patterned Co/Pt multilayers"*, in: Magnetic Storage Systems Beyond 2000 ed. by G. Hadjipanayis (Kluwer Academic Publishers, **41**, 157 (2001b)

[Kusinski - 2002] G.J. Kusinski, G. Thomas, G. Denbeaux, K.M. Krishnan, and B.D. Terris, *"Temperature and irradiation dose dependence of magnetic domains and microstructure in Co/Pt multilayers"*, Journal of Applied Physics **in press** (2002).

[Kuznetsov - 1965] V.G. Kuznetsov, M.A. Sokolova, K.K. Palkina, and Z.V. Popova, *"The Cobalt-Sulfur System"*, Inorganic Materials, Translated from Izvestiya Akademii Nauk SSSR, Neorganicheskie Materialy **1**(5), 617 (1965).

[Lambert - 1991] S.E. Lambert, I.L. Sanders, A.M. Patlach, M.T. Krounbi, and S.R. Hetzler, *"Beyond Discrete Tracks - Other Aspects of Patterned Media"*, Journal of Applied Physics **69**(8), 4724 (1991).

[Lambeth - 2000] D.N. Lambeth, *"Hard disk media: future problems and possible solutions"*, Vacuum **59**(2-3), 522 (2000).

[Landau - 1935] L.D. Landau and E. Lifshitz, *"On the theory of the dispersion of magnetic permeability in ferromagnetic bodies"*, Phys. Z. Sowjetunion **8**, 153 (1935).

[Lee - 1994] L.L. Lee, D.E. Laughlin, and D.N. Lambeth, *"Nial Underlayers for Cocrta Magnetic Thin Films"*, IEEE Transactions on Magnetics **30**(6), 3951 (1994).

[Lee - 1996] L.L. Lee, D.E. Laughlin, and D.N. Lambeth, *"Seed Layer Induced (002) Crystallographic Texture in NiAl Underlayers"*, Journal of Applied Physics **79**(8), 4902 (1996).

[Lemerle - 1998] S. Lemerle, J. Ferre, C. Chappert, V. Mathet, T. Giamarchi, and P. LeDoussal, *"Domain wall creep in an Ising ultrathin magnetic film"*, Physical Review Letters **80**(4), 849 (1998).

[Li - 1992] Z.G. Li and P.F. Carcia, *"Microstructural Dependence of Magnetic Properties of Pt/Co Multilayer Thin Films"*, Journal of Applied Physics **71**(2), 842 (1992).

[Li - 1993] Z.G. Li, P.F. Carcia, and Y. Cheng, *"Co Thickness Dependence of the Microstructure of Pt/Co Multilayers"*, Journal of Applied Physics **73**(5), 2433 (1993).

[Lu - 1999] B. Lu, D.E. Laughlin, D.N. Lambeth, S.Z. Wu, R. Ranjan, and G.C. Rauch, *"Texture evolution in CoCrPtTa/Cr/NiAl magnetic recording media"*, Journal of Applied Physics **85**(8.2A), 4295 (1999).

[Maclaren - 1994] J.M. Maclaren and R.H. Victora, *"Theoretical Predictions of Interface Anisotropy in the Presence of Interdiffusion (Invited)"*, Journal of Applied Physics **76**(10), 6069 (1994).

[Maclaren - 1995] J.M. Maclaren and R.H. Victora, *"Perpendicular Magnetic Anisotropies of (Pt/Co/Pt)/X Superlattices"*, Applied Physics Letters **66**(24), 3377 (1995).

[Massalski - 1990] *Binary Alloy Phase Diagrams*, ed. by T.B. Massalski, ASM International, The Materials Information Society, (1990)

[McFadyen - 1992] I.R. McFadyen and J.N. Chapman, *"Electron Microscopy of Magnetic Materials"*, EMSA Bulletin **22**, 64 (1992).

[McIntyre - 1997] P.C. McIntyre, D.T. Wu, and M. Nastasi, *"Interdiffusion in epitaxial Co/Pt multilayers"*, Journal of Applied Physics **81**(2), 637 (1997).

[McKendrick - 1976] W. McKendrick, J.N. Chapman, R.P. Ferrier, and D.A. Hukin, "Domain and domain-wall structures in gadolinium foils," presented at the International Conference on Magnetism, Amsterdam, Netherlands 6-10 Sept. 1976, 1976 (unpublished).

[Mirzamaani - 1994] M. Mirzamaani, M.A. Russak, and C.V. Jahnes, *"Thin Film Disks for High Density Recording with Textured Underlayers"*, Journal of Applied Physics **75**(10), 6159 (1994).

[Mirzamaani - 1998] M. Mirzamaani, X.P. Bian, M.F. Doerner, J.S. Li, and M. Parker, *"Recording performance of thin film media with various crystallographic preferred orientations on glass substrates"*, IEEE Transactions on Magnetics **34**(4.1), 1588 (1998).

[Moog - 1981] E.R. Moog and S.D. Bader, *"SMOKE signals from ferromagnetic monolayers: p(1X1) Fe/Au(100)"*, Superlattices and Microstructures **1**, 543 (1981).

[Moog - 1991] E.R. Moog, J. Zak, and S.D. Bader, *"Kerr effect from Pt/Co superlattices and the role of the magneto-optic activity of Pt"*, Journal of Applied Physics **69**(2), 880 (1991).

[Moore - 2002] K.T. Moore, E.A. Stach, J.M. Howe, D.C. Elbert, and D.R. Veblen, *"A tilting procedure to enhance compositional contrast and reduce residual diffraction contrast in energy-filtered TEM imaging of planar interfaces"*, Micron **33**(1), 39 (2002).

[Moser - 1999a] A. Moser and D. Weller, *"Thermal processes and stability of longitudinal magnetic recording media"*, IEEE Transactions on Magnetics **35**(5.1), 2808 (1999a).

[Moser - 1999b] A. Moser, D. Weller, and M.F. Doerner, *"Thermal stability of longitudinal magnetic recording media"*, Applied Physics Letters **75**(11), 1604 (1999b).

[Nakamura - 1990a] Y. Nakamura, K. Ouchi, and I. Watanabe, *"Evaluation of perpendicular magnetic rigid disk by non-flying single-pole*

head", IEEE Translation Journal on Magnetics in Japan **5**(10), 885 (1990a).

[Nakamura - 1990b] Y. Nakamura, K. Ouchi, S. Yamamoto, and I. Watanabe, *"Recording characteristics of perpendicular magnetic hard disk measured by nonflying single-pole head"*, IEEE Transactions on Magnetics **26**(5), 2436 (1990b).

[Nakamura - 1991] Y. Nakamura, Journal of the Magnetic Society of Japan **15**, 497 (1991).

[Nakamura - 1999] Y. Nakamura, *"Perpendicular magnetic recording - progress and prospects"*, Journal of Magnetism and Magnetic Materials **200**, 634 (1999).

[Néel - 1954] L. Néel, *"Anisotropie magnetique superficielle et surstructures dorientation"*, Journal de Physique et le Radium **15**(4), 225 (1954).

[Nowak - 1979] J. Nowak and W. Scharff, *"Magnetisation ripple structure in neodymium-cobalt thin films"*, Journal of Physics D (Applied Physics) **12**(11), L139 (1979).

[Ochiai - 1989] Y. Ochiai, S. Hashimoto, and K. Aso, *"Co/Pt and Co/Pd ultrathin-multilayered films as new magneto-optical recording materials"*, IEEE Transactions of Magnetics **25**(5), 3755 (1989).

[O'Grady - 1999] K. O'Grady and H. Laidler, *"The limits to magnetic recording - media considerations"*, Journal of Magnetism and Magnetic Materials **200**, 616 (1999).

[O'Keefe - 1992] M.A. O'Keefe, *"Resolution in High-Resolution Electron Microscopy"*, Ultramicroscopy **47**(1-3), 282 (1992).

[O'Keefe - 2001a] M.A. O'Keefe, C.J.D. Hetherington, Y.C. Wang, E.C. Nelson, J.H. Turner, C. Kisielowski, J.-O. Malm, R. Mueller, J. Ringnalda, M. Pan, and A. Thust, *"Sub-Ångstrom High-Resolution Transmission Electron Microscopy at 300keV"*, Ultramicroscopy **89**(4), 215 (2001a).

[O'Keefe - 2001b] M.A. O'Keefe, E.C. Nelson, Y.C. Wang, and A. Thust, *"Sub-Ångstrom resolution of atomistic structures below 0.8Å"*, Philosophical Magazine B **81**(11), 1861 (2001b).

[Osborne - 2001] I.S. Osborne, *"The Attraction of Magnetism"*, Science **294**(5546), 1483 (2001).

[Ouchi - 1994] K. Ouchi, S. Onodera, Y. Nakamura, and S. Iwasaki, *"Co-Cr perpendicular media with semi-soft magnetic and ultra thin back layer for ring-type head"*, Journal of Magnetism and Magnetic Materials **134**(2-3), 323 (1994).

[PetfordLong - 1998] A.K. PetfordLong, X. Portier, P. BayleGuillemaud, T.C. Anthony, and J.A. Brug, *"In situ transmission electron microscopy studies of the magnetization reversal mechanism in information storage materials"*, Microscopy and Microanalysis **4**(3), 325 (1998).

[Petford-Long - 1999] A.K. Petford-Long, X. Portier, E.Y. Tsymbal, T.C. Anthony, and J.A. Brug, *"In-situ Lorentz microscopy studies of spin-valve structures"*, IEEE Transactions on Magnetics **35**(2.1), 788 (1999).

[Plossl - 1993] R. Plossl, *"The Micromagnetic Structure of Magneto-Optic Materials"*, Ph.D Thesis, University of Regensburg (1993).

[Portier - 1997] X. Portier, A.K. PetfordLong, R.C. Dode, T.C. Anthony, and J.A. Brug, *"Lorentz transmission electron microscopy on NiFe/Cu/Co/NiFe/MnNi active spin valve elements"*, Applied Physics Letters **71**(14), 2032 (1997).

[Pu-Ling - 1994] L. Pu-Ling and S.H. Charap, *"Thermal instability at 10 Gbit/in/sup 2/ magnetic recording"*, IEEE Transactions on Magnetics **30**(6.1-2), 4230 (1994).

[Pu-Ling - 1995] L. Pu-Ling and S.H. Charap, *"High density magnetic recording media design and identification: susceptibility to thermal decay"*, IEEE Transactions on Magnetics **31**(6.1), 2767 (1995).

[Ramesh - 1989] R. Ramesh and G. Thomas, *"Interrelationship between structure and property in magnetic materials"*, Materials science and Engineering **B3**, 435 (1989).

[Rave - 1987] W. Rave, R. Schafer, and A. Hubert, *"Quantitative observation of magnetic domains with the magneto-optical Kerr effect"*, Journal of Magnetism and Magnetic Materials **65**, 7 (1987).

[Reimer - 1984] L. Reimer, *Transmission electron microscopy: physics of image formation and microanalysis*, Springer-Verlag, (1984).

[Rettner - submitted] C.T. Rettner, S. Anders, J.E.E. Baglin, T. Thomson, and B.D. Terris, *"Characterization of the magnetic modification of Co/Pt multilayre films by He+, Ar+, and Ga+ ion irradiation"*, Applied Physics Letters (submitted).

[Ross - 2001] C. Ross, *"Patterned magnetic recording media"*, Annual Review of Materials Research **31**, 203 (2001).

[Ross - 1999] C.A. Ross, H.I. Smith, T. Savas, M. Schattenburg, M. Farhoud, M. Hwang, M. Walsh, M.C. Abraham, and R.J. Ram, *"Fabrication of patterned media for high density magnetic storage"*, Journal of Vacuum Science & Technology B **17**, 3168 (1999).

[Sakurai - 1992] M. Sakurai, T. Takahata, and I. Moritani, *"Magnetic and magneto-optical properties of Co/Ru multilayers"*, IEEE Translation Journal on Magnetics in Japan **7**(2), 176 (1992).

[Sato - 1988] N. Sato, *"Crystallographic structure and magnetism of Co-Pd and Co-Pt films with an artificially layered structure"*, Journal of Applied Physics **64**(11), 6424 (1988).

[Saxton - 1978] W.O. Saxton, W.K. Jenkins, L.A. Freeman, and D.J. Smith, *"TEM observations using bright field hollow cone illumination"*, Optik **49**(4), 507 (1978).

[Schuller - 1999] I.K. Schuller, S. Kim, and C. Leighton, *"Magnetic superlattices and multilayers"*, Journal of Magnetism and Magnetic Materials **200**(1-3), 571 (1999).

[Schutz - 1987] G. Schutz, W. Wagner, W. Wilhelm, P. Kienle, R. Zeller, R. Frahm, and G. Materlik, *"Absorption of circularly polarized X rays in iron"*, Physical Review Letters **58**(7), 737 (1987).

[Shiomi - 1993a] S. Shiomi, T. Nakabayashi, M. Okada, T. Kobayashi, and M. Masuda, *"Magnetic properties and structure of Co/Pt multilayered films evaporated on heated substrates"*, Japanese Journal of Applied Physics, Part 1 (Regular Papers & Short Notes) **32**(2), 791 (1993a).

[Shiomi - 1993b] S. Shiomi, T. Nishimura, T. Kobayashi, and M. Masuda, *"Dependence of Magnetic Properties of Co/Pt Multilayers on*

Deposition Temperature of Pt Buffer Layers", Japanese Journal of Applied Physics Part 2-Letters **32**(4A), L495 (1993b).

[Shiomi - 1994] S. Shiomi and et al., Trans. Mat. Res. Soc. Jpn. **15B** (1994).

[Smith - 1994] D.J. Smith, Z.G. Li, A.R. Modak, S.S.P. Parkin, R.F.C. Farrow, and R.F. Marks, *"High resolution imaging of magnetic multilayers"*, Scripta Metallurgica et Materialia **30**(6), 689 (1994).

[Smith - 1995] D.L. Smith, *Thin-film deposition: principles and practice*, McGraw-Hill Inc., (1995).

[Song - 1993] I.M. Song, S. Ishio, M. Ishizuka, T. Tsunoda, and M. Takahashi, *"Perpendicular Magnetic Anisotropy and Rotational Hysteresis Loss in Co-Cr Films"*, Journal of Magnetism and Magnetic Materials **119**(3), 261 (1993).

[Speliotis - 1999] D.E. Speliotis, *"Magnetic recording beyond the first 100 Years"*, Journal of Magnetism and Magnetic Materials **193**, 29 (1999).

[Stohr - 1998] J. Stohr, H.A. Padmore, S. Anders, T. Stammler, and M.R. Scheinfein, *"Principles of X-ray magnetic dichroism spectromicroscopy"*, Surface Review and Letters **5**(6), 1297 (1998).

[Stohr - 2000] J. Stohr and S. Anders, *"X-ray spectro-microscopy of complex materials and surfaces"*, IBM Journal of Research and Development **44**(4), 535 (2000).

[Streetman - 2000] B.G. Streetman and S. Banerjee, *Solid State Electronic Devices*, Prentice Hall, Upper Saddle River, New Jersey (2000).

[Strzeszewski - 1982] J. Strzeszewski and K. Swiderczak, *"Electron microscopic studies of crystallization and magnetic domain structure of Mn-Ga thin films"*, Physica Status Solidi A **73**(1), 31 (1982).

[Studt - 1995] T. Studt, *"Moores Law Continues into the 21st Century"*, R&D Magazine **37**(12), 33 (1995).

[Suits - 1986] J.C. Suits, R.H. Geiss, C.J. Lin, D. Rugar, and A.E. Bell, *"Lorentz microscopy of micron-sized laser-written magnetic domains in TbFe"*, Applied Physics Letters **49**(7), 419 (1986).

[Tagawa - 1990] I. Tagawa and Y. Nakamura, *"Analysis of head to medium magnetic interaction in perpendicular magnetic recording by finite element method combined with magnetization model"*, IEEE Translation Journal on Magnetics in Japan **5**(3), 261 (1990).

[Tagawa - 1991] I. Tagawa and Y. Nakamura, *"Computer analysis of perpendicular magnetic recording medium for ultra-high density recording"*, IEEE Translation Journal on Magnetics in Japan **6**(8), 654 (1991).

[Tagawa - 1994] I. Tagawa and Y. Nakamura, *"Magnetic recording simulation and its applications"*, Journal of Magnetism and Magnetic Materials **134**, 382 (1994).

[Taylor - 1983] R.A. Taylor and J.P. Jakubovics, "Observations of magnetic domain structures in thick foils of Ni-Fe-Co-Ti alloy," presented at the International Conference on Magnetism, Kyoto, Japan 6-10 Sept. 1982, 1983 (unpublished).

[Terris - 1999] B.D. Terris, L. Folks, D. Weller, J.E.E. Baglin, A.J. Kellock, H. Rothuizen, and P. Vettiger, *"Ion-beam patterning of magnetic films using stencil masks"*, Applied Physics Letters **75**, 403 (1999).

[Terris - 2001] Personal communication: B.D. Terris (IBM Almaden Research Center).

[Thomas - 1981] G. Thomas and M.J. Goringe, *Transmission Electron Microscopy of Materials*, John Wiley & Sons, (1981).

[Thompson - 2000] D.A. Thompson and J.S. Best, *"The future of magnetic data storage technology"*, IBM Journal of Research and Development **44**(3), 311 (2000).

[Toporov - 2000] A.Y. Toporov, R.M. Langford, and A.K. Petford-Long, *"Lorentz transmission electron microscopy of focused ion beam patterned magnetic antidot arrays"*, Applied Physics Letters **77**(19), 3063 (2000).

[Verbist - 1998] K. Verbist, E.C. Nelson, T.C. Anthony, J.A. Brug, and K.M. Krishnan, *"Lorentz transmission electron microscopy in a standard CM200FEG"*, in: ICEM 14, Electron Microscopy 1998 ed. by 08/31 - 09/04, Cancun, Mexico) **2**, 503 (1998)

[Victora - 1994] R.H. Victora and J.M. Maclaren, *"Theoretical Predictions for Magnetic Anisotropy of Superlattice Defects"*, Journal of Applied Physics **75**(10), 6428 (1994).

[Visnovsky - 1995] S. Visnovsky, M. Nyvlt, V. Prosser, R. Lopusnik, R. Urban, J. Ferre, G. Penissard, D. Renard, and R. Krishnan, *"Polar magneto-optics in simple ultrathin-magnetic-film structures"*, Physical Review B (Condensed Matter) **52**(2), 1090 (1995).

[Warin - 2001] P. Warin, R. Hyndman, J. Glerak, J.N. Chapman, J. Ferre, J.P. Jamet, V. Mathet, and C. Chappert, *"Modification of Co/Pt multilayers by gallium irradiation - Part 2: The effect of patterning using a highly focused ion beam"*, Journal of Applied Physics **90**(8), 3850 (2001).

[Watanabe - 1984] M. Watanabe, *"Semiconductor industry in Japan-past and present"*, IEEE Transactions on Electron Devices **ED-31**(11), 1562 (1984).

[Watanbe - 1983] M. Watanbe, "The industry in the '80s," presented at the 1983 Symposium on VLSI Technology. Digest of Technical Papers, Maui, HI, USA 13-15 Sept. 1983, 1983 (unpublished).

[Weiss - 1907] P. Weiss, *"L'hypothese du champ moleculaire et la propriete ferromagnetique (The hypothesis of the molecular field and the property of ferromagnetism)"*, Journal de Physique et le Radium **6**, 661 (1907).

[Weiss - 1926] P. Weiss and G. Foex, *Le Magnetisme (Magnetism)*, Armand Colin, Paris (1926).

[Weller - 1993] D. Weller, R.F.C. Farrow, R.F. Marks, G.R. Harp, H. Notarys, and G. Gorman, *"Interface and volume anisotropy of MBE-grown Co/Pt(111), (110) and (001) and sputtered Co/Pt multilayers"*, in: Magnetic Ultrathin Films. Multilayers and Surfaces, Interfaces and Characterization Symposium ed. by B. T. Jonker, S. A. Chambers, R. F. C. Farrow et al.

(Materials Research Society, San Francisco, CA, USA 12-16 April 1993) **313**, 791 (1993)

[Weller - 1999] D. Weller and A. Moser, *"Thermal effect limits in ultrahigh-density magnetic recording"*, IEEE Transactions on Magnetics **35**, 4423 (1999).

[Weller - 2000] D. Weller, J.E.E. Baglin, A.J. Kellock, K.A. Hannibal, M.F. Toney, G. Kusinski, S. Lang, L. Folks, M.E. Best, and B.D. Terris, *"Ion induced magnetization reorientation in Co/Pt multilayers for patterned media"*, Journal of Applied Physics **87**, 5768 (2000).

[Weller - 2001] D. Weller, L. Folks, M. Best, E.E. Fullerton, B.D. Terris, G.J. Kusinski, K.M. Krishnan, and G. Thomas, *"Growth, structural, and magnetic properties of high coercivity Co/Pt multilayers"*, Journal of Applied Physics **89**, 7525 (2001).

[White - 1992] R.L. White, *"Giant Magnetoresistance - a Primer"*, IEEE Transactions on Magnetics **28**(5), 2482 (1992).

[White - 1994] R.L. White, *"Giant Magnetoresistance Materials and Their Potential as Read Head Sensors"*, IEEE Transactions on Magnetics **30**(2), 346 (1994).

[White - 1997] R.L. White, R.M.H. New, and R.F.W. Pease, *"Patterned media: A viable route to 50 Gbit/in(2) and up for magnetic recording?"* IEEE Transactions on Magnetics **33**(1.2), 990 (1997).

[White - 2000] R.L. White, *"The physical boundaries to high-density magnetic recording"*, Journal of Magnetism and Magnetic Materials **209**, 1 (2000).

[White - 1985] R.M. White, *Introduction to magnetic recording*, IEEE Press, New York (1985).

[Williams - 1996] D.B. Williams and C.B. Carter, *Transmission electron microscopy: a textbook for materials science*, Plenum Press, (1996).

[Williams - 1951] H.J. Williams, F.G. Foster, and E.A. Wood, *"Observation of magnatic domains by the Kerr effect"*, Physical Review **82**, 119 (1951).

[Wittig - 1998] J.E. Wittig, T.P. Nolan, C.A. Ross, M.E. Schabes, K. Tang, R. Sinclair, and J. Bentley, *"Chromium segregation in CoCrTa/Cr and CoCrPt/Cr thin films for longitudinal recording media"*, IEEE Transactions on Magnetics **34**(4.1), 1564 (1998).

[Wong - 1999] J. Wong, A. Scherer, M. Todorovic, and S. Schultz, *"Fabrication and characterization of high aspect ratio perpendicular patterned information storage media in an Al2O3/GaAs substrate"*, Journal of Applied Physics **85**(8.2B), 5489 (1999).

[Woolley - 1964] J.C. Woolley, J.H. Phillips, and J.A. Clark, *"Ordering in CoPt-CrPt and CoPt-MnPt alloys"*, Journal of the Less-Common Metals **6**, 461 (1964).

[Yamamoto - 1990] S. Yamamoto and Y. Nakamura, *"Feasibility of multi-track perpendicular magnetic recording"*, IEEE Translation Journal on Magnetics in Japan **5**(11), 984 (1990).

[Yamamoto - 1991] S. Yamamoto, A. Fujimura, I. Watanabe, and Y. Nakamura, *"Some considerations on increase of storage capacity of perpendicular magnetic hard disk system"*, IEEE Translation Journal on Magnetics in Japan **6**(10), 848 (1991).

[Yang - 1997] W. Yang, D.N. Lambeth, L. Tang, and D.E. Laughlin, *"Epitaxial Ag templates on Si(001) for bicrystal CoCrTa media"*, Journal of Applied Physics **81**, 4370 (1997).

[Yu - 1997] Y. Yu, D. Ping, H. Peng, D. Li, and H. Ye, *"The application of energy-filtered imaging to materials research"*, Acta Metallurgica Sinica **33**(3), 233 (1997).

[Zak - 1991] J. Zak, E.R. Moog, C. Liu, and S.D. Bader, *"Magneto-optics of multilayers with arbitrary magnetization directions"*, Physical Review B (Condensed Matter) **43**(8), 6423 (1991).

[Zeper - 1989a] W.B. Zeper, F. Greidanus, and P.F. Carcia, *"Evaporated Co/Pt Layered Structures for Magneto-Optical Recording"*, IEEE Transactions on Magnetics **25**(5), 3764 (1989a).

[Zeper - 1989b] W.B. Zeper, F.J.A.M. Greidanus, P.F. Carcia, and C.R. Fincher, *"Perpendicular magnetic anisotropy and magneto-*

optical Kerr effect of vapor-deposited Co/Pt-layered structures", Journal of Applied Physics **65**(12), 4971 (1989b).

[Zeper - 1991] W.B. Zeper, H.W. Van Kesteren, B.A.J. Jacobs, J.H.M. Spruit, and P.F. Carcia, *"Hysteresis, Microstructure, and Magneto-Optical Recording in Co/Pt and Co/Pd Multilayers"*, Journal of Applied Physics **70**(4), 2264 (1991).

[Zhang - 1993a] B. Zhang, K.M. Krishnan, and R.F.C. Farrow, *"Crystallography of Co/Pt Multilayers and Nanostructures"*, Ultramicroscopy **51**, 298 (1993a).

[Zhang - 1993b] B. Zhang, K.M. Krishnan, C.H. Lee, and R.F.C. Farrow, *"Magnetic Anisotropy and Lattice Strain in Co/Pt Multilayers"*, Journal of Applied Physics **73**, 6198 (1993b).

[Ziegler - 1985] J.F. Ziegler, J.P. Biersack, and U. Littmark, *The Stopping and Range of Ions in Solids*, Pergamon Press, Inc., New York (1985).

[Ziegler - 1992] *Handbook of Ion Implantation Technology*, ed. by J.F. Ziegler, Elsevier Science Publishers B.V., (1992)

Ernest Orlando Lawrence Berkeley National Laboratory
One Cyclotron Road | Berkeley, California 94720

Prepared for the U.S. Department of Energy under Contract No. DE-AC03-76SF00098